UNIVERSITY OF COPENHAGEN
FACULTY OF SCIENCE
NIELS BOHR INSTITUTE

DAWN

PhD Thesis

Resolving Stellar Populations in Galaxies Across 13 Billion Years of Cosmic Time

Clara Giménez Arteaga

Advisor: Gabriel B. Brammer

Submitted: November 30, 2023

This thesis has been submitted to the PhD School of The Faculty of Science, University of Copenhagen

Cover image: Galaxy cluster SMACS 0723 (JWST First Deep Field)
Credit: NASA, ESA, CSA, STScI

ABSTRACT

The study of galaxy formation and evolution is a humbling exercise of acknowledging the monumental discrepancy between human lifespans and cosmic timescales and distances. We can observe how galaxies have formed and evolved from when the Universe was in its infancy to the present day, establishing connections between galaxies across cosmic time. Galaxies are complex systems made out of gas, dust, stars, and dark matter, and all but the latter emit radiation that we can detect and interpret. By observing the light from galaxies, we can infer their physical properties, characterising each component, and understanding the processes that take place in the largest chemistry and physics laboratories in the Universe.

This thesis embarks on a comprehensive exploration of galaxies, from 1 Gyr after the Big Bang to today, using the *Hubble* and *James Webb Space Telescopes*. A significant gap emerges in the study of galaxies when contrasting the local and the early Universe. Historically, high-redshift galaxies have been hindered by limited sensitivity and spatial resolution, which restricts our ability to resolve their components and conduct detailed studies of their internal structure and diversity of their stellar populations. On the other hand, local studies are enriched with an abundance of data and information, allowing us to characterise them even down to scales of tens of parsecs of individual star-forming clouds. The central theme of this thesis resolves this disparity in the study of galaxies throughout 13 billion years of cosmic time. I use spatially-resolved modelling techniques to infer the physical properties of galaxies on a pixel-by-pixel basis.

The first part of the thesis focuses in a sample of 24 local star-forming galaxies observed with the *Hubble Space Telescope* at $z \sim 0$. By developing methods to extract robust emission line fluxes from narrow-band photometry, I investigate obscured star forming regions with rarely used hydrogen recombination lines. The Paschen-series line emission probes systematically higher star formation rates than the commonly used Balmer Hα line, suffering less obscuration. With observations of Paschen lines at high redshift now enabled by *JWST*, we can better determine the star formation history in the $z > 1$ Universe produced by dusty star-forming galaxies.

In the second part I present the implications that arise from studying high-redshift galaxies in a resolved approach now possible with *JWST*, in contrast with the broadly adopted simplified and unresolved methods. Surprisingly, the inferred stellar masses are heavily impacted by this, potentially challenging current galaxy and cosmology models. In a sample of five galaxies at $5 < z < 9$, I find that stellar masses can be underestimated by up to a factor of ten when not resolved,

given the outshining by the youngest stellar populations that can dominate the integrated light of the galaxy. Recognizing the limitations of photometric-only studies, the last work combines spectroscopic information to demonstrate that our methodology is robust. I explore the contribution of a strongly-lensed galaxy to the end of reionisation, finding large variations of the ionising photon production efficiency across the galaxy.

This thesis provides valuable insights into the intricate evolution of galaxies and highlights the importance of spatially-resolved analyses to understand galaxies as the complex systems that they are.

RESUMÉ PÅ DANSK

Studiet af galaksedannelse og -udvikling er en ydmyg øvelse i at erkende den monumentale forskel mellem menneskets levetid og kosmiske tidsskalaer og afstande. Vi kan observere, hvordan galakser er blevet dannet og har udviklet sig fra Universets barndom til i dag, og vi kan etablere forbindelser mellem galakser på tværs af den kosmiske tid. Galakser er komplekse systemer, der består af gas, støv, stjerner og mørkt stof, og alle undtagen sidstnævnte udsender stråling, som vi kan registrere og fortolke. Ved at observere lyset fra galakser kan vi udlede deres fysiske egenskaber, karakterisere hver komponent og forstå de processer, der finder sted i Universets største kemi- og fysiklaboratorier.

Denne afhandling tager hul på en omfattende udforskning af galakser, fra 1 Gyr efter Big Bang til i dag, ved hjælp af *Hubble* og *James Webb Space Telescopes*. En betydelig kløft viser sig i studiet af galakser, når man sammenligner det lokale og det tidlige Univers. Historisk set har galakser med høj rødforskydning været hæmmet af begrænset følsomhed og rumlig opløsning, hvilket begrænser vores evne til at opløse deres komponenter og udføre detaljerede studier af deres interne struktur og mangfoldigheden af deres stjernepopulationer. På den anden side er lokale studier beriget med en overflod af data og information, der gør det muligt for os at karakterisere dem helt ned til skalaer på ti parsecs af individuelle stjernedannende skyer. Det centrale tema i denne afhandling løser denne forskel i studiet af galakser gennem 13 milliarder års af kosmisk tid. Jeg bruger rumligt opløste modelleringsteknikker til at udlede galaksernes fysiske egenskaber på pixel-for-pixel-basis.

Den første del af afhandlingen fokuserer på et udvalg af 24 lokale stjernedannende galakser observeret med *Hubble Space Telescope* ved $z \sim 0$. Ved at udvikle metoder til at udtrække robuste emissionslinjefluxer fra smalbåndsfotometri undersøger jeg støvfyldte stjernedannende regioner med sjældent anvendte hydrogenrekombinationslinjer. Paschen-seriens linjeemission viser systematisk højere stjernedannelsesrater end den almindeligt anvendte Balmer Hα-linje, der påvirkes mindre af støv. Med observationer af Paschen-linjer ved høj rødforskydning, som nu er gjort mulig af *JWST*, kan vi bedre bestemme stjernedannelseshistorien i $z > 1$-Universet produceret af støvfyldte stjernedannende galakser.

I anden del præsenterer jeg de konsekvenserne af at studere galakser med høj rødforskydning i den opløsning, der nu er mulig med *JWST*, i modsætning til de bredt anvendte forenklede og uopløste metoder. Overraskende nok er de udledte stjernemasser stærkt påvirket af dette, hvilket potentielt udfordrer de nuværende galakse- og kosmologimodeller. I et udvalg af fem galakser ved $5 < z < 9$ finder jeg, at stjernemasserne kan undervurderes med op til en faktor ti, når de

ikke er opløste, eftersom de overstråles af de yngste stjernepopulationer, der kan dominere galaksens integrerede lys. I erkendelse af begrænsningerne ved udelukkende fotometriske studier kombinerer det sidste arbejde spektroskopisk information for at demonstrere, at vores nye metode er robust. Jeg undersøger en stærkt linset galakses bidrag til reioniseringens slutning og finder store variationer i produktionen af ioniserende fotoner på tværs af galaksen.

Denne afhandling giver værdifuld indsigt i galaksernes komplicerede udvikling og fremhæver vigtigheden af rumligt opløste analyser for at forstå galakser som de komplekse systemer, de er.

RESUMEN EN ESPAÑOL

El estudio de la formación y evolución de las galaxias es un ejercicio de humildad en el que se reconoce la monumental discrepancia entre la duración de la vida humana y las escalas de tiempo y distancias cósmicas. Podemos observar cómo las galaxias se han formado y evolucionado desde que el Universo estaba en su infancia hasta nuestros días, estableciendo conexiones entre galaxias a través del tiempo cósmico. Las galaxias son sistemas complejos formados por gas, polvo interestelar, estrellas y materia oscura, y todas menos esta última emiten radiación que podemos detectar e interpretar. Observando la luz de las galaxias podemos inferir sus propiedades físicas, caracterizando cada componente y comprendiendo los procesos que tienen lugar en los mayores laboratorios de química y física del Universo.

Esta tesis se embarca en una exploración exhaustiva de las galaxias, desde mil millones de años después del Big Bang hasta hoy, utilizando los telescopios espaciales *Hubble* y *James Webb*. Al contrastar el Universo local con el Universo primitivo, surge una importante laguna en el estudio de las galaxias. Históricamente, las galaxias de alto *redshift* se han visto obstaculizadas por una sensibilidad y resolución espacial limitadas, lo que restringe nuestra capacidad para resolver sus componentes y realizar estudios detallados de su estructura interna y la diversidad de sus poblaciones estelares. Por otro lado, los estudios locales están enriquecidos con abundantes datos e información, lo que nos permite caracterizarlos incluso hasta escalas de decenas de parsecs de nubes individuales de formación estelar. El tema central de esta tesis resuelve esta disparidad en el estudio de las galaxias a lo largo de 13.000 millones de años de tiempo cósmico. Utilizo técnicas de modelización espacialmente resueltas para inferir las propiedades físicas de las galaxias píxel-por-píxel.

La primera parte de la tesis se centra en una muestra de 24 galaxias locales observadas con el *Telescopio Espacial Hubble* a $z \sim 0$. Mediante el desarrollo de métodos para extraer de forma robusta flujos de líneas de emisión a partir de fotometría de banda estrecha, investigo regiones de formación estelar oscurecidas con líneas de recombinación de hidrógeno poco utilizadas. La emisión de la línea de la serie Paschen sondea sistemáticamente mayores tasas de formación estelar que la línea Balmer Hα, comúnmente utilizada, sufriendo menos oscurecimiento. Con las observaciones de las líneas de Paschen a alto *redshift* que permite ahora el *JWST*, podemos determinar mejor la historia de la formación estelar en el Universo $z > 1$ producida por galaxias con alta actividad de formación estelar y alto contenido de polvo interestelar.

En la segunda parte presento las implicaciones que surgen del estudio de galaxias de alto *redshift* en un enfoque con resolución espacial que ahora es posible con el *JWST*, en contraste con los métodos simplificados y no resueltos ampliamente adoptados. Sorprendentemente, las masas estelares inferidas se ven fuertemente afectadas por esto, desafiando potencialmente los modelos galácticos y cosmológicos actuales. En una muestra de cinco galaxias a $5 < z < 9$, encuentro que las masas estelares pueden subestimarse hasta en un factor de diez cuando no se resuelven, dado el eclipsamiento por las poblaciones estelares más jóvenes que pueden dominar la luz integrada de la galaxia. Reconociendo las limitaciones de los estudios únicamente fotométricos, el último trabajo combina información espectroscópica para demostrar que nuestra metodología es robusta. También exploro la contribución de una galaxia fuertemente magnificada al final de la reionización, encontrando grandes variaciones de la producción de fotones ionizantes a lo largo de la galaxia.

Esta tesis aporta valiosas perspectivas sobre la complicada evolución de las galaxias, y pone émfasis en la importancia de los análisis espacialmente resueltos para entender las galaxias como los complejos sistemas que son.

RESUM EN CATALÀ

L'estudi de la formació i l'evolució de les galàxies és un exercici d'humilitat en què es reconeix la monumental discrepància entre la durada de la vida humana i les escales de temps i distàncies còsmiques. Podem observar com les galàxies s'han format i evolucionat des que l'Univers estava a la seva infància fins als nostres dies, establint connexions entre galàxies a través del temps còsmic. Les galàxies són sistemes complexos formats per gas, pols interestel·lar, estrelles i matèria fosca, i totes menys aquesta darrera emeten radiació que podem detectar i interpretar. Observant la llum de les galàxies podem inferir-ne les propietats físiques, caracteritzant cada component i comprenent els processos que tenen lloc en els laboratoris de química i física més grans de l'Univers.

Aquesta tesi s'embarca en una exploració exhaustiva de les galàxies, des de mil milions d'anys després del Big Bang fins avui, utilitzant els telescopis espacials *Hubble* i *James Webb*. En contrastar l'Univers local amb l'Univers primitiu, sorgeix una llacuna important a l'estudi de les galàxies. Històricament, les galàxies d'alt *redshift* s'han vist obstaculitzades per una sensibilitat i una resolució espacial limitades, cosa que restringeix la nostra capacitat per resoldre els seus components i realitzar estudis detallats de la seva estructura interna i la diversitat de les seves poblacions estel·lars. D'altra banda, els estudis locals estan enriquits amb abundants dades i informació, cosa que ens permet caracteritzar-les fins i tot fins a escales de desenes de parsecs de núvols individuals de formació estel·lar. El tema central d'aquesta tesi resol aquesta disparitat a l'estudi de les galàxies al llarg de 13.000 milions d'anys de temps còsmic. Utilitzo tècniques de modelització espacialment resoltes per inferir les propietats físiques de les galàxies píxel-per-píxel.

La primera part de la tesi està centrada en una mostra de 24 galàxies locals observades amb el *Telescopi Espacial Hubble* a $z \sim 0$. Mitjançant el desenvolupament de mètodes per extreure de forma robusta fluxos de línies d'emissió a partir de fotometria de banda estreta, investigo regions de formació estel·lar enfosquides amb línies de recombinació d'hidrogen poc utilitzades. L'emissió de la línia de la sèrie Paschen sondeja sistemàticament majors taxes de formació estel·lar que la línia Balmer Hα, habitualment utilitzada, patint menys enfosquiment. Amb les observacions de les línies de Paschen a alt *redshift* que permet ara el *JWST*, podem determinar millor la història de la formació estel·lar a l'Univers $z > 1$ produïda per galàxies amb alta activitat de formació estel·lar i alt contingut de pols interestel·lar.

A la segona part presento les implicacions que sorgeixen de l'estudi de galàxies d'alt *redshift* en un enfocament amb resolució espacial que ara és possible

amb el *JWST*, en contrast amb els mètodes simplificats i no resolts àmpliament adoptats. Sorprenentment, les masses estel·lars inferides es veuen fortament afectades per això, desafiant potencialment els models galàctics i cosmològics actuals. En una mostra de cinc galàxies a $5 < z < 9$, trobo que les masses estel·lars poden subestimar-se fins a un factor de deu quan no es resolen, atès l'eclipsament per les poblacions estel·lars més joves que poden dominar la llum integrada de la galàxia. Reconeixent les limitacions dels estudis únicament fotomètrics, el darrer treball combina informació espectroscòpica per demostrar que la nostra metodologia és robusta. També explora la contribució d'una galàxia fortament magnificada al final de la reionització, trobant grans variacions de la producció de fotons ionitzants al llarg de la galàxia.

Aquesta tesi aporta valuoses perspectives sobre la complicada evolució de les galàxies, i posa èmfasi en la importància dels anàlisis espacialment resolts per entendre les galàxies com els complexos sistemes que són.

ACKNOWLEDGEMENTS

I would like to start by expressing my gratitude to Gabe Brammer. Thank you for always helping and guiding me whenever I knocked on your door. I am very grateful for the independence you have given me during this PhD and your trust in my work. A huge thanks goes to Kasper Heintz, Francesco Valentino and Seiji Fujimoto, for being fantastic mentors and a great help throughout this PhD. As well as Charlotte, Victoria, Francesca, Sune and Lise. A very special thanks goes to the best admin team Guarn and Helena. Thanks to my fellow PhDs Malte, Vadim, Meghana, Kate, my office squad and everyone else at DAWN that has joined during these years.

I want to thank the thesis committee Prof. Alexandra Pope, Dr. Pablo Pérez González and Prof. Sune Toft, for showing interest in my research and taking the time to assess this dissertation.

I want to express my gratitude to Luis Colina, for hosting me in Madrid at Centro de Astrobiología, and being instrumental in the completion of my first paper. I also want to deeply thank Pascal Oesch, for mentoring me during my stay abroad at the University of Geneva. Thanks to Tanita and the rest of the Observatory in Genève for welcoming me, feeding me fondue, and making it such a fun time there. Thanks to the rest of international collaborators that have helped me throughout the years.

Thank you to the professors that guided me as teaching assistant, Martin Pessah, Johan Fynbo and Troels Petersen. Thanks to co-TA Mikkel Kristensen and the wonderful students I have had.

I would like to endlessly thank my parents for their constant support. Thanks to you I made it to Denmark in the first place. Thanks for always encouraging and supporting my curiosity, allowing me to try every possible hobby there is, and any interest I would find along the way. I am forever grateful for my brother Pablo, who is probably the only person who might read this thesis, as well as for the rest of my family back home.

I would like to thank Michelle Mary Turley for her unwavering support and always being a joy to have around. Thanks to the rest of my friends here and especially at home, for not forgetting about me.

This thesis is dedicated to my grandparents Juan José, Inés, Secundino and Leonor. A very special shout-out goes to my *abuela* Inés, who thinks I have been studying astrology in Sweden for the past three years, and has been very supportive nonetheless.

Last but not least, grazie mille Irene. This PhD will forever be worth it, because it led me to you.

CONTENTS

1

INTRODUCTION

"Science progresses best when observations force us to alter our preconceptions."
- Vera Rubin

ASTRONOMY is often regarded as the oldest of the natural sciences, devoted to studying celestial objects. For millennia, humans have looked at the night sky in awe, and tried to unravel the mysteries of the cosmos. A source of inspiration and knowledge for some, a source of endless questions for others, the Universe has continuously impacted humanity throughout its history.

At the heart of this cosmic exploration lies the study of galaxies, which serve as the building blocks of the Universe and are key to understanding its evolution. Galaxies are cosmic architectural marvels, made out of stars, gas, dust, and dark matter, bound together by gravity. Galaxies are not static objects, but dynamic entities in constant motion and activity. In them, stars are born, they evolve and eventually die, some producing spectacular supernova explosions, which enrich their surroundings with heavier metals. Galaxies also collide and merge, forging new structures and reshaping their intergalactic neighbourhoods.

1.1 A HISTORICAL JOURNEY

The study of galaxies has been a cornerstone of human curiosity and scientific exploration for centuries. The roots of astronomy trace back to ancient civilisations. Mesopotamian cultures, such as the Babylonians, meticulously recorded celestial events and identified recurring patterns among the stars (Rochberg 2004). In ancient Greece, scientists like Claudius Ptolemy developed geocentric models of the cosmos, attempting to explain the motions of celestial bodies. During this time, galaxies were perceived as “nebulous” or fuzzy patches in the night sky, often mistaken for comets or unresolved star clusters.

The turning point in our understanding of the cosmos came with the invention of the telescope in the early 17th century. Galileo Galilei, a pioneer in the use of telescopes for astronomical observations, turned his gaze towards the

Milky Way. He was amongst the first to discern that it consisted of countless individual stars, dispelling the notion that it was a luminous cloud (Galilei 1710). This revolutionary revelation laid the foundation for the modern understanding of galaxies as vast collections of stars.

The true nature of galaxies as distinct, self-contained entities began to emerge in the 18th and 19th centuries. Astronomers like William Herschel, armed with more advanced telescopes, embarked on systematic surveys of the night sky (Herschel 1802). Herschel's observations and cataloguing efforts unveiled the existence of galaxies beyond our own Milky Way, including the Andromeda Galaxy, previously thought to be a nebulous patch.

The 20th century brought profound advancements in our understanding of galaxies. Edwin Hubble, through meticulous observations and the use of the luminosity-distance relationship found by Henrietta Leavitt (Leavitt & Pickering 1912), demonstrated that galaxies were not static entities but were instead receding from one another. Hubble's work led to the formulation of Hubble's Law (Hubble 1929), and the realization that the Universe was expanding. This marked a pivotal moment in the history of astronomy, as it laid the groundwork for modern cosmology and the Big Bang theory. Further, he realised that galaxies come in many shapes and sizes, presenting the first morphology and evolution sequence (Hubble 1926).

Today, the study of galaxies has entered a new era. Space-based observatories like the *Hubble Space Telescope* (HST) and, more recently, the *James Webb Space Telescope* (*JWST*), offer unprecedented capabilities for capturing high-resolution images and spectra of galaxies across the Universe. These observatories have unveiled the intricacies of galactic structures, the dynamics of star formation, and the composition of galaxies in remarkable detail. As we stand at the beginning of a new era in the exploration of galaxies, we continue to probe deeper into the cosmos, seeking answers to fundamental questions, and unlocking the mysteries of these cosmic entities that have fascinated humanity for centuries.

1.2 GALAXY FORMATION AND EVOLUTION

The field of galaxy formation and evolution has witnessed remarkable progress in recent years. The multifaceted nature of this field revolves around fundamental questions related to the timeline of cosmic events, the mechanisms governing galaxy formation, the evolution of galaxies over cosmic time, and the intricate processes that lead to the cessation of star formation within galaxies, also known as quenching.

In the research of galaxy evolution, one cannot simply select a single galaxy and observe its evolution, given the unbelievable disparity between the human lifespan and the cosmic timescales. Instead, one must try to connect different galaxies at low and high redshifts. This involves identifying progenitors of our

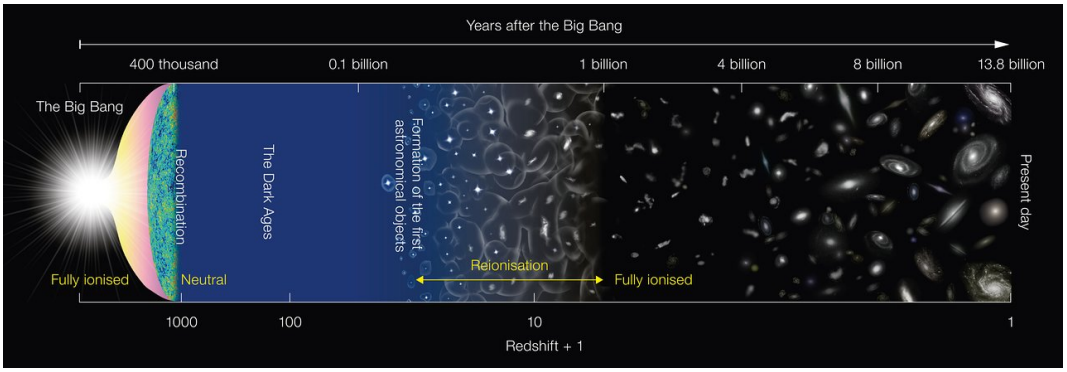

Figure 1: A brief history the Universe across 13.8 billion years of cosmic time, from the Big Bang to the present day. Credit: NAOJ.

present-day neighbouring galaxies, establishing links based on their physical properties, morphologies, merging mechanisms, and striving to understand how their evolution took place. This introductory chapter provides an overview of these topics, highlighting key issues and unknowns that continue to drive research in the field, and finally motivates the research goals of this thesis.

1.2.1 *A Brief History of Time and its Unknowns*

Understanding galaxies goes beyond mere observation, it delves into the very fabric of the history of the Universe. By examining galaxies across cosmic time, we can unravel the story of its evolution, from the primordial moments after the Big Bang to the diverse web of structures we see today. We seek answers to profound questions: When did galaxies first light up the Universe? How do galaxies form and evolve? What triggers the quenching of star formation within galaxies?

In the early moments after the Big Bang, the Universe was extremely hot and dense. No photon could escape from being constantly scattered and absorbed by fundamental particles, including protons and electrons. When the Universe had expanded and cooled enough, electrons combined with protons to form neutral hydrogen and helium atoms. Photons were finally able to travel freely, producing what is known as the cosmic microwave background (CMB, Penzias & Wilson 1965), the first image we can obtain of the early Universe ($z \sim 1100$, see Figure 1). After this process of recombination, the Universe delved into the cosmic Dark Ages, when it was fully neutral, before any star or galaxy had yet shed any light.

At a still unknown time, the first stars and galaxies began to form in the early Universe. The formation of galaxies is a complex interplay of gravitational collapse, gas accretion, and hierarchical merging. Current theoretical models, including cold dark matter simulations, have made significant strides in elucidating

the initial conditions of galaxy formation. Nevertheless, critical questions persist regarding the precise mechanisms that drive the assembly of galaxies and their subsequent evolution (see Bromm & Yoshida 2011, for a review). Simulations within the framework of the Lambda Cold Dark Matter (ΛCDM) cosmological model suggest that galaxies formed at redshifts in the range $10 < z < 30$ (see e.g., Dayal & Ferrara 2018, for a review), corresponding to $\sim 100-400$ Myr after the Big Bang. These suggest that the first generation of stars, known as Population III stars (Heger & Woosley 2002; Bromm 2013), began to form from the gravitational collapse of dark matter haloes (White & Rees 1978; Springel et al. 2005). After the gas collapsed, it cooled until it could form molecular clouds and eventually stars. With the unprecedented capabilities of *JWST*, Pop III signatures such as strong He II (λ1640 Å) emission are being studied (e.g., Maiolino et al. 2023; Trussler et al. 2023). The most distant star observed so far, called Earandel, has been detected with *JWST* at $z = 6.2$ (Welch et al. 2022a,b), possible given its extreme magnification. These first stars then assembled into the first galaxies in the Universe (White & Frenk 1991). Multiple studies have explored dark matter haloes as key drivers of galaxy evolution (e.g., Lyu et al. 2023).

Deep extragalactic surveys have been instrumental in finding galaxies in the early Universe (e.g., Cosmic Assembly Near-infrared Deep Extragalactic Legacy Survey, CANDELS, Grogin et al. 2011; Koekemoer et al. 2011; Cosmic Evolution Survey, COSMOS, Scoville et al. 2007; Laigle et al. 2016; Weaver et al. 2022; Hubble Ultra Deep Field, HUDF, Ellis et al. 2013; Illingworth et al. 2013; Hubble Frontier Fields, HFF, Shipley et al. 2018; and most recently the *JWST* Advanced Deep Extragalactic Survey, JADES, Eisenstein et al. 2023; the Cosmic Evolution Early Release Science, CEERS, Finkelstein et al. 2023; and the First Reionization Epoch Spectroscopically Complete Observations survey, FRESCO, Oesch et al. 2023). Up until the advent of *JWST*, the furthest known galaxy was GN-z11 (Oesch et al. 2016), spectro-photometrically confirmed with the *Hubble Space Telescope*. In the last year, multiple candidates have been proposed to be galaxies at even higher redshifts (e.g., Naidu et al. 2022b; Atek et al. 2023; Harikane et al. 2023b; Casey et al. 2023), getting us closer into the formation epoch. Currently, the new milestone in the redshift frontier has been reached by JADES-GS-z13-0, a Lyman-break galaxy at $z = 13.2$ (Curtis-Lake et al. 2023; Robertson et al. 2023), when the Universe was merely ~ 300 Myr old. In fact, *JWST* observations have revealed that UV luminous galaxies are much more abundant than expected in the early ($z > 9$) Universe (e.g., Harikane et al. 2023a). The study of these early objects has highlighted the contrast with respect to the galaxies that we see in the present day, having significant differences in terms of metallicity, morphology, chemical abundances, dust content, amongst others (e.g., Curti et al. 2023b; Heintz et al. 2023a,b). These galaxies have undergone billions of years of evolutionary processes that have led them to become their present day

counterparts. These processes are still yet to be fully understood (e.g., Crain & van de Voort 2023).

A pivotal epoch in the history of the cosmos is the period of reionisation, marking the transition from a predominantly neutral to an ionised Universe. This transformation occurred in the early Universe, but pinpointing its precise timing remains a challenge. Observations estimate the end of this epoch to be at $z \sim 6$ (Fan et al. 2006; Yang et al. 2020). Studies of high-redshift galaxies, Lyman-α emitters, and the CMB radiation have contributed to a refined understanding of reionisation, yet uncertainties persist (see Robertson 2022, for a review). It is a fundamental question in galaxy evolution what the primary contributor to the reionisation of the intergalactic medium (IGM) is. The predominant theory is that UV ionising radiation in galaxies from young massive stars is the main driver of this transition (e.g., Rosdahl et al. 2018; Trebitsch et al. 2020), although the active galactic nuclei (AGN) contribution might be more prominent than previously thought (Maiolino et al. 2023). Most recently, an abundance of AGN have been detected at $z > 4$ with *JWST*, with an estimated contribution to reionisation of up to $\sim 50\%$ at $z \sim 6$ (Harikane et al. 2023c). AGN are a vital ingredient in the evolution of galaxies (Richstone et al. 1998; Kormendy & Gebhardt 2001). During the last decades, many works have tried to dissect the co-evolution between super-massive black holes (SMBHs) and their host galaxies, given the multiple correlations between their observed properties (e.g., Magorrian et al. 1998; Ferrarese & Merritt 2000; Tremaine et al. 2002; Häring & Rix 2004; Graham & Driver 2007; Kormendy & Ho 2013; Pope et al. 2019).

As the Universe evolved, small early galaxies and the first stars merged and accreted more matter, gradually forming more massive galaxies. The stellar, dust and metal contents increased over time (e.g., Nakajima et al. 2023; Heintz et al. 2023a). The lifecycle of stars enriched the Universe with heavy elements and dust (Curti et al. 2023a). The peak of star formation activity in galaxies is estimated to have occurred around $z \sim 2$ (Figure 2, from Madau & Dickinson 2014), an epoch that is also known as Cosmic Noon. Significantly, the rate of galaxy mergers is believed to also peak around $z \sim 2$ (e.g., O'Leary et al. 2021), reinforcing the connection between star-formation activity triggered by mergers. After that, the cosmic star formation history gradually declined to the present day, which simulations attribute to a reduction in the rate of gas accretion into galaxies (e.g., Mitchell et al. 2014; Sparre et al. 2015), yielding less available gas to form stars. Nowadays, our local Universe is filled with a diverse landscape of galaxies, with low galaxy growth and evolution when compared to past epochs.

1.2.2 *Galaxy Diversity*

Observations across cosmic epochs reveal a dynamic landscape of evolving galaxies. While the hierarchical merging paradigm provides a framework for

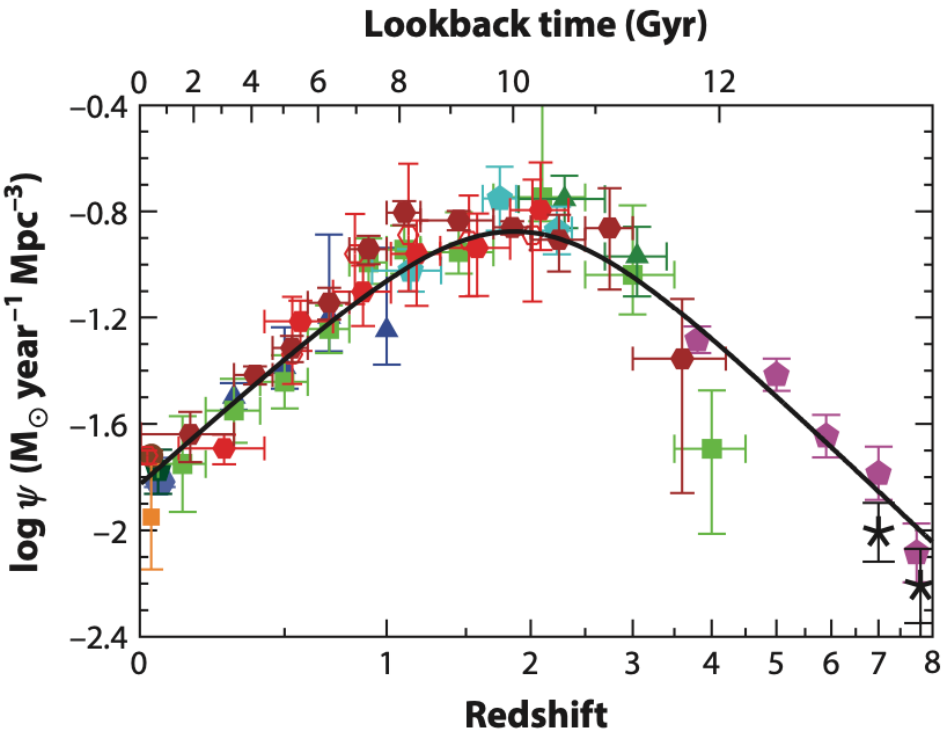

Figure 2: The history of cosmic star formation from far-ultraviolet and infrared rest-frame measurements, compiled by Madau & Dickinson (2014). The cosmic star formation history rises until $z \sim 2$, reaching the peak when the Universe was ~ 3.5 Gyr old, and then it gradually declines to the present day.

galaxy evolution (Hopkins et al. 2006), the specifics of how galaxies transform over time remain an active area of investigation. Studies employing multi-wavelength surveys, integral field spectroscopy, and deep imaging have unveiled a rich tapestry of galaxy morphologies, sizes, and stellar populations. Yet, the factors governing the diversity of galaxy types and their evolutionary trajectories remain an open question (Förster Schreiber & Wuyts 2020).

In terms of galactic morphology, two distinct populations emerge – spiral galaxies and elliptical galaxies. Moreover, the shape appears to correlate with other significant differences between the two (see e.g., Conselice 2014, for a review). Spiral galaxies are characterized by their flattened, disk-like structure, featuring a central bulge with a dense concentration of stars, and often a supermassive black hole (Lynden-Bell 1969). They are recognized by their prominent spiral arms, which extend outward from the central nucleus. These arms showcase clusters of luminous stars, and they host regions of active star formation, fostering the birth of for example massive O and B-type stars, which are young and short lived ($\leq$100 Myr). They display a broad range of spectral characteristics, reflecting ongoing star formation from a variety of stellar populations.

Additionally, spiral galaxies often contain significant reservoirs of dust and gas, essential components for star formation and the creation of planetary systems. Dust can particularly obscure regions of intense star formation, with hydrogen recombination lines tracing ionised H II regions where new stars are being born ("birthclouds", see e.g., Greener et al. 2020). Uncovering the obscured star formation activity is vital to comprehend these systems.

Conversely, elliptical galaxies present a distinct morphology, appearing spherical or ellipsoidal in shape. They exhibit a roughly uniform luminosity across their structure, and are characterized by aging stellar populations with fewer young, massive stars compared to spirals (Djorgovski & Davis 1987). These galaxies often rank amongst the most massive and densely populated in the Universe (Toft et al. 2014). Elliptical galaxies are commonly described as "quenched" or "quiescent" galaxies, due to their limited or complete lack of ongoing star formation, showing little to no emission in the UV range. Understanding the mechanisms behind quenching is a critical puzzle piece in galaxy evolution. Processes such as feedback from AGN, environmental effects, and depletion of the gas and dust reservoirs have been proposed as quenching agents (see e.g., Man & Belli 2018, and references therein), yet the relative contributions and their dependence on galaxy properties remain uncertain.

The study of spiral and elliptical galaxies not only sheds light on the morphology and properties of these galactic objects but also raises intriguing questions about their origins, evolutionary trajectories, and their contributions to our comprehension of the broader cosmic narrative. The bimodality between both galaxy populations becomes apparent when studying the star formation activity (SFR) as a function of the stellar mass content (M_*), in what is called the main sequence (MS) of star formation (Brinchmann et al. 2004; Noeske et al. 2007; Whitaker et al. 2012). Here, spiral star-forming galaxies (SFGs) fall in a tight MS relation, whereas quenched galaxies appear in a different plane (see Figure 3). Quiescent elliptical galaxies fall below the MS, displaying negligible star formation. A distinct in-between population appears above the MS, referred to as starburst galaxies (Goto 2005; French 2021), which undergo a rapid and intense phase of very active star formation, and often present irregular morphology. Evolutionary theories suggest them as a population transitioning from star forming disk galaxies into quiescent ellipticals (Pawlik et al. 2019). The MS relationship holds across redshifts, with the specific SFR (sSFR=SFR/M_*) increasing with redshift (Schreiber et al. 2015; Leslie et al. 2020). Simulations are able to reproduce the SFR MS even at $z \sim 7$ (e.g., Pallottini et al. 2022).

Morphology also correlates with observed colours – star-forming galaxies appear bluer, whereas massive elliptical galaxies tend to be red. The latter creates degeneracies with high-redshift or dusty galaxies, given the reddening that all these properties yield in the observed colour of a galaxy (Conroy 2013). This

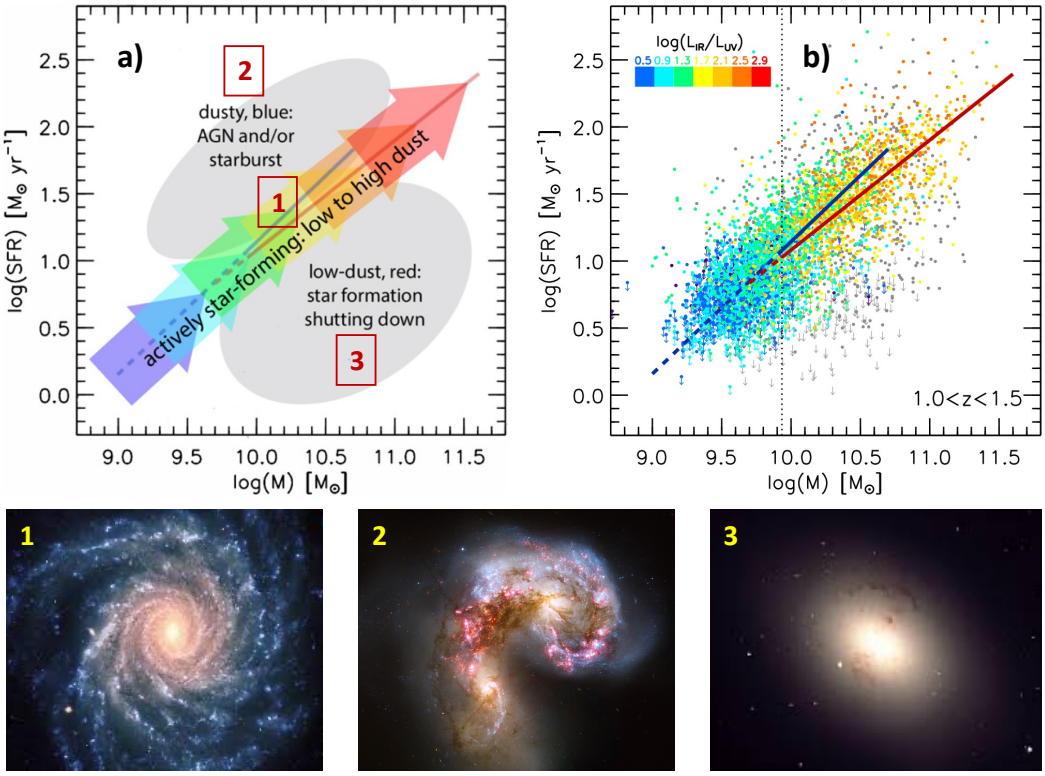

Figure 3: **Top:** The star-forming Main Sequence. *a)* Cartoon indicating the position of each type of galaxy, given its star formation activity, dust content, and observed colour. *b)* SFR versus stellar mass for galaxies at redshift $1.0 < z < 1.5$, colour-coded according to their infrared excess (IR luminosity over UV luminosity), which traces the amount of dust. Figures from Whitaker et al. (2012). **Bottom:** Three examples of different galaxy morphologies – Star-forming spiral (1), irregular starburst (2), and elliptical quenched galaxy (3). Their position in the MS sequence is indicated on plot *a*.

is one of the main issues in the modelling of spectral energy distributions of galaxies based on photometric observations, as will be discussed later on.

1.2.3 *How Do Galaxies Transform and Evolve?*

We have explored the variety of galaxies we observe throughout cosmic history. However, what are the evolutionary processes and transformations that galaxies undergo during their lifecycles? How do we reconcile the observed galaxy population in the nearby Universe with their high-redshift progenitors, which can appear vastly different and challenging to link across different cosmic eras? Galaxies can be transformed by multiple processes, including the above-mentioned mergers, quenching, gas accretion, and dust and metal enrichment, amongst others.

Mergers have been extensively studied both in observations as well as simulations (e.g., Lacey & Cole 1993; Sanders & Mirabel 1996; Le Fèvre et al. 2000; De Lucia & Blaizot 2007; Lambas et al. 2012; Renaud et al. 2019). Mergers occur when two or more galaxies come into close proximity and gravitationally interact with each other. Galaxy mergers often result in a significant morphological transformation of the involved galaxies. Spiral galaxies can be distorted and transformed into elliptical galaxies (e.g., Duc et al. 2015), and irregular galaxies can be created through the merger process. Galaxy mergers can trigger intense bursts of star formation. As the galaxies collide and their gas clouds interact, the compression and shockwaves can lead to the formation of new stars (U et al. 2019). This can result in the creation of star clusters, enhancing the overall stellar population of the merged galaxy. Given all these important impacts, galaxy mergers are thought to have played a significant role in the cosmic evolution of galaxies, leading to the growth of more massive galaxies over time (Bell et al. 2006). Nevertheless, some works have deemed improbable that significant galactic mergers occur frequently enough to be the primary means of galaxy transformation (Weigel et al. 2017). On the other hand, recent studies (e.g., Romano et al. 2021) provide new constraints on the merger fraction at high redshifts, indicating their prominent role in the galaxy build-up in the early Universe.

Dust and chemical enrichment influence significantly the evolution and transformation of galaxies (Heintz et al. 2023b). Dust particles within galaxies consist primarily of carbon, silicon, and other heavy elements (Savage & Mathis 1979). Dust grains heavily impact our observations, as will be expanded upon later on. Most importantly, dust grains serve as catalysts for the formation of molecular hydrogen, fundamental ingredient for the formation of new stars (e.g., van Dishoeck & Black 1988; van Dishoeck & Blake 1998; Wakelam et al. 2017). Thus, the presence and distribution of dust can either promote or impede star formation within galaxies. Dust can also facilitate star formation by shielding gas clouds from strong ionising radiation. Dust and chemical enrichment are intertwined within galaxies. Dust grains serve as carriers and reservoirs of heavy elements, and can serve as condensation sites for heavier elements, contributing to the overall metallicity of the interstellar medium (ISM).

As galaxies evolve, dust can experience diverse physical processes (Dwek 1998). Dust grains are predominantly created in supernova events of massive stars (Hoyle & Wickramasinghe 1970; Sarangi et al. 2019; Witstok et al. 2023), the circumstellar envelopes of red giants (assymptotic giant branch stars, AGB, Schneider et al. 2014), and non-stellar formation mechanisms such as grain growth and coalescence in the ISM (see e.g., Michałowski et al. 2010). Over time, they can grow through accretion (Draine 2009), be disintegrated in harsh radiation fields (Jones & Nuth 2011), and be expelled into the ISM via outflows and galactic winds, enriching it with heavy elements (e.g., Curti et al. 2020; Ramburuth-Hurt et al. 2023). The dynamic equilibrium between dust formation,

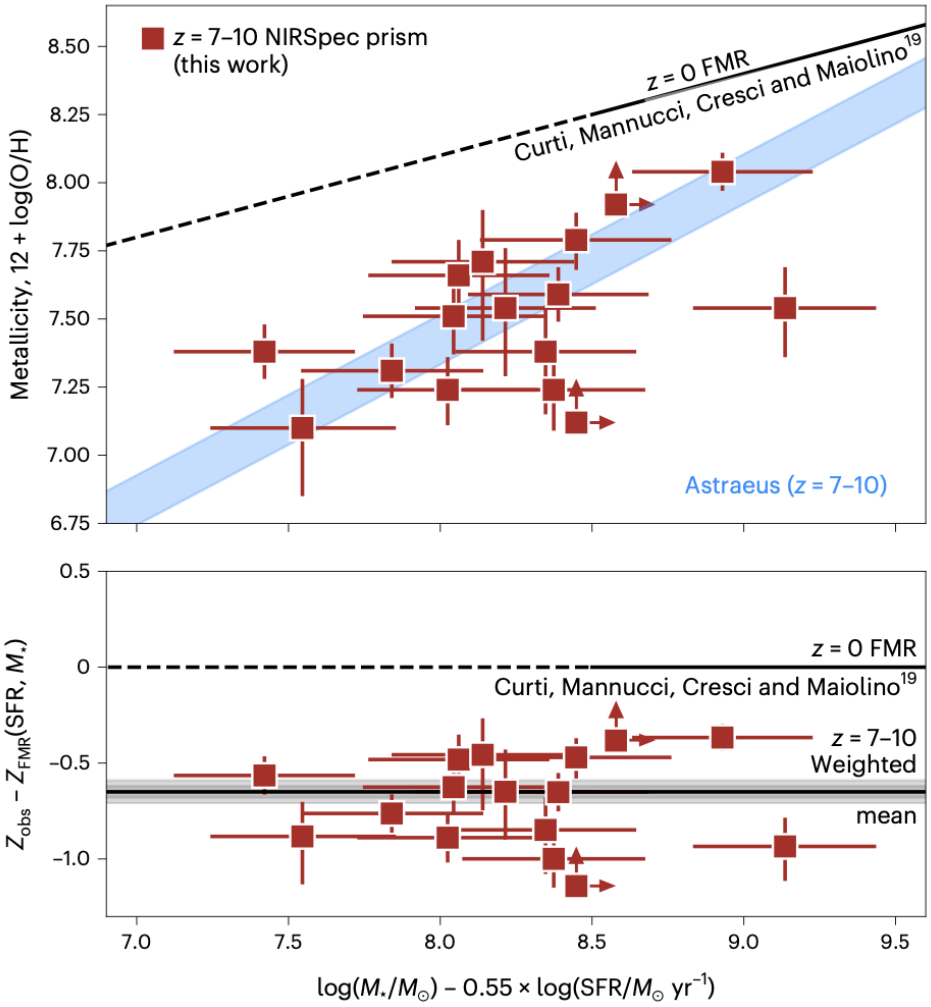

Figure 4: The fundamental metallicity relation (FMR) of $z = 7-10$ galaxies. The top panel shows the local FMR ($z = 0$) from Curti et al. (2020), and the bottom panel shows its offset from the high-redshift galaxies. The Astraeus simulations (Hutter et al. 2021) agree with the observational measurements. Figure from Heintz et al. (2023a).

growth, and destruction influences the overall dust content of galaxies. The start of dust enrichment is still unknown, but the past decade has brought the first dust continuum detections through far-infrared observations at $z \sim 7-8$ (e.g., Watson et al. 2015).

Chemical enrichment starts from the nuclear cores of massive stars, which release heavy elements into the ISM during supernova explosions, and in low-mass AGB stars as well. As subsequent generations of stars form from this enriched gas, they inherit a higher metallicity, altering their spectral characteristics. Galaxies have been observed to experience continuous chemical enrichment through cosmic time (Rafelski et al. 2014; Nakajima et al. 2023), as they forge new stars, from an almost null early metal and dust content (Fumagalli et al. 2011). Through

a galaxy's lifetime, however, metallicity can vary given the balance between the different creation and depletion mechanisms. The overall metallicity increase of a galaxy influences various galactic processes. An elevated metallicity can affect the cooling and fragmentation of gas clouds, thereby influencing the star formation rate.

The metal content of galaxies has been observed to correlate with the stellar mass and SFR, in what is called the fundamental metallicity relation (FMR, Mannucci et al. 2010). All galaxies lie in a single plane across redshifts. Most recently, using *JWST* observations, Heintz et al. (2023a) have found galaxies at $z \sim 7-10$ following a unique FMR (see Figure 4), and chemical abundances below what the local FMR predicts, and below the FMR of galaxies through most of cosmic time ($\sim$ 12 Gyr). This can be explained by continuous pristine gas accretion from the IGM.

A galaxy can also transform by interacting with its environment. This can occur in various ways (Noguchi 2023). Galaxies can accrete pristine gas from the circumgalactic medium (CGM, Tumlinson et al. 2017) and IGM, as well as ejecting dust and metal-enriched gas through outflows and stellar feedback (e.g., Ginolfi et al. 2020). Gas accretion thus plays a fundamental role in replenishing the gas reservoir of galaxies, enabling star formation (see e.g., Somerville & Davé 2015).

Ultimately, a dramatic transformation in a galaxy is its death. There are multiple processes proposed to cause such fate, although it is not yet well understood what is the dominant quenching mechanism, if any, or how much each mode contributes to the overall star formation cessation in a galaxy. A compilation of quenching processes was reviewed by Man & Belli (2018) (shown in Figure 5). In summary, all processes involve the lack of *appropriate* star-forming gas. Either the gas is not being accreted into the galaxy, or it is being removed due to e.g. AGN feedback (King & Pounds 2015; Veilleux et al. 2020). Regarding the gas within the galaxy, it could be that it cannot cool enough to collapse into stars given several processes (see Figure 5), or that the already cold gas is not capable of forming stars, or finally, that the galaxy is too efficient at forming stars, consuming rapidly the available cold gas. A comprehensive understanding of quenching remains one of the main topics and goals in the field of galaxy formation and evolution.

Hopkins et al. (2008) provided a schematic of the co-evolution of SMBHs and elliptical galaxies, following a merger-induced burst of star formation. Figure 6 shows this evolutionary path, starting from an isolated spiral galaxy (cutout *a*). The central panels show the star formation history (top) and the evolution of the galaxy luminosity (bottom). Cutouts *b* and *c* display the local galaxy group that gets gravitationally bound until there is a major merger. Here, the SFR begins to rise, and the feedback in the galaxy is dominated by stellar winds. Afterwards, the star formation and the luminosity peak during the starburst phase. Then,

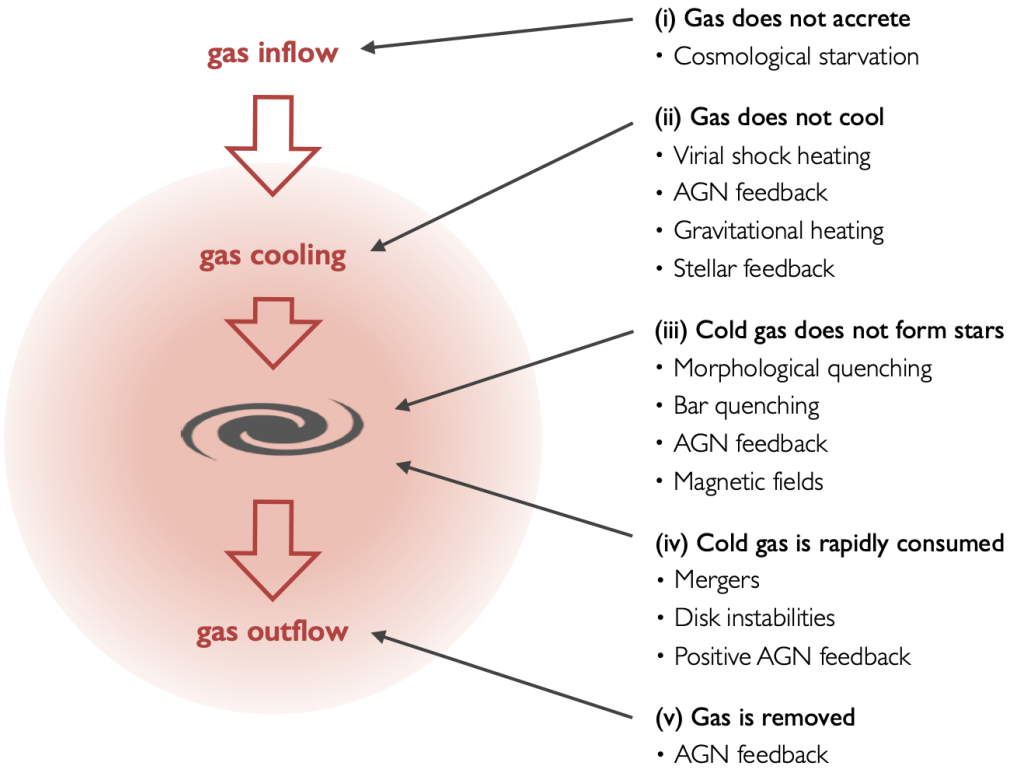

Figure 5: Quenching mechanisms in galaxies. Figure from Man & Belli (2018).

the black hole growth dominates the luminosity and the feedback within the galaxy during the blowout phase (panel *e*), depleting the remaining dust and gas reservoirs. This yields a quasi-stellar object (QSO, quasar), which is a galaxy dominated in emission by its central AGN. The luminosity of the QSO quickly dims. Lastly, cutout *h* displays a typical elliptical galaxy, which has ceased to form stars, and continues growing by "dry" mergers, in which the galaxy increases in mass but no star formation is induced (e.g., Ciotti et al. 2007). Later studies have added more evidence in agreement with this evolutionary path of elliptical galaxies, proposing sub-millimeter galaxies (SMGs) as their progenitors (see e.g., Pope et al. 2008; Toft et al. 2014; Valentino et al. 2020b).

1.3 OBSERVATIONAL STUDY OF GALAXIES

The study of galaxies is a multidimensional endeavor that relies on a diverse range of observational techniques and instruments. Understanding these methods and the wealth of information they provide is crucial for unraveling the mysteries of galaxy formation, evolution, and the composition of the Universe itself. This introductory chapter provides an overview of the observational tools

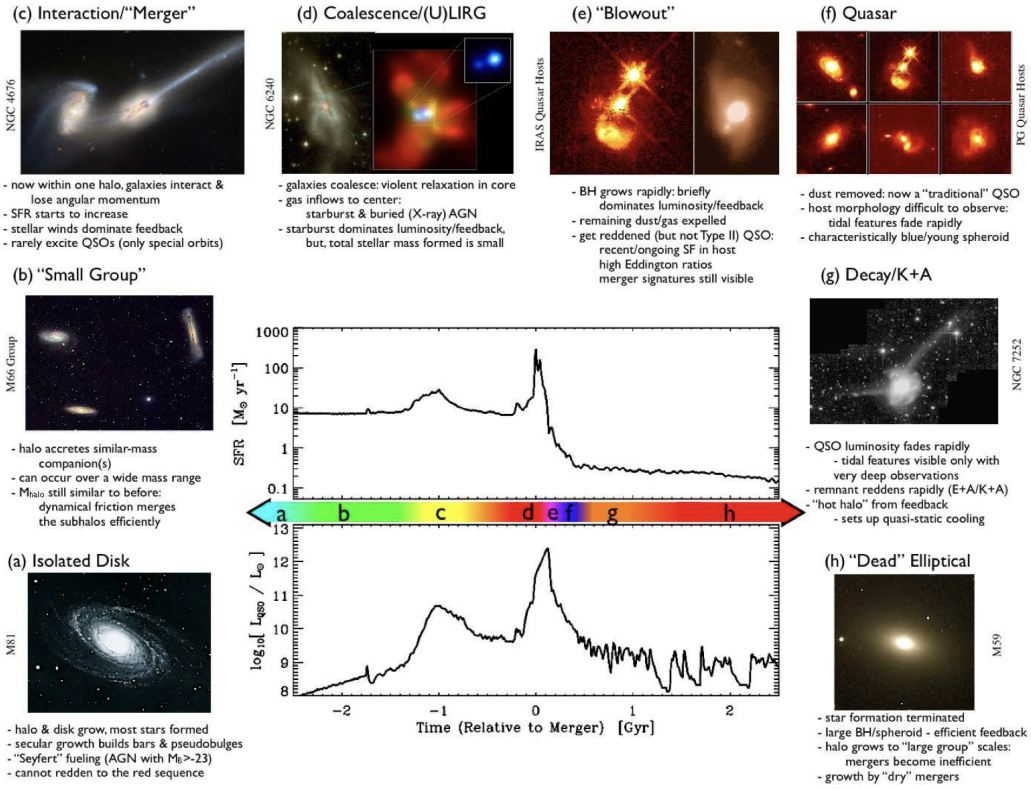

Figure 6: The evolution from an isolated disk galaxy to an elliptical galaxy, including a star-forming burst caused by a gas-rich major merger. The central plots display the star formation history (top) and the evolution of the luminosity (bottom). Figure from Hopkins et al. (2008).

and techniques employed to explore galaxies, emphasizing the complementary nature of different wavelengths and spectroscopic and photometric approaches.

1.3.1 *Photometry and Spectroscopy*

Galaxies emit across the electromagnetic spectrum. One can infer an abundance of information from a galaxy spectrum. Firstly, spectroscopic observations have extensively provided robust redshifts, key to disentangle high-redshift galaxy candidates from low-z interlopers (e.g., Zavala et al. 2023). Additionally, through tracers and empirical relations, we can infer the physical properties of galaxies from their observed spectral features (see e.g. Kewley et al. 2019; Maiolino & Mannucci 2019, for a review). As a caveat, spectroscopy demands a substantial amount of observing time, to get the necessary sensitivity and detections to perform significant analyses. In particular, faint and distant galaxies require considerably long exposure times, which can be hard to achieve in practice with state-of-the-art telescopes such as *JWST*.

Photometric observations measure the intensity of light at various wavelengths. By constructing spectral energy distributions (SEDs) from photometric data (see the next section for more information), we can in a complementary way determine galaxy properties like stellar mass, SFRs, and dust content, amongst others. Imaging observatories have a series of filters that are sensitive to a specific wavelength range, providing an image of the galaxy in each bandpass. Conversely to spectroscopy, where we can only obtain an integrated measurement of the spectral properties of a galaxy, photometry provides us with pixel-by-pixel measurements, allowing us to characterise the spatial properties of a galaxy. On top of that, photometry has the benefit of much shorter observing times, when compared to spectroscopy. A short exposure in a patch of the sky can provide data to study and characterise thousands of galaxies (e.g., the Hubble Deep Field, Williams et al. 1996).

When studying the high-redshift Universe, galaxies become very faint and small both in our detectors and intrinsically, so that our photometric observations are reduced to a handful of pixels. An established approach to then treat the data and analyse it is aperture photometry. An aperture is placed in the detected source, and the flux within that aperture is integrated. Thus, the emission from that galaxy is reduced to one single data point at each wavelength covered. This technique has been very useful to perform large statistical studies across cosmic time, but suffers the loss of an in-depth understanding of the complexity of galaxies, reducing them instead to point sources, given that we then only study the spatially-integrated properties of galaxies. Historically, only lower redshift studies exploit the abundance of information on a pixel-by-pixel basis.

Photometric filters can capture the light within a broad, medium or narrow wavelength range – broad, medium, and narrow-band filters. If a galaxy emission line falls within the narrow-band filter, one can remove the stellar continuum and obtain a map of the line emission. In Chapter 2 we discuss the intricacies of continuum subtraction, and make use of narrow-band photometry to target two hydrogen recombination lines, which allow us to derive important 2D properties such as dust obscuration and SFRs. On the other hand, broad-band filters capture the blended light from the stellar continuum and emission lines. A rich photometric coverage across the electromagnetic spectrum helps constrain and characterise galaxies effectively.

In regions of the sky that are crowded with objects, instead of aperture photometry, where sources can be blended and contaminate each other's integrated fluxes, a common approach is model-based flux extraction (also know as profile-fitting photometry). Instead of integrating directly the observed image, first a model is fit to the source, to try to reproduce its surface brightness profile (see e.g., THE TRACTOR, Lang et al. 2016). Once the object is modelled, the total brightness of the model gets computed, and the flux of the galaxy in that bandpass is obtained, without contamination from nearby sources.

Large photometric surveys have provided number counts across redshifts, general galaxy population properties and statistics, and photometric redshifts, with different levels of robustness depending on e.g. the coverage. Albeit the observational biases encountered in photometric-only studies, discussed briefly in Section 1.5.4, photometry is vital in the study of galaxy evolution and formation, and large efforts are focusing on studying and resolving these biases.

1.3.2 *Galaxy Components*

Galaxies are complex systems made out of stars and the ISM, composed of gas and dust, which emit light at different wavelengths. Thus, one can separate and understand these components by dissecting the light radiated by galaxies. No single observatory in the world (and beyond) is sensitive to the whole electromagnetic (EM) spectrum. Therefore, we must combine multiple instruments and telescopes to gather the light of galaxies across all wavelengths, which is paramount to gain a comprehensive view of their properties. Telescopes and instruments have been designed to capture radiation spanning from radio to gamma rays. Each wavelength range unveils specific aspects of the composition, dynamics, and history of galaxies.

Some galaxies have been observed across most of the electromagnetic spectrum, as is the case for the nearby galaxy M51 (Whirlpool Galaxy, also known as NGC 5194), shown on Figure 7. Briefly, here we outline the principal components of the galaxy that we can capture across wavelengths. Starting from the low energy range, a remarkable emission line in the sub-mm regime is the $J = 1-0$ transition from the carbon monoxide (CO) molecule, which traces the molecular gas content (e.g., Leroy et al. 2011), fundamental in the formation of stars. Radio telescopes can also detect synchrotron radiation and the emission from other molecular transitions. Radio observations are also pivotal in studying AGN. Moving into the infrared regime, we find the continuum emission to be dominated by the absorbed light from stars and re-emitted by dust. The contribution from dust can be traced into the far-IR continuum (e.g., Bowler et al. 2018; Béthermin et al. 2020; Bouwens et al. 2022; Fujimoto et al. 2023c), as well as FIR emission lines ([C II] , [O III], see e.g., Fujimoto et al. 2022). Infrared and sub-millimeter telescopes reveal the thermal emission from interstellar dust and cool, obscured regions within galaxies. These wavelengths are essential for tracing star formation (e.g., Casey et al. 2012). In this regime we can also trace the emission from polycyclic aromatic hydrocarbons (PAHs) at $\sim$8 μm. Older stellar populations can additionally contribute to the NIR emission.

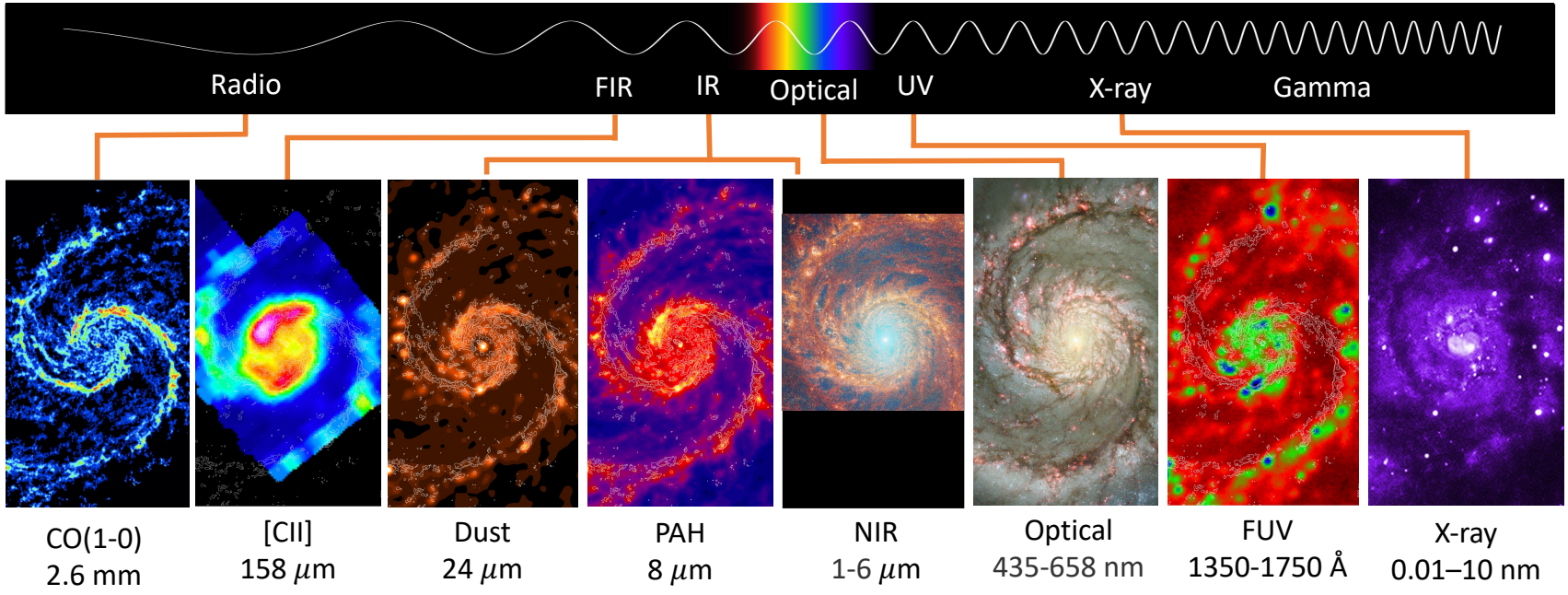

Figure 7: Imaging of the M51 Whirpool galaxy across the electromagnetic spectrum. From left to right: radio emission from the CO(1-0) transition tracing molecular gas, observed with the Plateau de Bure interferometer (PdBI) (credit: Institut de radioastronomie millimétrique, IRAM, Schinnerer et al. 2013); FIR [CII]-158 μm transition observed with Herschel, tracing photo-dissociation (credit: Parkin et al. 2013); the hot dust emission at 24 μm observed with the Spitzer Multiband Imaging Photometer for SIRTF (MIPS) (credit: Dumas et al. 2011); Spitzer Infrared Array Camera (IRAC) 8 μm map tracing PAH emission (credit: Kennicutt et al. 2003); IR composite image obtained with the Near Infrared Camera (NIRCam) and Mid-Infrared Instrument (MIRI) onboard *JWST* (credit: ESA/Webb, NASA & CSA, A. Adamo (Stockholm University) and the FEAST JWST team); HST composite optical image (credit: NASA/ESA/S. Beckwith and The Hubble Heritage Team STScI/AURA); FUV emission from young ($\leq$100 Myr) stars, observed with the Galaxy Evolution Explorer, GALEX (credit: Bigiel et al. 2010); X-ray emission captured with the Chandra X-ray Observatory Advanced Imaging Spectrometer (ACIS) (credit: NASA/CXC/Wesleyan Univ./R.Kilgard, Kilgard et al. 2014); The CO, [CII], dust, PAH and FUV maps are from Schinnerer et al. (2013).

Moving to shorter wavelengths, the optical regime is dominated by the stellar continuum emission by stars of all ages. Both the optical and UV observations provide information about stellar populations, star formation rates, and metallicity (Kennicutt 1998). The visible light also hosts numerous emission lines from ionised regions. Recombination lines from the hydrogen atoms are used extensively to trace dust and ionised gas around young stellar populations (e.g. Liu et al. 2013). The UV is also where dust obscures the most light, both scattering and absorbing it, and its effect weakens towards longer wavelengths. The dust lanes are clearly visible in the optical image of M51, obscuring regions across the star-forming spiral arms. The far-UV (FUV) traces the emission from the younges stars ($\leq$100 Myr). Figure 8 shows the spectral energy distribution (SED) of the integrated light of a galaxy in the UV–IR regime, where the different components and their contributions are displayed.

Finally, in the highest energy range, X-ray observatories detect high-energy emission from the hottest regions of gas and AGN activity. Gamma-ray telescopes explore extremely high-energy processes within galaxies, including the interactions of cosmic rays with interstellar gas and radiation from gamma-ray bursts.

An important observation that one can quickly make with the images across the EM spectrum, is the fact that the different components are not necessarily co-spatial. The regions where there is most dust obscuration do not correspond to the regions where stars of all ages emit most, or where we can find CO emission tracing molecular gas. The regions within a galaxy can be very distinct and not share the same properties. The typical scales of star forming regions are orders of magnitude lower than how we usually approach the study of galaxies when we lack resolution or signal-to-noise, as will be discussed later on. These are all important factors that have motivated the topics studied in this dissertation.

An accurate detection and thorough study are fundamental to interpret and comprehend each component independently, so we can get the full picture of galactic systems. We need to observe each piece of the puzzle to fully characterise the complex host. By inferring the characteristics of each component, as well as dependencies with each other, and their evolution with redshift, we can connect galaxies across cosmic time and study their evolution.

1.3.3 *Emission Line Diagnostics*

Spectra offer insights into the temperature, density, element composition and kinematics of galaxies. Spectral lines that are emitted or absorbed by galaxies serve us as tracers of their physical properties, such as the abundances and ionisation states. Several lines are used for this purpose, and here we introduce some of the most commonly used spectral lines and their associated tracers.

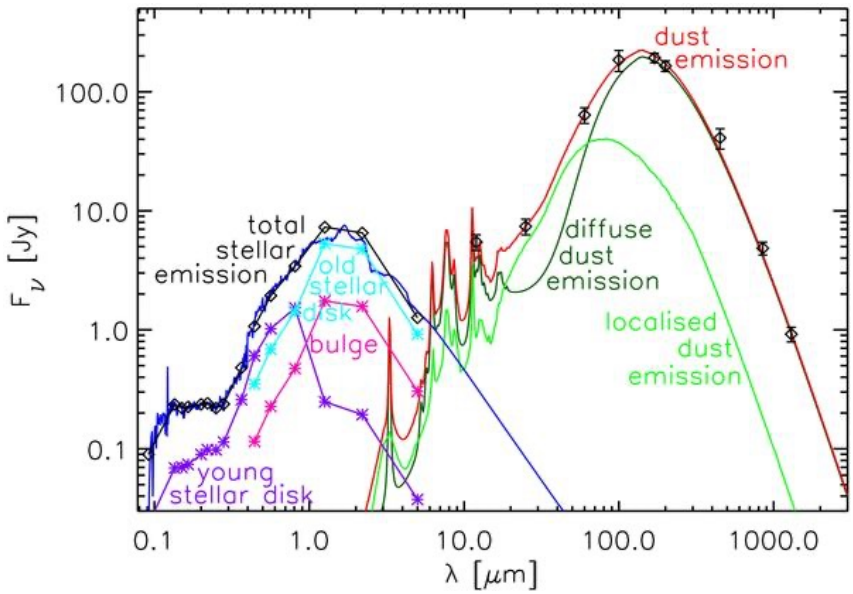

Figure 8: Spectral energy distribution of a galaxy split into the contribution from various components. The stellar populations dominate the emission from the UV to the NIR, where dust becomes the main source of radiation. Figure from Popescu et al. (2011).

Starting from the most abundant atom in the Universe, we have the Hydrogen recombination lines. The Balmer series (e.g. Hα, Hβ, etc., see Figure 9a) are widely used to constrain both the star formation activity and the dust obscuration. Hα (λ6563 Å), the transition from the third to the second energy level in a hydrogen atom, is one of the most prominent and important spectral lines in astrophysics. This line is an important SFR tracer of the most recent star formation activity ($\sim$ 10 Myr). Hα is produced from recombination of electrons in ionised H II regions around hot, young stars, thus providing a good diagnostic of the star formation activity. The intensity of Hα emission is proportional to the rate of ionizing photon production, providing an important insight in reionisation studies.

The combination of hydrogen recombination lines can trace dust obscuration, as will be studied in detail later on (Chapter 2). The intrinsic line ratios from the hydrogen series are remarkably invariant across multiple ISM conditions. When varying the electron temperature and density, these ratios remain relatively constant. Therefore, observational variations from the theoretical values are attributed to the presence of dust, which attenuates the lines with a wavelength dependency. Thus, with the observed and intrinsic ratios, we can derive the colour excess $E(B-V)$ as a measure of dust content (see Equation 1). The Paschen series (blue in Figure 9a), lies redder than the Balmer series, and is thus less affected by dust obscuration (e.g., Liu et al. 2013). Therefore, Paschen lines can be better to probe more dusty regions. Moreover, hydrogen recombination line ratios can also be used to infer the dust geometry. By comparing the dust ex-

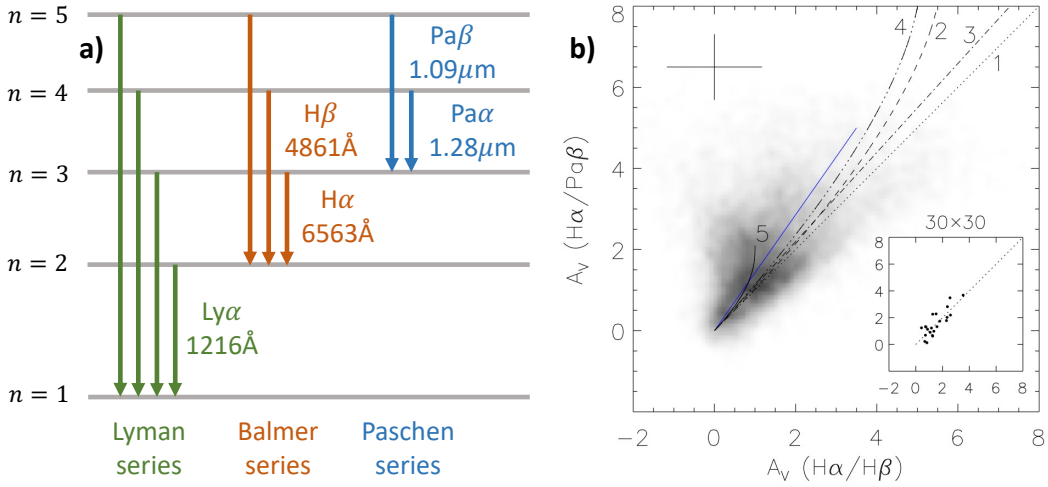

Figure 9: **a)** Sketch of the transitions from the first three levels of the Hydrogen atom. The Balmer Hα and Hβ lines are indicated, as well as the Paschen-α and Paschen-β, and the Lyman-α transition. **b)** Visual extinction inferred with the classic Balmer decrement (Hα/Hβ) versus the Hα/Paβ. The numbers indicate different dust geometries (1-foreground screen; 2-clumpy dust screen; 3-uniform scattering slab; 4-clumpy scattering slab; 5-uniform mixture). Figure from Liu et al. (2013).

tinction probed with two different ratios, the classic Balmer decrement Hα/Hβ and Hα/Paschen-β, Liu et al. (2013) try to constrain the geometry of dust from five different models (see Figure 9b). A commonly assumed simplistic geometry corresponds to number 1, where dust is assumed to lie in a uniform foreground screen in front of the stars that produce the light that we measure.

$$E(B-V) = \frac{2.5}{k(\mathrm{Pa}\beta) - k(\mathrm{H}\alpha)} \log\left(\frac{(\mathrm{H}\alpha/\mathrm{Pa}\beta)_{\mathrm{obs}}}{(\mathrm{H}\alpha/\mathrm{Pa}\beta)_{\mathrm{int}}}\right) \tag{1}$$

Moving on from Hydrogen, another emission line that is used as a SFR indicator is the [O II] $\lambda\lambda$3726, 3729 Å doublet (e.g., Kennicutt 1998; Kewley et al. 2004). It is additionally useful for determining electron densities, a critical component of chemical enrichment studies. The ratio of [O II] / [O III] $\lambda\lambda$4959, 5007 Å lines to Balmer lines are commonly used to trace the metallicity of ionised gas in galaxies. The nitrogen lines [N II] are also valuable as metallicity indicators. The presence of an AGN can be confirmed by characteristic emission lines such as C IV and Ne IV (e.g., Maiolino et al. 2023). On top of this, nebular emission lines (Hα/[N II] and [O II]/Hβ) can also reveal whether the gas is predominantly star forming or AGN ionised, through the Baldwin-Phillips-Terlevich diagram (BPT, Baldwin et al. 1981; Kewley et al. 2013a,b).

In the far-infrared (FIR) regime, the major cooling lines such as [C II]-158μm and [O III]-88μm probe vital mechanisms in the ISM of galaxies. They can help constrain the electron density (e.g., Fujimoto et al. 2022; Killi et al. 2023), and the

ionisation state of the gas (e.g., Harikane et al. 2020). Additionally, [C II]-158μm emission can be used to infer the dynamical mass of galaxies (e.g., Wang et al. 2013; Capak et al. 2015; Smit et al. 2018; Heintz et al. 2023c), and has recently been proposed as a tracer of H I gas mass (Heintz et al. 2021; Vizgan et al. 2022a,b). Moreover, neutral [C I] and [O I] are used as tracers for non star-forming cool gas (Valentino et al. 2020a; Rizzo et al. 2023).

As introduced above, from the molecular lines, perhaps the most important one in this field are the rotational transitions from carbon monoxide (CO), which have been found to be tightly connected to molecular hydrogen H_2 (e.g., Narayanan et al. 2012). FIR CO emission lines can thus be used to probe the properties of molecular clouds and estimating the mass and the column density of H_2 (Bolatto et al. 2013). Knowing how much cold molecular gas is available is fundamental to estimate the formation of new stars, as we can see by the correlation between increasing SFR and molecular gas content at high redshift (Tacconi et al. 2020). Recently, the emission from PAHs has been proposed as a new tracer of the molecular gas content (Cortzen et al. 2019).

Within the absorption in galaxies, the Balmer absorption lines (Hδ, Hγ, etc.) are perhaps the most used. These optical lines are indicative of the stellar populations in galaxies. Their strengths can be used to estimate the age and metallicity of the dominant stellar population. Elliptical galaxies, for example, distinctive by their predominantly old stellar populations, display strong absorption features of hydrogen lines (Hδ in particular, see e.g., Valentino et al. 2020b). A significant continuum absorption feature in a galaxy spectrum is the Balmer break, which appears on either side of the limit of the Balmer series. It arises from the complete ionization of electrons directly from the second energy level of a hydrogen atom, a process known as bound-free absorption, particularly evident at wavelengths shorter than 3645 Å. Additionally, another significant absorption feature is the Lyman break. Due to absorption by the neutral IGM, a continuum break appears at the redshifted Lyman-α wavelength. The Lyman and Balmer breaks can yield biases in our observations, as is discussed in Section 1.5.4.

1.3.4 *Multi-Object and Integral Field Spectroscopy*

A practice that has revolutionised the spectroscopic characterisation of large statistical samples of galaxies is multi-object spectroscopy (MOS). Within a single observation, one can obtain the spectrum of every source in the field. On a first level, this provides accurate redshift determinations of all galaxies (e.g., Steidel et al. 2003; Le Fèvre et al. 2005), allowing the robust identification of high redshift objects. On top of that, one can measure the emission lines discussed above, and thus investigate the evolution across cosmic time of the physical properties that they trace. An example of a recent survey that has used this technique with *JWST* is FRESCO (Oesch et al. 2023). Figure 10 displays the acquisition image on

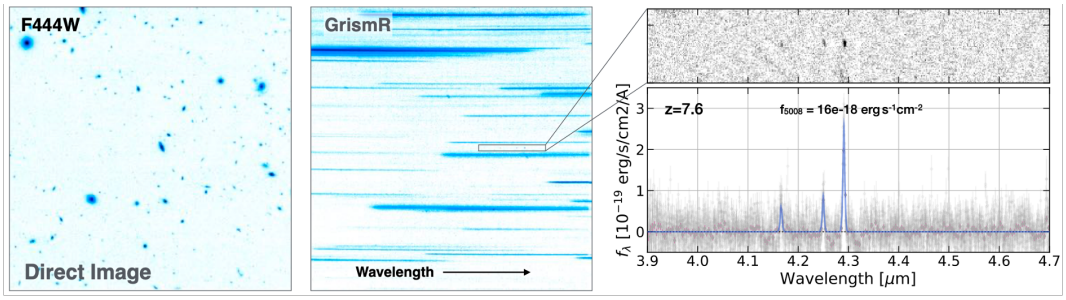

Figure 10: Spectroscopic characterisation of all galaxies in a field of view using multi-object spectroscopy. Figure from the FRESCO survey (Oesch et al. 2023).

the left panel, with the F444W band; the middle panel shows the spectra of every individual source in the field, and the right panel shows an example spectrum of one source at $z = 7.6$, with clear emission line detections. Previously, HST also made this statistical characterisation possible with grism surveys, such as 3D-HST (Brammer et al. 2012).

A rather new technique that merges the advantages of photometry and spectroscopy is integral field spectroscopy (IFS). Several surveys (e.g., Calar Alto Legacy Integral Field Area Survey, CALIFA, Sánchez et al. 2012; Mapping Nearby Galaxies at APO, MaNGA, Bundy et al. 2015) have made use of IFS instruments, such as the Multi-Unit Spectroscopic Explorer (MUSE, Bacon et al. 2010) and the Visible Multi-Object Spectrograph (VIMOS, Le Fèvre et al. 2003) mounted on the Very Large Telescope (VLT). Figure 11 shows an example of the IFS technique on MaNGA galaxies. IFS instruments are made out of fibers, where a spectrum is obtained for each fiber or spatial element. The left panel displays the available fibers in MaNGA. On the right, the resulting spectra of two different regions within a galaxy are displayed, indicating different stellar populations – a quenched bulge (red curve) versus a star forming outskirt (blue curve). Thus, IFS provides us with 3D data – the two spatial dimensions, and the wavelength dimension, resulting in a data cube.

Most recently, the Near Infrared Spectrograph (NIRSpec, Jakobsen et al. 2022) Integral Field Unit (IFU, Closs et al. 2008; Böker et al. 2022) onboard *JWST*, has the capability to extend previous IFS studies to the high redshift Universe, providing an unprecedented characterisation of the spatial distribution of e.g., emission lines into the epoch of reionisation and beyond. In Chapter 4, we discuss the importance of NIRSpec IFU measurements to study the accuracy of photometric-only estimates on a $z \sim 6$ galaxy. IFU data can play a fundamental role in breaking some of the degeneracies from photometric observations (see Section 1.5.4 below).

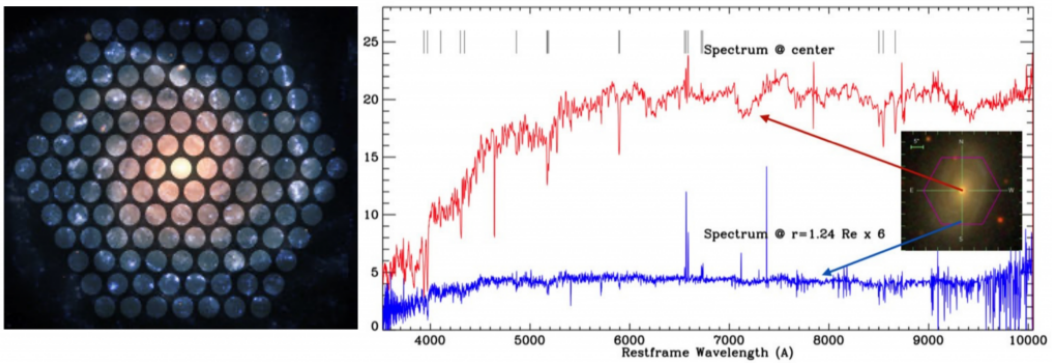

Figure 11: Example of Integral Field Spectroscopy in the MaNGA survey. The left panel shows an example MaNGA galaxy, and the circles indicate the positions of the IFS fibers, for each of which a spectra is measured. On the right, two spectra from the central (red curve) and outskirts (blue curve) regions of a galaxy are displayed, showcasing different stellar populations. Image credit: SDSS Collaboration, adapted from Fraser-McKelvie et al. (2018).

1.3.5 *Our Eyes in the Sky*

The bulk of this PhD thesis has been possible because of the observations gathered by two space telescopes, the *Hubble Space Telescope* and *JWST*. These observatories offer unique advantages for studying galaxies in unprecedented detail. Both are free from atmospheric distortions and absorption, enabling sensitive, high-resolution imaging and precise spectroscopy of galaxies.

The *Hubble Space Telescope* has been a pioneer in galactic exploration since its launch in 1990. It spans the wavelength range from the ultraviolet, across optical into the near-infrared. The first major impact of the *Hubble Space Telescope* into the field of extragalactic astronomy came with the Hubble Deep Field (HDF, Williams et al. 1996). Over ten consecutive days on December 1995, HST observed an area of 6.8 arcmin^2. Unexpectedly, it found thousands of galaxies in an otherwise apparently empty and dark region of the sky. On top of that, multiple of the observed galaxies were found to be high-redshift objects, providing for the first time a peek into the early Universe. After that, HST has provided us with a wealth of galaxy observations across cosmic time. Aided by the high sensitivity of the Wide Field Camera 3 (WFC3) with infrared coverage, HST identified high redshift galaxies up to $z \sim 11$ (e.g., McLure et al. 2013; Coe et al. 2013; Ellis et al. 2013; Oesch et al. 2013, 2014, 2015; Bouwens et al. 2015a,b; Oesch et al. 2016).

The *JWST* launched on Christmas Day of 2021, and has already revealed an unprecedented view into the infrared part of the spectrum. *JWST* has seven times more collecting power than HST, coverage to longer wavelengths and higher sensitivity. This allows us to peer through cosmic dust and study obscured regions within galaxies at epochs and resolutions that have been out of our reach so far. *JWST* allows us to measure rest-frame optical properties of galaxies at

$z > 6$, which has only been studied at rest-frame UV wavelengths until now. The advent of NIR medium-bands and instruments such as NIRSpec IFU can help us probe the stellar continuum accurately, to infer robust stellar masses and be able to delve into the assembly history of galaxies. With barely a year of operation, *JWST* has already provided a pool of $z > 7$ galaxies (e.g., Naidu et al. 2022b; Labbé et al. 2023; Donnan et al. 2023b; Rodighiero et al. 2023; Bouwens et al. 2023a; Harikane et al. 2023a; Hainline et al. 2023), which may challenge galaxy formation models, including semi-analytical methods and hydrodynamic simulations (see e.g., Mason et al. 2023) given their high UV luminosity and inferred stellar masses, although multiple solutions have been proposed (e.g., Whitler et al. 2023).

Extensive and open source efforts such as the DAWN *JWST* Archive (DJA[1]) have reduced and produced homogenised data sets of all available *JWST* public data, allowing open access to the highest quality astronomical observations to the whole research community. Figure 12 shows some of the *JWST* mosaics that are publicly available, produced within the DJA.

The extended lifetime of HST, combined with the upcoming decade of *JWST* observations, will provide unparalleled high-resolution images, enabling the study of galaxy morphology, structure, and the identification of key features like spiral arms, bars, and mergers, at unprecedented cosmic epochs. Their spectroscopic capabilities will reveal crucial information about the kinematics, chemical compositions, and physical conditions within galaxies, aiding in the understanding of their evolution. The combination of these space instruments with Earth observatories such as ALMA, which can add valuable FIR emission line detections and dust continuum measurements (e.g., Fujimoto et al. 2022; Heintz et al. 2023c), will provide an unprecedented characterisation of the stellar, gas, metal and dust content of galaxies across cosmic time.

[1] https://dawn-cph.github.io/dja/

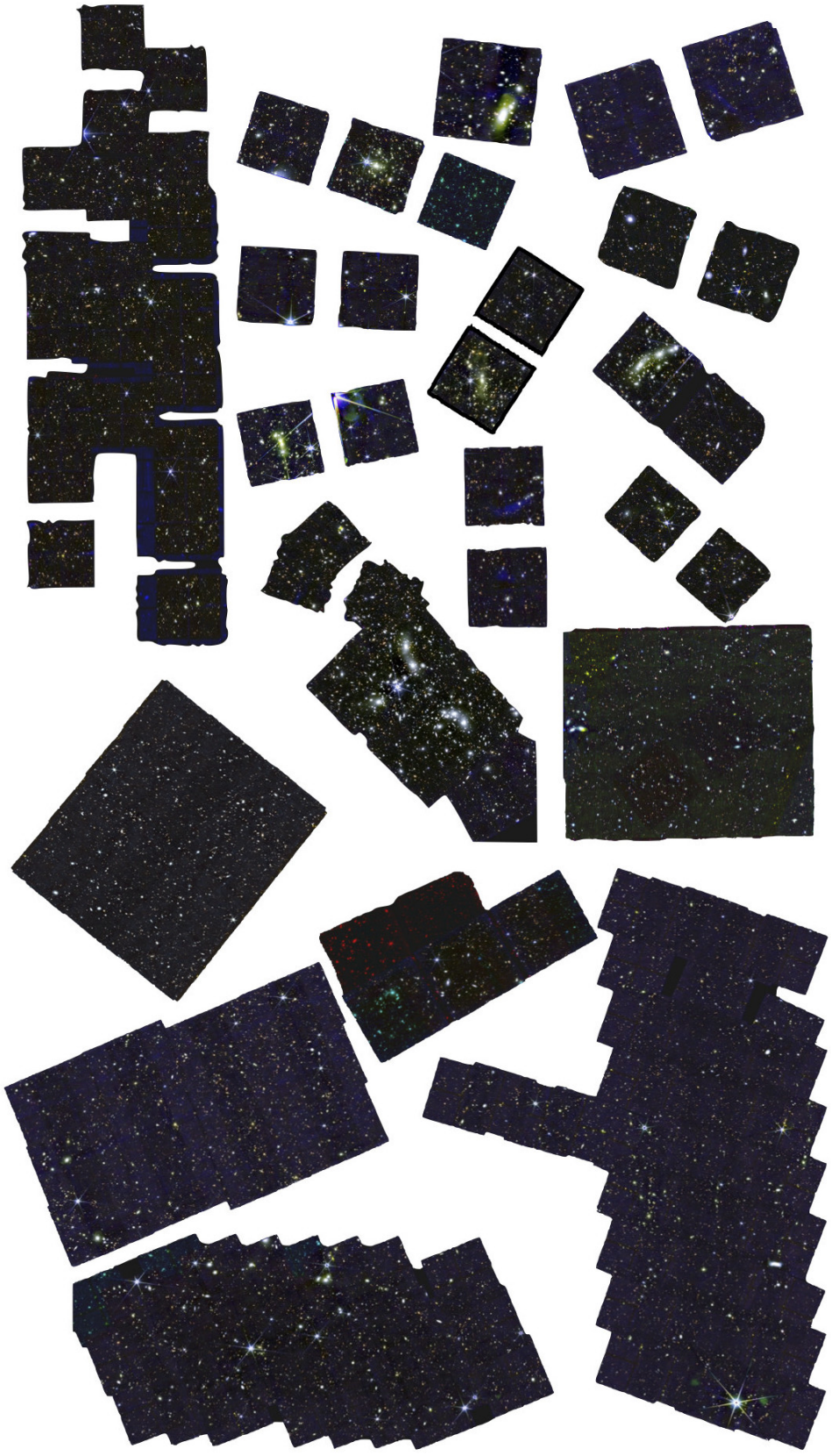

Figure 12: Mosaics of some of the *JWST* survey fields observed so far. Credit: Gabe Brammer, DAWN *JWST* Archive (DJA).

1.4 MODELLING GALAXIES

Galaxy spectral energy distributions (SEDs) are influenced by numerous physical factors, such as star-formation history, metal content, dust characteristics, and more. Stellar population synthesis (SPS) aims to extract these variables from observed SEDs. This introductory section provides an SPS overview, covering key measurements like stellar masses, SFRs, metallicities, dust properties, and the stellar initial mass function, which are the foundation of modern galaxy formation and evolution studies.

1.4.1 *How to Build a Galaxy SED*

Efforts spanning decades have focused on deciphering and modelling galaxy SEDs across a wide spectral range, from far-ultraviolet to far-infrared. Dust, a significant factor in our observations, absorbs and scatters UV light while re-radiating it in the IR. UV emissions primarily originate from young and hot massive stars. Modelling galaxies is a complex task that involves multiple components and a careful assessment of uncertainties and unknowns (see e.g., Faber 1977; Tinsley 1980; Frogel 1988; Maraston 2005; Conroy & Gunn 2010a; Walcher et al. 2011; Conroy 2013).

Figure 13 provides a comprehensive overview of the complete process involved in constructing composite stellar populations (CSPs), devised and reviewed by Conroy (2013). Starting from the top row, the ingredients that comprise a simple stellar population are displayed. An SSP is made of an initial mass function (IMF), isochrones to describe the theory of stellar evolution, and spectral libraries of stars. These set the age, mass and metal content of the formed stellar population.

Isochrones define the positions of stars with common age and metallicity in the Hertzsprung-Russell (HR) diagram (Russell 1914), encompassing a wide range of stellar masses and evolutionary phases. Several isochrone models exist, but none cover all age and metallicity ranges. Implementing these diverse models in SPS is challenging due to differing assumptions. Stellar evolution calculations, the basis of isochrones, involve approximations for complex processes, introducing uncertainties in isochrones and SPS predictions, which extend into systematic uncertainties in SED modelling (e.g., Conroy et al. 2009).

Stellar spectral libraries play a crucial role in converting stellar evolution outputs, such as metallicities and effective temperatures, into observable SEDs. However, there is not a single comprehensive spectral library, whether theoretical or empirical, that covers the entire parameter range needed for SPS models. As a result, it is common to combine various libraries. Theoretical spectral libraries offer extensive coverage of the parameter space, but some of their issues include incomplete atomic and molecular line lists, uncertainties in strengths

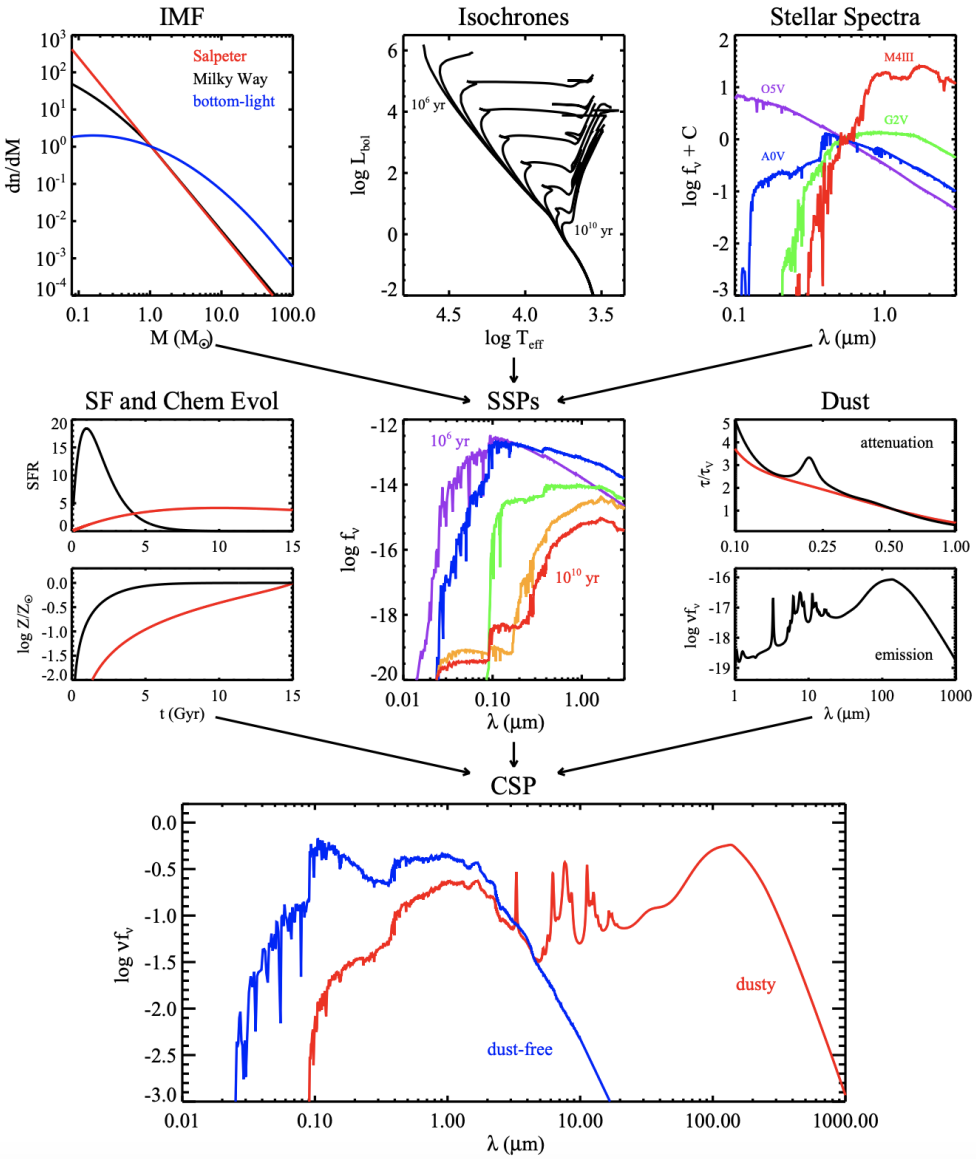

Figure 13: Figure from Conroy (2013), reviewing the process involved in constructing composite stellar populations. The top row shows the components that go into building a simple stellar population. The middle row combines SSPs with different characteristics into a composite stellar population, which can be dust-free or dusty (bottom row).

and wavelengths of theoretical lines, and challenges in reproducing observed features in stars. On the other hand, empirical spectral libraries avoid issues with line lists and modelling, but face challenges related to atmospheric correction, flux calibration, and limited wavelength coverage. They also suffer from incomplete coverage of parameter space due to their reliance on stars from the solar neighbourhood.

The initial mass function (IMF), describing the distribution of star masses at their birth, has been studied extensively in galaxies (e.g., Salpeter 1955; Miller

& Scalo 1979; Kroupa 2001; Chabrier 2003). It is a widely common practice to assume a universal IMF, and to thus study indistinctly galaxies in the local and the early Universe. Currently, stronger evidence is rising that this might not be the case, and we instead might be observing a varying IMF at different epochs and within the diverse galaxy population (see e.g., Sneppen et al. 2022; Steinhardt et al. 2022; Rusakov et al. 2023). More and more studies are reporting considerable differences in our inferred properties from SED modelling when varying our IMF assumptions, dominating the systematic uncertainties with values up to 1 dex (Wang et al. 2023).

The IMF is a vital consideration in SED modelling, affecting the stellar mass-to-light ratio (M/L), luminosity evolution, and spectral properties of galaxy populations. In a galaxy, the bulk of both stellar mass and number of stars resides in low-mass stars, although their contribution to the bolometric light is minimal. The widely used Salpeter IMF (Salpeter 1955) follows a power-law form, $\mathrm{d}N/\mathrm{d}M \propto M^{-x}$, with $x = 2.35$ (see top left corner of Figure 13). Several studies have tried to suggest non-Galactic IMFs for high-redshift galaxies, such as top-heavy (Conroy & van Dokkum 2012), bottom-heavy (Martín-Navarro et al. 2015), and a temperature-dependent IMF that accounts for variation in temperatures (Jermyn et al. 2018; Sneppen et al. 2022). Most recently, a top-heavy IMF has been proposed to explain the high star formation rate density observed at $z > 10$ by *JWST* (Harikane et al. 2023b; Yung et al. 2023). Given the considerable degeneracies that the IMF has with the dust obscuration, the star formation history, the metallicity and age of the stellar populations, accurately inferring the IMF from high-redshift observations becomes practically impossible. Improving the IMF assumptions remains an important challenge of this field.

Once we have a simple stellar population, the middle row in Figure 13 displays the additional ingredients needed to build a more complex composite stellar population. We first need SSPs of different ages, to which we add dust. The UV–NIR radiation from stars is scattered and absorbed by dust, which then re-emits it at longer wavelengths, typically in the IR range. The effect of dust is introduced in modelling through attenuation curves. These arise as a combination of the dust content and spatial distribution, dust grain characteristics, and different stellar populations (see Salim & Narayanan 2020, for a review). In practice, most works assume an attenuation curve with fixed shape and fit the normalisation, with very simplistic underlying geometrical considerations such as the dust screen model (homogeneous foreground screen covering the stars, see Calzetti 2001, for a discussion on dust geometries and its effects on SED modelling). By observing individual stars, the total extinction along the line of sight can be inferred by comparing it with the unobscured spectra of stars. Common curves include the Calzetti et al. (2000) law, calculated with a sample of eight low-redshift starburst galaxies, the Milky Way curve (e.g., Cardelli et al. 1989; Fitzpatrick & Massa 1990; Clayton et al. 2000; Fitzpatrick & Massa 2007, 2009), the Large Magellanic Cloud

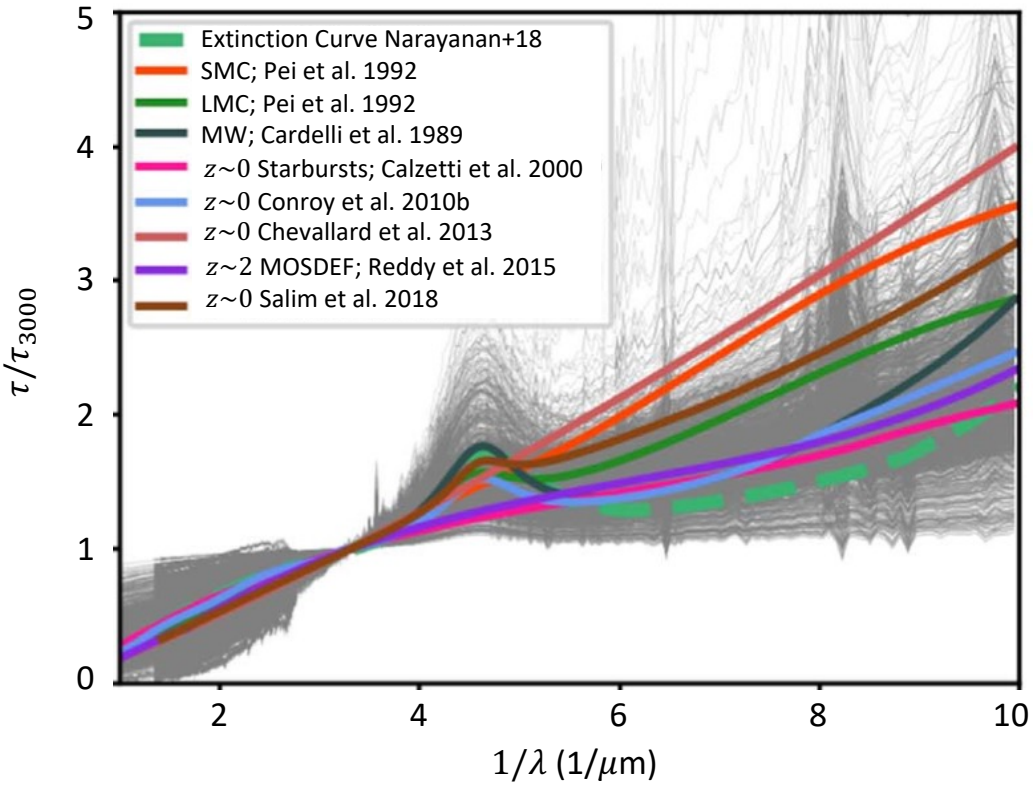

Figure 14: Some of the most used attenuation curve parameterisations, which display different bump 2175 Å strengths and slopes. The optical depth (normalised to the 3000 Å optical depth) is displayed as a function of wavelength. The underlying grey curves display the diversity of curves obtained from the simulations of Narayanan et al. (2018), where this figure is taken from.

(LMC, e.g., Gordon et al. 2003), the Small Magellanic Cloud (SMC, Prevot et al. 1984; Gordon & Clayton 1998), and the more recent Salim et al. (2018) attenuation curve. Figure 14 gathers some of the most commonly used attenuation curves. A particular feature that some of these curves can display is the 2175 Å bump, which is thought to be caused by the presence of PAHs, but its origin remains uncertain (see e.g., Draine 2003). This bump feature has been observed even at $z \sim 7$ with *JWST* (Witstok et al. 2023), suggesting early and rapid production of carbonaceous dust grains.

Similar to the IMF, local measurements of extinction curves are assumed to hold also for higher redshift galaxies (e.g., Reddy et al. 2012), albeit this might not be the case (Gallerani et al. 2010; Buat et al. 2012; Kriek & Conroy 2013; Reddy et al. 2015; Salmon et al. 2016). Both via observations and simulations (e.g., Ferrara et al. 1999; Salim et al. 2018; Narayanan et al. 2018), a wide range of slopes and bump strengths has been found in attenuation curves. The choice of attenuation curve can have significant implications for the derived properties

of galaxies, e.g., inferring wrong stellar masses from broad-band photometry because of dust obscuration (Mitchell et al. 2013).

Regarding dust emission, the SED of galaxies beyond $\sim 10\mu$m is shaped by the emission from dust grains. Models such as Draine & Li (2007) include PAHs emission features, and account for dust grain heating from different strengths of the interstellar radiation field, using results from the *Spitzer Space Telescope*. The newest fleet of observations coupled with simulations, is bringing improvements in the dust emission modelling (e.g., Narayanan et al. 2023b).

The stars in a CSP span a broad age range, given by their star formation histories (SFHs). Current modelling softwares implement both parametric and non-parametric SFH models. Parametric models are based on predefined functional forms, such as exponential or constant star formation rates, which are then fitted to the observed data to infer the temporal evolution of the star formation activity of the galaxy. Parametric models offer computational speed, simplicity and easier interpretation, but may oversimplify the true complexities of SFHs. Parametric models are a valuable assumption when dealing with large datasets or with limited observational data. The most commonly adopted parametric SFH form is the exponential τ decay, where SFR $\propto e^{-t/\tau}$ (e.g., Mortlock et al. 2017; Sorba & Sawicki 2018). These models can be extended into delayed exponentially declining SFHs (e.g., Ciesla et al. 2017). It has also become increasingly popular to use rising SFHs to model high-redshift galaxies (e.g., Papovich et al. 2011). Most recently, bursty star formation for high redshift galaxies has been proposed as a solution to *JWST* observations indicating a high SFR density (SFRD) at $z > 10$ (e.g., Yung et al. 2023; Shen et al. 2023b; Harikane et al. 2023b; Bouwens et al. 2023a,b).

On the other hand, non-parametric models were envisioned to be flexible enough to describe all SFH shapes. They do not assume a specific functional form, but attempt to reconstruct the star formation history directly from the observed properties of galaxies. However, non-parametric modelling requires well-motivated priors, given their not fully constrained flexibility. These priors can dominate the recovered SFH (Leja et al. 2019). While non-parametric models are more adaptable to complex SFHs, they can be computationally intensive and may require extensive observational data, to constrain the large parameter space. When compared to parametric models, non-parametric models are better suited for capturing the intricate details of star formation histories in individual galaxies, but may be less practical when dealing with extensive galaxy samples.

SFH modelling is vital to accurately infer star formation rates, dust and metal content, and stellar masses from observed SEDs (e.g., Conroy 2013; Leja et al. 2017). Recent studies have found that the choice of SFH can yield up to 1 dex different stellar masses (Pforr et al. 2012; Whitler et al. 2023). Additionally, parametric SFHs can yield biased SFR values, with SFR overestimated for starbursts

and underestimated for temporarily-quenched galaxies (Haskell et al. 2023). Non-parametric SFHs can mitigate this bias.

Going back to Figure 13, the last ingredients to obtain a CSP is the metallicity and chemical evolution. The usual assumption is to simplify this property, so that essentially one metallicity value is set for all stars. Additionally, nebular emission is added both as continuum and as recombination lines. For this, photoionization codes are used, such as CLOUDY (Ferland et al. 2017; Chatzikos et al. 2023). Nebular emission becomes increasingly relevant for young ages of the stellar populations and in the low metallicity regime (Conroy 2013). Once we combine the dust and metal content with the SFH, we finally obtain galaxy model SEDs with and without dust obscuration (bottom panel of Figure 13).

1.4.2 *SED Modelling*

Once we have built galaxy SED models, we can fit them to photometric and spectroscopic observations (e.g., Section 1.3) to infer the physical properties of galaxies. There is a broad variety of SED modelling software packages that use different assumptions and techniques in order to fit the models to the data. The most common fitting method relies on χ^2 minimisation, or more recently, sampling techniques such as Markov Chain Monte Carlo (MCMC) are being used. Understanding the assumptions that a code implements is vital for choosing the appropriate software for a particular analysis problem. Additionally, further selecting the appropriate priors and inputs is fundamental when fitting galaxy SEDs and inferring physical properties.

A common practice in the literature is to compare multiple SED fitting codes in order to assess the systematic uncertainties of the parameters inferred from them. However, recent studies find that this can yield an underestimation of the true systematic uncertainties (e.g., Wang et al. 2023). A significant challenge that fitting photometric observations yields is the degeneracy between the intrinsic colour of a source and its redshift. Different combinations of intrinsic colours and redshifts can lead to similar observed colours. Therefore, it can be challenging to disentangle both effects. On top of this, the colours of a stellar population depend on both its age and metallicity, yielding also an age-metallicity degeneracy that is challenging to break (e.g., Yin et al. 2023). The presence of interstellar dust can also introduce degeneracies in broad-band photometry, particularly with age and redshift. Different software and analysis techniques try to break, or at least fully characterise, these degeneracies in various ways, but still no solution yet prevails to resolve all SED modelling issues.

In this dissertation, we perform SED modelling by using mainly three codes — PROSPECTOR (Leja et al. 2019), BAGPIPES (Carnall et al. 2018) and an adaptation of EAZY (Brammer et al. 2008) that we develop, in order to fit the contribution

from the emission lines and the stellar continuum separately (see Chapter 2). Here, we provide a brief overview of the basic properties of these approaches.

EAZY (Brammer et al. 2008) is an SED-fitting code that focuses on inferring robust redshift estimates from photometric measurements (photo-z). For more than a decade, it has been extensively used to estimate photo-z in large galaxy surveys, given its excellent computational speed. EAZY relies on χ^2 minimisation to find the combination of a basis set of templates that best fits the photometric data, over a redshift grid defined by the user. Contrary to most photometric codes that select a single best fit template, and given the complexity of galaxies, EAZY (following GREGZ, Rudnick et al. 2001, 2003) instead finds a linear combination of templates that best describes the emitted light. A fundamental requirement to obtain robust estimates is the optimization of template sets. An advent brought by EAZY is the introduction of a *template error function*, which aims to incorporate into the set of templates some of the uncertainties that were discussed in the previous section. These include e.g. the variations in the attenuation curves, the stellar evolutionary track uncertainties, and the diversity of star formation histories. Thus, this function will for example display large uncertainties in the UV wavelengths, accounting for the strongest dust extinction regime, as well as in the NIR, accounting for the uncertain stellar isochrones and PAH features. The main strengths of EAZY are its flexibility and speed, but the weaknesses include not sampling the whole parameter space, which makes it less optimal to infer physical properties.

The more recent SED sampling softwares PROSPECTOR (Leja et al. 2017, 2019) and BAGPIPES (Bayesian Analysis of Galaxies for Physical Inference and Parameter EStimation, Carnall et al. 2018, 2019) provide similar Python-based methodological approaches for the analysis of galaxy SEDs through stellar population modelling. Instead of "simply" fitting generated templates to data as EAZY does, these codes sample the posterior distribution of multiple parameters and evaluate their likelihood, finding the maximum likelihood in the parameter space that best represents the data. PROSPECTOR provides flexible attenuation curves and metallicity, as well as the innovation of non-parametric SFHs. This code uses Bayesian statistics coupled with a nested MCMC sampler, to provide accurate uncertainties on SFH parameters by fully exploring the whole parameter space and posterior probabilities. PROSPECTOR generates models using the Flexible Stellar Population Synthesis code (FSPS, Conroy et al. 2009). BAGPIPES provides galaxy models across continuous parameter spaces with Bayesian tools, as well as using the MULTINEST nested sampling algorithm (Feroz & Hobson 2008; Feroz et al. 2009), to fit them to observational data. BAGPIPES allows for several user-input priors that specify the SFH, the dust and nebular-emission components. BAGPIPES uses pre-defined SPS models from Bruzual & Charlot (2003).

1.5 MOTIVATION FOR THIS DISSERTATION

The overarching theme of this dissertation is to study galaxies as the complex systems that they are, resolving their stellar populations and ISM when possible. We approach this through different studies, which are further motivated by the points briefly discussed below.

1.5.1 *Obscured Star Formation*

As introduced in Section 1.2.1, the SFRD of the Universe peaked at $z \sim 2$ (Madau & Dickinson 2014; Harikane et al. 2023b,a). Several works have investigated how galaxies with different characteristics contribute to the integrated SFRD, and found that dust-obscured star formation dominates the star formation activity at $z \sim 2$ (Pérez-González et al. 2005; Magnelli et al. 2013; Bouwens et al. 2020; Zavala et al. 2021). Obscured star formation is difficult to study when observations are limited to relatively blue rest-frame wavelengths (i.e., a given optical/NIR instrumental bandpass at increasingly high redshifts), but is thus fundamental to characterising and understanding galaxy evolution.

Figure 15 shows the cosmic SFRD (bottom panel), separated in the contribution from dust-obscured (orange curve and points) and the unobscured star formation history (blue shaded region). The middle panel shows the obscured star formation fraction. Dust-obscured galaxies have thus dominated the cosmic SFRD for the past ∼12 Gyr and only at $z \gtrsim 5$ does the unobscured star formation begin to dominate the total SFRD. The top panel displays the contribution by galaxies with varying infrared luminosities to the dust-obscured star formation. We can see that it is mostly dominated by two interesting populations, the luminous infrared galaxies (LIRGs, $10^{11} < L_{IR}/L_{\odot} < 10^{12}$) and ultra-luminous infrared galaxies (ULIRGs, $L_{IR} > 10^{12} L_{\odot}$) (Sanders & Mirabel 1996).

Being able to accurately infer the obscured star formation activity happening in galaxies is fundamental to understand the full picture of star formation and galaxy evolution across cosmic time. In Chapter 2, we delve into this issue, and study how the Paschen-β NIR hydrogen recombination line can be used to probe deeper into obscured star formation (SF) than the Hα/Hβ Balmer decrement, more commonly used to constrain dust-obscuration in H II regions. With our work, we investigate whether Paschen series lines can be more effective at recovering dust-obscured SF, thus helping us constrain more accurately the cosmic SFRD. Given their contribution to the dust-obscured SFRD, in this work we focus on a sample of mostly LIRGs and ULIRGs.

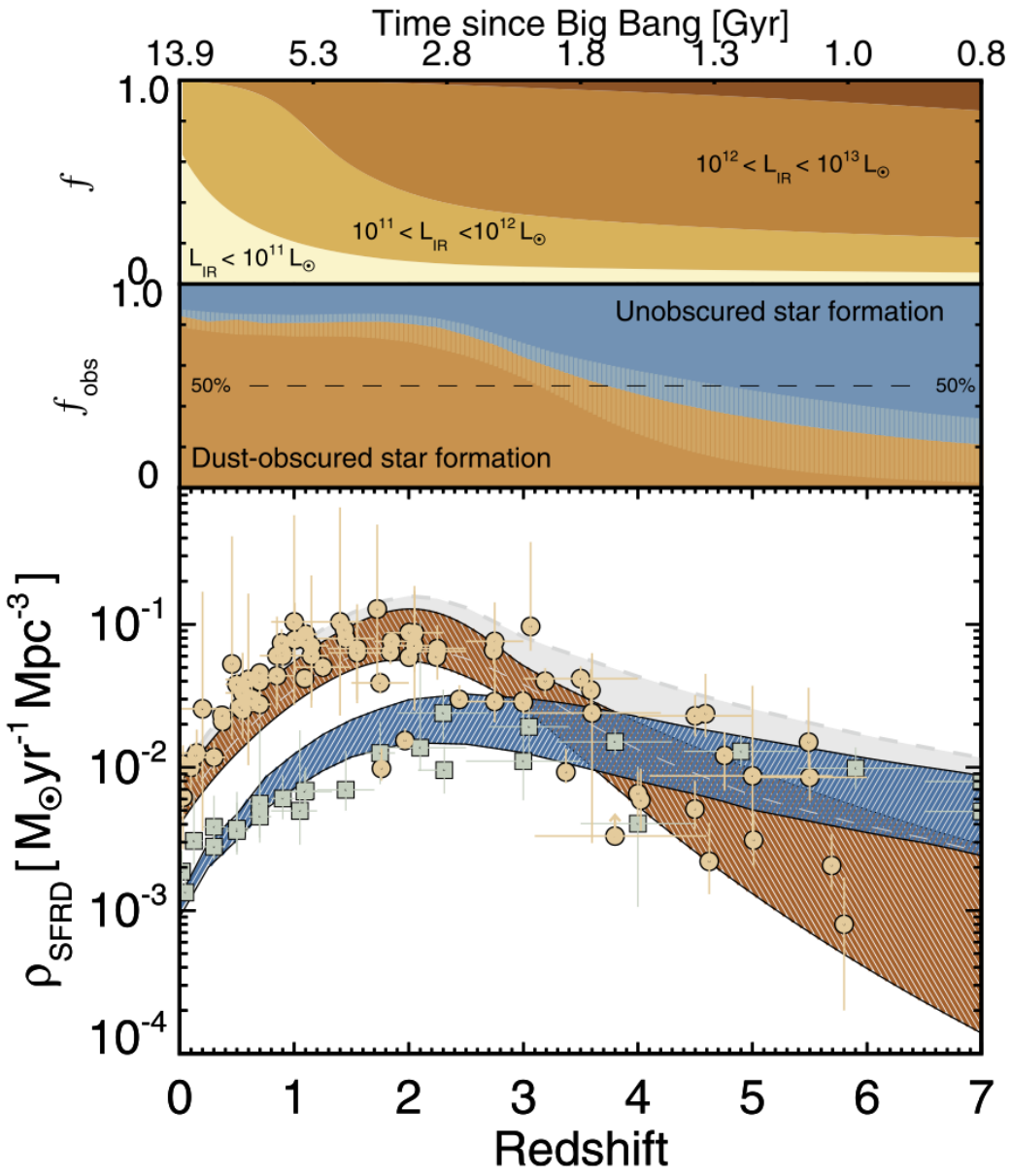

Figure 15: Contribution to the cosmic SFRD by dust-obscured star formation. At the peak of SFRD ($z \sim 2$, Madau & Dickinson 2014), the dust-obscured star formation (orange curve and points) dominates the SF activity. Only in the high redshift Universe ($z > 5$), the unobscured star formation (blue curve and squares) takes over. The grey shaded region indicates the total SFRD. Figure from Zavala et al. (2021).

1.5.2 *Physical Scales*

To study galaxy evolution we try to connect different galaxies across cosmic time, given their overall physical properties. However, there is a disparity in the study of galaxies between the local and the early Universe. Historically, high

redshift studies have lacked the spatial resolution and depth necessary to perform detailed resolved analyses of the internal structure of galaxies. Instead, as introduced in Section 1.3.1, they have mostly been considered as single discrete sources, losing their incredible complexity along the way. In contrast, local studies are often *drowning* in an abundance of data and information, working with thousands of spatial resolution elements even across a single galaxy. This has enabled studies that fully characterise the dust, gas, stellar, and metal content of local galaxies on a pixel-by-pixel basis, down to scales of tens of parsecs.

Given the substantial differences in how we study local galaxies versus sources in the distant early Universe, the questions arise: Can we reliably connect them across the history of the Universe to understand galaxy evolution? What impact does studying high-redshift galaxies in a simplified, unresolved manner have on the physical properties we infer? Does studying early Universe galaxies with the same approach as nearby sources alter our understanding of their nature, internal structure, and evolutionary processes? These questions serve as the overarching theme of this thesis, and the driving force behind the numerous research endeavors presented here.

1.5.3 *Non Co-Spatial Components*

Besides the different scales at which we can study galaxies and their components, we introduced and saw in Section 1.3.2 that these are not necessarily co-spatial. At high-z, more and more galaxies are being found that display an offset between their stellar and ISM components. For example, the highest redshift galaxy studied in this dissertation, a galaxy at $z \sim 8.5$ in the SMACS0723 field (Pontoppidan et al. 2022), has a $0\farcs5$ offset between the [C II]-158μm emission captured by ALMA and the *JWST* source (Fujimoto et al. 2022; Heintz et al. 2023c), whereas [O III]-88μm appears co-spatial (see Figure 16). On top of this, the [C II] emission is much more extended than the UV components, which has been observed typically at $z > 6$ (e.g., Smit et al. 2018; Fujimoto et al. 2019; Matthee et al. 2019; Fudamoto et al. 2022). Additionally, other galaxies have been found to have an offset between the dust continuum and the UV emission, by e.g. Bowler et al. (2022) at $z \sim 7$, as well as in simulations (e.g., Sommovigo et al. 2020). All these findings further motivate the need to study galaxies without neglecting the spatial information.

1.5.4 *Observational Biases*

Since the first studies arised that introduced SED fitting with SPS models (e.g., Sawicki & Yee 1998; Giallongo et al. 1998; Brinchmann & Ellis 2000; Papovich et al. 2001; Shapley et al. 2001), stellar masses have been considered a robust parameter to infer. However, multiple factors have been found to affect the

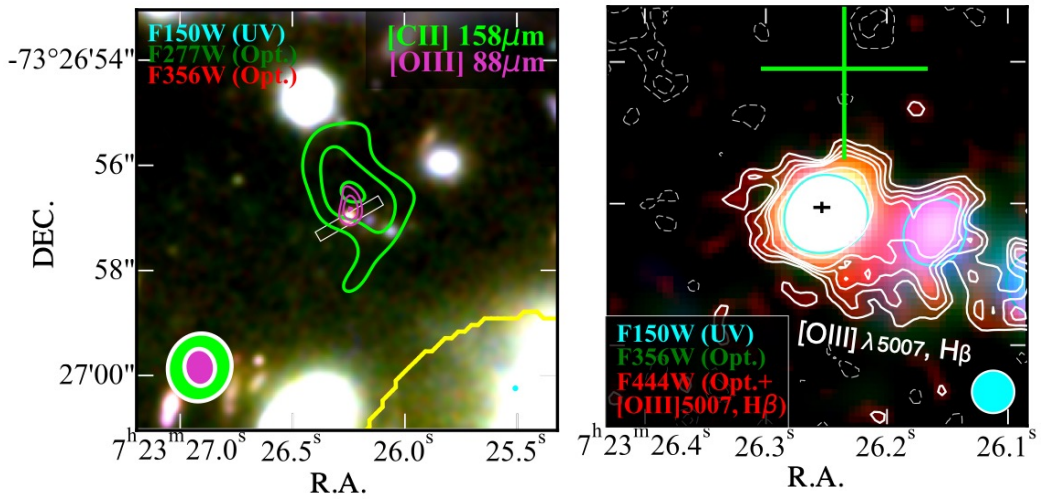

Figure 16: ALMA and *JWST* observations for a galaxy at $z \sim 8.5$ in the SMACS0723 field (Pontoppidan et al. 2022). The left panel shows the underlying RGB image built with the F150W, F277W and F356W bands from *JWST*/NIRCam, and the ALMA [C II]-158μm (green) and [O III]-88μm (purple) emission line contours. The [O III] emission is co-spatial with the *JWST* source. The [C II] is $\sim$ 10 times more extended than the UV component, and is offset by 0.″5, as can be seen in the right panel, where the green cross indicates the peak [C II] emission, and the black cross the peak *JWST* F444W emission. Figure from Fujimoto et al. (2022).

inferred stellar masses. For example, the choice of SFH can significantly impact the best-fit stellar mass (e.g., Whitler et al. 2023). The mass is obtained via mass-to-light ratios, which tend to be lower limits to the true M/L ratios when estimated via simple SFHs. This is due to the fact that young stars can outshine underlying older stellar populations and make it challenging to infer the correct stellar ages and thus masses. With broad-band rest-frame optical photometry, it is difficult to break the degeneracy between contamination by strong emission lines from the youngest stars, or the emission by underlying older stellar continuum (e.g., Schaerer & de Barros 2009; Stark et al. 2013; Smit et al. 2015, 2016). This can be particularly relevant in galaxies with high SFRs (Papovich et al. 2001). Some studies have suggested that NIR data is necessary to provide more accurate masses (e.g. Zibetti et al. 2009; Bisigello et al. 2019). The problem of outshining has been extensively studied (e.g., Papovich et al. 2001; Shapley et al. 2001; Daddi et al. 2004; Shapley et al. 2005; Trager et al. 2008; Maraston et al. 2010; Graves & Faber 2010; Pforr et al. 2013; Sorba & Sawicki 2015, 2018; Paulino-Afonso et al. 2022; Suess et al. 2022; Topping et al. 2022; Tacchella et al. 2023; Whitler et al. 2023). In Chapters 3 and 4 we investigate the severe impact that outshining can have in the inferred stellar ages and masses, and how it biases our observational studies of galaxies at high-z.

Another observational bias that one must be wary of is the degeneracy between strong emission lines and the Balmer break (e.g., Roberts-Borsani et al. 2020). With broad-band photometric bandpasses, it can be challenging to distinguish whether a spectral feature is primarily due to the continuum break associated with an evolved stellar population or if it is dominated by emission lines from ionised gas. In certain cases, redshift ambiguities may exacerbate the degeneracy. Different combinations of redshift and underlying stellar population properties can produce similar observed features, making it challenging to uniquely constrain these parameters from broad-band photometry alone. Moreover, the combination of weak emission lines can have a non-negligible contribution to broad-band photometry (e.g., Nakajima & Maiolino 2022). With both outshining and the Balmer break degeneracy, medium-band photometry (e.g., Laporte et al. 2023; Suess et al. 2023) or IFS observations are essential to distinguish between the different emission components and infer unbiased physical estimates. Combining spectroscopic and photometric observations can be fruitful, given that the inferred parameters are affected by distinct systematic uncertainties. For example, spectroscopic masses exhibit considerably less susceptibility to dust attenuation than their photometric counterparts (e.g., Drory et al. 2004; Conroy 2013).

The discussion of these observational biases has been one of the main topics in the first year of *JWST* observations. The major result that sparked the debate was Labbé et al. (2013), which found six galaxy candidates with $M_* > 10^{10} M_\odot$ at $7.4 < z < 9.1$. The striking result comes particularly from one of the galaxies, with a stellar mass of $\sim 10^{11}$ solar masses. This defies the ΛCDM cosmology, given that this galaxy would have more stellar mass than baryon mass available at that cosmic epoch. Multiple solutions have been proposed to this problem, such as non-parametric SFHs (Endsley et al. 2023; Whitler et al. 2023) and changes in the IMF (Steinhardt et al. 2022), which can lower the inferred stellar masses by $\sim$1 dex and potentially resolve the conflict. Regardless of which study has managed to report the *true* stellar mass, these recent findings highlight some of the issues that still persist in SED modelling based on photometric observations. By dissecting the adopted assumptions and studying all systematics, the observational study of galaxies can keep evolving to improve how physical properties are recovered.

Another important observational bias that has been highlighted in the last year comes from the Balmer and Lyman breaks, introduced before as two major absorption features that a spectrum can exhibit (see § 1.3.3). A Lyman break of a high redshift galaxy can be difficult to distinguish from strong line emission or a Balmer break at low redshift (e.g., van der Wel et al. 2011; Vulcani et al. 2017). Due to this, with the newest *JWST* observations, the hunt for the highest redshift objects has encountered some low-redshift interlopers instead. This is the case for a galaxy in the CEERS survey (Finkelstein et al. 2023), which, given its 0.6–5μm photometry appeared to be at $z \sim 17$ (Naidu et al. 2022b; Donnan

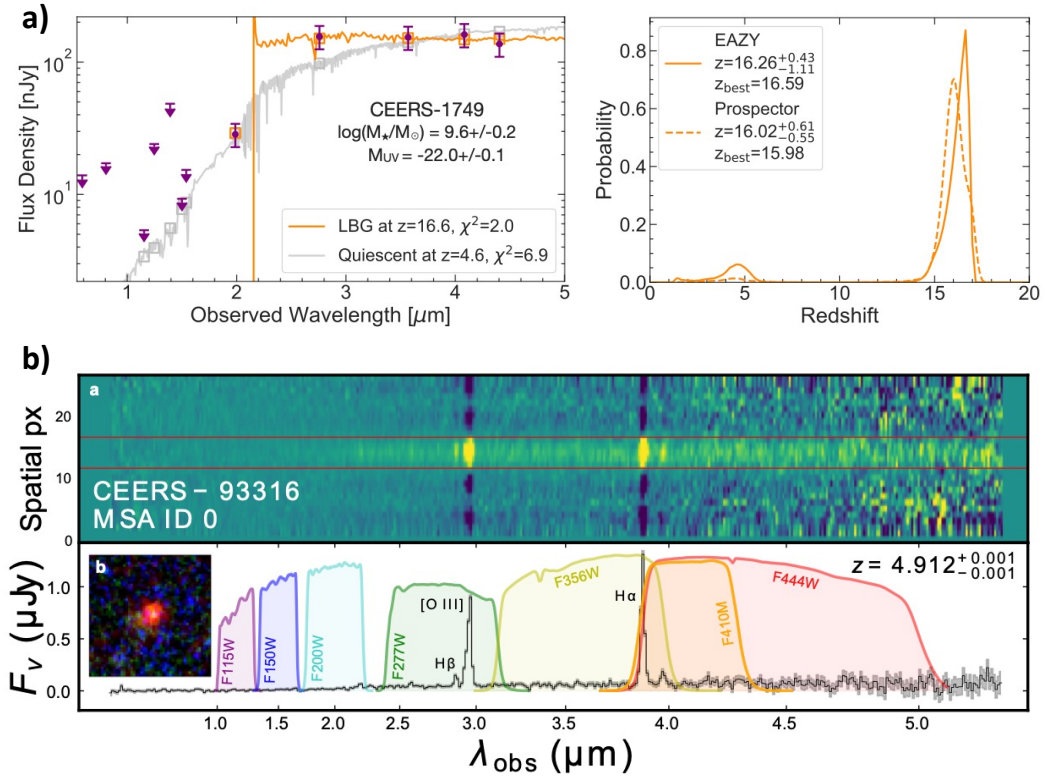

Figure 17: **a)** Photometry and spectral energy distributions of a CEERS galaxy potentially at $z \sim 17$, or a lower redshift interloper, a quiescent or dusty galaxy at $z \sim 5$. The right plot shows the probability density function of the photometric redshift, which clearly favours the high redshift solution. Figure from Naidu et al. (2022a). **b)** *JWST* spectrum of the source, and NIRCam coverage indicated with the filter curves. The source is found to be at $z = 4.912$. Figure from Arrabal Haro et al. (2023).

et al. 2023a; Harikane et al. 2023b), which would make it the furthest galaxy ever known. On the other hand, the SED could also be explained by intense line emission (see Figure 17a) from a dusty or quiescent galaxy at $z \sim 5$ (e.g., Naidu et al. 2022a; Zavala et al. 2023). In the end, this galaxy has been confirmed through spectroscopy to be at $z = 4.9$ (Arrabal Haro et al. 2023, see Figure 17b).

Spatially-resolved studies can potentially disentangle regions where lines or continuum dominate, and often find discrepant ages and stellar masses when compared to spatially-integrated studies (e.g., Zibetti et al. 2009; Wuyts et al. 2012; Sorba & Sawicki 2018). Our understanding of the high-redshift Universe is based on integrated observations. To date, we have not been able to access spectrally- or spatially-resolved information of high-z galaxies, with HST being able to only marginally resolve galaxies at $z \sim 3$ with its reddest filter. With *JWST* we can finally map and resolve the rest-frame infrared and optical emission at $z > 3$, but still with the uncertainty that relying only on broad-band photometry brings.

These issues highlight some of the intricacies and difficulties of studying galaxies observationally, and motivate new studies, techniques and approaches that might mitigate or resolve them.

1.6 THESIS OUTLINE

This thesis delves into the study of galaxies across 13 billion years of cosmic time, from our closest neighbours to the early Universe. Throughout this work, I present the various publications and studies done during this PhD.

In Chapter 2, we start by studying a sample of 24 nearby galaxies ($z \sim 0$) with the *Hubble Space Telescope*. By developing an SED-fitting code based on EAzY (Brammer et al. 2008), we infer line fluxes from narrow-band photometry, and get maps of the physical properties such as the stellar mass, SFR, and dust obscuration. As introduced before, we can derive maps of the extinction towards H II regions by using hydrogen recombination lines, in order to reveal obscured star formation happening across the galaxies. During this work, we get acquainted with studying galaxies at very high resolution, and dealing with a large amount of pixels and information per source, being able to resolve internal structures and distinct stellar populations. This sets the overarching theme of this thesis.

In July 2022, when the first public images of *JWST* were released, we decided to extend the approach of our first work to study the early Universe. In Chapter 3 I present this study. We select the highest spectroscopically-confirmed redshift galaxies in the SMACS0723 field, and infer the spatially resolved properties of these objects. We conduct a comparison with what is obtained with the commonly adopted single-aperture photometry approach. Given the implications of our results, we discuss the importance of studying galaxies as the complex systems that they are, resolving their stellar populations when possible.

In the previous two works, we only make use of photometry, in order to infer the properties of galaxies across cosmic time. As introduced in the previous sections, photometric-only studies have been extensively proven to present many assumptions and difficulties, such as degeneracies between age, dust and redshift. On top of this, the unknown strength of emission lines can contaminate broad-band photometry, making quantities such as stellar ages and line fluxes very uncertain, or even unconstrained. Thus, it is vital to compare our photometric resolved studies to spectroscopic measurements. In Chapter 4, I present a study on a $z \sim 6$ galaxy, a beacon into the end of reionisation. This galaxy is significantly lensed and extended. We choose this target because it has recently been observed with both NIRCam imaging, as well as NIRSpec IFU, so that we have spectral measurements on a pixel-by-pixel basis. This study allows us to test our conclusions from the previous work, as well as extending the resolved analysis by testing various star formation history parameterisations. We also study the contribution of this target to the end of reionisation.

Finally, I present the conclusions of this dissertation in Chapter 5, placing into the context of the field our various results, as well as discussing an outlook for future work and perspectives of the field.

2

NEARBY GALAXIES WITH THE HUBBLE SPACE TELESCOPE

This chapter contains the following article:

"High-resolution *Hubble Space Telescope* Imaging Survey of Local Star-forming Galaxies. I. Spatially Resolved Obscured Star Formation with Hα and Paschen-β Recombination Lines"

Published in The Astrophysical Journal Supplement Series (ApJS): Volume 263, Issue 1, id.17, 32pp., November 2022, DOI: 10.3847/1538-4365/ac958c

Authors: Clara Giménez-Arteaga, Gabriel B. Brammer, Danilo Marchesini, Luis Colina, Varun Bajaj, Malte Brinch, Daniela Calzetti, Daniel Lange-Vagle, Eric J. Murphy, Michele Perna, Javier Piqueras-López and Gregory F. Snyder

ABSTRACT

We present a sample of 24 local star-forming galaxies observed with broadband and narrowband photometry from the Hubble Space Telescope (HST) that are part of the Great Observatories All-sky Luminous Infrared Galaxies Survey of local luminous and ultraluminous infrared galaxies. With narrowband filters around the emission lines Hα (and [N II]) and Paβ, we obtain robust estimates of the dust attenuation affecting the gas in each galaxy, probing higher attenuation than can be traced by the optical Balmer decrement Hα/Hβ alone by a factor of >1 mag. We also infer the dust attenuation toward the stars via a spatially resolved spectral energy distribution fitting procedure that uses all available HST imaging filters. We use various indicators to obtain the star formation rate (SFR) per spatial bin and find that Paβ traces star-forming regions where the Hα and the optical stellar continuum are heavily obscured. The dust-corrected Paβ SFR recovers the 24μm-inferred SFR with a ratio -0.14 ± 0.32 dex and the SFR inferred from the 8—1000 μm infrared luminosity at -0.04 ± 0.23 dex. Both in a spatially-resolved and integrated sense, rest-frame near infrared recombination lines can paint a more comprehensive picture of star formation across cosmic time, particularly with upcoming JWST observations of Paschen-series line emission in galaxies as early as the epoch of reionization.

2.1 INTRODUCTION

Past and recent multi-wavelength extra-galactic surveys both on the ground and in space (e.g., COSMOS, Laigle et al. 2016; Weaver et al. 2022; CANDELS/3D-HST, Grogin et al. 2011; Koekemoer et al. 2011; Skelton et al. 2014; UltraVISTA, McCracken et al. 2012; Muzzin et al. 2013; UKIDSS, Lawrence et al. 2007; HFF, e.g., Shipley et al. 2018), have allowed us to closer examine the evolutionary processes in many thousands of stellar-mass-selected galaxies back to when the Universe was only 1.5 Gyr old. Well sampled photometry of these objects enables us to robustly model their spectral energy distributions (SEDs) and thus estimate their redshifts and study the properties of their stellar populations (e.g. stellar mass, star formation rate/history, dust attenuation) over a wide range of redshifts. We can then study how these galaxies form, evolve and interact across cosmic time. However, the SED-fitting approach relies on a number of assumptions (e.g., the initial mass function, the dust geometry and extinction law, star formation history; see e.g. Conroy 2013 for a review), which are often overly simplified and surprisingly poorly constrained, even in the nearby Universe.

To derive the intrinsic properties of a galaxy, one must have an in-depth understanding of the dust content of the sources, since it modifies the galaxies' inherent SEDs in a wavelength-dependent way, in terms of both extinction and reddening. The dust in a galaxy absorbs the stellar emission in the UV and re-

emits it at longer wavelengths. A commonly used dust obscuration prescription is the local starburst attenuation curve (e.g., Calzetti et al. 2000). For normal star-forming galaxies, a Milky Way-like or Magellanic-Clouds attenuation curve may be more appropriate (e.g., Kriek & Conroy 2013). Therefore, even in the local Universe the attenuation curve is not universally Calzetti et al. (2000). As we look back in time, the conditions we observe and measure in galaxies change (star formation rate, metallicity, dust content, etc.), and it remains unknown whether these attenuation curves are valid for high-redshift galaxies or the variations in these properties make them also dependent on redshift (see, e.g., Roebuck et al. 2019; Salim & Narayanan 2020).

Hydrogen recombination lines can be used to derive both the dust extinction and geometry. The most common pair of recombination lines used for this purpose is the Balmer decrement, Hα/Hβ. However, recent works find that the classic Balmer decrement underestimates the attenuation in galaxies when compared to the Balmer-to-Paschen decrement (Hα/Paβ). For instance, Liu et al. 2013 (hereafter L13) show that the ratios between redder lines (e.g. Hα/Paβ) can probe larger optical depths than bluer lines such as the Balmer decrement by >1 mag. Calzetti et al. (1996) find equivalent results with the Paβ/Brγ ratio on a sample of local starburst galaxies. The Balmer-to-Paschen decrement (Hα/Paβ) technique has been demonstrated for local-group H II regions (Pang et al. 2011; De Marchi & Panagia 2014), for a portion of the nearby starburst M83 (L13), and more recently employed at somewhat higher redshifts (Cleri et al. 2022). However, to date this technique has not been used extensively for systematic study of the extinction properties of local galaxies, nor with the quality and high spatial resolution of the *Hubble Space Telescope* (HST). Local Seyfert, luminous and ultra-luminous infrared galaxies often have significant attenuation with $A_V > 2$ mag over a large fraction of the visible extent of the galaxies (e.g., Kreckel et al. 2013; Mingozzi et al. 2019; Perna et al. 2019, 2020); all above mentioned arguments suggest that even larger attenuations might be present in these classes of sources.

The strength of using hydrogen recombination lines to infer dust obscuration lies in the fact that the intrinsic line ratios show relatively little variation across a broad range of physical conditions of the ionized gas. As shown in L13, assuming Case B recombination, with changes in the temperature between $5{\times}10^3$ and 10^4 K, and in the electron density of an H II region between 10^2 and 10^4 cm^{-3}, the Hα/Paβ line ratio only changes between 16.5 and 17.6 ($\sim$ 7%, Osterbrock 1989). For the analysis below, we adopt an electron density $n_e = 10^3$ cm^{-3} and temperature T_e=7500 K (as in e.g. L13 for M83), resulting in an intrinsic ratio (Hα/Paβ)$_{int}$=17.56 (Osterbrock 1989). Under the assumption of constant electron density and temperature, deviations measured from this intrinsic value can thus be directly associated to dust attenuation.

Near infrared Paschen-series lines (e.g., Paα and Paβ at wavelengths 1.876 and 1.282 μm, respectively) have been used to reveal star formation activity that is otherwise obscured for visible hydrogen recombination lines such as Hα and Hβ, as well as for the optical emission from the stellar continuum (e.g., Tateuchi et al. 2015; Piqueras López et al. 2016; Cleri et al. 2022). They have also been compared to IR-based SFR indicators (e.g., $L(8\text{—}1000\,\mu\text{m})$; Kennicutt 1998), to check whether one can recover the star formation activity after applying dust corrections. Other studies directly suggest that one cannot use rest-optical lines to estimate physical properties of entire starburst systems, and one should instead aim to obtain rest-frame near-IR observations (Puglisi et al. 2017, Calabrò et al. 2018). Other recent works have used radio emission (specifically free-free emission) to measure star formation, in addition to IR and recombination lines (e.g., Murphy et al. 2018; Linden et al. 2019, 2021; Song et al. 2021). Free-free emission does not have the caveat of being affected by extinction as is the case for recombination lines. However, no study has had both the high quality and spatial resolution that HST can offer. This work opens an exciting avenue in spatially-resolved studies that will become increasingly available with upcoming JWST observations.

Recent works show larger amount of dust obscuration with increasing redshift among the most massive galaxies ($\log(M/M_{\odot}) > 10.5$; Brammer et al. 2009; Marchesini et al. 2014; Skelton et al. 2014; Marsan et al. 2022). The detection of many of these objects in the *Spitzer*/MIPS 24μm band implies that they have $L_{IR} > 10^{11} L_{\odot}$, typical of luminous and ultra-luminous infrared galaxies (LIRGs and ULIRGs; Sanders & Mirabel 1996). At $z < 1$, this population of galaxies seems to have generally diminished (Marchesini et al. 2014, Hill et al. 2017). The major complication to comprehend these systems is that at high-redshift they might be multiple unresolved objects in the process of merging (Decarli et al. 2017; Silva et al. 2018; Marsan et al. 2019; Jones et al. 2020; Bischetti et al. 2021), as well as how little we know about the dust distribution in them, leading to oversimplified assumptions of their dust modelling.

Understanding the dust distribution in local LIRGs and ULIRGs is imperative to further our comprehension of the population of massive galaxies at the peak of star formation ($z \sim 2$, Madau & Dickinson 2014). Beyond $z > 1$, U/LIRGs begin to play an important part in the evolution of the star formation history of the Universe, increasing its contribution with redshift, to the point of even dominating the SFR activity at $z \sim 2$ (e.g., Pérez-González et al. 2005; Magnelli et al. 2013; Zavala et al. 2021). These LIRGs studies show that obscured star formation contributes the most to the SFR density. Instruments such as WFC3 onboard of the HST allow us to closely examine this by obtaining Hα and Paβ extinction maps and star formation estimates. Although separated by billions of years of evolution, local highly luminous objects appear similar to very distant massive dusty galaxies, in terms of for example their high infrared luminosity,

large amounts of dust obscuration, Hα size and surface brightness (see e.g., Arribas et al. 2012). Therefore, by exploiting the high spatial resolution and high signal-to-noise ratio (S/N) of these local systems, we can at the same time aid our closer examination of the distant Universe. On the other hand, these local objects appear to be different to higher redshift systems in terms of the distribution of the star formation and the dust temperature (Muzzin et al. 2010; Bellocchi et al. 2022). Furthermore, high redshift U/LIRGs are more extended and display a cooler IR SED (Elbaz et al. 2011).

In this paper we present the observations and first results of a multi-wavelength study of 24 nearby galaxies ($z < 0.035$) observed with HST, to study the spatially-resolved properties of their dust-obscured stellar populations and star formation activity. Using data from our own recent program along with archival observations, we obtain, at a minimum, narrow-band images centered on the redshifted Hα and Paβ recombination lines and corresponding optical and near-infrared broad-band continuum images in filters similar to rest-frame I- and J-bands. Archival observations of a subset of the full sample provide additional broad-band images extending the SED sampling to the near-ultraviolet wavelengths. We develop a spatial binning procedure with Voronoi tessellation that probes spatial scales as small as 40 pc at the median redshift of our sample ($z = 0.02$), and a SED-fitting technique that robustly infers emission line fluxes from the narrow-band images.

This paper is structured as follows: In Section 2.2, we introduce the HST observations and data processing procedure. Section 2.3 describes the methodology we develop for the spatially-resolved image analysis, including spatial binning and multi-band SED-fitting software. In Section 2.4, we present the main results and properties of our sample, as well as discussing the implications of our findings. Finally, Section 2.5 presents a summary of our work and corresponding conclusions. Throughout this paper, we assume a Chabrier (2003) initial mass function (IMF) and a simplified ΛCDM cosmology with $H_0 = 70$ km/s/Mpc, $\Omega_m = 0.3$ and $\Omega_\Lambda = 0.7$. We use the biweight location and scale statistics defined by Beers et al. (1990), when referring to derived mean values and their uncertainties.

2.2 DATA AND OBSERVATIONS

We conducted an HST snapshot survey program in Cycle 23 (HST-14095, PI: Gabriel Brammer; Brammer 2015) to obtain narrow-band images of nearby galaxies centred on the (redshifted) Hα and Paβ hydrogen recombination lines. The full target list of the survey was defined as essentially any nearby galaxy ($z < 0.05$) that had existing wide-field HST archival imaging in either narrow-band Hα from ACS/WFC or WFC3/UVIS, or Paβ from WFC3/IR, to which we added the missing narrow-band and an associated broad-band continuum filter.

The combination of the parent selection and the fact that a random subset of them were observed as snapshots, yields a heterogeneous sample in terms of star formation rate, stellar mass, morphology, etc. ($0.01 < \mathrm{SFR}\,[M_\odot/\mathrm{yr}] < 200$; $10^{7.5} < M_*[M_\odot] < 10^{15.5}$; and in terms of morphology, from spirals to irregulars and mergers). The observations are available for a sample of 53 galaxies, 24 of which are in the GOALS survey of local luminous and ultraluminous infrared galaxies (Armus et al. 2009, $z < 0.088$, $L_{\mathrm{IR}} > 10^{11}\ L_\odot$).

The number of available imaging filters from the ultraviolet through the near infrared varies significantly across the full sample. At the very least, each target has narrow-band images for Hα, Paβ, and an associated continuum filter for each line. The filters used in the continuum also vary due to the availability of archival observations – the optical continuum may be F606W, F621M, F555W, F625W or F814W and the near-infrared continuum is either the broad F110W filter and/or off-band narrow-band images (the continuum filters were WFC3/UVIS F814W for Hα and WFC3/IR F110W for Paβ for the observations from our program). The narrow-band filters were chosen as appropriate for the redshift of a given source. The full sample and filter coverage are summarized in Tables 1 and 9.

Each image was processed/created using the `DrizzlePac` (Gonzaga et al. 2012) modules `TweakReg` for relative alignment and `AstroDrizzle` for image combination and stacking. The original pixel size of the images obtained with the WFC3/IR channel is $0\farcs128$ pixel^{-1}. The images are drizzled to combined mosaics with $0\farcs1$/pixel for the IR filters and $0\farcs05$/pixel for the optical ACS/WFC and WFC3/UVIS filters[1]. Our sample spans redshifts from 0.0001 to 0.035, with a median $z \sim 0.02$. This corresponds to a physical size of 0.3 to 70 pc/pixel, ∼40 pc/pixel at the median redshift (for the $0\farcs1$ WFC3/IR pixels).

Our galaxies span a wide range in infrared luminosity ($8.9 < \log(L_{IR}/L_\odot) < 12.3$), as can be seen in Figure 18, which yields a very heterogeneous sample, also in terms of e.g., stellar mass and morphology. A large number of our galaxies are undergoing starbursts (as we would expect for the GOALS sample selection criteria, which are all above the main sequence in Figure 18), most likely driven by mergers in some cases, since we can see paired galaxies in our HST images. In the work presented in this first paper, where we focus on the study of the star formation activity inferred with different tracers, we only use the targets from the GOALS sample in our analysis (Table 1), due to the availability of measurements for their infrared luminosities and 24μm fluxes. We present additional galaxies in the Appendix (Table 9), for which we have processed the HST data as explained above, but that are not part of the analysis in this work. These targets often have spatial extent larger than the Field of View (FoV) of the instrument.

[1] All of the aligned image mosaics are available at `http://cosmos.phy.tufts.edu/dustycosmos/`

Target	R.A. [deg]	Decl. [deg]	z	$\log(\frac{L_{IR}}{L_\odot})$	UV WFC3/UVIS	Optical WFC3/UVIS, ACS/WFC	IR WFC3/IR
Arp 220**	233.7375	23.5031	0.01813	12.27	F336W	F435W, FQ508N, F621M, F665N, F680N, F814W	F110W, F130N, F160W
ESO550-IG025**	65.33333	-18.81333	0.03209	11.50	F225W	F435W, f673n, F814W	f110w, f132n
IRAS03582+6012	60.63374	60.34383	0.03001	11.42		f625w, f673n	F110W, F130N, F132N, F160W
IRAS08355-4944**	129.25761	-49.90841	0.02590	11.61	F225W	F435W, f673n, F814W	F110W, F130N, F132N
IRAS12116-5615**	129.25761	-49.90841	0.02710	11.64		F435W, f673n, F814W	f110w, f132n
IRAS13120-5453*	198.77660	-55.15628	0.03076	12.31	F225W	F435W, f673n, F814W	F110W, F130N, F132N
IRAS18090+0130**	272.91010	1.52771	0.02889	11.64		F435W, f673n, F814W	f110w, f132n
IRAS23436+5257	356.52380	53.23235	0.03413	11.56	F225W	F435W, f673n, F814W	F110W, F130N, F132N
IRASF10038-3338**	151.51938	-33.88503	0.03410	11.77		F435W, FR656N, f673n, F814W, FR914M	F110W, F130N, F132N
IRASF16164-0746*	244.799	-7.90081	0.02715	11.61		F435W, f673n, F814W	F110W, F130N, F132N
IRASF16399-0937**	250.66709	-9.7205	0.02701	11.62		F435W, FR656N, f673n, F814W, FR914M	F110W, F130N, F132N
MCG-02-01-051	4.71208	-10.376803	0.02722	11.47		F435W, f673n, F814W	F110W, F130N, F132N
MCG+12-02-001**	13.51643	73.084786	0.01570	11.49	F225W	F435W, f665n, F814W	f110w, f130n
NGC1614**	68.50011	-8.57905	0.01594	11.64	F225W	F435W, f665n, F814W	f110w, f130n
NGC2146**	94.65713	78.35702	0.00298	11.11	F225W, F336W	F658N, F814W	F110W, F128N, F160W, F164N
NGC2623*	129.60039	25.75464	0.01851	11.59		F435W, F555W, FR656N, f665n, F814W	f110w, f130n

Table 1. (Continues below)

Target	R.A. [deg]	Decl. [deg]	z	$\log(\frac{L_{IR}}{L_\odot})$	UV WFC3/UVIS	Optical WFC3/UVIS, ACS/WFC	IR WFC3/IR
NGC5256*	204.57417	48.27806	0.02782	11.55		F435W, f673n, F814W	F110W, F130N, F132N
NGC5331**	208.06729	2.10092	0.03304	11.65		F435W, f673n, F814W	F110W, F130N, F132N
NGC6090**	242.91792	52.45583	0.02984	11.57	F336W	F435W, F502N, F550M, FR656N, f673n, F814W	F110W, F130N, F132N, F160W
NGC6240*	253.24525	2.40099	0.02448	11.92	FQ387N	F435W, F467M, FQ508N, F621M, F645N, F673N, F680N, F814W	F110W, F130N, F132N
NGC6670**	278.3975	59.88881	0.02860	11.64	F225W	F435W, f673n, F814W	f110w, f132n
NGC6786	287.7247	73.41006	0.02511	11.48		F435W, f673n, F814W	F110W, F130N, F132N, F160W
NGC7592*	349.59167	-4.41583	0.02444	11.39		f625w, f673n	f110w, f132n
VV340A*	224.25127	24.606853	0.03367	11.73		F435W, f673n, F814W	F110W, F130N, F132N

*Targets that host an AGN, X-ray selected based on Iwasawa et al. (2011), Torres-Albà et al. (2018) or Ricci et al. (2021).

**Targets that do not host an AGN, based on Iwasawa et al. (2011), Torres-Albà et al. (2018) or Ricci et al. (2021).

Table 1: Sources in the sample of nearby star-forming galaxies presented in this work that are also part of the GOALS Survey (Armus et al. 2009). The infrared luminosity is from GOALS (normalised to our cosmological parameters using Wright (2006)). The redshift is from Chu et al. (2017). The filters added by the Cycle 23 SNAP program (HST-14095, Brammer 2015) are indicated with small caps, whereas the rest are archival data.

2.3 METHODOLOGY

In this work we develop two main methodologies to first derive spatial bins that homogenize the measurement signal-to-noise across the extent of each target galaxy, and second to analyse the (binned) multi-wavelength SEDs, that include measurements from as many as 12 broad- and narrow-band imaging filters from NUV to NIR wavelengths.

2.3.1 *Voronoi Binning*

Modern instruments allow us to spatially resolve nearby extended sources, although these observations can display a significant anisotropy in the signal-to-noise-ratio (S/N) across the target. Sometimes these variations differ by orders-of-magnitude, and some pixels often have poor S/N. To resolve this, the spatial elements can be grouped locally (binned) to obtain a more uniform S/N across the image, however this results in a loss of spatial resolution.

Disk galaxies typically have "exponential" surface brightness profiles (Boroson 1981), thus the outskirts are much fainter than the centers. With this in mind, we implement an adaptive binning scheme: for lower S/N, larger bins are created, whereas for high S/N regions, the bins are smaller and a high resolution is maintained. For this, we adapt the Voronoi binning procedure from Cappellari & Copin (2003). This method implements adaptive spatial binning of integral-field spectroscopic (IFS) data to achieve a specified constant signal-to-noise ratio per spatial bin.

The Cappellari & Copin (2003) Voronoi algorithm[2] is inefficient for handling datasets with millions of data points as is the case for the large image mosaics used here. Furthermore, the algorithm is not robust in the regime of low S/N per original data point (Cappellari & Copin 2003), as in the outskirts of the galaxies in our HST images. Therefore, we adopt a hybrid approach of block-averaging the galaxy mosaics in progressively-shrinking box sizes and applying the Voronoi algorithm on the blocked image. A detailed explanation of our binning procedure[3] is provided in Appendix 2.5.

For the spatial binning, we set a target signal-to-noise (S/N) ratio of at least 20 per bin in the narrow-band image that includes Paβ, to ensure a minimum constant S/N across the resulting Paβ emission line image once the continuum is subtracted, where the per-pixel uncertainties are provided by the *HST* imaging

[2] https://www-astro.physics.ox.ac.uk/~mxc/software/

[3] https://github.com/claragimenez/voronoi

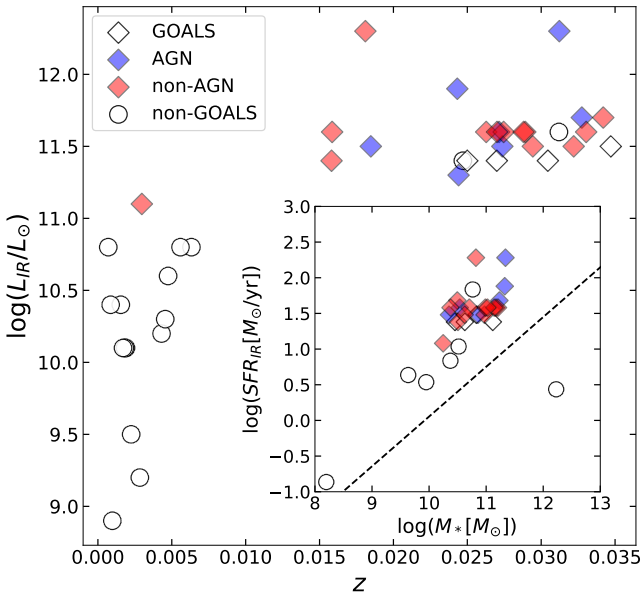

Figure 18: Infrared luminosity as a function of redshift for the galaxies where L_{IR} is available, as tabulated in Tables 1 and 9. The targets from the GOALS sample are indicated with the diamond markers (as opposed to white circles). The X-ray selected AGNs are blue-coloured, whereas the non-AGN are red. The inset plot shows the SFR$_{IR}$ (derived from L_{IR} using Eq.7) versus the stellar mass (inferred with our SED-fitting code), with the $z = 0.02$ main sequence from Whitaker et al. (2012) indicated as the dashed line.

calibration pipelines (e.g., §3.3.5 of the WFC3 Data Handbook; Sahu 2021). The spatial bins derived from the Paβ narrow band image are then applied to all other available filters for a given target, so that we can measure photometry for each spatial bin across the filters. The threshold S/N imposed on the Paβ narrow band image is not necessarily achieved in all the other filters (e.g. UV filters, where S/N can be low), whereas it can also be higher in broad band filters such as F110W. Rather than matching the wavelength-dependent PSFs of the different filters, which involves a convolution with an imperfect matching kernel and modifies the pixel variances in a nontrivial way, we adopt a minimum bin size of 2×2 0.″1 pixels so that the bins are larger than the PSF FWHM of any of the individual images. Figure 19 shows a demonstration of the binning scheme for the targets MCG-02-01-051 (top panels) and NGC1614 (bottom panels).

2.3.2 *Continuum Subtraction*

The raw flux density measured in a narrow-band filter centered on an emission line includes contributions from both the line itself and any underlying continuum, where the fractional contribution of the continuum increases with the width of the filter bandpass. To produce pure hydrogen emission line images (Hα and Paβ line fluxes in our case), we first need to remove the contribution

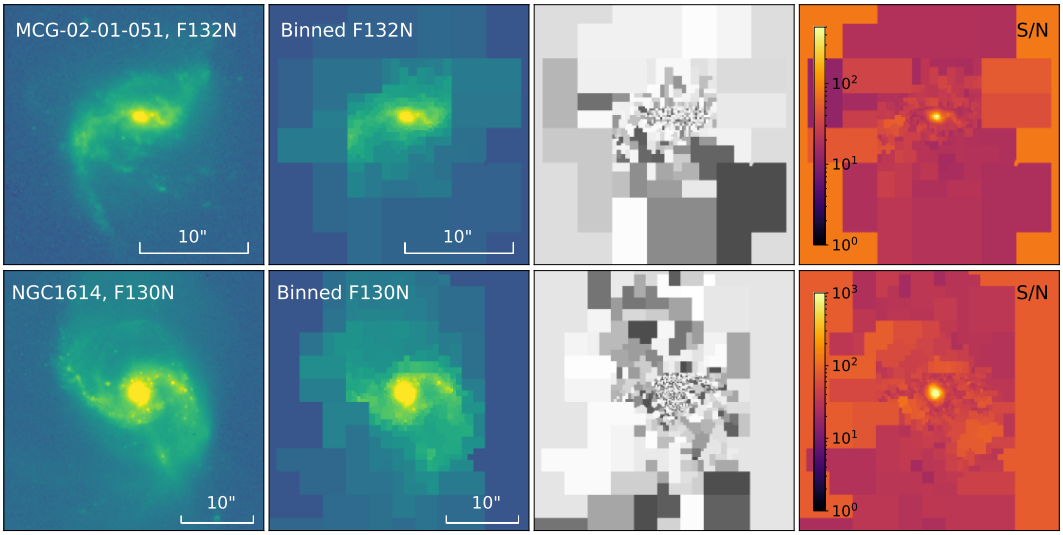

Figure 19: Voronoi binning for the targets MCG-02-01-051 (top panels) and NGC1614 (bottom panels). From left to right: original HST narrow-band image that targets Paβ; binning on the narrow-band image where we impose a S/N threshold of 20; Voronoi binning pattern, where the colourmap separates each individual bin from its neighbours; resulting signal-to-noise maps on the narrow-band image after binning.

from the stellar continuum. A common approach to deal with this issue is to perform a "simple" background subtraction, in which a nearby broad-band filter (or an interpolation of multiple broad-band filters) is scaled and subtracted from the respective narrow-band filter containing the emission line of interest using some estimate of the continuum shape across the various bandpasses. A linear continuum shape is generally either assumed explicitly or implicitly (e.g., a flat spectrum that defines the photometric calibration of the various filters) or estimated empirically from the colour of a pair of continuum filters bracketing the narrow line bandpass (as is done in e.g., Liu et al. 2013; Calzetti et al. 2021). The adopted broad- or medium-band continuum filters may or may not contain the line of interest. A narrow band filter adjacent to the narrow band line filter can provide a relatively robust continuum estimate, though it is relatively more expensive to reach a given continuum sensitivity as the bandpass shrinks. In all of the cases above, the continuum shape is likely the dominant source of systematic uncertainty on deriving the emission line flux from the narrow-band image.

In this work we develop a new approach to derive the continuum and emission line contributions that uses all of the available information by fitting population synthesis templates to the spatially resolved photometry in all available filters for a given target. It is inspired by the photometric redshift fitting code EAZY (Brammer et al. 2008), with the motivation to precisely fit the contribution from the stellar continuum and the lines separately, in order to produce

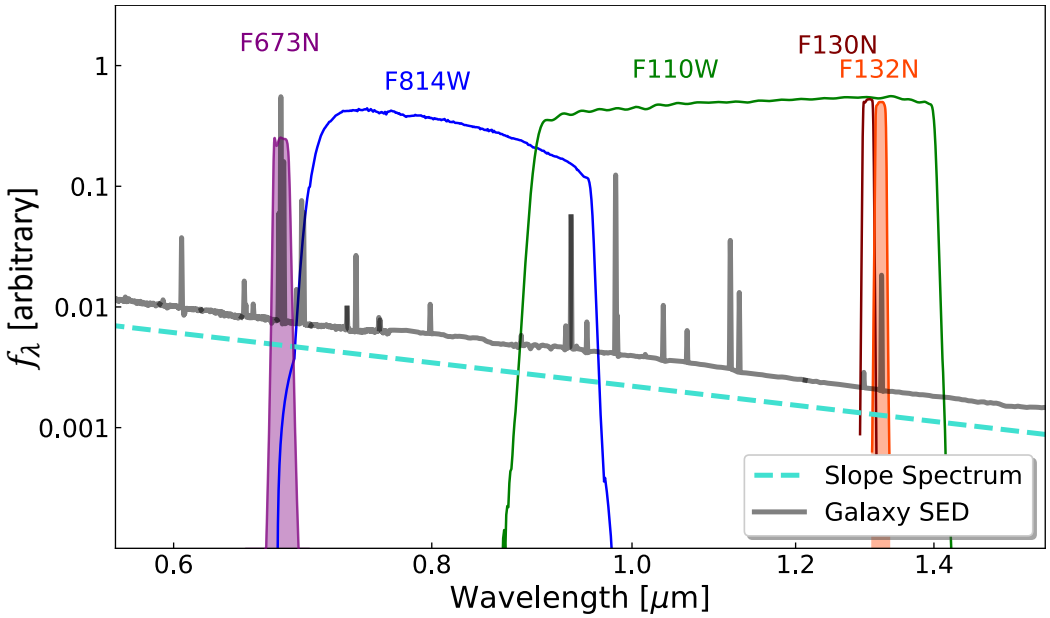

Figure 20: Transmission of some of the HST filters that cover our sample, indicated by the coloured solid lines and the name for each filter, taken from the Spanish Virtual Observatory Filter Profile Service (Rodrigo & Solano 2020). The solid grey line corresponds to a galaxy SED redshifted to $z = 0.03$. The dashed turquoise line corresponds to a slope spectrum model used to fit the continuum in the 'simple' approach. The position of the Hα and Paβ emission lines are indicated by the coloured narrow bandpasses.

robust line fluxes without stellar continuum contamination. Our code fits a set of continuum and line emission templates on a bin-to-bin basis, in order to infer spatially-resolved physical properties of our nearby galaxies. In the next section, as well as in Appendix 2.5, we explain our SED-fitting code in further detail.

Figure 20 shows an example of the HST coverage that we can have for one of our targets. We have two narrow-band filters targeting Hα (purple colouring) and Paβ (orange colouring), as well as broad-band neighbouring filters, F814W and F110W in this case. A flat sloped spectrum (turquoise dashed line) and a redshifted galaxy SED (black line) are plotted, and could be used in "simple" continuum subtraction methods to remove the stellar continuum emission from the narrow-band filters. As we can see, the F110W broad-band filter contains the emission line, and would lead to over-subtraction if used for this purpose. On the other hand, we could have off-band narrow-band filter coverage, such as F130N in Figure 20, which would allow an analytical solution to subtract the continuum (in this case, iterative subtraction methods are used), but this is not always available, therefore justifying our need to develop a novel methodology. Sections §2.3.4 and §2.3.4 display comparisons between different subtraction methods in further detail.

2.3.3 *SED-Fitting*

As introduced in the previous section, we develop an SED-fitting code to accurately fit the continuum and line emissions in order to obtain the Hα and Paβ line fluxes. Furthermore, our method allows us to derive spatially-resolved physical properties, fitting each galaxy on a bin-to-bin basis, obtaining local estimates such as the star-formation rate (SFR) and stellar mass.

We develop an adaptation of the python-based version of EAZY[4] (Brammer et al. 2008), which we make publicly available[5]. Like EAZY, our code finds the linear combination of templates that best fits all of the observed photometry of each spatial bin. We use a set of four continuum templates and two extra line templates, one with Hα+[N II] in a fixed ratio of 0.55, (see §2.3.4 below) and the other with Paβ emission, that allow us to fit the emission lines separately[6]. Analogous to the stepwise SFH parameterization of the `Prospector-`α software (Johnson & Leja 2017; Leja et al. 2017), we choose four continuum templates to reasonably sample the star formation histories, but without adding excessive flexibility that would lead to the SFHs not being properly constrained by the limited data that we have. The continuum templates are generated with python-fsps (Flexible Stellar Population Synthesis; Conroy et al. 2009, Conroy & Gunn 2010b, Johnson et al. 2021), that allows us to specify our own SFHs, for stepwise time bins between 0, 50, 200, 530 Myr, 1.4 Gyr with constant SFR across each bin (see §2.5). However, by deriving the template scaling coefficients using standard least-squares optimization we do not impose any priors on the relative contributions of the step-wise SFH bins. The template normalization coefficients are transformed to emission line fluxes and star formation rates and stellar masses of the continuum-emitting stellar population, and the analytic covariance of the fit coefficients is used to compute the posterior distributions of those derived parameters. This fitting approach is dramatically faster than sampling codes such as `Prospector`—running ∼800 spatial bins of a single target galaxy with `Prospector` requires 1–2 weeks on a supercomputer on average, whereas we can perform the full fit in the same galaxy in under 5 minutes with our code and a fairly standard laptop computer[7]—. In Appendix 2.5 we discuss additional considerations of the choice of templates and the SED-fitting code.

A new implementation with respect to the EAZY machinery is the addition of a reddening grid. Instead of fitting for redshift, which is well-known for the nearby galaxies in our sample, we construct a reddening grid where we redden the continuum templates by a given amount, and fit the normalization coefficients of the two emission lines and reddened continuum templates. The attenuation

[4] `https://github.com/gbrammer/eazy-py`

[5] `https://github.com/claragimenez/sed_fit_photometry`

[6] We do not fit for additional near-infrared emission lines (e.g., [S III] $\lambda\lambda$9070,9530, He I λ10830) that can contribute up to ∼12% of the signal in the broad F110W filter.

[7] Tested on a 2GHz Quad-Core i5 CPU.

curve used to redden the continuum templates can be input by the user. In this work we use a Calzetti et al. (2000) attenuation curve. The introduction of the line templates to directly fit the line fluxes is the main novelty and motivation behind developing our spatially-resolved SED-fitting code. This allows us to constrain on the one hand the attenuation traced by the stellar continuum, which is due to the diffuse interstellar medium (ISM), and on the other hand, we are able to evaluate the attenuation that the gas suffers, traced by the inferred empirical decrement Hα/Paβ. As discussed in e.g. Greener et al. (2020), the "extra" attenuation experienced by the gas is due to stellar birth clouds, which are H II regions enshrouded in dust, where dust is clumpier than in the diffuse ISM, and it can be traced with nebular emission lines (Hα and Paβ in our study).

Our SED-fitting code finds the best fit solution by minimizing χ^2, defined as in Brammer et al. (2008):

$$\chi^2_{A_V} = \sum_{j=1}^{N_{filt}} \frac{(T_{A_V,j} - F_j)^2}{(\delta F_j)^2}, \tag{2}$$

where N_{filt} is the number of filters, $T_{A_V,j}$ is the synthetic flux of the linear combination of templates in filter j for reddening A_V, F_j is the observed flux in filter j, and δF_j is the uncertainty in F_j, obtained combining the observed uncertainty and the template error function (see Brammer et al. 2008 for more information). Once we find our best fit linear combination, we directly infer the line fluxes Hα and Paβ from the fitted line emission templates. We do this on a bin-to-bin basis, and the ensemble result is the spatially-resolved fit across the face of the target galaxy. Our SED-fitting code allows user input for a variety of parameters and files, such as the templates that are used to fit both the continuum and the lines, making the code flexible to fit both contributions across all wavelength ranges, as long as the input templates cover the desired interval and line emissions.

In summary, our SED-fitting procedure outputs the line fluxes Hα and Paβ in erg/s/cm^2, as well as various physical properties: the extinction (A_V) obtained from the "empirical" Balmer-to-Paschen decrement (A_V(Hα/Paβ)) and the A_V inferred from the stellar population (A_V or $A_{V,\text{continuum}}$, derived with the continuum templates). We also obtain the star-formation rate (SFR) and stellar mass (M_*) (surface density) in each spatial bin.

Additionally, while the SFR from the SED-fit estimates the star formation activity throughout the last ∼100 Myr, we derive the instantaneous (∼10 Myr) star formation rate from the Hα luminosity, following the Kennicutt (1998) relation, and dividing by 1.8 (Calzetti et al. 2007; Kennicutt et al. 2009) to convert from a Salpeter (1955) IMF to Chabrier (2003):

$$\text{SFR}[\text{M}_\odot\text{yr}^{-1}] = 4.4 \times 10^{-42} L_{\text{H}\alpha,\text{corr}}[\text{erg s}^{-1}], \tag{3}$$

where $L_{\text{H}\alpha,\text{corr}}$ is the dust-corrected Hα luminosity, calculated as:

$$L_{\text{H}\alpha,\text{corr}} = L_{\text{H}\alpha,\text{obs}} \times 10^{0.4 A_{H\alpha}}, \tag{4}$$

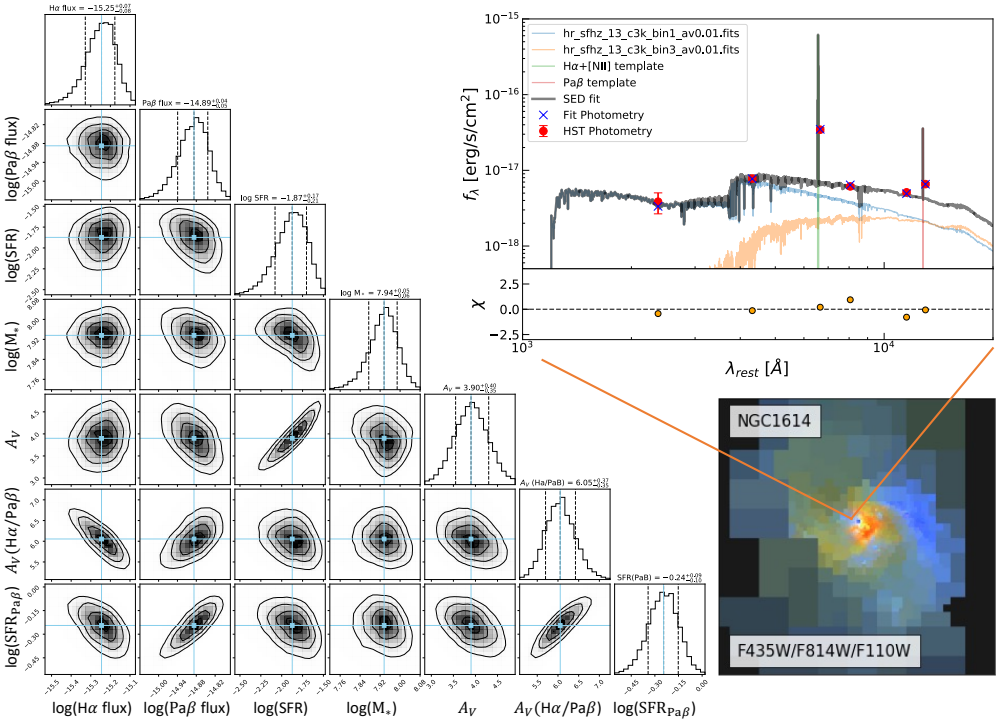

Figure 21: Example of our SED-fitting code applied on the galaxy NGC1614. The bottom right cutout shows the RGB image built combining the F435W, F814W and F110W broad-band filters. The top right plot shows the resulting SED-fit on an example bin from the galaxy. The red points and uncertainties correspond to the original HST photometry. The blue crosses are the resulting synthetic photometry of the best fit. The black curve shows the best fit resulting SED, which is a combination of the different coloured continuum templates and the two line emission templates. The bottom panel shows the residual χ from the fit. On the left, we display the corner plot for the whole fit parameter space for this example bin, displaying the different correlations and distributions between the physical parameters that our code infers.

where $A_{H\alpha}$ is the extinction at the Hα wavelength, and can be obtained using the parameterisation of the attenuation $A_\lambda = k(\lambda)E(B-V)$, where $k(\lambda)$ is given by an attenuation curve, that we must assume, and $E(B-V)$ is the color-excess, which we can calculate in terms of the Paschen-β and Hα observed ratio (e.g. Calzetti et al. 1996):

$$E(B-V) = \frac{2.5}{k(\mathrm{Pa}\beta)-k(\mathrm{H}\alpha)} \log\left(\frac{(\mathrm{H}\alpha/\mathrm{Pa}\beta)_{obs}}{(\mathrm{H}\alpha/\mathrm{Pa}\beta)_{int}}\right), \tag{5}$$

where $(\mathrm{H}\alpha/\mathrm{Pa}\beta)_{int}$ is the intrinsic ratio (that we set to be 17.56, as explained before). Following Calzetti et al. (2000) and subsequent work, the emission lines follow the standard MW curve (Fitzpatrick 1999), so $k(\mathrm{Pa}\beta) = 0.76$ and $k(\mathrm{H}\alpha) = 2.36$. Equivalently, we can infer the most recent SFR with the Paβ

emission instead, which later on is analysed in depth and compared with other star-formation tracers in §2.4. The SFR inferred with the Paβ luminosity is given by:

$$\mathrm{SFR}[\mathrm{M}_{\odot}/\mathrm{yr}] = 4.4\times10^{-42}\times\left(\frac{\mathrm{H}\alpha}{\mathrm{Pa}\beta}\right)_{int}\times L_{\mathrm{Pa}\beta,\mathrm{corr}}[\mathrm{erg/s}], \quad (6)$$

where, equivalently to Equation 4, the dust-corrected Paβ luminosity can be obtained with $A_{\mathrm{Pa}\beta} = k(\mathrm{Pa}\beta)\times E(B-V)$, and we can use Equation 5 to obtain the color excess.

Finally, we can also infer the visual attenuation $A_V = R_V E(B-V)$, obtaining $E(B-V)$ from the line ratio as before. The Balmer-to-Paschen ratio only provides the actual value of $E(B-V)$ – and therefore A_V – if the dust is distributed homogeneously and as a foreground screen, and the attenuation curve employed is appropriate for the case. Following Calzetti et al. (1994, 2000), we set R_V=4.05 for the stellar continuum and R_V=3.1 for the nebular lines.

Figure 21 shows an example of the results our spatially-resolved SED-fitting code produces for each individual bin in a galaxy. The code is run on NGC1614, and it produces a best fit SED (black line), shown in the upper right plot for one example bin towards the bulk of the galaxy. We show the original HST available photometry (red points and errorbars), as well as the best fit synthetic photometry (blue crosses). The choice of continuum and line templates that linearly combine to produce the best fit SED are also displayed in different colour curves. The bottom panel shows the residual χ of the fit (data−model). On the left of Figure 21, we display the corner plot[8] with the parameter space for the selected example bin. We can explore the different correlations between the various physical parameters, as well as seeing the distribution of best fit solutions for each of them. This constitutes an upgrade in the treatment of correlations between parameters and resulting uncertainties in the physical properties that we infer, when compared to previous fast-running codes, and with the advantage of computational speed when compared to other MCMC (Markov Chain Monte Carlo) routines in other codes.

2.3.4 *Robustness of our Inferred Parameters*

We can conduct some tests and diagnostics to analyse the robustness of the inferred physical properties, estimated with our spatially-resolved SED-fitting scheme. For this, we can use archival observations obtained with different instruments, as well as other SED-fitting codes.

[8] We use the visualisation Python package `corner.py` (Foreman-Mackey 2016)

Hα emission line strength

Firstly, we test how reliable our line fluxes are, which is vital if we want robust and trustworthy $A_V(\mathrm{H}\alpha/\mathrm{Pa}\beta)$, $\mathrm{SFR}_{H\alpha}$ and $\mathrm{SFR}_{Pa\beta}$ estimates. The narrow-band filter that targets Hα (λ6564.61Å) is wide enough so that we get contamination from the [N II]$\lambda\lambda$6549.86, 6585.27Å doublet, so we need to correct for this. A common approach is to consider a fixed ratio throughout the galaxy; however, the [N II]/Hα ratio can vary significantly not only between galaxies, but also spatially within a galaxy (e.g., Kennicutt et al. 2007; Wuyts et al. 2013; Belfiore et al. 2016, 2017). Multiple processes can be responsible for these variations, e.g. ionisation, shocks, outflows, differences in the electron density and metallicity, amongst others (see e.g., Kewley et al. 2019, for a review). It is common to use a correction of [N II]/Hα=0.55 (e.g., Moustakas et al. 2010; Jin et al. 2019), which we also apply in this work, although the user can choose which correction to implement. We also calculate and account for the corresponding contaminant factor of [N II], computed as the throughput of the narrow-band filter of [N II] with respect to Hα.

Some of the galaxies in our sample have ground-based archival integral field spectroscopy available (e.g., Very Large Telescope (VLT) Multi-Unit Spectroscopic Explorer (MUSE) for 6 objects from the GOALS sample), which can be used to measure the spatial variation of the [N II]/Hα line ratio, though at somewhat lower spatial resolution than the HST maps. Here we use MUSE integral field cubes of the target MCG-02-01-051, to test the robustness of our method for inferring Hα emission line fluxes from the multiband HST images.

We convolve the HST images with a Moffat kernel (Moffat 1969), to match the larger ground-based MUSE PSF (FWHM ∼0.″6) and resample them to the MUSE spatial pixel grid. We then recompute the Voronoi bins on the resampled HST images as described above in §2.3.1 and Appendix 2.5, and apply the bins to the calibrated MUSE spectral cubes downloaded from the ESO archive. We fit for the fluxes of the Hα+[N II] emission lines in the resulting binned spectra with a triple Gaussian model, finding excellent agreement with our MUSE fits and previously published Hα maps on our targets (e.g. IRAS13120-5453 from the PUMA Project, Perna et al. 2021).

Figure 22 shows an example on the target MCG-02-01-051, on the Hα+[N II] fit from MUSE compared to our HST SED-fit Hα+[N II] estimate. The Hα fluxes derived with our fits to the HST broad- and narrow-band photometry (left) agree remarkably well with the independent measurement from the MUSE spectral cube (right).

In Figure 23, we show a comparison of the resulting Hα emission inferred with the simple subtraction method, interpolating two continuum templates and subtracting from the narrow-band that targets Hα (top panel), and the full SED-fitting scheme (bottom panel) for the galaxy MCG-02-01-051. We compare each of these with the direct Hα fit from the MUSE cube available for this target. The

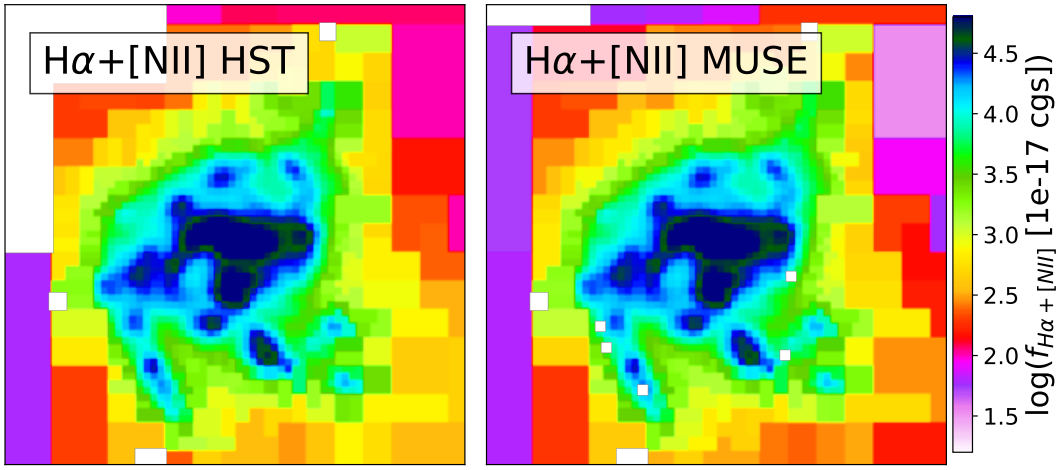

Figure 22: Maps of the Hα+[N II] line flux for the target MCG-02-01-051 inferred from the HST images with our SED-fitting code (left), and the Hα+[N II] emission measured from the MUSE IFU cube (right) of the same source.

result clearly shows greater discrepancy between the inferred Hα from the simple subtraction method and the MUSE fit (with a mean difference of -0.04 ± 0.04 dex), than the Hα from our SED-fit method, which agrees considerably better with the MUSE measurement (with an improved mean discrepancy of only -0.02 ± 0.04 dex). Focusing on the bottom panel, we see that the large majority of the SED-fit Hα fluxes agree well with the MUSE "ground truth", with larger scatter at low HST flux that can be explained by the uncertainties. The slight tilt in the comparison likely arises from imperfections in the PSF and alignment matching between the MUSE and HST frames; if we perform the same analysis with the HST F673N (the narrow-band that targets Hα) versus a synthetic F673N on MUSE (we integrate the MUSE spectra through the filter curve), we obtain the same trend, as well as if we perform the same test on the F814W filter, which does not contain the line.

We run this study for six targets that have MUSE cubes available, and derive the same conclusions – that our Hα+[N II] fluxes agree considerably well with the Hα+[N II] emission measured directly from MUSE spectra, and we even see that our composite SED-fit obtained with the different templates, fits the MUSE spectrum on a bin-to-bin basis, and not only the emission lines.

Finally, we can check the [N II]/Hα spatially resolved correction, inferred from the MUSE IFU cube. Figure 24 shows the spatial map and histogram of the derived ratio for MCG-02-01-051. We see that the ratio is not uniform across the face of the galaxy, but the constant value that we assume (0.55) –following the assumption that most studies make– falls within 1σ of the mean value for this galaxy. This value is reasonable for most HII-like galaxies and isolated LIRGs that comprise our sample, but we might encounter some targets that can have [N II]>Hα across much of the extent of the galaxy, such as the extreme starburst

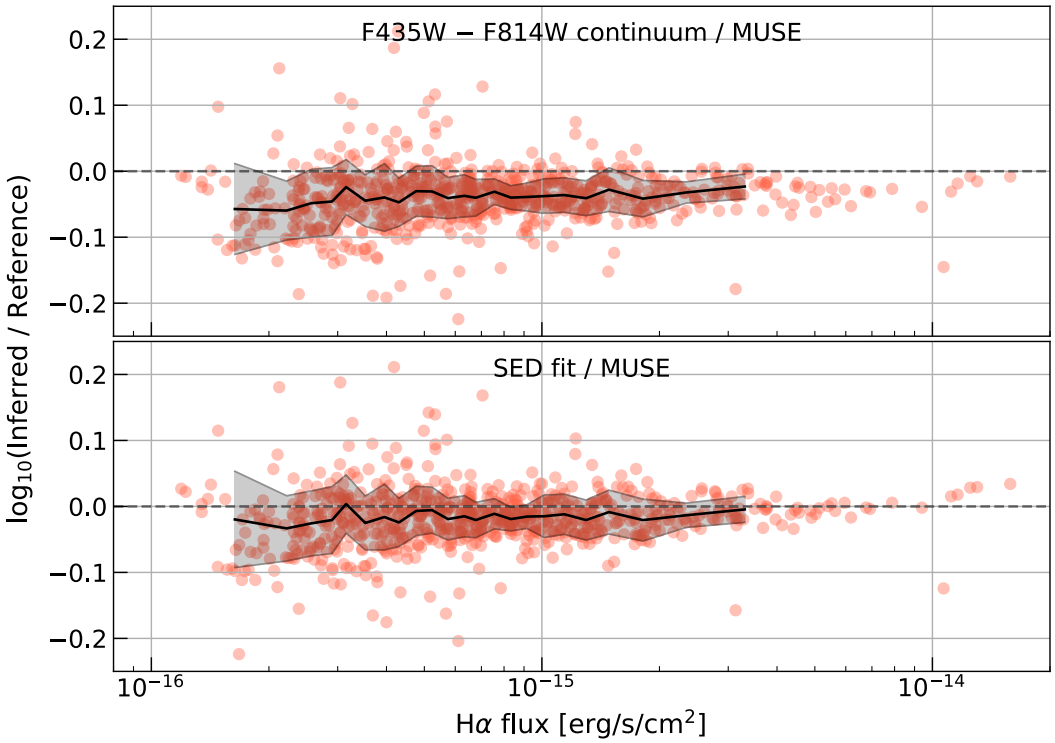

Figure 23: Comparison of the resulting Hα flux with a simple background subtraction method (top panel, interpolating two broad-band filters) and our full SED machinery (bottom panel), on the galaxy MCG-02-01-051. The vertical axis shows the logarithm of the ratio between each HST subtraction method inferred line estimates, and the reference MUSE Hα of this source. The SED-fit Hα matches the MUSE one better than the commonly used simple subtraction method. The running median and uncertainty are shown as a solid black line and surrounding shaded region, respectively.

Arp 220 (see Figure 14 in Perna et al. 2020) or galaxies with extended LINER emission (Low-Ionization Nuclear Emission-line Region, e.g. Belfiore et al. 2015). Section 2.5 in the Appendix shows the resulting [N II]/Hα histograms for the 5 additional targets from the GOALS sample that have MUSE observations available. Naturally, where our assumed constant [N II]/Hα value differs from the actual ratio, the inferred A_V will be affected directly. For the extreme galaxy in our sample for which we have a MUSE cube, Arp 220, the mean [N II]/Hα= 1.92 ratio observed in the cube corresponds in a systematic shift of 1.3 mag for A_V relative to our assumed value of 0.55 (see Eq. 9).

Paβ emission line strength

While we do not have an IFU cube to test the Paβ line flux that we infer with our SED-fitting code, we consider a subset of galaxies in our sample where a robust

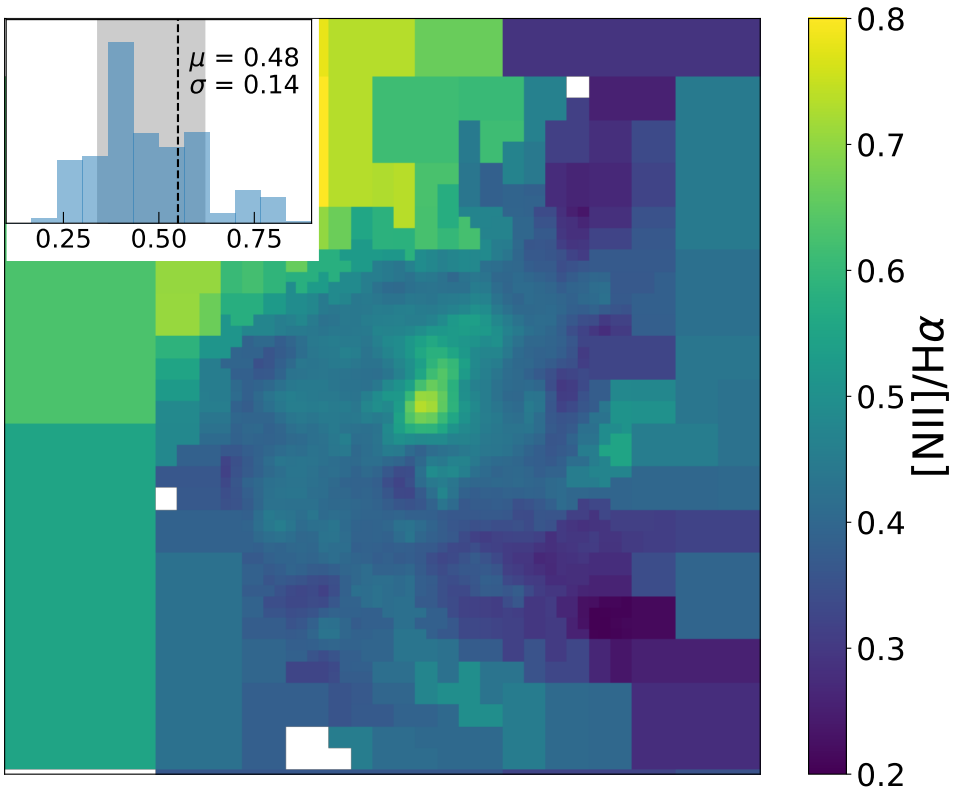

Figure 24: Histogram (top left inset plot) and spatial map (main plot) of the [N II]/Hα ratio for MCG-02-01-051 as measured in the MUSE IFU cube. The value we adopt for the ratio (black dashed line on the histogram) falls within 1σ of the mean (grey shaded region).

empirical subtraction can be performed with the paired narrow-band images on and off of the emission line.

Figure 25 shows the comparison between the Paβ line flux that we infer from our SED fit and the one obtained using the offset narrow-band filter F130N. By scaling the F130N we can perform a simple empirical subtraction from the F132N measurement, and remove the stellar continuum from the narrow-band that targets the recombination line. We see that our Paβ estimate for this galaxy agrees with the empirical simple method (with a mean difference of 0.03 ± 0.05 dex). There is a slight flux dependent residual towards the bright end of the Paβ flux, where the discrepancy reaches ~ 0.05 dex, which is still a good agreement overall.

This and the previous study allow us to show that our line fluxes are within 0.05 dex of their respective reference values, making them reliable and robust on a bin-to-bin basis. Furthermore, the resulting $A_{V,\mathrm{gas}}$ inferred from the decrement and the SFRs inferred from both lines are also trustworthy.

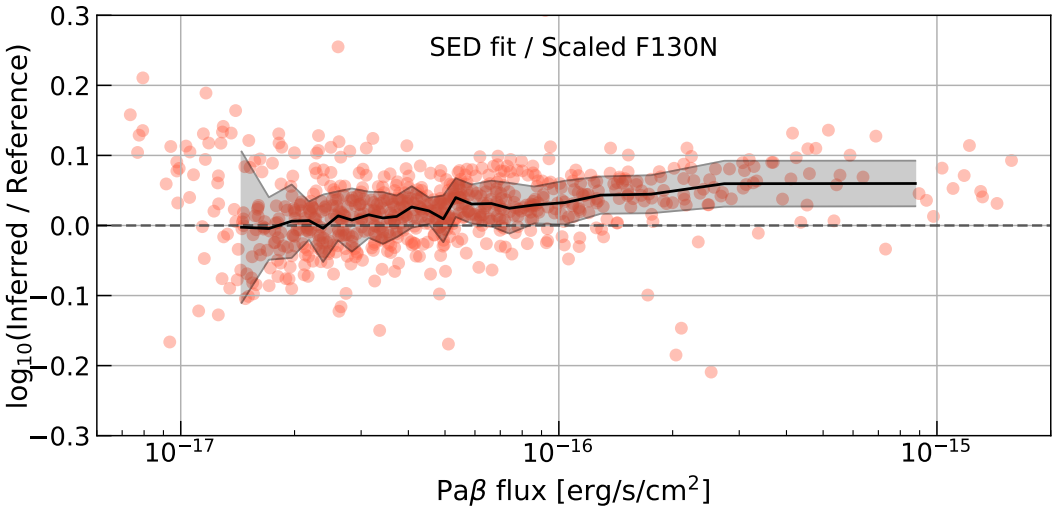

Figure 25: Comparison between the Paβ inferred from our SED-fitting scheme and the scaled F130N off-band subtraction for each spatial bin. The running median and scatter are shown as a solid black line and surrounding shaded region, respectively.

Physical Properties from `Prospector`

To prove the robustness of firstly our $A_{V,\mathrm{stars}}$ estimates, we use a different SED-fitting code to fit our photometric observations, and compare the inferred A_V. For this, we use the SED-fitting code `Prospector`[9] (Johnson & Leja 2017; Leja et al. 2017). Both EAZY (and therefore our code) and `Prospector` incorporate FSPS (Flexible Stellar Population Synthesis; Conroy et al. 2009; Conroy & Gunn 2010b) models, which are composite stellar population models that allow user input.

Until now, SED-fitting techniques of galaxies have broadly adopted basic models to obtain stellar masses, with fixed stellar metallicities, simple parametric star formation histories (SFHs), rigid and simplistic dust attenuation curves, and minimisation of chi-squared. On the other hand, `Prospector` includes a flexible attenuation curve and metallicity. `Prospector` uses FSPS, which contains nebular emission and considers both attenuation and re-radiation from dust. It also provides some innovation on flexible SFHs, as well as techniques for sampling parameter distributions. It comprises a 6-component non-parametric star formation history. With such a wide and adjustable range of parameters, `Prospector` is able to supply realistic uncertainties and unbiased parameters.

We run `Prospector` on the target IRASF10038-3338 with both a parametric star-formation history and a non-parametric star-formation history. Both yield very similar results. Figure 26 (top left panel) shows the resulting A_V maps inferred from `Prospector` with a non-parametric SFH (left) and with our SED-

[9] `https://github.com/bd-j/prospector`

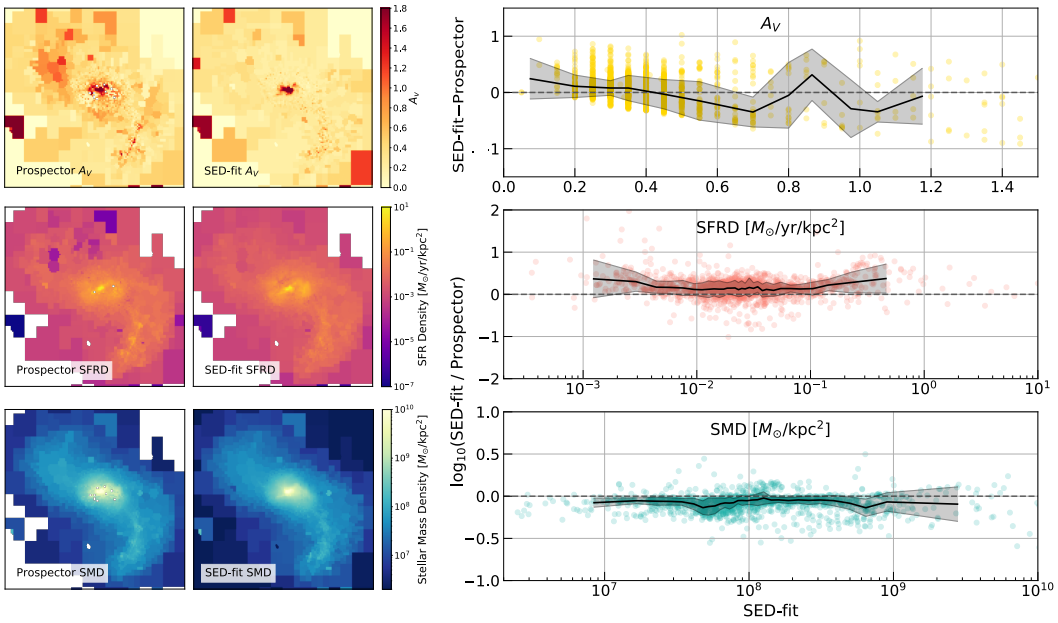

Figure 26: Comparison on IRASF10038-3338 between the physical properties inferred by `Prospector` and our SED-fitting code. **Left:** Resulting maps obtained with both codes, of the estimated A_V (top), the star formation rate density (middle) and the stellar mass density (bottom). **Right:** Scatter plots of each physical property, with our SED-fit inferred parameters on the x axis, and the comparison (difference for A_V and ratio for SMD and SFRD) of the Prospector and SED-fit properties on the vertical axis. Each point corresponds to an individual bin of IRASF10038-3338. The black line and shaded region indicate the running median and standard deviation, respectively. Both qualitatively and quantitatively, the SMD seems the most robust parameter.

fitting code (right). A priori, the maps seem to agree considerably well. Quantitatively (see the top right scatter plot in Figure 26), the mean difference between both A_V estimates across the galaxy is 0.06 ($\sim$ 6%), with a standard deviation of 0.25, reflecting on the good agreement between the two.

Furthermore, to do a sanity check on our SFR and stellar mass estimates (both inferred from the SED fitting and not the lines alone), we can compare them with the `Prospector` estimates for the same galaxy, IRASF10038-3338. With `Prospector`, we obtain the star-formation rate density (SFRD) and stellar mass density (SMD), so to compare one-to-one, we simply divide our estimates by the corresponding physical bin size. At our average redshift of 0.02, for a minimum bin size of 4×4 pixels (0.″4 per side), this corresponds to 160 pc across, which results in a minimum bin area of 0.0256 kpc^2.

Figure 26 shows the resulting qualitative and quantitative comparison between the two codes, using the non-parametric SFH for `Prospector`, although the parametric SFH run gives equivalent results. We see that both the SMD and SFRD maps (left middle and bottom panels of the figure, respectively) seem to

agree considerably well on a bin-to-bin basis for this galaxy, especially the stellar mass density, which our code samples particularly smooth, even in central bins where the `Prospector` fit seems to fail. Our code seems to infer a higher star forming bulge than `Prospector`, most likely driven by the differences in SFH sampling from both codes and the SFH priors used. On a quantitative point of view (middle and bottom scatter plots of Figure 26), for the SMD, the mean discrepancy between the two estimates is -0.07 ± 0.08 dex, which is a remarkable agreement. On the other hand, for the SFRD, we obtain a median difference between `Prospector` and our code of 0.15 ± 0.19 dex. We see that the largest difference is obtained at the bright end of the SFRD. Although this may seem like a large discrepancy, the SFR from SED modelling is one of the more uncertain stellar population properties to derive (see e.g., Muzzin et al. 2009), and highly influenced in this comparison by the differences in SFH sampling. Broadly used SED-fitting codes such as EAZY would yield equivalent results when compared to `Prospector` in terms of the SFRD.

To summarise, our inferred physical properties agree well both qualitatively and quantitatively (see Figure 26), which gives us confidence that our estimates are robust and trustworthy.

2.4 RESULTS AND DISCUSSION

For all galaxies in our sample, we have produced Hα and Paβ maps, as well as extinction maps from the decrement and the stellar continuum, that allow us to measure the typical size scales and extinction levels of the dust obscuration. In this section we present the results. Maps of the various physical properties inferred with our SED-fitting code can be found in the Appendix 5.1 for each individual galaxy in our sample.

2.4.1 *Case Example*

Before conducting a quantitative analysis on the various inferred line fluxes and physical properties, we present here a case example on our whole methodology applied to one target, NGC1614. As has been discussed in §2.3.1 (and Appendix 2.5), the first step with our sample has been to employ a Voronoi tesselation binning scheme. Figure 19 showed the binning applied on NGC1614 on the bottom panels. We apply the binning generated on F130N to the rest of available filters for this target, which are 6 images from the UV to the NIR.

Once we have the binned images, we apply our spatially-resolved SED-fitting code (see §2.3.3 and Appendix 2.5), and obtain the resulting physical estimates that are shown in Figure 27. The top row, from left to right, shows the RGB image (built combining the F435W, F814W and F110W broadband filters), the stellar mass density map, and the SFRD maps inferred with the stellar continuum

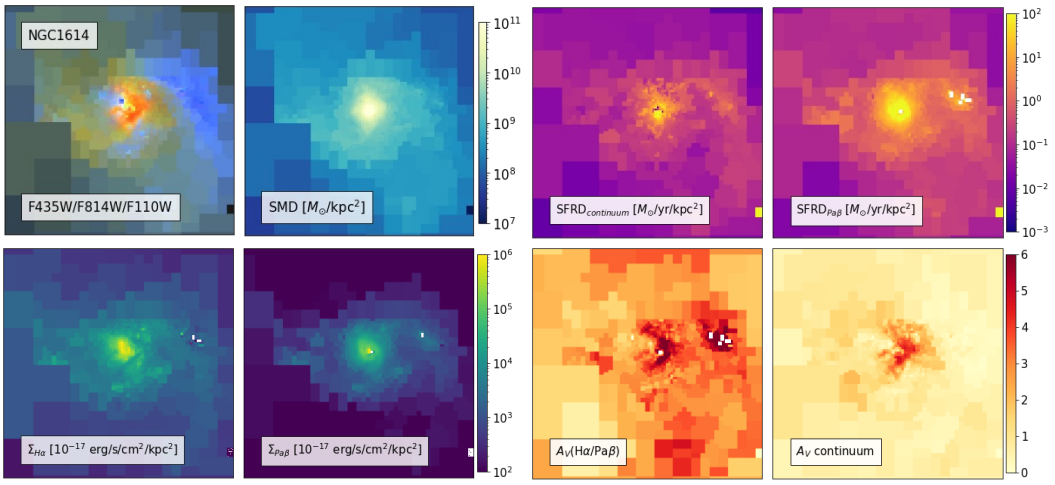

Figure 27: Output of the spatially-resolved SED-fit on NGC1614. The top row, from left to right, shows the RGB image (built combining the F435W, F814W and F110W broadband filters), the stellar mass density map, and the SFRD maps inferred with the stellar continuum and with the Paβ emission line flux. The bottom row shows the resulting Hα and Paβ surface density flux maps, as well as the A_V inferred from the empirical Balmer-to-Paschen decrement, and the stellar continuum.

and with the Paβ emission line flux. The bottom row shows the resulting Hα and Paβ surface density flux maps, as well as the A_V inferred from the empirical Balmer-to-Paschen decrement, and from the stellar continuum. We see that most line emission, star-formation, dust content and stellar mass reside in the dusty star-bursty core of NGC1614, which is debated to contain an AGN (Pereira-Santaella et al. 2015). Furthermore, we see noticeable differences in the dust maps inferred from the gas (Hα/Paβ) and the stellar population (A_V inferred from the continuum). The differential attenuation inferred from each component will be addressed in detail in a forthcoming publication.

2.4.2 *SFR Indicators*

Accurately determining the star-formation rate is a vital step in understanding galaxy evolution. There are numerous tracers of recent and past star forming activity, and one can infer a comprehensive picture of the star formation history and burstiness in galaxies by comparing different star formation rate indicators (Madau & Dickinson 2014).

In this section, we focus on exploiting our Paschen-line observations to trace the obscured star-formation in our sample of nearby star-forming galaxies. First, we compare the optical and NIR SFRs inferred with Hα, Paβ and the stellar continuum emission. Later on, we investigate whether the dust-corrected SFR inferred with Paβ can recover the SFR derived from the infrared luminosity and

the 24μm emission observed with MIPS/*Spitzer*. We conduct both spatially-resolved and integrated comparisons for the various tracers. As mentioned before, we conduct this study only on the galaxies of our sample that are also part of GOALS, due to their L_{IR} and 24μm flux measurements availability.

Spatially-Resolved Optical and NIR SFRs

As introduced before, we can infer the SFR over the last ∼100 Myr from the stellar continuum emission. On the other hand, hydrogen recombination lines trace the most recent star formation (∼10 Myr), occurring in H II regions throughout the galaxy (Kennicutt & Evans 2012).

Using Equations 3 and 6, we can infer the SFR from the Hα and Paβ line fluxes, and divide by the physical size to obtain the star formation rate surface densities (in $M_{\odot}$/yr/kpc^2). Both SFRDs match once we apply the dust correction inferred from the Hα/Paβ decrement. On the other hand, for the targets where we have MUSE cubes available, we can correct for dust obscuration using the classic Balmer decrement (Hα/Hβ). This allows us to explore whether Paβ reveals obscured star formation that is invisible to optical lines, even after applying a dust correction.

Figure 28 shows the spatially-resolved comparison between $\mathrm{SFRD}_{\mathrm{H}\alpha}$ and $\mathrm{SFRD}_{\mathrm{Pa}\beta}$ for the galaxy MCG-02-01-051, without (top panel, blue points) and with (bottom panel, orange points) dust correction prescription applied, using the Balmer decrement obtained from the MUSE cube (indicated by the superscript "Balmer"). In both cases, the SFRD inferred with Paβ is systematically higher. There is a clear trend with the $\mathrm{SFRD}_{\mathrm{Pa}\beta}$, the disagreement between both estimates is much larger (up to 1 dex) for the bright end of $\mathrm{SFRD}_{\mathrm{Pa}\beta}$, and less than 0.5 dex at the lower $\mathrm{SFRD}_{\mathrm{Pa}\beta}$ end. This is what we could expect, since more star-forming regions are also more obscured by dust. The bottom panel illustrates that the Balmer decrement is not enough correction to see the most obscured star forming regions, with an average offset of -0.1 ± 0.2 dex between $\mathrm{SFRD}^{\mathrm{Balmer}}_{\mathrm{H}\alpha}$ and $\mathrm{SFRD}^{\mathrm{Balmer}}_{\mathrm{Pa}\beta}$. Moreover, the discrepancy on the faint end on both panels may arise from differences in the surface brightness sensitivity of the Hα observations relative to the Paβ, and we would require deeper Paβ observations in the faint regions to study this regime better.

Furthermore, we can directly see the relationship between the dust-corrected $\mathrm{SFRD}_{\mathrm{Pa}\beta}$ (using Hα/Paβ), and the visual extinction inferred with the Balmer-to-Paschen decrement. Figure 29 (right panel) shows the relation between the two for the spatially-resolved data of MCG-02-01-051, colour-coded according to the A_V inferred with the classic Balmer decrement. We see that both quantities correlate, indicating that higher star-forming activity will also be more obscured. On top of this, on the left panel we compare the A_V inferred with each decrement,

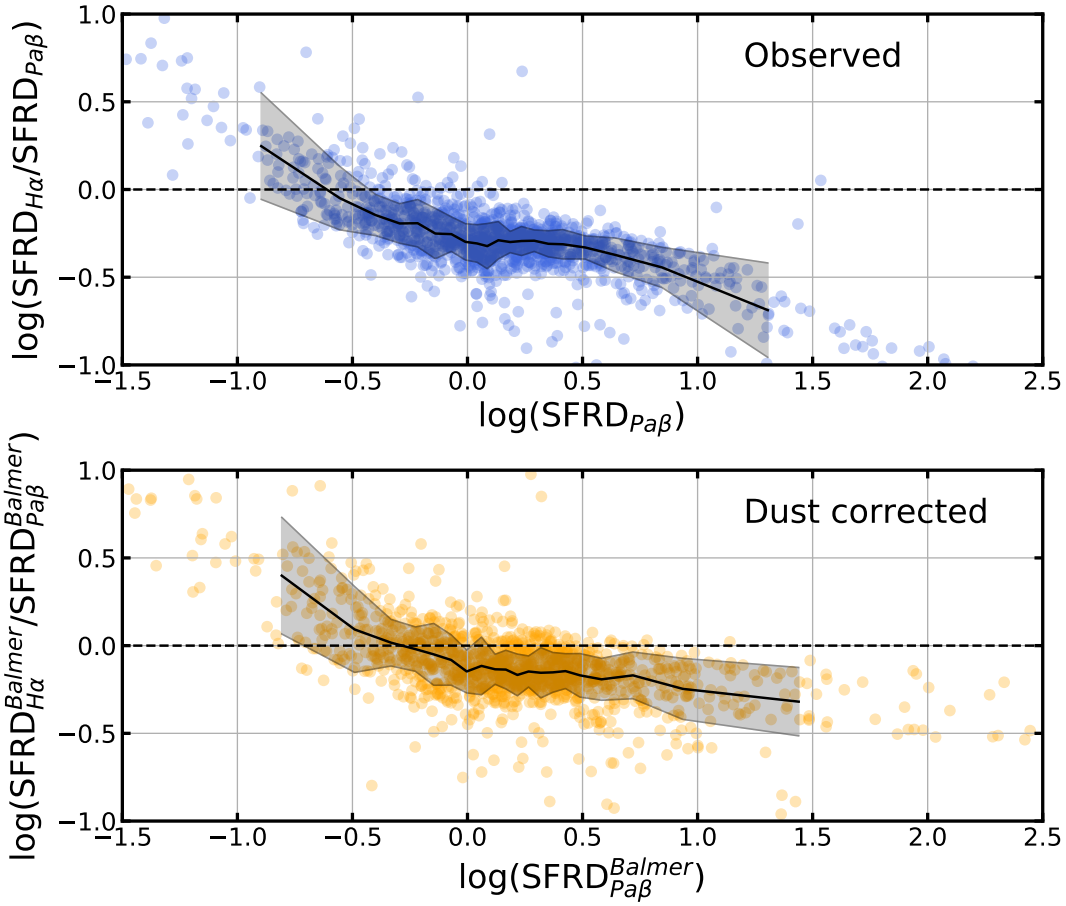

Figure 28: Comparison of the spatially-resolved SFRD inferred from Hα versus from Paβ for the galaxy MCG-02-01-051. The dashed line indicates the one-to-one ratio. The solid black line and shaded region indicate the running median and standard deviation, respectively. **Top:** SFRDs estimated from the observed Hα and Paβ, without correcting for dust extinction. **Bottom:** Dust corrected SFRDs, using the Balmer decrement (Hα/Hβ), obtained from the MUSE cube.

and we clearly see that the A_V inferred with Paschen lines probes larger optical depths than A_V(Hα/Hβ) by >1 mag, agreeing with works such as L13.

These results agree with previous comparisons with Paschen-line SFRs such as Piqueras López et al. (2016), where they find that the SFR$_{\mathrm{Pa}\alpha}$ is on average a factor ×3 larger than SFR$_{\mathrm{H}\alpha}$, even after applying extinction corrections. They conduct this study on a sample of local U/LIRGs, using Brackett and Paschen lines to correct SFR$_{\mathrm{Pa}\alpha}$, and the classic Balmer decrement to dust-correct SFR$_{\mathrm{H}\alpha}$. Tateuchi et al. (2015) also report that SFR$^{\mathrm{corr}}_{\mathrm{Pa}\alpha}$ is systematically larger than SFR$^{\mathrm{corr}}_{\mathrm{H}\alpha}$ in a sample of nearby star-forming galaxies (33 of them from the IRAS Revised Bright Galaxy Sample catalog), which implies that Paschen-lines can reveal star-formation that is otherwise obscured for Hα, reaching dustier regions than the optical Balmer lines. Albeit with spectroscopic data and non

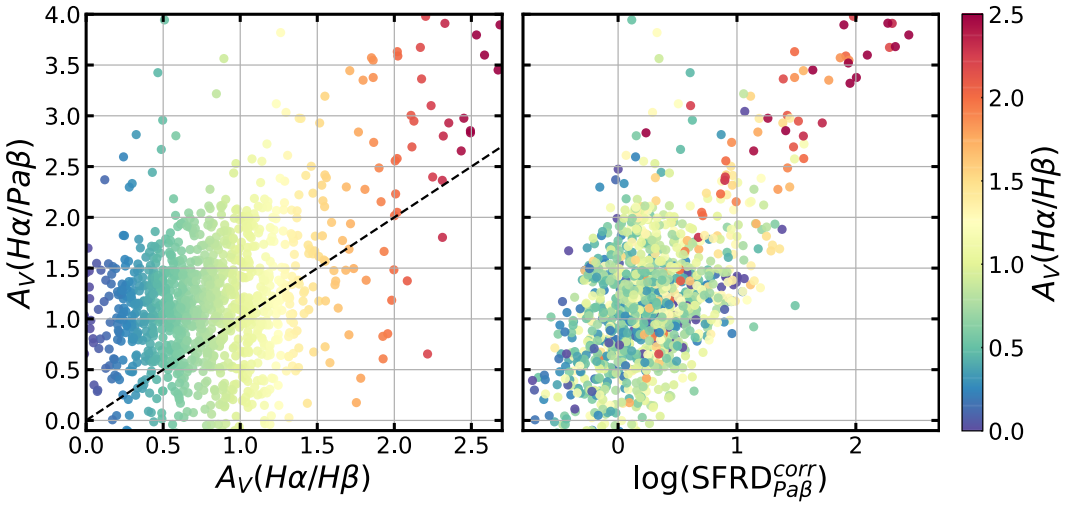

Figure 29: Spatially-resolved visual extinction inferred from the Balmer decrement (left) and SFRD inferred from the dust-corrected Paβ (right) versus the visual extinction from the Balmer-to-Paschen decrement. The colour-code indicates the A_V inferred with the classic Balmer decrement.

spatially-resolved observations, Cleri et al. (2022) have Paβ and Hα measurements, and report the same conclusions found in this work.

Besides the nebular lines, we can also study whether Paβ "sees" more star formation than the SFR inferred from the stellar continuum (estimated with our spatially-resolved SED-fitting code, which is computed directly as the normalisation of the two youngest continuum templates, where the reported SFR is averaged over 100 Myr). Figure 30 shows in the vertical axis the difference between these two indicators, as a function of $\mathrm{SFRD}^{\mathrm{corr}}_{Pa\beta}$, dust-corrected with the Balmer-to-Paschen ratio, for the galaxy MCG-02-01-051 (top panel) and for the whole sample of our galaxies that belong to GOALS (bottom panel). The individual bins are colour-coded according to their A_V inferred with the SED-fitting code, which applies to the stellar continuum templates. For MCG-02-01-051, we clearly see that the SFRD inferred with Paβ is systematically higher than with the stellar continuum for the wide majority of bins, with a mean discrepancy of -0.3 ± 0.3 dex. There is a slight decrease in the difference towards lower $\mathrm{SFRD}^{\mathrm{corr}}_{Pa\beta}$. On top of this, the bins with higher obscuration traced by the stellar continuum (A_V) seem to yield bigger difference between both SFR indicators. Besides the fact that the NIR line is less obscured than the optical continuum, the discrepancy between both indicators can also be explained by the different star formation timescales that they both trace. This could be the case particularly for the plot of the whole sample (bottom panel in Figure 30), where the mean discrepancy between the SFR tracers is -0.3 ± 0.7 dex. For small $\mathrm{SFRD}^{\mathrm{corr}}_{Pa\beta}$ values, the continuum yields higher star formation. This could be due to the recent star formation being lower than the star formation over the last 100 Myr, or it could

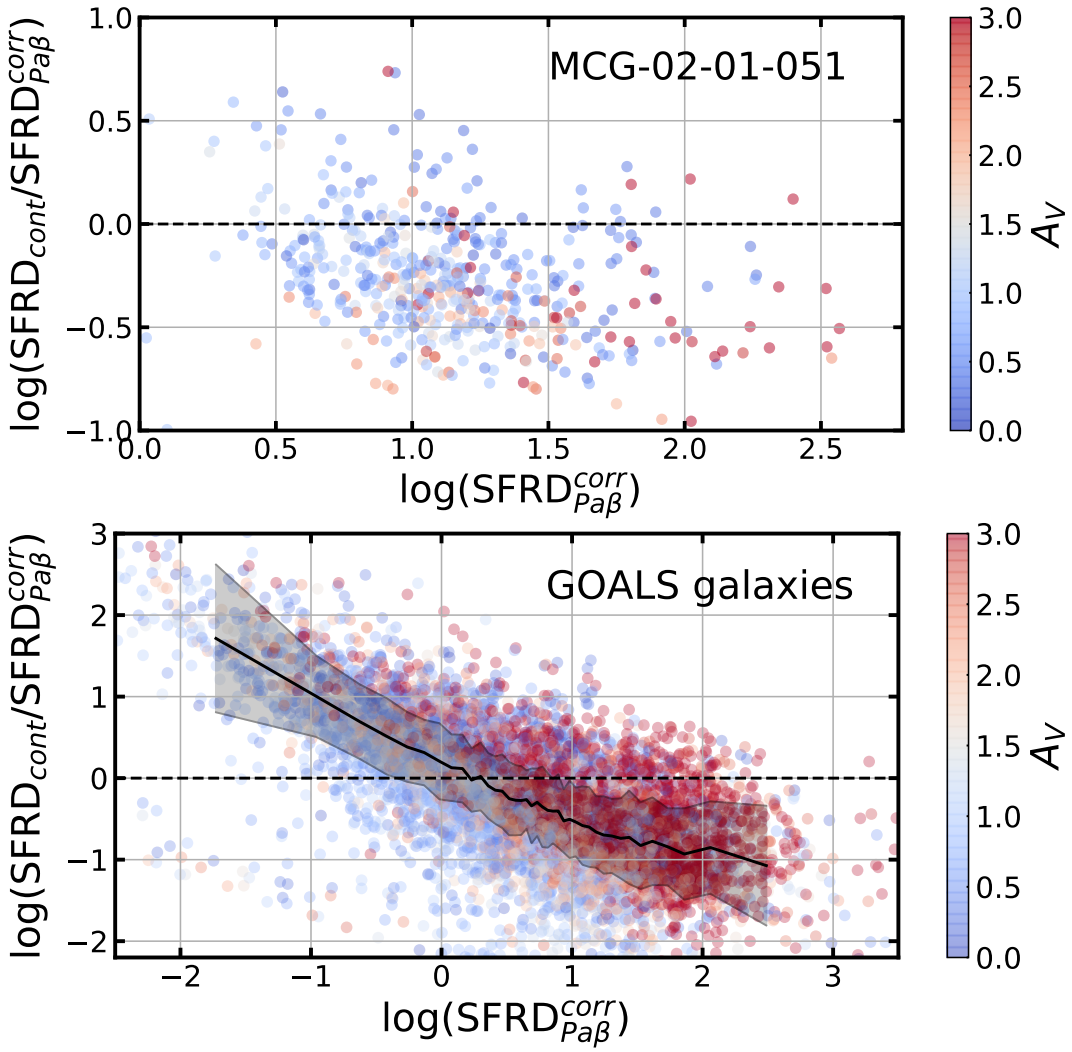

Figure 30: Comparison of the spatially-resolved SFRDs inferred from stellar continuum versus from the dust-corrected Paβ. The dashed line indicates the one-to-one ratio. The colour-code indicates the stellar continuum A_V. **Top:** For the target MCG-02-01-051. **Bottom:** For the targets in our sample that are part of GOALS. The black line and shaded region indicate the running median and standard deviation, respectively.

be the same effect observed in Figure 28 (where both indicators trace identical timescales), resulting from the depth of the images. On the other end of high SF activity, where the mean discrepancy goes beyond 1 dex, dust might dominate the difference between the two indicators, as we can see by the enhanced A_V, since we see that the most obscured bins infer larger SFRD with the nebular line than with the stellar continuum. This leads us to conclude that near-IR lines are able to see star formation that is invisible to the stellar continuum, reaching further depths than any optical component.

Furthermore, the attenuation experienced by the stars is due to the diffuse ISM, whereas the nebular lines tracing the gas are obscured also by birth clouds,

where dust is clumpier and more patchy (Greener et al. 2020). Calabrò et al. (2018) illustrate obscured starburst as an optically thick core with an enclosing layer, emitting NIR and optical nebular lines, which explains both the larger SFR and extinction inferred by NIR lines when compared to optical tracers (Puglisi et al. 2017). The combination of all of these factors results in having differential attenuation and SFRs inferred by nebular lines and the stellar continuum.

With upcoming observations of JWST of Paschen-line emission in galaxies, our results suggest that we will be able to reveal star-formation activity that is otherwise currently obscured for optical observations, and it will allow us to paint a more complete picture of the evolution of galaxies and their star formation activity across cosmic time.

Integrated IR SFR Indicators

We have found that Paschen-lines can reveal obscured star formation invisible to optical indicators, but now it remains to be explored whether these lines can recover the star formation activity that we can infer with mid- and far-IR indicators, arising from re-emitted absorbed UV starlight. Infrared and far-IR luminosities have been shown to be good star-formation tracers in dusty starburst galaxies (e.g., Kennicutt 1998; Kewley et al. 2002). Past studies have found a tight agreement between the SFR inferred from dust corrected Paschen-lines and $\mathrm{SFR}_{24\mu m}$, derived from the MIPS/*Spitzer* 24 μm observations (e.g. Piqueras López et al. 2016). On top of this, a reasonable linear correlation has also been found between Paschen star formation rates and the SFR inferred from the infrared luminosity (e.g. Tateuchi et al. 2015).

The light that dust absorbs in the UV range of the spectrum, is later re-emitted at longer wavelengths, in the IR regime. Therefore, IR indicators of reprocessed stellar light have been broadly employed to infer SFRs. Here we focus on the L_{IR} and 24μm emission. We can derive the SFR_{IR} using the calibration by Kennicutt (1998), for a Chabrier (2003) IMF:

$$SFR_{IR}[M_{\odot}\mathrm{yr}^{-1}] = 2.5 \times 10^{44} \times L_{IR}[\mathrm{erg\,s}^{-1}] \tag{7}$$

where L_{IR} is defined as the luminosity in the spectral range 8—1000 μm. Since we do not have multiple available measurements along the IR part of the SED, we cannot infer a spatially-resolved analysis with our code. Therefore, we conduct these comparisons in an integrated manner.

Firstly, we compare $\mathrm{SFR}^{\mathrm{corr}}_{Pa\beta}$ and SFR_{IR}. The $\mathrm{SFR}^{\mathrm{corr}}_{Pa\beta}$ is inferred from the Paschen-beta line flux following Equation 6, and applying a dust correction using the Balmer-to-Paschen decrement (Hα/Paβ) (calculated on a bin-to-bin basis and then integrating over the whole galaxy). As introduced before, previous studies have found that redder hydrogen recombination lines than Hα and Hβ, reach further depths than the common Balmer decrement (e.g. Calzetti et al.

1996, Liu et al. 2013), and therefore infer higher obscuration. In agreement with this, in the previous section we have found that Paβ systematically traces more star-formation than Hα, even when the Balmer decrement is used for applying a dust correction. For the next comparisons, we use the integrated $\mathrm{SFR}^{\mathrm{corr}}_{Pa\beta}$ and we obtain the infrared luminosity values from the GOALS survey measurements (Armus et al. 2009), that can be found on Table 1 in this work.

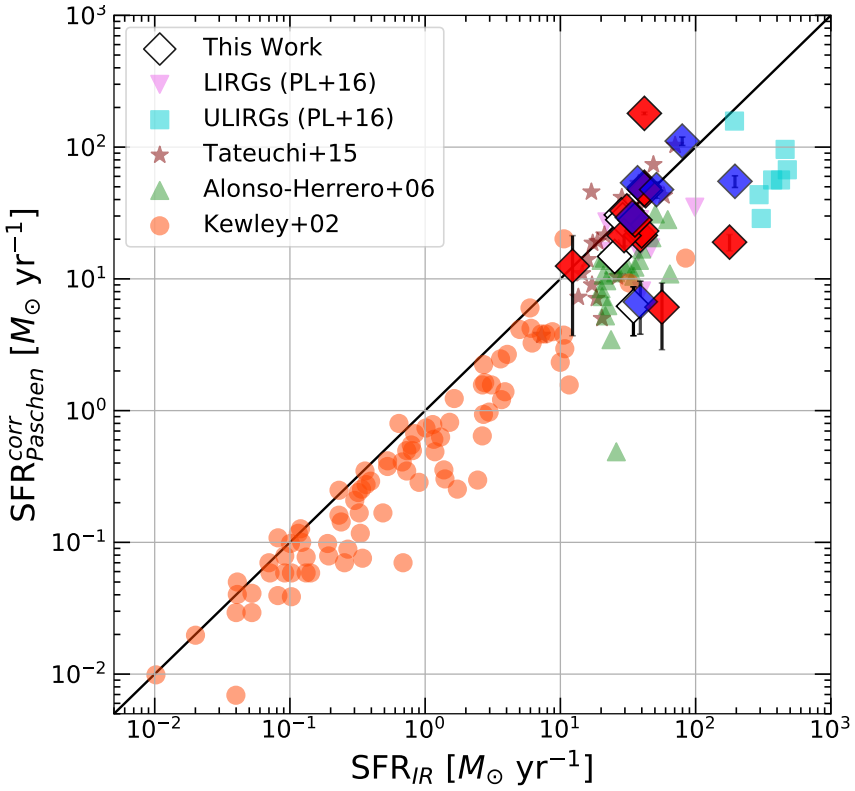

Figure 31: Extinction corrected $\mathrm{SFR}^{\mathrm{corr}}_{\mathrm{Paschen}}$ as a function of the SFR inferred from the infrared luminosity. The various datasets are detailed in the main text. Our sample is indicated by the diamond symbol, blue colored if they host an AGN and red colored if not.

Figure 31 shows the comparison between the extinction-corrected SFR inferred with Paschen lines and SFR_{IR} for various studies. The targets from our sample are indicated with the diamond symbol, and following the colour-coding from Figure 18, where blue means that the galaxy hosts and AGN and red that it does not. Our data is plotted inferring the y-axis SFR with Paβ. On the other hand, to put our results into the context of previous studies, we include other works that infer the SFR with Paα instead. Some discrepancy between both Paschen lines SFRs might be encountered, but the effect of dust between the two tracers should not be as significant as for example the previous study between Paβ and Hα. Figure 31 includes data from various samples. The turquoise squares (ULIRGs) and violet downward triangles (LIRGs) are data from the Piqueras López et al.

(2016) sample (PL+16), observed with VLT-SINFONI, using Brackett and Paschen lines to dust-correct $SFR_{Pa\alpha}$ and a Calzetti et al. (2000) attenuation curve with a 0.44 ratio between the ionized gas and stellar continuum applied. The green upward triangles correspond to local LIRGs from Alonso-Herrero et al. (2006), obtained measuring the Paα fluxes and comparing them with their Hα and Brγ measurements, respectively, and estimating the extinction to the gas using the Rieke & Lebofsky (1985) extinction law and a foreground dust screen model. The orange circles are measurements of normal galaxies from the Nearby Field Galaxy Survey (NFGS, Kewley et al. 2002). For these galaxies the SFR is inferred with Hα and dust-corrected with the classic Balmer decrement. The maroon stars correspond to H II galaxies from the sample of local LIRGs presented in Tateuchi et al. (2015), where they use the Hα/Paα ratio to correct for the extinction their Paα measurements and a Calzetti et al. (2000) attenuation curve with $R_V = 4.05$.

Overall, we find a considerable agreement between the SFR inferred from Paschen-lines and the IR luminosity, with some targets having higher SFR_{IR}, as also encountered and discussed in e.g. Piqueras López et al. (2016). Tateuchi et al. (2015) also find a systematic offset of −0.07 dex of $SFR^{corr}_{Pa\alpha}$ with respect to SFR_{IR}, and a scatter of 0.27 dex. The targets presented in this work seem to agree well with all previous published results. The discrepancy between both indicators for our galaxies is -0.04 ± 0.23 dex, with the majority of targets lying on the one-to-one relation. We also find some extreme cases where both indicators considerably disagree. This could be due to very high obscuration, or other extreme environments within the galaxy, such as is the case for Arp 220, a known extreme starbursty ULIRG, which is the biggest outlier in Figure 31. Previous studies such as Calabrò et al. (2018), report that SFRs inferred with tracers from the UV to the NIR are systematically underestimated when compared to SFR_{IR} in ULIRGs, which we also find here.

The discrepancy that we find could also be due to the choice of radii within which we integrate the Paβ flux, and its difference with respect to the GOALS choice to integrate L_{IR} in these targets. Furthermore, ULIRGs infrared luminosity may originate from very compact regions (Pereira-Santaella et al. 2021).

On the other hand, the SFR_{IR} might trace star formation occurring in longer timescales than the most recent star formation (Calabrò et al. 2018), which is traced by hydrogen recombination lines arising from H II regions, such as we explored before when comparing the SFR from the optical stellar continuum and the lines. This could be the case for example for the NFGS sample (Kewley et al. 2002), that appears to have systematically lower $SFR_{Pa\alpha}$ than SFR_{IR}, while our results are closer to the 1:1 line, on average. This might be due to their SFRs being inferred with Hα and dust corrected with the Balmer decrement, instead of redder Paschen lines. Or it could also be explained by an age effect, i.e. we see a recent star formation that was a systematic factor lower than the star formation over the last 100 Myrs. This is mainly due to the fact that old stellar

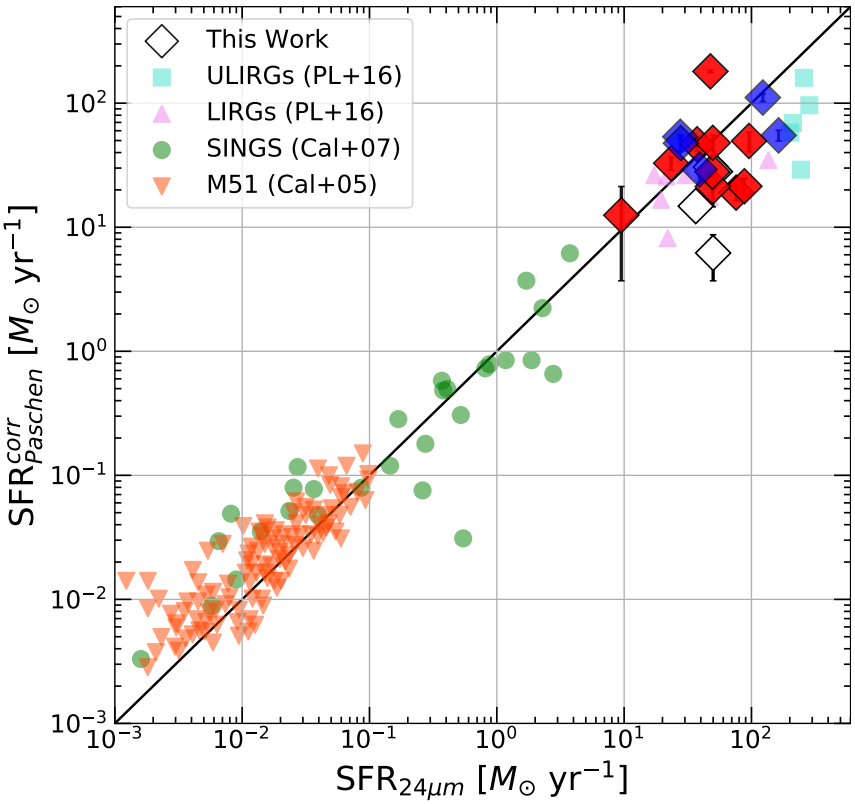

Figure 32: Extinction corrected $SFR^{\rm corr}_{\rm Paschen}$ as a function of the SFR inferred from the 24μm continuum emission. The various datasets are detailed in the main text. Our sample is indicated by the diamond symbol, blue colored if they host an AGN and red colored if not.

populations can still heat the dust that emits in the far-IR, a known effect that has been observed at the level of a factor of ~ 2 in the SFRs difference.

Tateuchi et al. (2015) attribute the discrepancy between the inferred SFRs to high dust obscuration, IR cirrus component or the presence of AGNs in the galaxies, which could be possible sources of systematic differences. If we focus on our sample, the targets that are known to host an AGN do not exhibit a particular trend in Figure 31. The presence of an AGN could explain the discrepancy for 2/6 targets, but the other four are on top of the 1:1 agreement. Therefore, we cannot report a systematic trend on the $\rm SFR^{corr}_{Pa\beta}$ and $\rm SFR_{IR}$ relationship due to the presence of an AGN in our galaxies.

Besides using the L_{IR} to infer the SFR, we can also use another mid-IR indicator, namely the emission from the continuum at 24 μm. We use Equation 10 presented in Rieke et al. (2009), to infer the SFR from the 24μm luminosity:

$$SFR_{24\mu m}[M_\odot \mathrm{yr}^{-1}] = 7.8 \times 10^{-10} \times L_{24\mu m}[L_\odot] \tag{8}$$

We can now compare $\rm SFR^{corr}_{Pa\beta}$ and $\rm SFR_{24\mu m}$. Figure 32 shows the resulting comparison. We retrieve a similar linear correlation to the previously discussed

with SFR_{IR}. For our targets, the discrepancy between both indicators is 0.14 ± 0.32 dex, so the 24μm emission and Paβ are providing consistent SFR estimates. Previous studies have found similar conclusions, as well as deviations at the high-luminosity end (e.g., Alonso-Herrero et al. 2006; Rieke et al. 2009; Piqueras López et al. 2016). Figure 32 also includes results from previous studies, to be able to place our conclusions into context. As for the SFR_{IR} comparison displayed before, these studies use Paα to infer SFRs instead of Paβ for our study. In Figure 32, the turquoise squares (ULIRGs) and violet upward triangles (LIRGs) are data from PL+16. The green circles correspond to SINGS (SIRTF Nearby Galaxy Survey, Kennicutt et al. 2003) galaxies from Calzetti et al. (2007). The orange downward triangles are measurements from individual star-forming regions of M51 from Calzetti et al. (2005). The available 24μm galaxies from our sample are displayed with white diamonds, and can be seen in Figure 32 perfectly agreeing with the other works, as well as falling on top of the one-to-one line, on average. As before, we do not see a trend in the SFRs relationship due to the presence of an AGN. It is quite remarkable to see the agreement over almost six orders of magnitude in $SFR_{24\mu m}$, and covering sizes from individual star forming regions in M51 to integrated LIRGs and ULIRGs. On the other hand, we would expect both SFRs to agree if the 24μm emission was entirely due to star formation alone, since $SFR_{24\mu m}$ is calibrated from Paschen recombination lines (e.g. Calzetti et al. 2007). The contribution from evolved older stellar populations could also explain the deviations from the one-to-one trend in both comparisons in this section. Various studies imply that SFRs inferred from IR tracers are overestimated due to the emission from the dust heated by old stars (see e.g. Fumagalli et al. 2014). On top of this, the uncertainty in the dust temperature determination and possible evolution with redshift, leads to considerable uncertainties on the inferred physical galaxy properties, such as the obscured SFR and L_{IR} (e.g., Sommovigo et al. 2020, 2022), which is an important factor to consider particularly at higher redshifts. All tabulated values from our sample used for Figures 31 and 32 can be found on Table 2.

In summary, we report that the SFR inferred with dust-corrected Paβ emission can recover the star formation estimated via mid-IR tracers, therefore being enough to estimate the SFR for each individual galaxy, in an integrated sense. A good agreement is found both with the MIPS 24 μm emission and the SFR_{IR}, following previously published results. Other works in the literature indicate that SFRs derived from MIPS 24μm + UV emission may overestimate the SFR when compared to the SFR derived from modelling the entire UV-to-IR SEDs, especially at the low-SFR end (e.g., Martis et al. 2019; Leja et al. 2019). MIPS 24μm derived SFRs may be robust for starbursting galaxies, but this might not be the case for all galaxies, in particular those with low specific SFRs and evolved stellar populations.

Target	$SFR_{Pa\beta}^{corr}$	SFR_{IR}	$SFR_{24\mu m}$	$\log(\frac{M_*}{M_\odot})$
Arp 220	19.0	178.2	75.8†	10.8
ESO550-IG025	32.8	31.0	23.4†	11.0
IRAS03582+6012	14.8	25.2	36.5*	10.3
IRAS08355-4944	21.4	39.0	88.0*	10.0
IRAS12116-5615	180.4	41.8	47.6*	10.9
IRAS13120-5453	55.0	195.4	163.3*	11.3
IRAS18090+0130	-	41.8	39.1*	11.1
IRAS23436+5257	6.2	34.7	50.0*	10.8
IRASF10038-3338	6.1	56.4	-	10.5
IRASF16164-0746	6.7	39.0	-	10.5
IRASF16399-0937	23.1	39.9	-	11.0
MCG-02-01-051	30.6	28.2	48.0†	10.6
MCG+12-02-001	21.3	29.6	49.7*	10.5
NGC1614	49.6	41.8	95.7†	10.7
NGC2146	12.5	12.3	9.5*	10.2
NGC2623	53.6	37.2	27.6†	10.4
NGC5256	29.2	34.0	39.1†	10.9
NGC5331	46.7	42.7	37.4*	11.2
NGC6090	28.0	35.6	49.2†	10.6
NGC6240	111.1	79.6	122.8*	11.3
NGC6670	47.9	41.8	49.7*	11.0
NGC6786	28.1	28.9	51.7*	10.7
NGC7592	-	23.5	29.9†	-
VV340A	47.6	51.4	27.9†	11.2

*SFR from the 25μm flux from Sanders et al. (2003).

†SFR from the 24μm flux from U et al. (2012)

Table 2: Integrated measurements of the SFR inferred with different tracers for the targets in our sample that are part of GOALS (Armus et al. 2009). All SFRs are in units of $M_\odot$/yr. The integrated stellar mass is obtained with our SED-fitting code.

2.5 SUMMARY AND CONCLUSIONS

In this work we have presented a sample of 53 local star-forming galaxies, covering the SFR range from normal star-forming spirals to LIRGs and up to ULIRGs, 24 belonging to the GOALS survey (Armus et al. 2009). For each target we have HST narrow-band observations targeting the Hα and Paβ emission lines, as well as nearby broad-band continuum filters. This allows us to constrain the dust obscuration in these objects with the Balmer-to-Paschen decrement, which has been demonstrated to reach further depths and therefore obscuration than the commonly used Balmer decrement (Hα/Hβ). This provides the first system-

atic study on a large sample of very high quality observations, with this level of high-resolution and for the first time, both sub-kpc resolved Hα and Paβ measurements.

For 24 of our targets that are also part of the GOALS survey of local luminous and ultra-luminous infrared galaxies, we have presented a methodology to treat spatially resolved observations, as well as obtaining robust parameters from local or high-z photometric observations with our SED-fitting technique. Our code provides trustworthy emission line fluxes from photometric measurements, that match those obtained from direct spectra on the same targets (within 0.05 dex). Our inferred physical parameters match those estimated with other SED-fitting codes, at a much smaller computational cost when compared to i.e. `Prospector`, and help us analyse in detail the nature of our targets.

We have performed an in depth analysis of the different SFR indicators that we can infer to probe the star formation in our galaxies at various wavelengths and timescales. We have demonstrated in a spatially-resolved manner, that the SFRD inferred with Paβ is systematically higher than with Hα, even when a dust correction is applied using the Balmer decrement, with a mean offset of 0.1 ± 0.2 dex. Our results agree with previous published works, although this had not been tested on a bin-to-bin basis before. Furthermore, Paβ seems to recover more star-formation than the optical stellar continuum in the most obscured parts of each galaxy. This could also indicate a bursty nature of our sources, as the SFR inferred with the stellar continuum provides the star formation convolved over a larger period of time. Besides this, the emission from the stellar continuum and the nebular lines come from different regions within the galaxies.

On top of this, we have tested whether $\mathrm{SFR}_{Pa\beta}$ can recover the star formation inferred by IR indicators. We find consistent SFR estimates both with the emission traced by the 24μm continuum (with a ratio 0.14 ± 0.32 dex) and with the SFR_{IR} (with a ratio 0.04 ± 0.23 dex). This agrees with previous studies on the different SFR tracers, and gives us confidence in using Paschen-lines to paint a more complete picture of star formation at all redshifts.

We obtain high resolution and robust extinction maps for all targets, probing unusually high A_V inferred by the gas, especially towards the core of the galaxies. Forthcoming publications will analyse this in detail, in particular the differential attenuation experienced by the gas (traced by the Balmer-to-Paschen decrement) and the stars (traced by the stellar continuum). Accurately inferring large obscuration in galaxies could yield very exciting new avenues, such as discussed in Calabrò et al. (2018), where it is introduced that one could identify mergers by their extreme obscuration levels. At high redshift, one cannot rely in the morphological signs to identify merging galaxies, and severe values of A_V have not been able to be explained by other mechanisms. Upcoming JWST observations of NIR lines could help us test this idea, and possibly find a new way of identifying high-z mergers.

Our study paves the way to very exciting upcoming works, that will benefit from the first high quality spatially-resolved observations at higher redshifts to be obtained with JWST. This telescope will be able to observe Paschen-line emission in high-z galaxies at $z > 1$, breaking the ice for extending studies and methodologies like the ones presented in this work to higher redshifts. This will aid us in our pursuit to understand how galaxies form and evolve across cosmic time, helping us constrain their star formation activity by seeing through the dust like we have not been able before. Paschen lines will also provide a better estimate of the star formation history in the $z \sim 1-3$ Universe produced in dusty star forming galaxies.

ACKNOWLEDGEMENTS

The authors thank the anonymous referee for the helpful and constructive comments received. The Cosmic Dawn Center is funded by the Danish National Research Foundation (DNRF) under grant #140. DM and DLV acknowledge the very generous support by HST-GO-14095, provided by NASA through a grant from the Space Telescope Science Institute, which is operated by the Association of Universities for Research in Astronomy, Incorporated, under NASA contract NAS5-26555. LC acknowledges support by grant No. MDM-2017-0737 Unidad de Excelencia "Maria de Maeztu"-Centro de Astrobiología (INTA-CSIC) by the Spanish Ministry of Science and Innovation/State Agency of Research MCIN/AEI/10.13039/501100011033, and grant PID2019-106280GB-I00. MP is supported by the Programa Atracción de Talento de la Comunidad de Madrid via grant 2018-T2/TIC-11715, and acknowledges support from the Spanish Ministerio de Economía y Competitividad through the grant ESP2017-83197-P, and PID2019-106280GB-I00.

Facilities: HST (ACS), HST (WFC3)

Software: Astropy (Astropy Collaboration et al. 2013), Matplotlib (Hunter 2007), NumPy (Harris et al. 2020), SciPy (Virtanen et al. 2020), Grizli (Brammer & Matharu 2021)

APPENDIX

A. VORONOI BINNING

As stated in §2.3.1, we develop an adaptation of the Voronoi binning procedure from Cappellari & Copin (2003) to be able to perform the binning in large datasets and in regimes of low S/N per original data point.

Our hybrid block-averaging approach starts by defining a reference image that is used in the binning, and selecting the desired S/N threshold. We choose this to be the narrow-band image that targets Paβ, usually being F130N or F132N, since it is important for our further use of the line fluxes to obtain robust S/N line detections in the narrow-band images, particularly Paβ, being usually fainter than Hα. The code starts by creating a block averaged image, where each block has 32×32 original pixels. We mask any pixels where these large bins have S/N less than a minimum threshold, which is one of our binning parameters. Then, we run Cappellari & Copin (2003) optimal Voronoi 2D-binning algorithm on this large blocked image. We adopt as a Voronoi bin anything with more than one individual (blocked) pixel ($N > 1$), and these pixels are now "frozen" in the binning. Individual pixels that satisfy the target S/N (i.e., $N = 1$ blocked bins) are sent to the next step, which consists in reducing the block size by a factor of two (e.g., 16×16 at the second stage). Pixels in blocks where there is not enough S/N to reach the target S/N, and therefore the Voronoi code bins multiple blocks together, are not sent to the next step and remain in that assigned Voronoi bin. The code repeats these steps until the desired minimum bin size is achieved (e.g., if the minimum possible size is wanted, it stops when it reaches 1×1, i.e., native pixels). For our study we stop at 2×2 pixels as the minimum size of a bin, reducing the number of points to be able to perform further analyses, but at the same time not losing drastically the high resolution in our images. For example, for a 2×2 pixels bin, which would be 0.″2 across, we still achieve a resolution of 80 pc at $z \sim 0.02$.

Once we create the Paβ narrow-band binned image, we apply the derived binning to the other filter images available for that galaxy. However, this means that for some bins the target S/N criteria is not necessarily met in all bands, which could later on affect the robustness of the derived physical parameters in that bin. By imposing the S/N threshold on the Paβ narrow-band image, which is usually the band with least S/N across the image, we reduce this issue. Nonetheless, it is important to have the same binning in all images to be able to perform different studies on them. Specific information on how to run the binning code can be found on the Github repository[10].

[10] https://github.com/claragimenez/voronoi

B. SED-FITTING

We develop an adaptation of the pythonic version of EAZY[11] (Brammer et al. 2008), which includes an extra-reddening grid, which allows 4 continuum templates to fit A_V from 0.0 to 5.0, and two emission line templates —Hα+[N II] and Paβ—. The set of templates that we use are shown in Figure 33. Analogous to the step-wise SFH parameterization of Prospector (Leja et al. 2017), the continuum templates are generated for stepwise time bins between 0, 50, 200, 530 Myr, 1.4 Gyr with constant SFR across each bin. The line templates are created as Gaussian peaks with a continuum set to zero, and a sigma width of 100 km/s. We set the [N II]/Hα ratio to 0.55. We note that these templates are not identical to those that EAZY uses for photometric redshift estimates. Here we fit explicitly for dust reddening, whereas in EAZY the reddening is a property of the linear combination of basis templates that have diversity of SFH and dust reddening (Brammer et al. 2008).

Our code receives a catalog as input (which can have multiple targets, or in our study it has multiple bins to study spatially-resolved properties), performs the fit, and outputs the inferred physical estimates. The SED-fitting code works as follows. Firstly, it imports the templates (that can be defined by the user, as can multiple other features that follow) and the photometric measurements. For this, it follows how EAZY reads in catalogues given by the user. The reddening grid is then defined, and the templates are integrated through the filter bandpasses to produce synthetic photometry. Then the fit at each point of the grid and bin is performed, calculating the resulting χ^2 between the observed data and synthetic photometry and saving it at each step. After this, the covariance matrix is calculated, and we draw 1000 random coefficients, that we later use to better sample our uncertainties. We can directly infer the line fluxes from the combined draws and reddening grid that is built, as well as other physical properties such as A_V(Hα/Paβ), SFR, stellar mass, etc. We then implement a prior, requiring that the stellar mass map is smooth. From the χ^2 grid we can calculate the normalised probability density function (PDF), that we modify with the mass prior. Once we have the prior normed PDF, we can calculate the uncertainties and values of our inferred physical properties by calculating the percentiles, interpolating the 16%, 50% and 84% with the cumulative sum of the normed PDF and each parameter evaluated in the full grid space. From the 0.5 percentile we get an estimate of the parameter value in each bin — as well as saving the full sampling of each parameter —, and from the half difference of the 0.84 and 0.16 percentiles we estimate its uncertainty. Finally, we can estimate the χ^2 of the fit (as well as the coefficients and "best" model) where the sampling grid has the maximum posterior distribution value.

[11] https://github.com/gbrammer/eazy-py

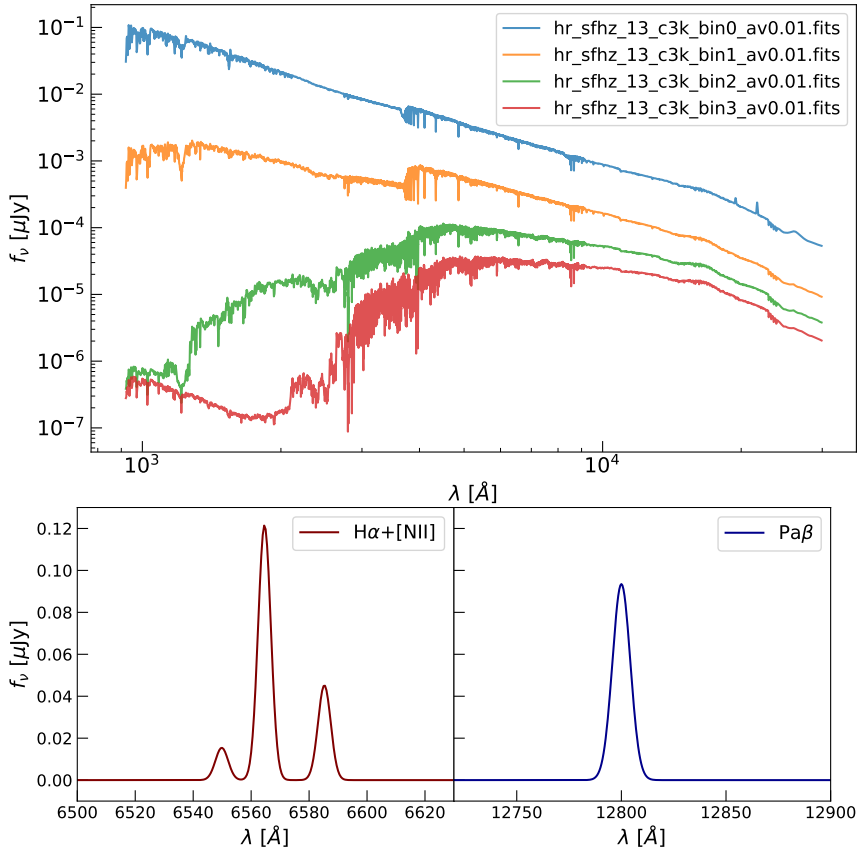

Figure 33: **Top:** Set of continuum templates that we use in our SED-fitting code. **Bottom:** Hα+[N II] (left) and Paβ (right) pure line emission templates.

Our SED-fitting code outputs the line fluxes Hα and Paβ, as well as various physical properties: the A_V obtained from the 'empirical' Balmer-Paschen decrement (A_V(Hα/Paβ)), the A_V inferred from the stellar population ($A_{V,\mathrm{stars}}$). We also obtain the star-formation rate (SFR) and stellar mass (M_*) per individual bin. We can also derive the most recent star formation with the Hα luminosity, as well as the better tracer for obscured star formation, the SFR derived from the Paβ luminosity, dust-corrected with the Balmer-to-Paschen decrement.

C. MUSE ARCHIVAL DATA

As discussed in §2.3.4, 6 of the galaxies in our sample have archival MUSE observations that we use to test the reliability of our inferred Hα fluxes from the HST photometric data. Here we present the resulting [N II]/Hα histograms for the 5 additional targets that are not presented in §2.3.4. Figure 34 shows the histograms for the targets Arp 220, IRAS13120-5453, IRAS18090+0130, MCG-02-01-051 (presented also in the main text, displayed with a different colour below), NGC6240 and NGC7592. Half of the targets agree with our adopted value of 0.55

within 1σ of the mean, whereas the other 3 show quite extreme [N II]/Hα, with the majority or all bins having [N II]>Hα across the galaxy, as found in other works (e.g. Perna et al. 2021).

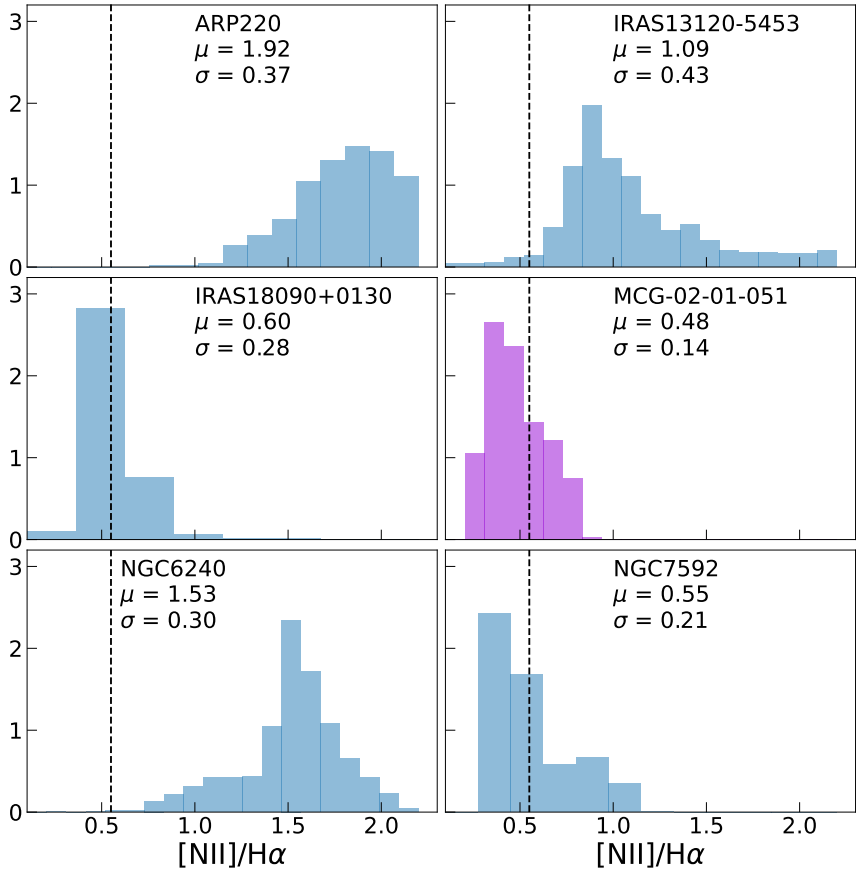

Figure 34: Histograms of the [N II]/Hα ratio for the 6 galaxies that are part of the GOALS survey, as measured in the MUSE IFU cube. The value we adopt for the ratio is indicated with a black dashed line on the histogram, and the grey shaded region shows the 1σ interval around of the mean. The y-axis is normalised.

The systematic shift in A_V, ΔA_V, caused by using two different [N II]-to-Hα correction factors, f_i^{corr}, will be given by:

$$\Delta A_V = C_1 \log\left(\frac{f_1^{corr}}{f_2^{corr}}\right) \tag{9}$$

Where C_1 is the following constant:

$$C_1 = R_V \times \frac{2.5}{k(\mathrm{Pa}\beta) - k(\mathrm{H}\alpha)} \tag{10}$$

And the correction factor is computed as follows:

$$f^{corr} = \frac{\mathrm{H}\alpha/[\mathrm{N\,II}]}{\mathrm{H}\alpha/[\mathrm{N\,II}]+1} \tag{11}$$

So that the resulting Hα flux that is corrected for [N II] contamination is given by $f_{H\alpha} = f^{corr} \times f_{H\alpha+[\mathrm{N\,II}]}$, where the last term is the measured combined [N II]+Hα flux.

D. FILTER COVERAGE

Here we present a test of how the specific filter coverage available for each object can affect the emission line maps derived with our method. We want to test if the different filter widths or number of available filters affect our ability to recover the physical properties that we infer, such as the Hα line flux. For this, we make use of the archival MUSE cube for MCG-02-01-051 (see also §2.3.4). We can integrate the MUSE spectra through various filter bandpasses to produce synthetic images. For MCG-02-01-051, we have 6 HST bands available (F673N, F130N, F132N narrow and F435W, F814W, F110W broad). We add synthetic observations from the MUSE cube of the HST ACS/WFC F555W, F606W and F775W bandpasses, to better sample the optical continuum. We then run our binned SED-fitting software with the same set-up as before with the observed HST and synthetic MUSE images.

Figure 35 displays the comparison of the resulting Hα flux inferred with both estimates, in maps (top panels) and as a scatter plot (bottom panel). We find that the emission line map derived from the limited available HST data is fully consistent with the best-case scenario with additional broad-band optical filters (with a median log ratio of 0.06 ± 0.07 dex). When considering the rest of inferred physical parameters, both runs are consistent, having less than 0.3 dex off between them when inferring the SFR, the stellar mass or the A_V.

In order to fully constrain the SFH and dust obscuration of the continuum, we prefer to have a broader wavelength coverage. Nonetheless, we conclude that with the average filter coverage of our sample, we can adequately infer physical properties with our SED-fitting code.

E. INDIVIDUAL GALAXIES

Additional figures can be found on Appendix 5.1.

F. ADDITIONAL GALAXIES

Additional tables can be found on Appendix 5.1.

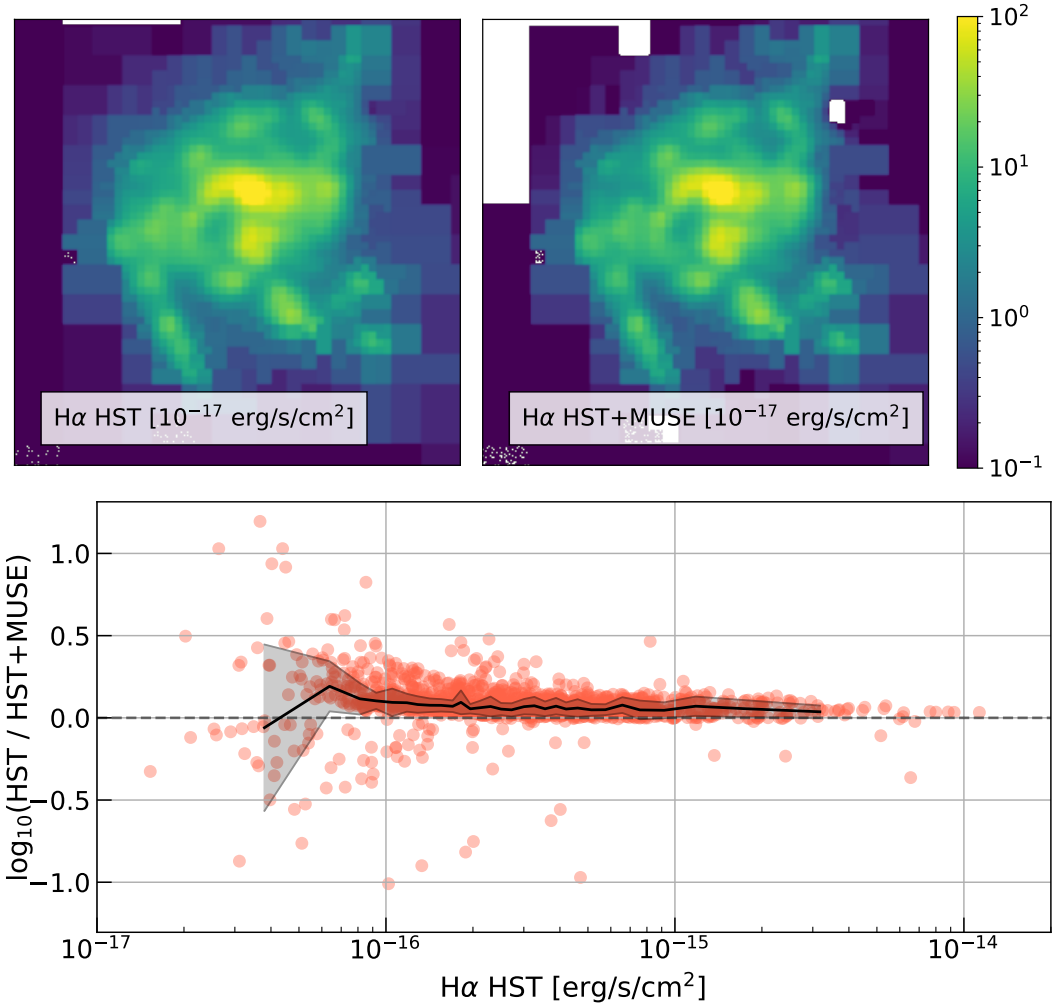

Figure 35: **Top:** Maps of the Hα line flux for the target MCG-02-01-051 inferred with only HST photometry (left), and with HST and extra synthetic photometry from MUSE (right). **Bottom:** Ratio of both Hα estimates in each spatial bin. The running median and scatter are shown as a solid black line and surrounding shaded region, respectively.

3

THE EARLY UNIVERSE WITH JWST

This chapter contains the following article:

"Spatially Resolved Properties of Galaxies at $5 < z < 9$ in the SMACS0723 *JWST* ERO Field"

Published in The Astrophysical Journal (ApJ): Volume 948, Issue 2, id. 126, 13 pp., May 2023, DOI: 10.3847/1538-4357/acc5ea

Authors: Clara Giménez-Arteaga, Pascal A. Oesch, Gabriel B. Brammer, Francesco Valentino, Charlotte A. Mason, Andrea Weibel, Laia Barrufet, Seiji Fujimoto, Kasper E. Heintz, Erica J. Nelson, Victoria B. Strait, Katherine A. Suess and Justus Gibson

ABSTRACT

We present the first spatially resolved measurements of galaxy properties in the *JWST* ERO SMACS0723 field. We perform a comprehensive analysis of five $5 < z < 9$ galaxies with spectroscopic redshifts from NIRSpec observations. We perform spatially resolved SED fitting with BAGPIPES, using 6 NIRCam imaging bands spanning the wavelength range $0.8-5\mu$m. This approach allows us to study the internal structure and assembly of the first generations of galaxies. We find clear gradients both in the empirical colour maps, as well as in most of the estimated physical parameters. We find regions of considerably different specific star formation rates across each galaxy, which points to very bursty star-formation happening on small scales, not galaxy-wide. The integrated light is dominated by these bursty regions, which exhibit strong line emission, with the equivalent width of [O III]+Hβ reaching up to $\sim 3000-4000$ Å rest-frame. Studying these galaxies in an integrated approach yields extremely young inferred ages of the stellar population (<10 Myr), which outshine older stellar populations that are only distinguishable in the spatially resolved maps. This leads to inferring $\sim 0.5-1$ dex lower stellar masses by using single-aperture photometry, when compared to resolved analyses. Such systematics would have strong implications in the shape and evolution of the stellar mass function at these early times, particularly while samples are limited to small numbers of the brightest candidates. Furthermore, the evolved stellar populations revealed in this study imply an extended process of early galaxy formation that could otherwise be hidden behind the light of the most recently formed stars.

3.1 INTRODUCTION

By characterizing the physical properties of galaxies in the redshift range $5 < z < 10$, we can study the epoch of reionization, when the Universe experienced its last phase transition (see e.g., Treu et al. 2013; Mason et al. 2018; Robertson 2022, for a review). With well-sampled photometry of high redshift galaxies, we can robustly model their spectral energy distributions (SEDs) and infer the properties of their stellar populations. Up until now, the rest-frame optical emission from galaxies was unavailable at $z > 7$, having been redshifted to the part of the near-infrared spectrum where our facilities lacked sensitivity and spatial resolution. While the rest-frame UV emission we have had access to is a good tracer of unattenuated star formation, it is a poor tracer of stars older and less massive than O and B-type, that make up the bulk of total stellar mass for populations older than a few Myr.

The latest addition to the space fleet of telescopes, the *James Webb Space Telescope* (*JWST*), has unprecedented sensitivity and spatial resolution in the near infrared. This has opened up a new window into the rest-frame optical emis-

sion of high redshift galaxies, allowing us to understand their stellar populations for the first time. The Near-Infrared Camera (NIRCam; Rieke et al. 2005, 2023) on board *JWST* allows us to reach this spectral range with a unique depth and resolution. The Near Infrared Spectrograph (NIRSpec; Jakobsen et al. 2022) provides high resolution spectroscopy in the near-infrared, which is key to robustly determine the redshift. This improves the modelling of the SEDs by constraining a free parameter, thus breaking the degeneracies that the redshift has with age and dust (see e.g., Conroy 2013, for a review).

Lower-redshift studies have been able to resolve galaxies and their components (up to $z \sim 2$ in e.g., Zibetti et al. 2009; Nelson et al. 2019; Morselli et al. 2019; Suess et al. 2019; Abdurro'uf et al. 2022; Giménez-Arteaga et al. 2022). At higher redshifts, resolved analyses have typically only been possible in lensed systems (e.g., Zitrin et al. 2011; Vanzella et al. 2017), or in particularly luminous galaxies that break up into multiple components (e.g., Matthee et al. 2020; Bowler et al. 2022). Nevertheless, integrated photometry has revealed the population demographics: stellar mass functions, number counts (e.g., Song et al. 2016; Stefanon et al. 2015, 2021).

With *JWST* we can extend for the first time resolved studies beyond redshift ~ 2, introducing the possibility to study in unique detail the first generations of galaxies (e.g., Hsiao et al. 2023; Chen et al. 2023). These resolved studies will allow us to place unique, new constraints on the formation and evolution of the first galaxies: their mass assembly histories, modes of growth, chemical enrichment, and earliest quenching mechanisms. In order to build a complete picture of galaxy assembly, a resolved view of its components is required, to fully understand the interplay between the stellar population, dust and gas in $z > 6$ galaxies.

The impact of having resolved observations has so far only been studied at low redshifts ($z \lesssim 3$). Various works have compared the inferred physical properties obtained with resolved and unresolved observations (see e.g., Wuyts et al. 2012; Sorba & Sawicki 2015, 2018; Vale Asari et al. 2020; Fetherolf et al. 2020), with diverse conclusions. A resolved approach can have multiple advantages, such as decreasing degeneracies in the stellar population synthesis models and producing more realistic star formation histories (Pérez-González et al. 2023). In highly star forming galaxies, the outshining of old stellar populations by young ones is of particular importance, which a resolved analysis could untangle. Sorba & Sawicki (2018) find that the total stellar mass derived from integrated SED fitting can be underestimated by a factor of ~ 5, compared to spatially-resolved SED modelling, which they attributed to the outshining effect by young stars.

In this paper, we present the observations and first results of a multi-wavelength analysis of five high redshift galaxies ($5 < z < 9$) observed with *JWST*, to study the spatially-resolved properties of their stellar populations. These galaxies are the highest spectroscopically confirmed targets in the *JWST* ERO SMACS0723 field.

Using NIRCam imaging in 6 bands spanning the wavelength range $0.8-5\mu$m, we perform spatially-resolved SED fitting with BAGPIPES (Carnall et al. 2018). There have been multiple works on these targets, albeit always from an integrated perspective (e.g., Schaerer et al. 2022; Trump et al. 2023; Rhoads et al. 2023; Curti et al. 2023a; Brinchmann 2023; Arellano-Córdova et al. 2022; Fujimoto et al. 2022; Carnall et al. 2023; Heintz et al. 2023c; Tacchella et al. 2023). These papers derive different stellar masses, some of them with extremely young ages of the stellar population. Here we present the first spatially resolved analysis on these high redshift galaxies, which we propose as a more robust approach to accurately calculate their stellar masses.

This paper is structured as follows. In Section 4.2, we introduce the *JWST* observations and data reduction procedure. Section 4.3 describes the methodology we use for the modelling of the SEDs with BAGPIPES. In Section 4.4, we present the main results and inferred properties of our sample, both in integrated and resolved approaches, as well as discussing the implications of our analyses. Finally, in Section 4.5 we present the summary and conclusions of our work. Throughout this paper, we assume a simplified ΛCDM cosmology with $H_0 = 70$ km s^{-1} Mpc^{-1}, $\Omega_m = 0.3$ and $\Omega_\Lambda = 0.7$. No lensing correction is applied throughout this work. Hence, intrinsic stellar masses and star formation rates can be obtained by dividing by the magnification factor (μ, see Table 3).

3.2 DATA AND OBSERVATIONS

We use the public data of the galaxy cluster SMACS J0723.3-7327 (SMACS0723), observed by *JWST* as part of the Early Release Observations (ERO; Programme ID 2736, Pontoppidan et al. 2022). We use the Near-Infrared Camera (NIRCam; Rieke et al. 2005) photometric data from the catalog reduced by Brammer et al. (in prep). The data has been reduced using the public software package `grizli` (Brammer 2019; Brammer & Matharu 2021; Brammer et al. 2022). The photometry is corrected for Milky Way extinction assuming $E(B-V) = 0.1909$ (Schlafly & Finkbeiner 2011) and the Fitzpatrick & Massa (2007) extinction curve. The images are PSF-matched to the F444W band on a common $0.''04$/pixel scale. We adopt the PSF models for use with the `grizli` mosaics[1], which are based on the `WebbPSF` models. We compute matching kernels for each of the PSFs to the F444W PSF using a Richardson-Lucy deconvolution algorithm (Richardson 1972; Lucy 1974), and then convolve the images with the resulting kernels to match the PSF resolution in F444W.

In this work we focus on the five galaxies at $5 < z < 9$ that have spectroscopic redshifts confirmed from NIRSpec observations, presented in Carnall et al. (2023). These are detected in the 6 deep NIRCam imaging filters F090W, F150W, F200W, F277W, F356W, and F444W. The targets also have shallower imaging data ob-

[1] `https://github.com/gbrammer/grizli-psf-library/tree/main/smacs0723`

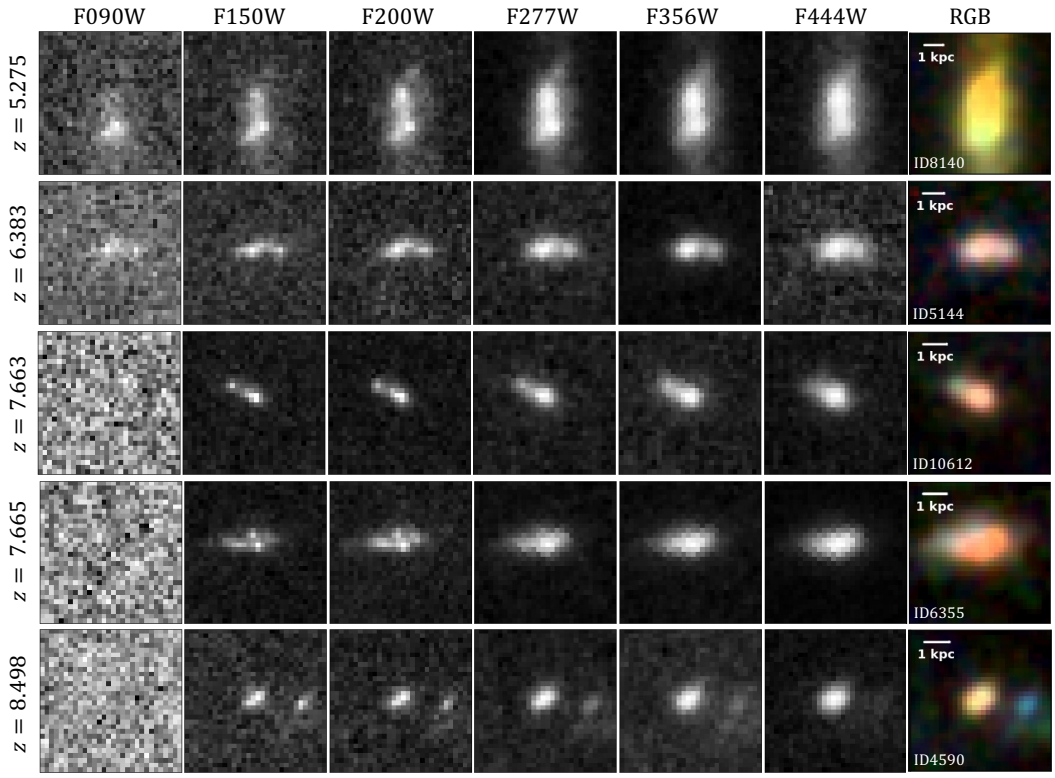

Figure 36: Cutout images of the five SMACS0723 galaxies in all available NIRCam bands. The cutouts are 1.″2 across and centered in the coordinates provided in Table 3. The RGB images are built combining the F150W (B), F277W (G) and F444W (R) PSF-matched images (to the F444W band). The physical scale is calculated in the lens plane.

tained with NIRISS with the F115W and F200W filters, which we exclude in the analysis presented in this work due to their lower spatial resolution. The sample spans a redshift range from 5.275 for the closest galaxy, up to 8.498 for the highest redshift object (Carnall et al. 2023). The sources have magnification factors between 1.6 up to 10.1 in the GLAFIC lens models from Oguri (2010). They are not significantly distorted by the gravitational lensing so that it affects the spatially resolved SED fitting. Table 3 provides the basic information for the targets. We do not apply any lensing correction to our results, although we report on Table 3 the lensing factors for these sources presented in Carnall et al. (2023). Figure 36 displays the cutout images of the five galaxies in all available observed bands, as well as the colour images built combining the F150W, F277W, and F444W filters.

Redshift	ID	RA	DEC	Lensing μ
5.275	8140	110.78804	−73.46179	1.7
6.383	5144	110.83972	−73.44536	2.9
7.663	10612	110.83395	−73.43454	1.6
7.665	6355	110.84452	−73.43508	2.7
8.498	4590	110.85933	−73.44916	10.1

Table 3: Redshift, coordinates and magnification factors for the 5 high-redshift galaxies studied in this work. The information is taken from Carnall et al. (2023), where the lensing factors (μ) are taken from Oguri (2010).

3.3 METHODOLOGY

3.3.1 *SED fitting with* BAGPIPES

To model the spectral energy distribution of the individual pixels and derive the physical properties, we use the SED fitting code BAGPIPES (Carnall et al. 2018). We set the NIRSpec spectroscopic redshifts indicated on Table 3, in order to break the degeneracy with age and dust that a photometric or uncertain redshift would introduce. We use the SPS models by Bruzual & Charlot (2003) and include the nebular emission with CLOUDY (Ferland et al. 2017), extending the BAGPIPES default grid (that normally reaches up to $\log_{10}(U) = -2$) so that the ionization parameter, U, varies from $-3 < \log_{10}(U) < -1$, since $z > 6$ galaxies display higher ionization parameters than low-redshift galaxies (e.g., Sugahara et al. 2022; Curti et al. 2023a). We assume a Kroupa (2001) initial mass function (IMF), and a Calzetti et al. (2000) attenuation curve, in order to reduce the number of free parameters in our fits (since other parameterisations such as the Salim et al. (2018) attenuation curve introduce extra parameters such as the bump strength and slope δ). We choose a constant star formation history model, following Carnall et al. (2023), which seems adequate to fit our galaxies (we obtain reduced χ^2 values within the range $0.1-7.5$, shown in further detail in the following sections). The formation of very young, low-mass, and low-metallicity galaxies is likely bursty, and a constant SFH accurately resembles this on short timescales. We let the maximum age grid to vary from 1 Myr to 1 Gyr, to allow for the presence of more evolved stellar populations, and further limited by the age at the given redshift. We set the visual extinction to vary from $A_V = 0$ to $A_V = 2$, and the metallicity from 0 to $Z_\odot$, with uniform priors. Even though the metallicity has been calculated with integrated NIRSpec spectra for these targets (see e.g., Schaerer et al. 2022; Curti et al. 2023a; Brinchmann 2023), they obtain varying results within our allowed range. Moreover, we want to allow for spatial variation across the galaxy, thus we do not set Z as a fixed parameter in the fit. Finally, we set the lifetime of birth clouds to 10 Myr.

3.3.2 *Pixel-based modelling*

In this work we perform SED fitting on a pixel-by-pixel basis. With the setup described in the previous subsection, we fit the spectral energy distribution and infer the physical parameters of each individual pixel. This allows us to recover the 2D distribution of properties such as the stellar mass and star formation rate (SFR). We use SExtractor (Bertin & Arnouts 1996) to derive the segmentation map of each source. The pixels in our maps correspond to physical sizes between 180 and 240 parsecs. In order to fit the SED of individual pixels, we impose a signal-to-noise ratio (S/N) threshold of 2 on both the F150W and F200W bands, which are the noisiest. We find that this threshold is enough to produce trustworthy fits, obtaining good reduced χ^2 values in the fits of individual pixels, as we show in more detail in the following section. Pixels that do not fulfil this S/N criteria are not fitted nor displayed in the output maps. To produce the maps of the physical properties and study their spatial distribution, we display the 50th percentile of the inferred parameter, calculated from the posterior distribution that BAGPIPES provides. We can also present the uncertainties for each pixel extracted from the 16th and 84th percentiles of the posterior distribution (see Carnall et al. 2018 for details).

3.4 RESULTS AND DISCUSSION

In this section we present and discuss the results of our study. We provide both an integrated and a spatially resolved analysis of the physical properties that we infer for the five targets that comprise this work.

3.4.1 *Spatially Resolved Physical Properties*

For all galaxies studied, we have produced maps of the physical parameters inferred with BAGPIPES. These include the star-formation rate surface density (SFRD), the stellar mass surface density (SMD), the visual extinction A_V, the mass weighted age, the UV slope β, and the equivalent width (EW) of the [O III] and Hβ emission lines. The last two are measured from the BAGPIPES posterior SEDs. We also display maps of the empirical colours F150W–F277W, which is a proxy for the UV slope, and F356W–F444W, which generally traces the strength of the inferred [O III]+Hβ emission (except for the lowest and highest redshift galaxies, where no available couple of bands capture the lines and continuum accordingly).

Figures 37–41 display the resulting maps for the five galaxies presented in this work, from the lowest redshift $z = 5.275$, to the highest $z = 8.498$. Firstly, we see that all galaxies are resolved and display strong empirical colour gradients, both in the blue bands as well as the red bands. These gradients appear on larger

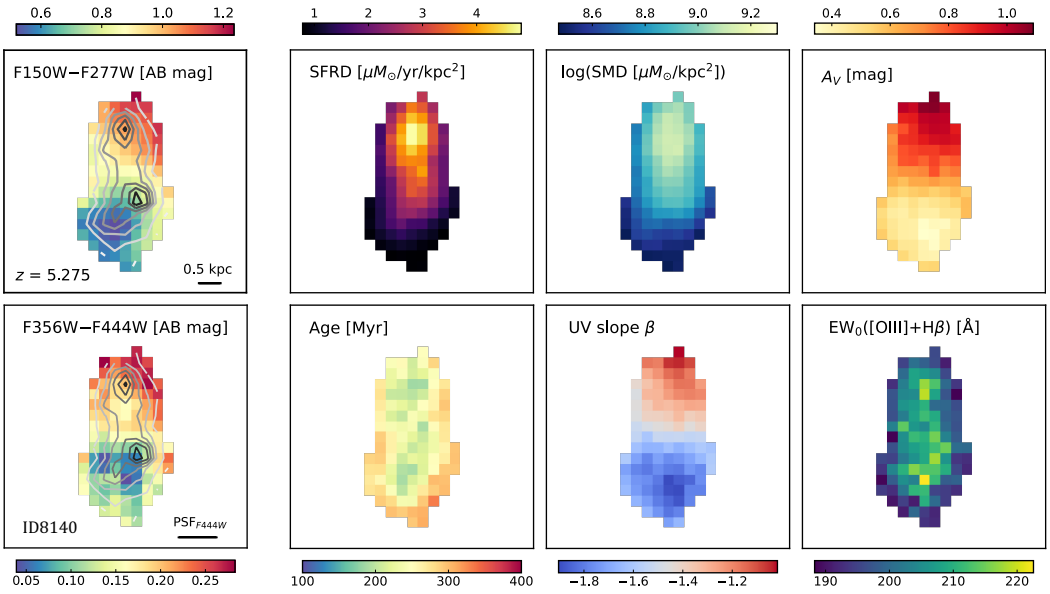

Figure 37: Maps of the galaxy ID8140 at $z = 5.275$. **First column:** Maps of the empirical colours in AB mag, inferred as the difference of the bands F150 and F277W (top) and the F356W and F444W (bottom). The contours correspond to the non PSF-matched F200W image. The physical scale is calculated in the lens plane. The FWHM of the F444W PSF is indicated. **Rest of panels:** Maps of the physical properties inferred with BAGPIPES. The top row, from left to right, shows the resulting maps for the star formation rate surface density (SFRD), the logarithm of the stellar mass surface density (SMD), and the visual extinction A_V. The bottom row shows the maps for the mass-weighted stellar age, the UV slope (β) and the equivalent width of the inferred [O III]+Hβ emission lines. No lensing correction has been applied.

scales than the FWHM of the F444W PSF (0.″145, equivalent to $\sim$ 3.6 pixels), confirming that we can resolve trends and structures in our sample. In general, we find that even at these early times, most of the galaxies display multiple star forming clumps, traced by the F200W contours, as is found also by other recent works (e.g., Claeyssens et al. 2023; Treu et al. 2023; Chen et al. 2023). These are regions of very high inferred equivalent widths of the [O III]+Hβ emission (in the range $\sim 300-4000$ Å rest-frame), embedded within larger structures that are not undergoing a burst of star formation. In these regions with extreme line EWs, the inferred ages are extremely young (<10 Myr), corresponding to a bursty clump of young stars that is resolved in targets ID10612 (Figure 39) and ID6355 (Figure 40), and marginally unresolved in ID5144 (Figure 38) and ID4590 (Figure 41), given the scale of the F444W PSF FWHM. Around these high-EW bursty clumps, we also find underlying older stellar populations (~100 Myr), which would be missed in an integrated analysis, as we will discuss in more detail in the next subsection.

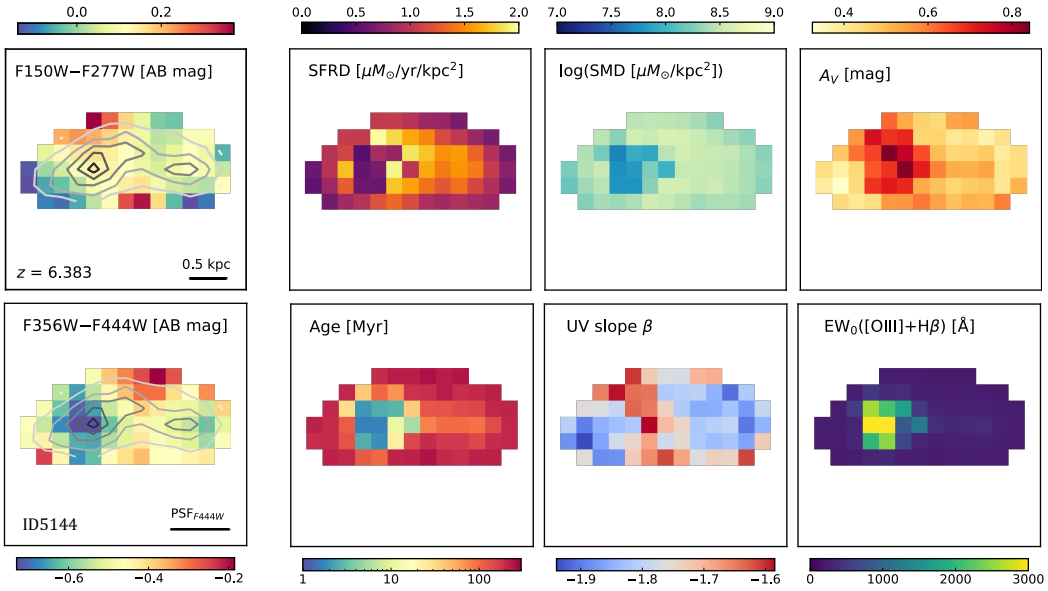

Figure 38: Maps of the empirical colours and the physical properties inferred with BAGPIPES on the galaxy ID5144 at $z = 6.383$. See Figure 37 for more details.

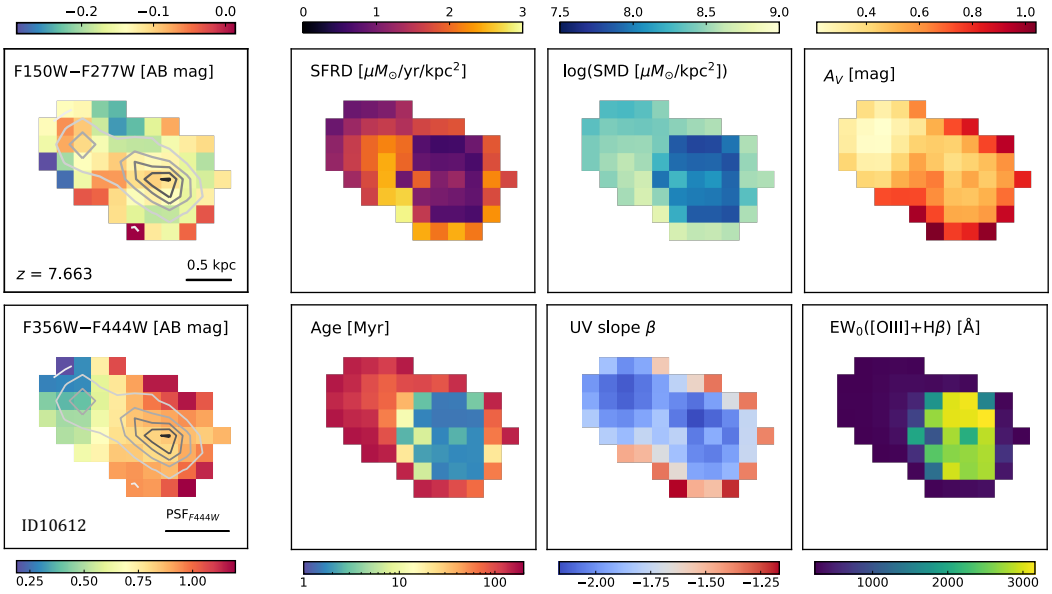

Figure 39: Maps of the empirical colours and the physical properties inferred with BAGPIPES on the galaxy ID10612 at $z = 7.663$. See Figure 37 for more details.

Figure 37 displays the maps for galaxy ID8140, at redshift $z = 5.275$. We obtain smooth maps for all physical properties and colours. The SFRD and SMD appear entirely co-spatial, and the UV slope traces perfectly the dust obscuration map. This galaxy has ~ 2 times older stellar populations compared to the average of the rest of the sample, in line with being the galaxy at lowest redshift. It shows strong colour, A_V and UV slope gradients, with two distinct clumps, one red

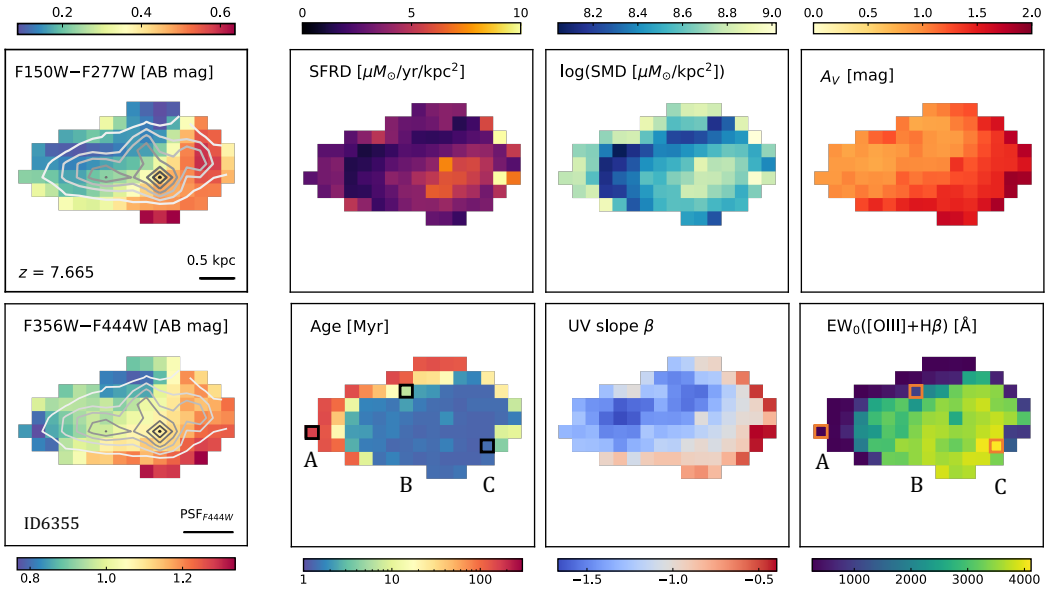

Figure 40: Maps of the empirical colours and the physical properties inferred with BAGPIPES on the galaxy ID6355 at $z = 7.665$. See Figure 37 for more details. The three boxes A, B, C indicate the pixels that are analysed in more detail in the text, as well as in Figure 42, where the best fit SEDs are shown for each individual pixel.

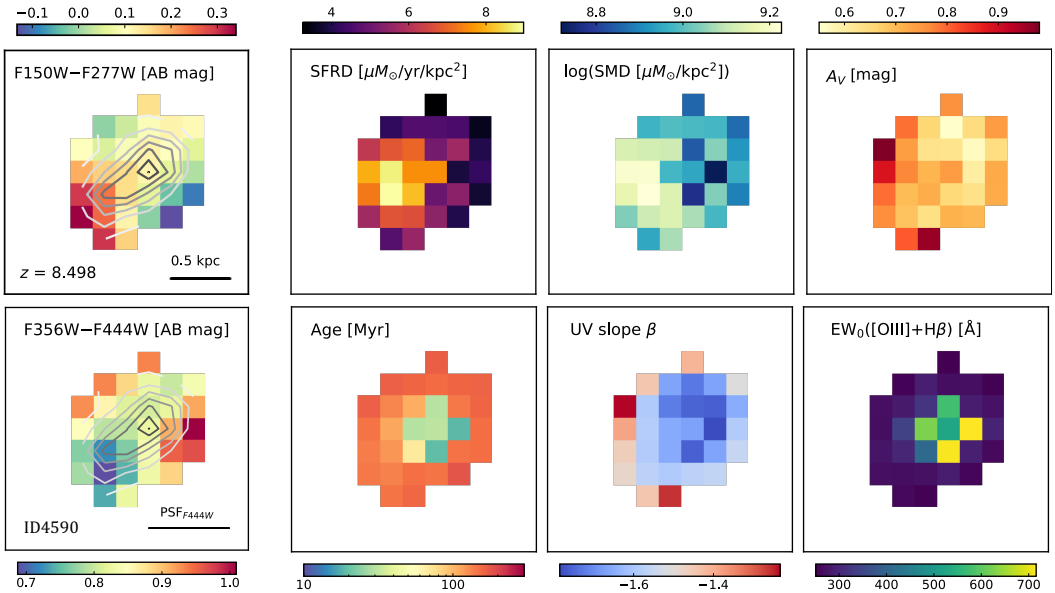

Figure 41: Maps of the empirical colours and the physical properties inferred with BAGPIPES on the galaxy ID4590 at $z = 8.498$. See Figure 37 for more details.

and one blue. This could indicate that this galaxy is undergoing a merger, even though the EWs (the lowest of all targets) and ages show little variation across the object.

Figure 40 shows the resulting maps for the galaxy ID6355 at $z = 7.665$. It is the galaxy with most extreme EWs (reaching ~ 4000 Å). We see that the region with very high EW is very extended for this galaxy, leaving barely a shell where we find underlying older stellar populations, which are otherwise outshined (or not present) by the younger stars in these strong line emission regions. The clear gradients in the empirical colours give us confidence that this shell is real and not an artifact of the age-dust degeneracy in the SED fitting process, which we also discuss in further detail in §3.4.4. On top of this, the shell is larger than the PSF scale. In Figure 42 we present and analyse the fits for three individual pixels within this source, so that we can study further whether the "shell" of older stars in this particular galaxy is real or an artifact. We select the pixels A, B, and C that are indicated in the age and EW maps in Figure 40, since they appear to be very distinct regions within this galaxy. Albeit being towards the edge of the galaxy, all three pixels fulfill our S/N threshold, so that we can produce robust fits (with reduced χ^2 values within $0.10-0.53$). These pixels are also far enough from each other so that the PSF is not blending the information they encode, and we can thus resolve their different stellar populations. We can clearly see that the SEDs look different, reflecting the gradients that we already see in Figure 40, both on the maps of the inferred physical parameters, as well as the empirical colour maps. The greatest difference is observed in the strength of the inferred [O III]+Hβ emission lines, since the SED for pixel C has extreme EW, reaching 4264 ± 533 Å rest-frame. This yields a considerable difference in the inferred ages, with pixel A having a mass weighted age of 159^{+115}_{-108} Myr, and pixels B and C displaying very young stellar ages under 10 Myr. The corner plots for each fit can be found on Appendix 3.5.

Figure 41 shows the results for the galaxy ID4590, which is the highest redshift $z = 8.498$ in this work. It is a very compact source, with only 31 pixels where S/N>2 for both F150W and F200W. We see a star forming clump, which also corresponds to the highest inferred stellar mass, and towards the dustiest zone in the A_V map. We see a marginally unresolved centrally located clump of young stellar population, which is not entirely co-spatial with the star-forming burst, but traces perfectly the higher equivalent width of the inferred [O III] and Hβ emission lines. On top of this, the empirical colour maps display a clear gradient, which follows the ones observed for the SFRD, SMD, A_V and β maps. The rest of targets exhibit similar trends for all physical properties, with the main characteristic being this region with extremely high EWs and therefore very young stellar populations.

3.4.2 *Integrated Analysis*

Besides providing an invaluable insight into the internal structure of galaxies, we want to test whether spatially resolved observations yield other consequences,

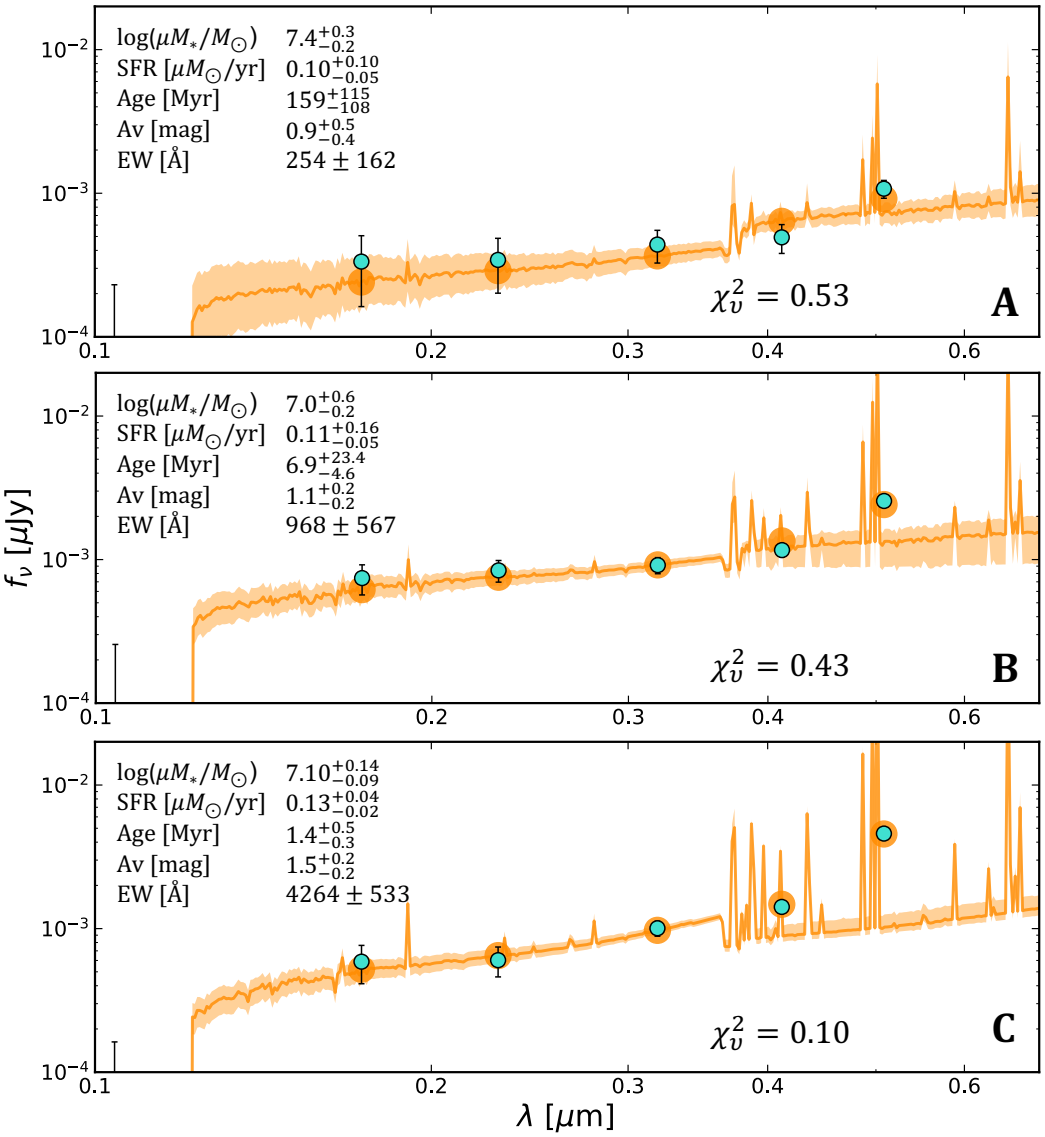

Figure 42: Best fit SEDs for the three pixels A, B and C indicated in Figure 40, from the galaxy ID6355 at $z = 7.665$. The turquoise points and errorbars correspond to the NIRCam photometry, the orange points to the best fit model, and the orange curve and shaded region is the best fit SED inferred with BAGPIPES, and corresponding 16th and 84th percentile uncertainty interval. The inferred physical parameters are indicated for each pixel, as well as the reduced χ^2 of the fit.

such as inferring different physical properties, compared to only integrated measurements.

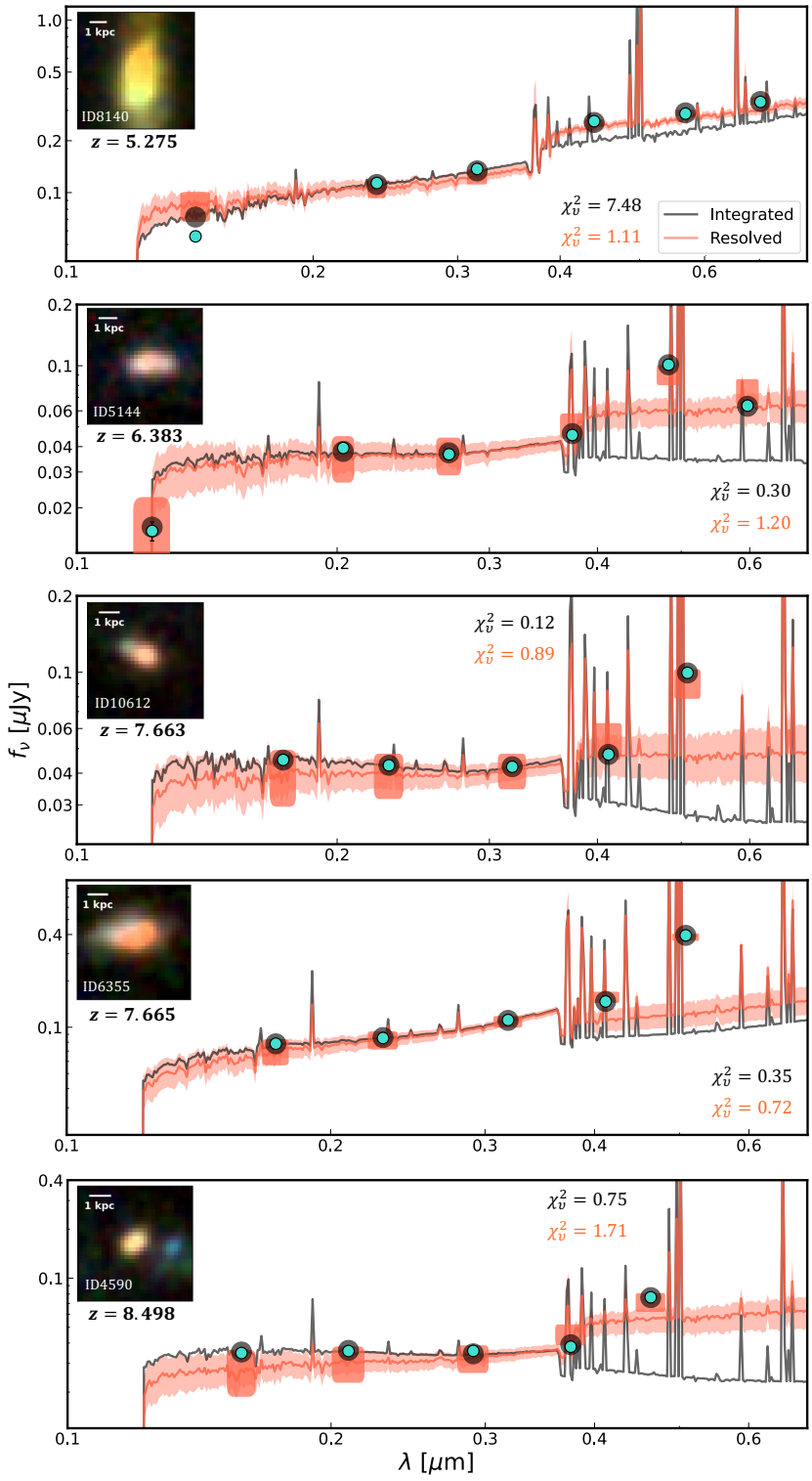

Figure 43: Best fit SEDs and models for the integrated (black curve and circles) and resolved (red curve and squares) modelling of the five galaxies studied in this work. The turquoise points and errorbars correspond to the integrated NIRCam photometry. The red curve is inferred by summing the posterior distributions in all pixels, and calculating the 50th percentile of the resulting one. The shaded regions correspond to the 16th and 84th percentile of the summed posterior distribution. The inset cutouts correspond to the same RGB images as in Figure 36. The reduced χ^2 values of each fit are indicated.

To perform this test, we sum the photometry in each observed band for the pixels that fulfil our S/N criteria, so that we only consider the same pixels that we fit in the spatially resolved analysis shown in Figures 37–41. With the sum of the photometry in each filter, we then use BAGPIPES to find the best fit SED and infer the integrated physical parameters. We use the exact same set up as for the spatially resolved run, described in §3.3.1. We present the integrated fits with the best fit SEDs in Figure 43. The inferred integrated physical properties for each galaxy can be found in Table 5, in Appendix 3.5. In Figure 43, we can see that both the resolved and integrated models (red and black curves, respectively) fit adequately the photometry (turquoise points), with reduced χ^2 values within the range $0.1-7.5$. The surprising finding is that both best fit SEDs are considerably different. For all galaxies, we find that the high equivalent widths that we could spatially locate in the resolved analysis within a clump, now completely dominate the overall fit. This results in inferring extremely young ages in the integrated light, and potentially too low stellar masses as a result.

Figure 44 shows the comparison between the stellar mass estimates that we infer in the spatially resolved analysis and the integrated fit. Table 4 provides these values, as well as the mass weighted ages. We obtain the spatially resolved mass estimate by summing the stellar mass inferred in each individual pixel. The resolved average age is inferred as the mean mass weighted age of all pixels. In both cases, the resolved uncertainties reported in Table 4 are calculated with the 16th and 84th percentile of the summed posterior distribution over all pixels. For the integrated run, the output from BAGPIPES is directly reported, and the uncertainties are calculated with the 16th and 84th percentiles from the posterior distribution. We find that the integrated run estimates systematically lower stellar masses than the spatially resolved one, from ∼0.5 up to 1 dex lower, seemingly without any trend with the redshift. This, as explained above, is a consequence of being forced to choose extremely young stellar populations to fit the integrated light, due to the strong emission lines dominating it completely. We see this in Table 4, since all galaxies have an integrated age of under 10 Myr, except the one at lowest redshift, with a best fit age of $14.9^{+1.7}_{-1.0}$ Myr. We demonstrate this by fixing the age in BAGPIPES to the average stellar age inferred in the spatially resolved analysis. By doing this, the estimate of the stellar mass in the integrated run increases, retrieving closer values to the spatially resolved masses. Moreover, we see that the average mass weighted ages in the resolved analysis are all > 10 Myr, and significantly older than the integrated ages, even when considering the large uncertainties associated with the age estimate.

Figure 45 shows how the SFH affects the inferred stellar mass. We plot the sum of the SFH inferred for the spatial pixels, as well as the SFH estimated in the unresolved analysis, for the galaxy ID10612 at $z = 7.663$. The integrated SFH consists of a single burst with very young age (~ 2 Myr), whereas the spatially resolved SFH is a distribution that covers a wider age range, reaching up to

$\sim$ 300 Myr. For this galaxy, this would mean a formation redshift of $z \sim 12$. We see that, whereas the integrated analysis forms all stellar mass within less than 10 Myr, this only corresponds to $\sim$6% of the spatially resolved stellar mass, directly proving where the mass discrepancy is coming from. We obtain the same results in the SFH comparison for all galaxies studied in this work.

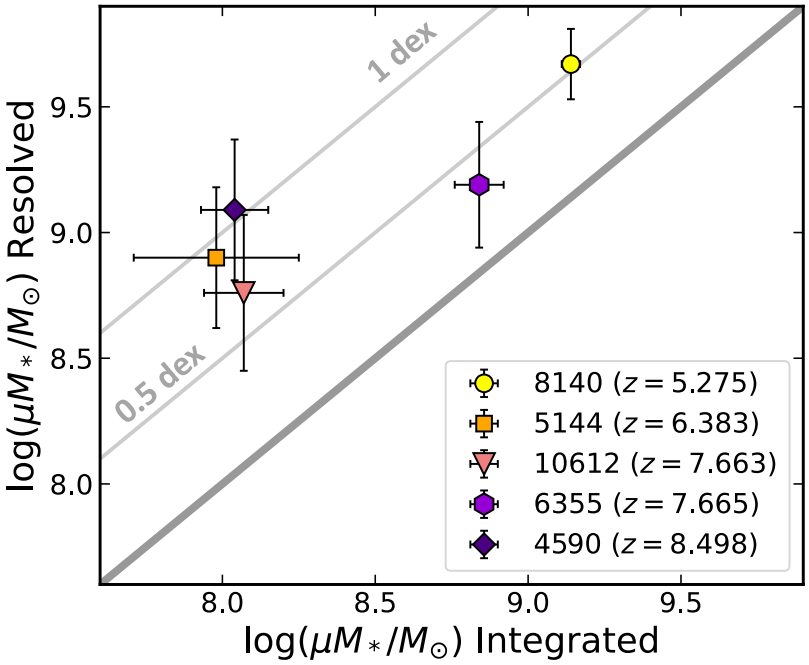

Figure 44: Comparison between the stellar mass that we infer in the spatially resolved analysis, versus the integrated fit. No lensing correction is applied in any of the two estimates. The plotted values are shown Table 4. The one-to-one line is indicated, as well as the 0.5 and 1 dex offset lines.

This could considerably change our current picture of mass assembly in the early Universe, particularly while our samples are limited to the brightest candidates in small numbers. These systematics would affect from the stellar mass functions that we have derived so far at high redshifts, to our cosmological models of galaxy formation and mass build-up, since all our observations and mass estimates at high redshift until now have been based on integrated measurements. Overall, the nature of these galaxies can completely change by having a resolved picture.

On top of this, we adopt a parametric constant SFH model. Some works have shown that using instead a non-parametric SFH model can lead to inferring larger stellar masses by up to 1 dex (all in an integrated approach), in particular for galaxies like the ones studied here, where a burst with very young stellar ages dominates the integrated light (e.g., Leja et al. 2019; Lower et al. 2020; Tacchella et al. 2023; Whitler et al. 2023). Non-parametric SFHs therefore seem like the

z	ID	$\log(\mu M_*/M_\odot)$		Age [Myr]	
		Integrated	Resolved	Integrated	Resolved
5.275	8140	$9.14^{+0.03}_{-0.02}$	$9.67^{+0.10}_{-0.14}$	$14.9^{+1.7}_{-1.0}$	251^{+172}_{-139}
6.383	5144	$7.98^{+0.27}_{-0.11}$	$8.90^{+0.20}_{-0.28}$	$2.5^{+1.1}_{-1.3}$	147^{+138}_{-103}
7.663	10612	$8.07^{+0.13}_{-0.08}$	$8.76^{+0.28}_{-0.31}$	$1.6^{+0.7}_{-0.5}$	71^{+85}_{-51}
7.665	6355	$8.84^{+0.08}_{-0.06}$	$9.19^{+0.25}_{-0.22}$	$1.3^{+3.6}_{-0.2}$	25^{+38}_{-18}
8.498	4590	$8.04^{+0.11}_{-0.06}$	$9.09^{+0.23}_{-0.28}$	$1.9^{+0.4}_{-0.5}$	111^{+108}_{-76}

Table 4: Values for the stellar mass and mass weighted stellar age that we infer with BAGPIPES, both in the integrated run and the spatially resolved analysis presented in this work. We plot the mass values in Figure 44.

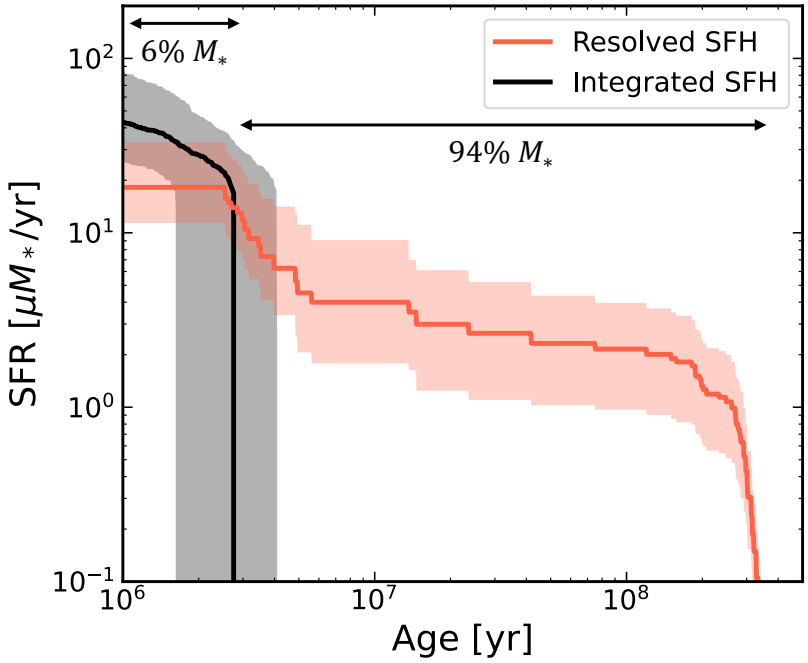

Figure 45: Comparison between the star formation history that we infer in the spatially resolved analysis (red curve), versus the integrated fit (black curve), for the galaxy ID10612 at $z = 7.663$. The shaded regions correspond to the 16-84th percentile range in each case.

better option when considering integrated SEDs, since we have shown that there can be significant spatial variation in star formation (see Figure 45). Moreover, works like Bisigello et al. (2019) argue that we need to include the two MIRI bands in order to constrain better the stellar mass estimates in high redshift galaxies, particularly in young galaxies with nebular emission lines, such as the ones we study here.

3.4.3 *Comparison with Other Works*

To put our results into context, we compare the physical parameters that we infer with other published works on these targets. As stated before, only integrated analyses are available in the literature. We expect our integrated measurements and estimates of some of the physical properties, such as the stellar mass and star formation rate, to be lower than any other work, since aperture photometry yields larger fluxes on all bands ($\sim$ 20% larger for the galaxy ID10612 at $z = 7.663$ if we use a 0.″5 aperture), given that we only consider pixels that fulfil our S/N criteria. On top of this, previous works have used varying data reduction, zero points, SED fitting codes, SFH models, attenuation curves, magnification corrections, amongst other differences. Therefore, here we mostly focus on comparing the physical nature of the sources, as inferred by different works.

The mass-weighted ages that we infer in our integrated analysis are all consistent within the uncertainties with those found for these same five targets by Carnall et al. (2023), from which we reproduce the SED fitting assumptions and parameters, except using a differently reduced photometry, a Calzetti et al. (2000) attenuation curve, as well as extending our nebular grid as explained in §3.3.

Tacchella et al. (2023) studies the stellar populations of three of our targets, the ones at highest redshifts $z = 7.663$, $z = 7.665$ and $z = 8.498$ (IDs 10612, 6355 and 4590, respectively). They use PROSPECTOR with a flexible non-parametric SFH prescription instead to model the SEDs. They find that the highest redshift galaxy (ID4590) is undergoing a recent burst, inferring a young stellar age under 10 Myr, like we obtain in our integrated analysis. They cannot rule out older stellar ages in their analysis. In our spatially resolved maps (see the age map in Fig. 41), we find that most pixels have a mass weighted age above $\sim$ 100 Myr, except the centrally located young burst, which dominates the integrated light. The particularly striking case is the $z = 7.665$ galaxy (ID6355). Tacchella et al. (2023) also infer an extremely young age of 3^{+29}_{-1} Myr, and they rule out the presence of older stellar populations, since the extreme [O III]+Hβ lines dominate the emission. In this work we find a shell of older stars, confirmed by the empirical colour gradients as well as the other tests discussed in §3.4.4 and §3.5. Finally, for the target ID10612 at $z = 7.663$, they argue that its SFH together with its morphology, could indicate that this source is undergoing a merger. This is consistent with what we find, both in terms of the empirical colour gradients, as well as the clumpiness of the blue F150W and F200W bands. Moreover, we find two distinct populations within the galaxy in the spatially resolved maps (see Figure 39). Consistent with our results here, they find that inferring older stellar ages (in their case by adding emission line constraints with NIRSpec spectra) leads to larger stellar masses of up to 1 dex for the galaxy ID4590 at $z = 8.495$, which is exactly what we find in our integrated versus spatially resolved comparison.

Our work confirms the issue discussed in Topping et al. (2022); Tacchella et al. (2023) and Whitler et al. (2023), where young stars outshine and dominate the emission when compared to older stars, the presence of which is difficult to rule out via integrated measurements. This leads to inferring lower stellar masses. In Tacchella et al. (2023) they conclude that the SFH prior is of vital importance, and they only infer stellar ages older than 10 Myr in their fits when using a non-parametric SFH model with a continuous prior and older populations present. This leads to an increase in the stellar masses of up to 0.6 dex. Whitler et al. (2023) also use various SFH models to explore the potential presence of old stellar populations in seemingly young galaxies. They find stellar masses larger by up to an order of magnitude with non-parametric SFH versus constant SFH models. The impact of the SFH model in the inferred stellar mass has been studied by other works (see e.g., Leja et al. 2019; Suess et al. 2022), with similar results.

Outshining and its effects on stellar mass estimates have been studied at lower redshifts (see e.g., Maraston et al. 2010; Pforr et al. 2012). Our results agree with previous works such as Sorba & Sawicki (2018), where they find a discrepancy in the inferred stellar masses of up to a factor of ~ 5, when having resolved SED fitting, albeit their study only reaches $z = 2.5$. Moreover, they propose that unresolved studies should apply corrections to their mass estimates. This resolves the mass missing problem, in which a tension is found between the observed stellar mass density of the Universe and the star formation rate density (see e.g., Leja et al. 2015). By correcting stellar mass functions with resolved estimates, they find that these agree better with the observed star formation densities collected by Madau & Dickinson (2014). Leja et al. (2020) also solve this discrepancy by using flexible non-parametric SFH priors, which produce older ages, thus inferring $\sim 50\%$ higher stellar mass density.

Endsley et al. (2023) study a population of UV-faint galaxies at a similar redshift range $z \sim 6.5-8$, also finding that the SEDs are dominated by young stellar populations, exhibiting low masses. They find the majority of their objects to appear very blue ($\beta \sim -2$), with some dusty galaxies ($\beta \sim -1$). With our integrated analysis, we find three galaxies with $\beta \sim -2$, and two targets with a value closer to -1. In the spatially resolved maps, we find values $-2 < \beta < -1$, with some very dusty regions reaching values around $\beta \sim -0.5$.

At this redshift range, the majority of targets with high EW([O III]+Hβ) have an inferred young stellar age when considering a constant SFH, just as we find in our integrated analysis (see Fig. 9 in Endsley et al. 2023). On the other hand, there are works that find evolved stellar populations (>100 Myr) at even higher redshifts, such as Furtak et al. (2023) with $z \sim 10-16$ candidates in the SMACS0723 field, and Leethochawalit et al. (2023) with $7 < z < 9$ photometrically-selected galaxies in the GLASS-JWST ERS program, which infer a median mass-weighted age of 140 Myr.

From a resolved point of view, in a sample of $z \sim 6-8$ galaxies in the Extended Groth Strip (EGS) field, Chen et al. (2023) find multiple clumps dominated by young stellar populations, as well as significant variations in the equivalent width of the [O III]+Hβ lines. They find EWs with extreme values such as the ones we find for most of our targets (of the order $\sim 300-3000$ Å), which also yield young ages in their fits (as also found by Vanzella et al. 2023 in the Sunrise arc at $z \sim 6$), confirming once more what we are finding for these high redshift targets. Moreover, Pérez-González et al. (2023) also find strong [O III]+Hβ emission in a spatially resolved analysis using *HST* and *JWST* data from the CEERS survey in the EGS. They also link these findings with very young starburst with possibly an underlying older stellar population.

In summary, our results are consistent with the works that have been published so far studying these same galaxies, or targets at a similar redshift range with *JWST*. By integrating our maps, we can produce similar results and draw equivalent conclusions to the integrated works performed so far in these sources. By producing a spatially resolved analysis, we can demonstrate the presence of underlying older stellar populations that are otherwise outshined in the integrated analyses, inferring larger stellar masses and considerably affecting our picture of the nature of these high redshift galaxies.

3.4.4 *Caveats*

As briefly mentioned before, one could argue that the “shells" of older stellar populations where the young stars with high EWs are embedded, could be instead a result of the dust-age degeneracy present in SED fitting softwares. To test if the gradient in age is real, we perform a test in which we fix the extinction to the value given by Tacchella et al. (2023). We find a similar gradient, where there is a shell of older stellar populations surrounding the bursty young star forming region. The effects of dust and age are now blended into the age map, since we fix the A_V, but the gradient persists. On top of that, the individual fits that we obtain fixing the dust obscuration are very poor, compared to leaving A_V as a free parameter in the BAGPIPES fit. This gives us confidence that our fits with A_V as a free parameter sample better the galaxy properties, and the gradient observed is real. In Appendix 3.5, we discuss in more details the age uncertainties, focusing on the target ID6355 at $z = 7.665$.

Another caveat that our spatially resolved analysis could have is whether the process of PSF-matching affects our inferred maps. One could argue that the mass weighted age map could result as an artifact of the PSF-matching procedure, where flux is re-distributed radially to match the resolution of the F444W band. We only observe this radial distribution on the age and EW maps. We observe non-radial flat gradients across the galaxies on all the rest of physical properties, as well as the empirical colours. These gradients extend across spatial scales

larger than the FWHM of the F444W PSF. We therefore conclude that this is not an effect of PSF-matching, but a true young stellar population clump centrally located in most galaxies.

Finally, besides the S/N threshold that we impose in the noisiest bands, one could still doubt whether there is enough S/N per pixel to be able to infer robust physical parameters. To test this, we apply a Voronoi tesselation binning method on the targets, in order to achieve bins with a constant minimum S/N across the image and filters. Imposing a minimum S/N of 5 or even up to 10 in all bands, we find the same gradients and trends that we observe in the maps of the various inferred physical parameters in all galaxies. This, combined with the fact that our fits display good reduced χ^2 values, gives us confidence that the S/N in each native pixel is sufficient to provide trustworthy estimates.

3.5 SUMMARY AND CONCLUSIONS

We present the first spatially resolved analysis of spectroscopically confirmed $5 < z < 9$ galaxies in the SMACS0723 ERO field. We use images in 6 bands obtained with NIRCam onboard *JWST*, spanning the wavelength range $0.8-5\mu$m. With the SED fitting software BAGPIPES, we model the spectral energy distributions on a pixel-by-pixel basis, being able to infer the physical parameters on a $180-240$ parsec scale. Our main findings and conclusions are the following:

- All galaxies are resolved and display strong empirical colour gradients. Even at these early times, these galaxies display multiple star forming clumps.
- We find regions that exhibit high EW of the [O III]+Hβ emission (up to $\sim 3000-4000$ Å). These extreme starbursts are embedded within regions with less specific star formation, which points to very bursty star formation happening on small scales (< 1 kpc), not galaxy-wide.
- The strong line emission regions dominate the integrated light, biasing the fits towards very young inferred ages of the stellar population (< 10 Myr). Only a resolved analysis demonstrates the presence of older stellar populations, which can be seen in the spatial maps.
- Resolving the stellar populations on a pixel-by-pixel basis leads to inferring from 0.5 up to ~ 1 dex larger stellar masses, when compared to an integrated analysis. Our analysis extends previous findings on the problem of outshining and its effects on stellar mass estimates, which so far has only been studied at lower redshifts (up to $z \sim 3$).

Current and upcoming observations with *JWST* will allow us to characterise the early Universe and first galaxies in a new and more complete way. The combination of having confirmed redshifts with NIRSpec, and the unprecedented

resolution and depth of NIRCam imaging, will transform how we study galaxies, changing our current views on their internal structure and mass assembly, amongst others. The systematics in stellar mass estimates found in this work would have strong implications in the shape and evolution of the stellar mass function at high redshift, particularly while samples are limited to small numbers of the brightest candidates. Furthermore, the process of galaxy formation could be more extended and earlier than previously thought, as is implied by the presence of evolved older stellar populations being outshone by the youngest stars. Only with a spatially resolved analysis, we can begin to untangle the complexity of the internal structure of galaxies at this epoch.

ACKNOWLEDGMENTS

The authors thank the anonymous referee for the helpful comments received. The Cosmic Dawn Center is funded by the Danish National Research Foundation (DNRF) under grant DNRF140. This work is based on observations made with the NASA/ESA/CSA *James Webb Space Telescope*. The data were obtained from the Mikulski Archive for Space Telescopes at the Space Telescope Science Institute, which is operated by the Association of Universities for Research in Astronomy, Inc., under NASA contract NAS 5-03127 for *JWST*. These observations are associated with program ID 2736, as part of the Early Release Observations. The specific observations analyzed can be accessed via DOI: 10.17909/kjms-sq75. P.O. is supported by the Swiss National Science Foundation through project grant 200020_207349. This work received funding from the Swiss State Secretariat for Education, Research and Innovation (SERI). C.A.M. acknowledges support by the VILLUM FONDEN under grant 37459. S.F. acknowledges the support from NASA through the NASA Hubble Fellowship grant HST-HF2-51505.001-A awarded by the Space Telescope Science Institute, which is operated by the Association of Universities for Research in Astronomy, Incorporated, under NASA contract NAS5-26555. Cloud-based data processing and file storage for this work is provided by the AWS Cloud Credits for Research program.

Facilities: JWST (NIRCam)

Software: Astropy (Astropy Collaboration et al. 2013, 2022), Matplotlib (Hunter 2007), NumPy (Harris et al. 2020), SciPy (Virtanen et al. 2020), `grizli` (Brammer 2019; Brammer & Matharu 2021; Brammer et al. 2022)

APPENDIX

3A. AGE UNCERTAINTY

As discussed in §3.4.4, the degeneracy between age and dust could yield uncertain estimates. This could be particularly concerning for the source ID6355 at $z = 7.665$, and one could argue that the shell that we see on the age map is not real. This would mean that there is no underlying older stellar population being outshined by the young stellar population that dominates the emission for this galaxy. Figure 46 displays the 16th, 50th and 84th percentiles of the mass weighted age, obtained with the posterior distribution that BAGPIPES infers for each individual pixel. In the 50th percentile, which is the one we choose to display for every inferred physical property in Figures 37–41, we see a shell of older stellar ages, as discussed in §3.4.1. With the 16th percentile image, we see that even if we assume the maximum lower uncertainty, the shell of old stars would still display ages above 10 Myr. That is still older than what is inferred by other works on this target, as well as in our integrated analysis, where we infer an age of $1.3^{+3.6}_{-0.2}$ Myr. With the 84th percentile image, we see that these old stars could be up to hundreds of Myr old. Therefore, even within the uncertainty range, we can confidently say that there are older stellar components present in this galaxy, opposite to what is concluded by Tacchella et al. (2023) and Carnall et al. (2023). This is only visible with a careful spatially resolved analysis. On the other hand, the very extended region where the EW is extremely high, can only be fit by young stellar templates. Considering the uncertainties, we still only obtain young stellar populations in that region.

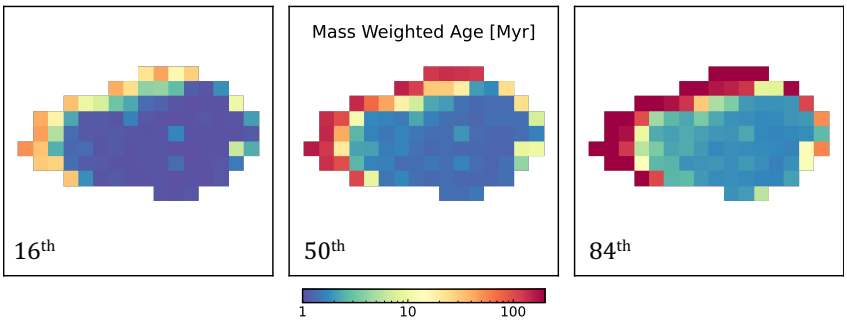

Figure 46: Mass weighted age 16th, 50th and 84th percentiles of the posterior distribution inferred with BAGPIPES on the galaxy ID6355 at $z = 7.665$.

3B. INTEGRATED PROPERTIES

Table 5 shows the resulting physical parameters inferred with BAGPIPES on the integrated fit for each galaxy. As a reminder, we expect these values to be lower

than the ones inferred by other works, since we only consider the pixels here that fulfil a certain S/N criteria, instead of performing aperture photometry, which would yield larger fluxes and different physical estimates. The integrated run is performed like this to be able to do a one-to-one comparison with the spatially resolved analysis, as discussed in §3.4.2.

Integrated Properties	ID8140 $z = 5.275$	ID5144 $z = 6.383$	ID10612 $z = 7.663$	ID6355 $z = 7.665$	ID4590 $z = 8.498$
$\log(\mu M_*/M_\odot)$	$9.14^{+0.03}_{-0.02}$	$7.98^{+0.27}_{-0.11}$	$8.07^{+0.13}_{-0.08}$	$8.84^{+0.08}_{-0.06}$	$8.04^{+0.11}_{-0.06}$
SFR $[\mu M_\odot/\mathrm{yr}]$	$16.0^{+1.3}_{-0.7}$	$1.0^{+0.5}_{-0.2}$	$1.2^{+0.3}_{-0.2}$	$6.9^{+1.3}_{-0.8}$	$1.1^{+0.3}_{-0.2}$
A_V [mag]	$1.16^{+0.02}_{-0.02}$	$0.58^{+0.18}_{-0.12}$	$0.45^{+0.11}_{-0.09}$	$1.01^{+0.07}_{-0.06}$	$0.48^{+0.12}_{-0.08}$
Age [Myr]	$14.9^{+1.7}_{-1.0}$	$2.5^{+1.1}_{-1.3}$	$1.6^{+0.7}_{-0.5}$	$1.3^{+3.6}_{-0.2}$	$1.9^{+0.4}_{-0.5}$
EW([O III]+Hβ) [Å]	729 ± 44	1996 ± 386	3048 ± 329	3884 ± 252	2565 ± 254
UV slope β	-1.20 ± 0.03	-1.88 ± 0.11	-2.08 ± 0.09	-1.40 ± 0.05	-2.03 ± 0.09

Table 5: Resulting physical properties inferred with BAGPIPES for the integrated measurements of the five galaxies.

3C. INDIVIDUAL FITS

Here we present the corner plots obtained with BAGPIPES on the fits for the individual pixels A, B and C (Figures 47 to 49, respectively) of the galaxy ID6355 at $z = 7.665$. The pixels are shown in the maps of Figure 40, and the best fit SEDs and physical properties are displayed on Figure 42. As we would expect, the fits for B and C are better constrained than for A, since the latter is the most outer pixel in the galaxy, thus with lowest S/N, albeit fulfilling our criteria. For this pixel, the distributions of age, $\log(U)$ and metallicity are broad, but we can still constrain the stellar mass even at low S/N.

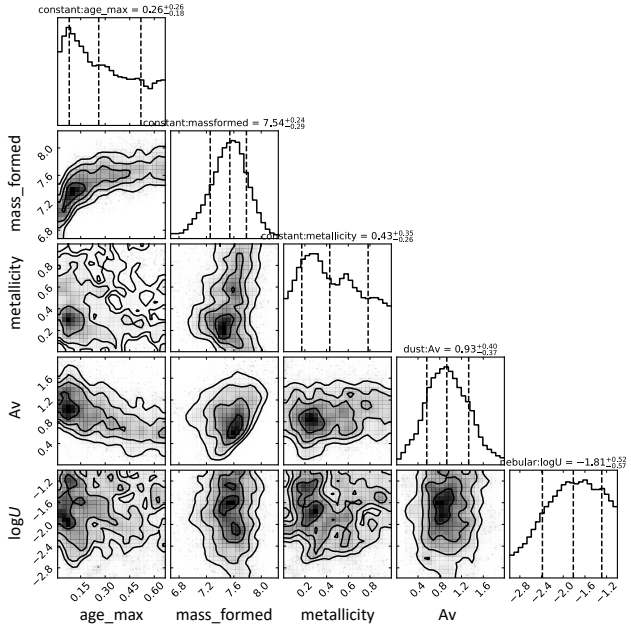

Figure 47: Corner plot of the BAGPIPES fit on pixel A of the galaxy ID6355 at $z = 7.665$.

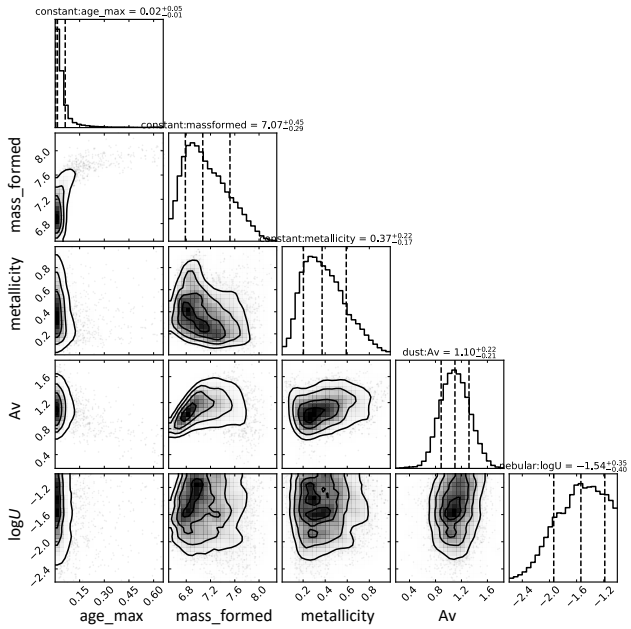

Figure 48: Corner plot of the BAGPIPES fit on pixel B of the galaxy ID6355 at $z = 7.665$.

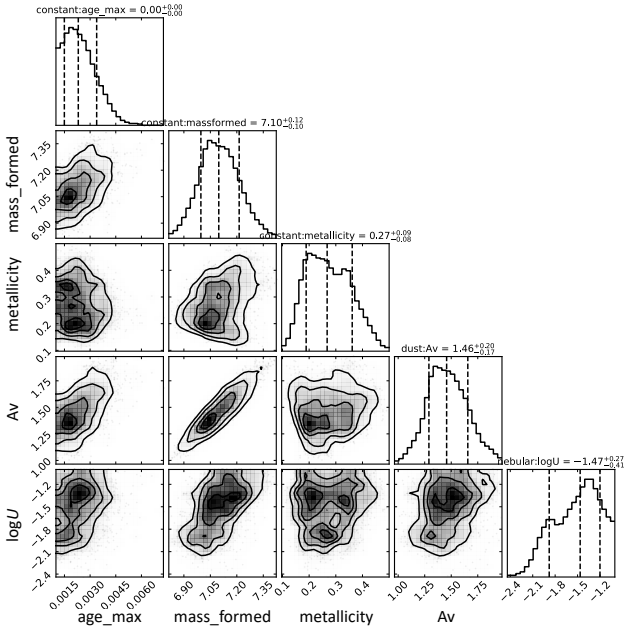

Figure 49: Corner plot of the BAGPIPES fit on pixel C of the galaxy ID6355 at $z = 7.665$.

4

A BEACON INTO THE END OF REIONISATION

This chapter contains the following prepared manuscript:
"Outshining in the Spatially Resolved Analysis of a Strongly Lensed Galaxy at $z = 6.072$ with *JWST* NIRCam"

To be submitted to Astronomy & Astrophysics

Authors: Clara Giménez-Arteaga, Seiji Fujimoto, Francesco Valentino, Gabriel B. Brammer, et al.

ABSTRACT

We present *JWST*/NIRCam observations of a strongly-lensed, multiply-imaged galaxy at $z = 6.072$. The galaxy has rich *HST*, *MUSE* and *ALMA* ancillary observations across a broad wavelength range. We perform a spatially-resolved analysis of the physical properties at scales of ~ 200 pc, where $\mu \gtrsim 20$ across the galaxy, inferred from SED modeling of 5 *JWST*/NIRCam imaging bands covering $0.16\ \mu\text{m} < \lambda_{\text{rest}} < 0.63\ \mu\text{m}$ on a pixel-by-pixel basis. We find centrally-located clumps of young stars surrounded by older stellar populations. By comparing [N II] and [O III]+Hβ maps inferred from the image analysis with our NIRSpec IFU data, we find that the spatial distribution and strength of the line maps are in agreement with the IFU measurements. We explore different star formation history parameterisations with the BAGPIPES software on the spatially-integrated photometry, finding that a double power-law star formation history retrieves the closest value to the spatially-resolved stellar mass estimate, and other SFH forms suffer from outshining thus underestimating the stellar mass (up to ∼0.5 dex). Additionally, the ionizing photon production efficiency is overestimated in a spatially-integrated approach by ∼0.4 dex, when compared to a spatially-resolved analysis. The IFU agreement implies that our pixel-by-pixel results derived from the broadband images are robust, and that the mass discrepancies we find with spatially-integrated estimates are not just an effect of SED-fitting degeneracies or lack of NIRCam coverage. Additionally, this agreement points towards the pixel-by-pixel approach as a way to mitigate the general degeneracy between the flux excess from emission lines and underlying continuum, especially when lacking medium-band coverage or IFU observations. This study stresses the importance of studying galaxies as the complex systems that they are, resolving their stellar populations when possible, or using more flexible SFH parameterisations. This can aid our understanding of the early stages of galaxy evolution by addressing the challenge of inferring robust stellar masses of high redshift galaxies.

4.1 INTRODUCTION

Currently, one of the most critical problems in the study of high-redshift galaxies is the challenge of inferring robust stellar masses. Recent works using the first data obtained with *JWST* have found surprisingly large stellar masses, which may be in conflict with the early growth of structure within the ΛCDM cosmological model (Labbé et al. 2023; Xiao et al. 2023). Various studies have found that varying the star formation history (SFH) parameterisation, or other assumptions such as the initial mass function (IMF), can have a significant impact in the inferred physical properties, potentially solving this conflict (see e.g., Suess et al. 2022; Whitler et al. 2023; Tacchella et al. 2023; Pacifici et al. 2023).

The superb spatial resolution and sensitivity of the Near-Infrared Camera (NIRCam; Rieke et al. 2005, 2023) onboard *JWST*, allows us to extend spatially resolved studies to new redshift ranges. A concerning outcome of this might be that our stellar mass estimates are surprisingly underestimated, making the conflict with theoretical models even worse. This has so far only been addressed at lower redshifts ($z < 2.5$), such as the work by Sorba & Sawicki (2018) on a statistically significant sample, finding that resolved stellar masses can be up to five times larger than unresolved estimates. This effect has also been observed at high redshift ($5 < z < 9$), albeit on a limited sample of five galaxies in the SMACS0723 ERO field (Giménez-Arteaga et al. 2023).

When resolving extended galaxies and studying their stellar populations on a pixel-by-pixel basis, one can partially disentangle the problem of outshining (Sawicki & Yee 1998; Papovich et al. 2001), where young stellar populations completely dominate the integrated light, hiding underlying older stellar populations, thus leading to an underestimation of the total mass of the stellar population. This has also been found in simulations (see e.g., Narayanan et al. 2023a). On the other hand, using only photometric observations is not enough to unequivocally determine accurately the "true" mass of a galaxy, as well as the many other challenges within stellar population synthesis modeling (see e.g., Conroy et al. 2009, 2010; Pforr et al. 2012; Conroy 2013; Maraston et al. 2013). One of the advantages of *JWST* is that we can also obtain spatially-resolved *spectra* of galaxies at $z > 6$ with the NIRSpec Integral Field Unit (IFU), providing spatial maps of emission lines and overall spectral properties. For our purposes, the IFU spectra can provide a crucial check on spatially-resolved characteristics derived from modeling the images alone.

In this paper, we present the NIRCam observations of a strongly-magnified galaxy at $z = 6.072$ (Fujimoto et al. 2021b; Laporte et al. 2021), observed also with NIRSpec IFU. The synergy of both instruments can allow us to perform a spatially-resolved analysis of the physical properties, as well as studying the effect on the stellar mass estimates. With the IFU data, we can disentangle the excess in the reddest photometric bands, which can be caused either by very strong emission lines from H II regions associated with young, recently-formed stars, or by continuum emission by older stellar populations (see e.g., Labbé et al. 2013; Stark et al. 2013; Smit et al. 2015, 2016; Clarke et al. 2021; Strait et al. 2021; Marsan et al. 2022).

This paper is structured as follows. In Section 4.2 we present the *JWST* NIRCam observations. Section 4.3 describes the methodology employed for the pixel-by-pixel SED modeling. In Section 4.4 we compare and discuss the results inferred from the images to "truth" provided by the IFU line maps. Finally, we summarise our work and present the conclusions in Section 4.5. Throughout this work, we assume a simplified ΛCDM cosmology with $H_0 = 70$ km s^{-1} Mpc^{-1}, $\Omega_m = 0.3$ and $\Omega_\Lambda = 0.7$.

4.2 DATA

In this work, we study a galaxy at $z = 6.072$ behind the massive $z = 0.43$ galaxy cluster RXCJ0600−2007, included in the Reionization Lensing Cluster Survey (RELICS; Coe et al. 2019). We refer the reader to Fujimoto et al. (2021b) for more information on the previous multi-wavelength observations for this target, including the rest-frame UV HST images from RELICS and far-infrared emission line and continuum measurements from the ALMA Lensing Cluster Survey (ALCS; PI: K. Kohno, Program ID: 2018.1.00035.L). In this work, we present and analyse *JWST*/NIRCam photometric observations targeting this galaxy (GO-1567, PI: S. Fujimoto) obtained in January 2023, centered at (R.A., Decl.)=(06:00:05.663, −20:08:20.86). The exposure time varies between bands, with 2491 s for F356W and F444W, 1890 s for F115W and F277W, and a deep integration of 4982 s in F150W. The photometric data has been reduced with the `grizli` software pipeline (Brammer 2019; Brammer & Matharu 2021; Brammer et al. 2022), following the procedures outlined by Valentino et al. (2023) and the DAWN JWST Archive (DJA). Further description of the NIRCam, NIRSpec IFU data and more recent ALMA observations will be provided by S. Fujimoto et al. (in prep.) and F. Valentino et al. (submitted).

We correct the reduced mosaics for Milky Way extinction assuming the curve by Fitzpatrick & Massa (2007) and $E(B-V) = 0.0436$ (Schlafly & Finkbeiner 2011). We then PSF-match all images to the F444W band using model PSFs computed with the `WebbPSF` software (Perrin et al. 2012, 2014) and a convolution kernel to match each of the PSFs to that of F444W PSF with the `pypher` software (Boucaud et al. 2016). Finally, we resize the PSF-matched images to a common pixel scale of 40 mas pixel^{-1}, which corresponds to a physical scale of ∼0.2 kpc pixel^{-1} at $z = 6.072$.

The strongly-magnified galaxy ($\mu \sim 20-160$) has five multiple images (see Fujimoto et al. 2021b, and S. Fujimoto et al. in prep.). In this work we focus on the image RXCJ0600-z6-3 ($z6.3$ in the nomenclature from Fujimoto et al. 2021b), located at (R.A., Decl.)=(06:00:09.55, −20:08:11.26). That image is resolved in all bands and does not show evidence of strong shears and differential magnification across the face of the source, with a magnification of $\mu = 29^{+4}_{-7}$. In contrast, the strongly-lensed arc $z6.1/z6.2$ is crossing the critical curve, resulting in significant variation in the very high magnification regime ($\mu \gtrsim 100$) across the arc. This requires a careful magnification correction to achieve the comparison between the spatially-resolved and integrated estimates, and thus we focus on $z6.3$ in this paper. The results obtained from the arc will be presented in Fujimoto et al. (in prep.) with the updated lens model. Moreover, RXCJ0600-z6-3 traces the entire galaxy, whereas the lensing of $z6.1/z6.2$ amplifies the emission from a peripheral region of the galaxy (Fujimoto et al. 2021b). Figure 50 shows the NIRCam observations on RXCJ0600-z6-3, for the five available broad bands

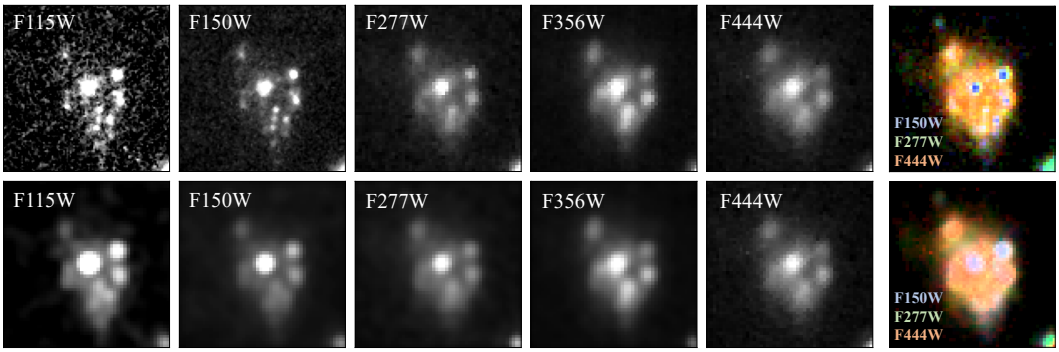

Figure 50: Cutouts of the RXCJ0600-z6-3 image in all available NIRCam bands. The cutouts are 2 arcsec on a side side and centered at $(\alpha, \delta) = (06{:}00{:}09.55, -20{:}08{:}11.26)$. The top row displays the observed images in their native resolution; the bottom row shows all images convolved with a kernel to match the F444W PSF. The right RGB three-colour images are constructed from the F150W (B), F277W (G) and F444W (R) bands with the scaling following the prescription from Lupton et al. (2004).

F115W, F150W, F277W, F356W, and F444W, which sample roughly $\lambda_{rest} = 0.16$, 0.21, 0.39, 0.50, and 0.63 μm, respectively. As can be seen in Figure 50, RXCJ0600-z6-3 has a moderate shear with the magnification variation within $\leq 30\%$ across the galaxy, making it an optimal target for this study.

Throughout this work, no lensing correction is applied on any images nor derived quantities. We focus mostly on the relative differences of the inferred properties when studying them in a resolved or an integrated approach, rather than obtaining the intrinsic values for, e.g., the stellar masses or star formation rates. Therefore, all quantities are reported in terms of the magnification factor μ.

4.3 METHODOLOGY

4.3.1 BAGPIPES *SED Fitting*

To analyse the spatially resolved physical properties of RXCJ0600-z6-3, we perform spectral energy distribution (SED) fitting on a pixel-by-pixel basis. We follow the same methodology as in Giménez-Arteaga et al. (2023) (GA23, hereafter). We use the SED modeling code BAGPIPES (Carnall et al. 2018). We fix the redshift to the spectroscopic $z_{[\mathrm{C\,II}]} = 6.072$, in order to reduce the number of free parameters in the modelling, given the limited band coverage, and break the degeneracy between redshift, age and dust. Following GA23, we use a Calzetti et al. (2000) attenuation curve, and extend the nebular grid so that the ionisation parameter (U) can vary between $-3 < \log_{10} U < -1$. The nebular emission is included with CLOUDY (Ferland et al. 2017), and the SPS models are generated by Bruzual & Charlot (2003). We assume a Kroupa (2001) initial mass function (IMF),

and set the lifetime of birth clouds to t_bc = 10 Myr. We set uniform priors for the visual extinction $A_V \in [0,3]$, and the mass of formed stars $\log_{10} M_*/M_\odot \in [5,11]$. Given the advent of having IFU spectra, we use the mean metallicity measured in the cube as a prior for our SED modeling. We thus set a Gaussian prior on the metallicity centered at 0.1 $Z_\odot$, with $\sigma = 0.2\ Z_\odot$.

Throughout this work, we discuss different parameterisations of the star formation history (SFH), testing parametric SFH forms implemented in BAGPIPES. Table 8 in the Appendix 4.6 provides the parametric shapes used, as well as the specific priors that we impose with each model.

4.3.2 *Segmentation and Pixel Selection*

To perform the pixel-by-pixel SED fitting, we first need to select the pixels will be modeled. We first use the Agglomerative Clustering package within `sklearn.cluster`, in order to isolate RXCJ0600-z6-3 and exclude nearby sources. Then, with the selected pixels associated to our desired source, we compute the S/N in all bands and apply a threshold requiring S/N > 1 in all bands. After that, we generate masks on each band with a threshold that corresponds to the mean S/N on each band. Finally, we combine (i.e., sum) these masks, so that the most extended band will dominate the segmentation, and ignore pixels outside the final combined mask. We obtain an image of RXCJ0600-z6-3 with 625 pixels that fulfil the S/N criteria, to provide a trustworthy modeling. In the results section §4.4, only these pixels are plotted in the various maps presented.

For single integrated measurements to compare to the pixel-by-pixel analysis, we sum the fluxes (and variances) in each band within the same total mask and then model the integrated photometry using the same setup as for the resolved case, explained in §4.3.1.

4.4 RESULTS AND DISCUSSION

In this section we present the results of the various analyses we perform with the NIRCam observations on the RXCJ0600-z6-3 image. We also discuss the implications of our study, from an integrated and spatially resolved perspectives. We reiterate that here we focus on the implications of inferring these properties in an unresolved versus resolved approach and do not attempt to discuss intrinsic properties affected by the lensing. A comparison with NIRSpec IFU data is presented, to test whether photometric observations can reproduce spectroscopic measurements.

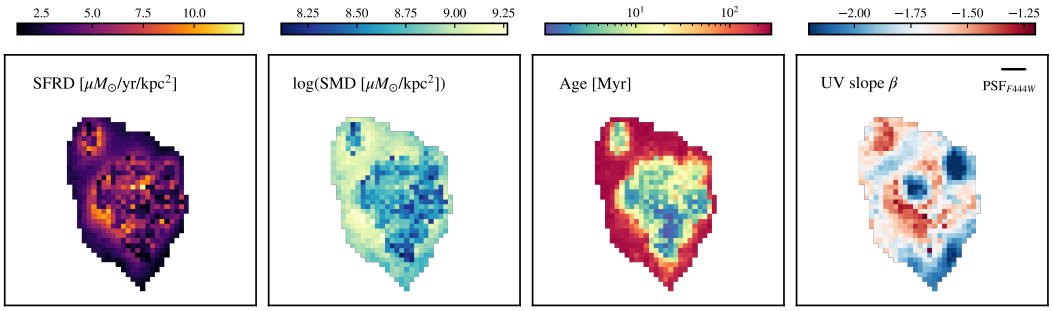

Figure 51: Resulting physical properties for RXCJ0600-z6-3 inferred with BAGPIPES using a constant SFH parameterisation. The maps are 2 arcsec per side and centered at (α, δ)=(06:00:09.55, −20:08:11.26). From left to right, we display the star formation rate density, the stellar mass density, the inferred mass-weighted age of the stellar population, and the UV slope (β). The size of the F444W PSF is also indicated on the top right.

4.4.1 *Spatially Resolved Analysis*

Following the methodology described in §4.3, we perform pixel-by-pixel SED fitting on RXCJ0600-z6-3. This allows us to build maps of the inferred physical properties. As described in §4.3.2, we only fit and display pixels that fulfil the imposed S/N criteria.

Figure 51 shows the resulting maps inferred with BAGPIPES given a constant star formation history (CSFH). This parameterisation is often used to model high-redshift galaxies (e.g., Heintz et al. 2023a; Carnall et al. 2023). Even though a constant SFH is a simplistic parameterisation of the star formation in a galaxy, one could expect it could be a reasonable approximation on a pixel-by-pixel basis, that would generally average over a smaller projected mix of non-coeval stellar populations.

We obtain an equivalent scenario to the one found and discussed in GA23 for five galaxies at $5 < z < 9$ in the SMACS0723 field. We find a centrally located clump of young stars, surrounded by a shell of older stellar populations. The central population has extremely young ages of <10 Myr, which yields lower stellar masses, therefore we see that most mass resides in the outer shell of older stars when considering a constant star formation history. We see that the central population is resolved, since it is larger than the size of the F444W PSF (FWHM∼0.″16), indicated on the top right corner of the UV slope map. In the UV slope map we find two very blue clumps, which match the F115W maps, surrounded by redder slopes. In the central region, given that the age of the stellar population is relatively constant, this indicates a varying presence of dust reddening the photometry, surrounding the unobscured blue central clump. The star formation rate density, which is averaged over the last ∼ 100 Myr, is relatively constant across the galaxy, displaying the highest activity in the most massive regions.

In summary, the RXCJ0600-z6-3 galaxy contains a centrally-concentrated clump of very young stars (< 10 Myr) embedded within a shell of somewhat older stars (> 100 Myr).

4.4.2 *The Integrated Field Spectrum from NIRSpec*

The photometry of RXCJ0600-z6-3 results in degenerate but distinct explanations of the rest-frame optical colors, e.g., from young stars and high equivalent-width [O III]+Hβ and Hα+[N II] emission lines from their associated H II regions, or an underlying red continuum arising with somewhat older stars[1]. With *JWST*/NIRSpec we can now directly observe the spatially-resolved spectrum itself with the IFU, and test our previously presented photometric-only estimates.

Strength of the Integrated Light

From the NIRSpec IFU cube, we can directly measure the strength and spatial distribution of the emission lines Hα(λ6564), [N II] (λ6585), Hβ (λ4861) and the [O III] ($\lambda\lambda$4959, 5007) doublet. We refer the reader to S. Fujimoto et al. (in prep.) for all reduction, results and measurements extracted from the IFU data, both in pixel-by-pixel maps and in integrated (summed over all pixels) estimates of the equivalent width (EW) and the line fluxes.

Given the previous analysis, we can now test whether our resolved estimates are consistent with the IFU spectrum. We start by summing the BAGPIPES models for all pixels, and we calculate the EW. We consider the sum of the emission line groups [O III]+Hβ and Hα+[N II] as they are spectrally unresolved by the broad-band imaging filters. It is important to note that the relative strengths of the lines within each group depends on the metallicity, the ionisation parameter, amongst others, that are perhaps not fully constrained when modeling the images alone. The line fluxes and equivalent widths are listed in Table 6. The observed line flux and EW are also measured integrating the IFU cubes within a spatial aperture radius of 0.″7 (S. Fujimoto et al. in prep.), and the resulting values are shown on the right column of Table 6.

We find that the NIRSpec IFU equivalent widths are quite large, of $\gtrsim$700 Å for [O III]+Hβ and Hα+[N II]. This is consistent with what has been found in many rest-UV-selected galaxies which display strong nebular lines (EW$_{\text{[O III]+H}\beta} \gtrsim$ 600 Å) (e.g., Labbé et al. 2013; Smit et al. 2014; De Barros et al. 2019; Stefanon et al. 2022), a population that seems to rise significantly into reionization (Whitler et al. 2023), becoming typical at $z \sim 6$ (Matthee et al. 2023). With the CSFH, we retrieve a consistent value for EW(Hα+[N II]), within the uncertainties. The NIRCam estimate for EW([O III]+Hβ) is larger than the IFU measurement, although still

[1] At $z = 6.072$ the groups of [O III]+Hβ and Hα+[N II] emission lines fall within the NIRCam F356W and F444W bandpasses, respectively.

	NIRCam	NIRSpec/IFU
EW([O III]+Hβ) [Å]	940 ± 20	711 ± 66
EW(Hα+[N II]) [Å]	596 ± 32	732 ± 125
$f_{[\mathrm{O\,III}]+\mathrm{H}\beta}$ [cgs]	2.8 ± 0.3	3.15 ± 0.02
$f_{\mathrm{H}\alpha+[\mathrm{N\,II}]}$ [cgs]	1.1 ± 0.2	1.44 ± 0.02

Table 6: Values for the rest-frame equivalent widths and line fluxes (in cgs units of $\times 10^{-16}$ erg/s/cm^2) of [O III]+Hβ and Hα+[N II] inferred from the pixel-by-pixel modeling with BAGPIPES on the NIRCam images, and inferred from the NIRSpec IFU measurements (S. Fujimoto et al. in prep.).

in agreement within 2.5σ. Regarding the line fluxes, the photometric estimate is in good agreement with the strength of the line fluxes inferred from the NIRSpec IFU data, within the uncertainties.

Line Emission Spatial Distribution

Besides the integrated comparison, we can also perform a spatially-resolved analysis. While the IFU pixel scale (0.″1 pixel^{-1}) is somewhat lower than that of the NIRCam images (0.″04 pixel^{-1}), the IFU resolution is still sufficient for ∼300 resolution elements across the magnified face of RXCJ0600-z6-3.

In Figure 52 we show the spatially-resolved comparison between the NIRSpec IFU and NIRCam Hα+[N II] and [O III]+Hβ emission lines. The underlying maps correspond to the line fluxes inferred from the pixel-by-pixel SED modeling of the NIRCam data with a CSFH. The overplotted countours are of the moment 0 (intensity) measurements of the emission line groups from the IFU cubes. The NIRCam maps accurately reproduce the spatial distribution of the IFU measured lines, as well as their strength, as has also been tested from the spatially-integrated perspective. The IFU confirms the presence of strong nebular emission in the central region of RXCJ0600-z6-3.

With these quantitative and qualitative comparisons, we conclude that the pixel-by-pixel SED modeling with BAGPIPES using 5 photometric NIRCam bands reproduces the spatial distribution and strength of the Hα+[N II] and [O III]+Hβ emission lines inferred from the NIRSpec IFU observations. This gives confidence in our results, given that the IFU confirms the presence of strong line emission in the central region, where then the SED software chooses younger ages of the stellar population to model the excess in photometry. The outskirts present weaker emission lines, and that yields older stellar populations.

A spatially-resolved analysis with only broad-band photometry, can bypass the degeneracies that not having medium-bands or IFU observations introduces on single-aperture photometric fits, as well as providing a more complete picture

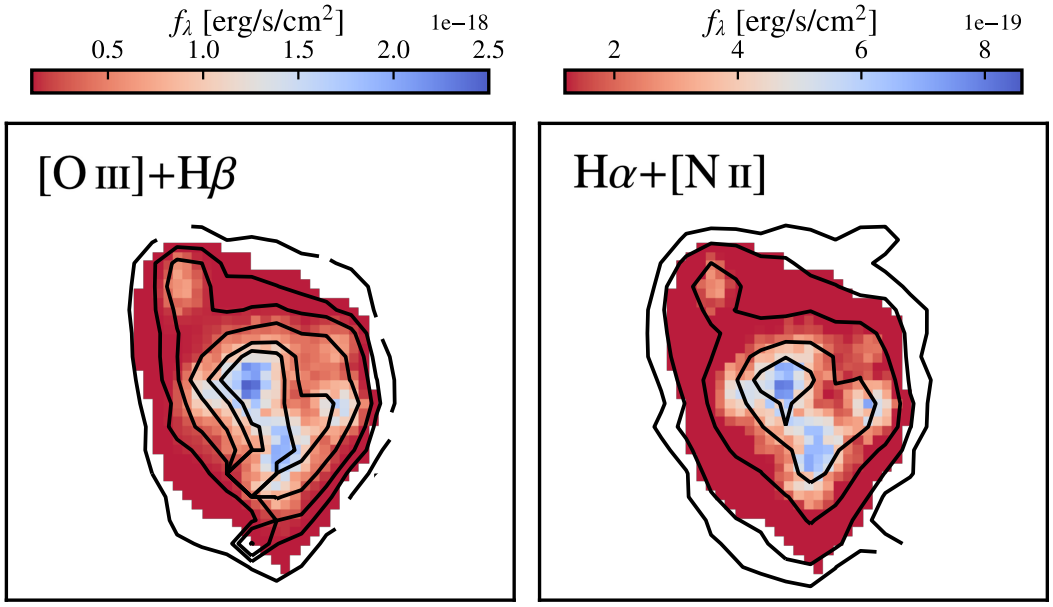

Figure 52: Maps of the emission line fluxes obtained from with the pixel-by-pixel SED fitting on the NIRCam images with a constant SFH. The contours correspond to the observed spectrum with the NIRSpec IFU (S. Fujimoto et al. in prep.). The maps are centered at (α, δ)=(06:00:09.55, −20:08:11.26) and 2 arcsec per side. **Left:** Map and contours for the [O III]+Hβ emission. The IFU contour levels are 0.3, 0.5, 1, 2, and 3 $\times 10^{-18}$ erg s^{-1} cm^{-2}. **Right:** Map and contours for the Hα+[N II] emission. The contour levels correspond to 1, 2, 3, 5, and 8 $\times 10^{-18}$ erg s^{-1} cm^{-2}.

of the internal structure and properties of galaxies. Having confidence in our spatially resolved estimates, we can now study and discuss their implications.

4.4.3 *The Spatial Resolution Effect on the Stellar Mass*

Analogous to GA23, we wish to test whether having spatially-resolved observations affects the inferred physical parameters of a particular galaxy. For this, as explained in §4.3.2, we add the pixel-by-pixel photometry in each band to create a spatially-integrated measurement with only the pixels that fulfil the above-mentioned S/N criteria, and be able to compare both scenarios one-to-one.

Earlier studies have found that stellar masses can be underestimated with spatially-integrated fits, given how a given model parameterization of the total light may not have sufficient flexibility to fully explain complex distributions of, e.g., dust attenuation and SFH within a single galaxy. Sorba & Sawicki (2015) use a mixture of underlying older stellar population and a more recent burst of star formation. Sorba & Sawicki (2018) use an exponentially declining SFH, finding a stellar mass discrepancy of factors up to 5. Using a constant SFH, GA23 found that the stellar mass can be underestimated ∼0.5–1 dex in an unresolved fit,

due to outshining from the young stellar populations (see also e.g., Narayanan et al. 2023a). Here we test if this is also the case for RXCJ0600-z6-3, or if we can reproduce the resolved CSFH with different SFH shapes in the integrated photometry.

We model the integrated photometry with BAGPIPES using the same setup as described in §4.3.1. We test additional parametric SFH forms available within BAGPIPES (see Appendix 4.6), and infer the integrated physical parameters. We choose a double-power law (DPL) SFH, which has been used to model high-redshift post-starburst galaxies (see e.g., Strait et al. 2023). We also test a log-normal SFH (Abramson et al. 2015, 2016), and an exponentially declining SFH (Sorba & Sawicki 2018).

Figure 53 shows the resulting SFH curves for the different models. The summed star formation histories of all individual pixels with CSFH (turquoise dashed-dotted curve and shaded region) shows that the total stellar population is built up over extended timescales. On the other hand, all integrated models except the double-power law (DPL) have a short, recent burst of star formation that dominates the light, but that has a lower total mass-to-light ratio. The DPL model gets closest to the summed CSFH, with older stellar populations dominating the star formation activity over long timescales.

The stellar masses derived with each spatially-integrated SFH form are reported in Table 7. The unresolved masses vary within $\log(M_*/M_\odot)$=9.7 and 10.4 by changing the SFH, i.e., a difference of 0.7 dex depending on the choice of SFH form, consistent with what has been found in previous studies regarding the effect of SFH choice on the stellar masses (see e.g., Whitler et al. 2023; Tacchella et al. 2023).

We define the difference between the logarithmic resolved CSFH and integrated stellar mass estimates as the "mass offset" or ΔM_r. If we add up the mass for all pixels in the resolved map presented in Figure 51, we obtain a resolved stellar mass of $\log(M_*/M_\odot)=10.2^{+0.2}_{-0.1}$. The mass offset between the CSFH resolved estimate and the additional SFH parameterisations on the integrated modeling are shown in Table 7. The parametric shape that provides the smallest mass offset is the double-power law SFH, differing ~ 0.2 dex from the constant SFH resolved case (a *larger* stellar mass than the resolved case). The largest ΔM_r is given by all the rest of SFH integrated runs, with a significant offset of 0.5 dex, so that the resolved mass is more than 3 times larger than the unresolved one. These models, as seen also in Figure 53, suggest very young burst of star formation, with ages of 5^{+9}_{-2}, 7^{+8}_{-4}, and 5^{+6}_{-2} Myr, for a constant, log-normal, and exponentially declining SFH, respectively. None of these parameterisations allows for any significant population of stars with ages greater than ∼50 Myr, that are apparent in the spatially-resolved analysis, yielding mass weighted ages of $\gtrsim 100$ Myr (Figure 51).

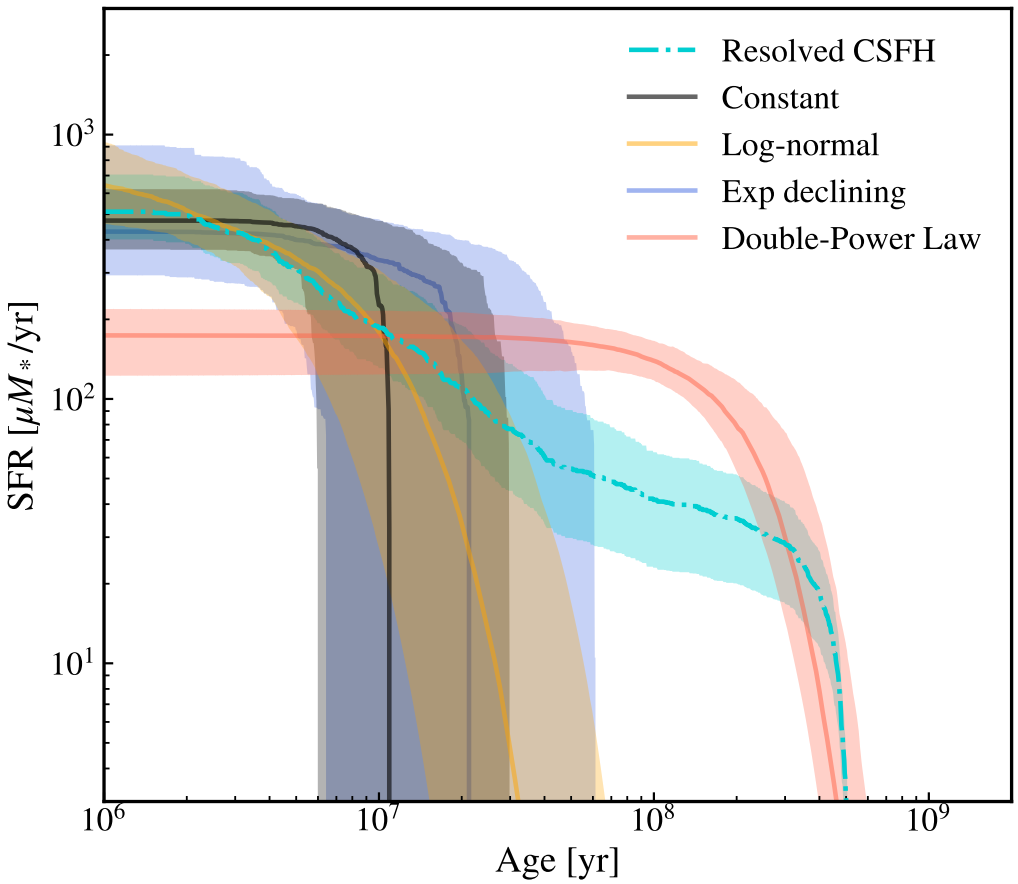

Figure 53: Star formation history of the resolved constant SFH analysis (turquoise dash-dotted curve), compared with the resulting SFH of the spatially-integrated fits obtained by varying the SFH form.

On Figure 54, we reproduce the comparison made by Sorba & Sawicki 2018 (SS18), plotting the mass offset as a function of the integrated specific star formation rate (sSFR). Points from SS18 are for galaxies at $z_{\rm spec} < 2.5$ in the Hubble eXtreme Deep Field (XDF; Illingworth et al. 2013) with *HST* images in nine bands. We add the SMACS0723 galaxies from Giménez-Arteaga et al. (2023) to the comparison, which have $5 < z_{\rm spec} < 9$ from JWST/NIRSpec, and similar NIRCam images as those used in this work. Our results for RXCJ0600-z6-3 are shown as the black square for the CSFH, and stars for the additional SFHs parameterisations, indicated with the different symbol colours.

The mass discrepancies of all high redshift galaxies ($z > 5$, GA23 and this work) are similar to those of the galaxies at lower redshifts with similarly high sSFR (SS18). Our constant SFH resolved model (black square) falls in the regime of the GA23 targets, which used the same modeling prescription. Additionally, the log-normal and exponentially declining SFH agree with this discrepancy. On

SFH	$\log(\mu M_*/M_\odot)$	ΔM_r [dex]
Constant	$9.7^{+0.5}_{-0.2}$	$0.5^{+0.2}_{-0.1}$
Exponentially declining	$9.7^{+0.3}_{-0.2}$	$0.5^{+0.2}_{-0.1}$
Log-normal	$9.7^{+0.3}_{-0.2}$	$0.5^{+0.2}_{-0.1}$
Double-Power Law	$10.4^{+0.1}_{-0.1}$	$-0.2^{+0.3}_{-0.2}$

Table 7: Values for the stellar mass inferred in a spatially-integrated fit with BAGPIPES using different star formation history parameterisations. The mass offset ΔM_r is calculated with respect to the resolved CSFH stellar mass of $\log(\mu M_*/M_\odot)=10.2^{+0.2}_{-0.1}$.

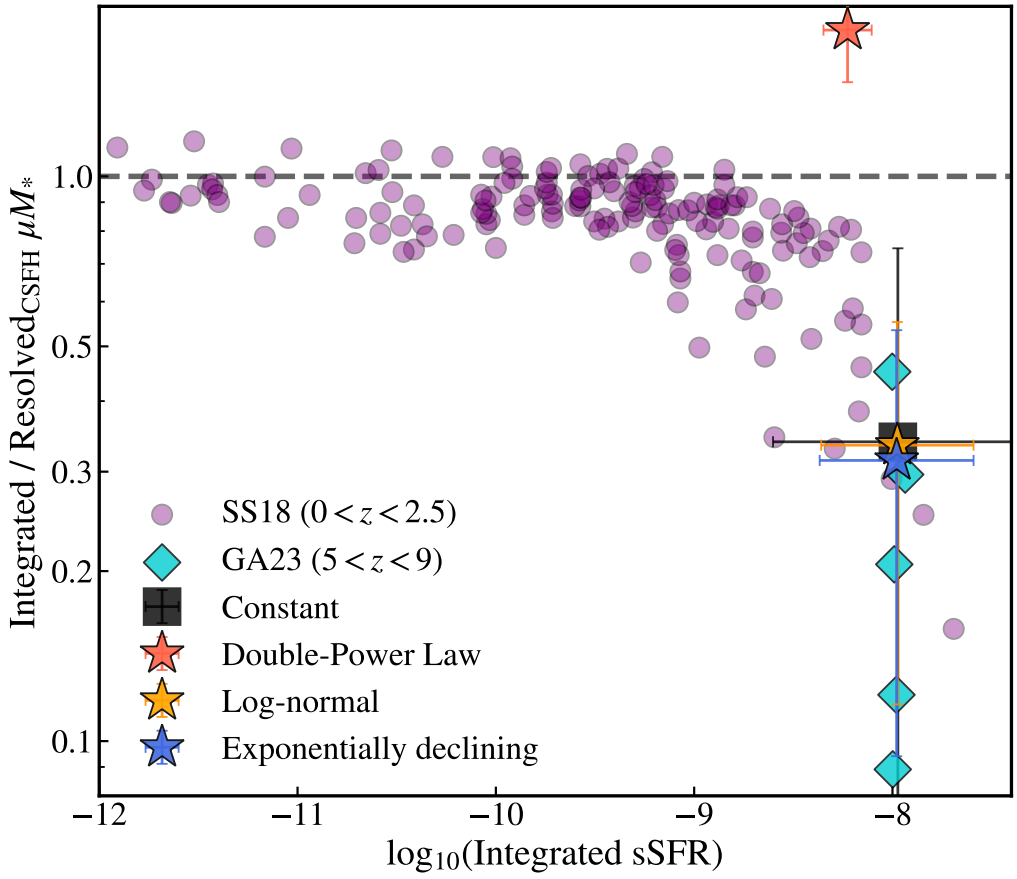

Figure 54: Mass discrepancy between the integrated cases and the resolved CSFH, as a function of the unresolved specific star formation rate. The dashed line indicated no offset (or ratio=1). The purple points correspond to spectroscopically-confirmed galaxies at $0 < z < 2.5$ from Sorba & Sawicki (2018). The turquoise diamonds are $5 < z < 9$ galaxies from Giménez-Arteaga et al. (2023). The square and stars correspond to this work. The black square indicates the fiducial CSFH case. The red, orange and blue stars indicate a double-power law, a log-normal, and an exponentially declining SFH parameterisations, respectively.

the other hand, the double power-law surpasses the ratio = 1 line, which means that the integrated mass is larger than the resolved one. This is not surprising given that on Figure 53 we already saw that this SFH is as extended as the resolved CSFH, with larger SF in the older stars regime. This allows for the presence of older stellar populations in the integrated fit, bypassing the outshining caused by the youngest stars that affect the other SFH parameterisations. This is also a feature of non-parametric SED-fitting codes (e.g., Leja et al. 2017, 2019; Iyer et al. 2020), which also tend to infer older and more massive galaxies (see e.g., Carnall et al. 2019; Tacchella et al. 2023).

Given the NIRCam observations alone, one might conclude that a double-power law or a SFH parameterisation that includes older stellar populations (e.g. non-parametric SFH), is a good model for targets like RXCJ0600-z6-3, in the case that we did not have enough resolution to perform a spatially-resolved analysis. For this target, we have complementary IFU observations. From the cube, as shown in §4.4.2, we find strong nebular emission in this galaxy. Given the power-law decline of the star formation rate in the DPL parameterisation, we can expect that it cannot produce extreme line emission. On top of this, if we integrate over the last ~ 10 Myr the DPL SFH curve (Figure 53), we can see that it will not be able to reproduce the line fluxes observed by the IFU such as Hα, which traces the most recent star formation. Thus, only by combining the NIRCam spatially-resolved analysis with the NIRSpec IFU measurements of the emission lines, we can see that the DPL cannot explain the strength of the lines, thus not being a good model to represent this galaxy. Therefore, all the rest of models have ~ 0.5 dex lower stellar mass when inferred in a spatially-resolved analysis, demonstrating once more the effect of outshining by the youngest stellar populations, as seen in previous studies (Sorba & Sawicki 2018; Giménez-Arteaga et al. 2023; Narayanan et al. 2023a). The implications of outshining are being studied at various redshifts (e.g., Roberts-Borsani et al. 2020; Tang et al. 2022; Topping et al. 2022).

4.4.4 *The Ionizing Photon Production Efficiency*

To place our target into the broader scope of its cosmic time, when reionization is thought to be almost completed ($z \sim 6$, Fan et al. 2006; Mason et al. 2018), we can calculate the Lyman continuum (LyC) photon production efficiency ($\xi_{\rm ion}$) of RXCJ0600-z6-3. We infer the production rate of ionizing photons that did not escape the galaxy (see e.g., Prieto-Lyon et al. 2023), denoted as $\xi_{\rm ion,0}$. We use the equation by e.g. Bouwens et al. (2016):

$$\xi_{\rm ion,0} \equiv \xi_{\rm ion}(1-f_{\rm esc}) = \frac{L^{\rm corr}_{\rm H\alpha}}{L_{\rm UV}/f_{\rm esc,UV}} \times 7.35\times10^{11}[{\rm Hz\,erg^{-1}}] \qquad (12)$$

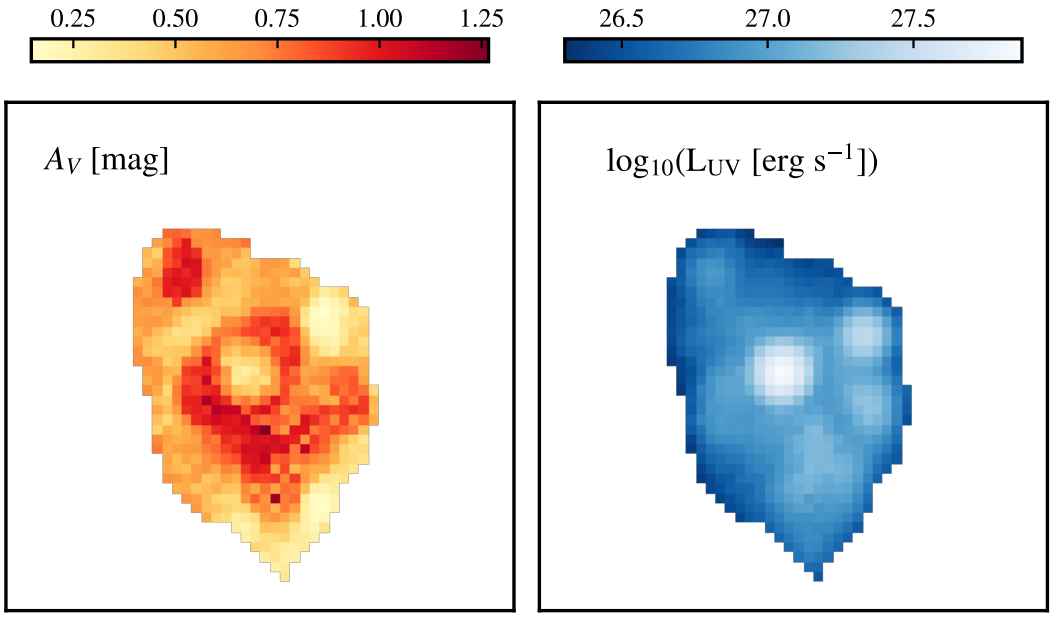

Figure 55: Maps of the A_V and $\log_{10}(L_{UV})$ inferred from the BAGPIPES SED modeling and posterior distributions, using a CSFH.

where $L_{H\alpha}^{corr}$ is the dust-corrected Hα luminosity, L_{UV} is the UV luminosity evaluated at 1500 Å, and $1/f_{esc,UV}$ accounts for the dust correction to obtain the intrinsic UV luminosity, before being obscured by dust. Using a Calzetti et al. (2000) attenuation curve, we employ the relation $A_{UV} = 1.99\,(\beta + 2.23)$, where β is the UV slope. From A_{UV} we can infer $f_{esc,UV} = 10^{-A_{UV}/2.5}$. Finally, from the H$\alpha$ flux we infer the luminosity, and correct for dust using the A_V estimated by the SED modelling (see e.g. Eq. 3 in Giménez-Arteaga et al. 2022).

The prescription for computing $\xi_{ion,0}$ can be used on a pixel-by-pixel basis, given that we have Hα (Figure 52, right panel), the UV β slope (Figure 51, right map), and A_V and L_{UV} maps (Figure 55). Combining these maps according to Equation 12, we obtain the 2D distribution of the ionizing photon production shown in Figure 56. We find variations of almost an order of magnitude in $\xi_{ion,0}$ across the galaxy, from a minimum $\log_{10}(\xi_{ion,0})$=25.17, to a maximum of $\log_{10}(\xi_{ion,0})$=26.04. This could be explained by the presence of distinct stellar populations (as the spatially-resolved analysis indicates, see §4.4.1), by a varying escape fraction f_{esc} in the different regions within the galaxy, or by a combination of both, which may be potentially correlated. As expected, given the strong correlation between age and $\xi_{ion,0}$, the region where most ionizing photons are coming from corresponds to the youngest inferred ages of the stellar population (see age map in Figure 51).

We can additionally derive the $\xi_{ion,0}$ from our spatially-integrated estimates. Using the fiducial CSFH, we obtain $\log_{10}(\xi_{ion,0})$=25.7 ± 0.1. Figure 57 shows the evolution of the ionizing photon production rate, where we place the mea-

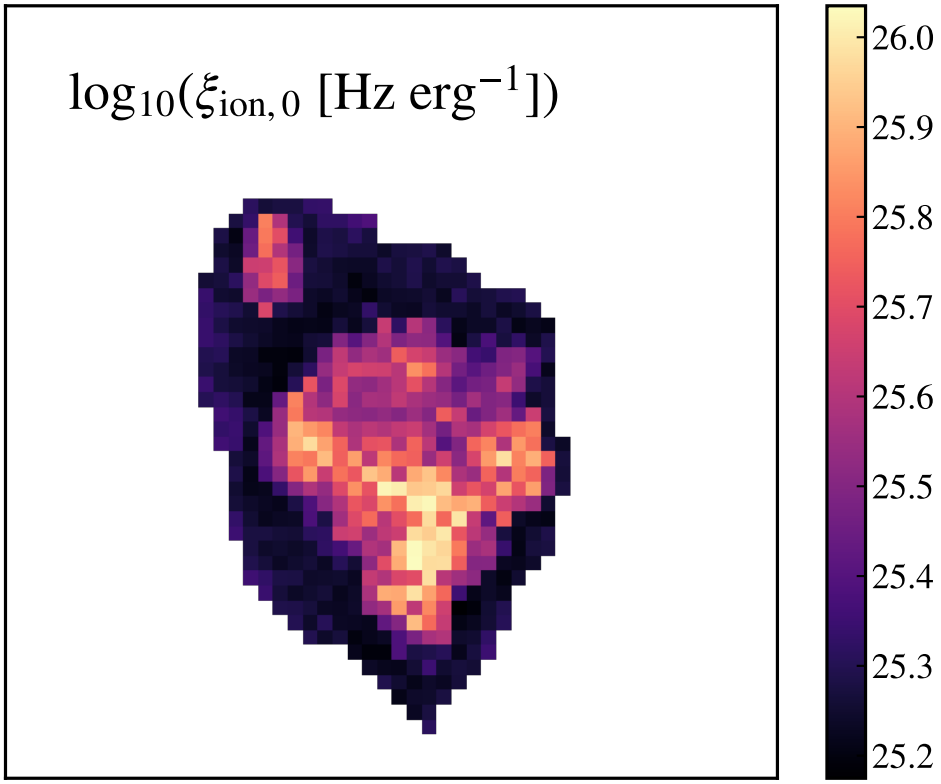

Figure 56: Inferred 2D distribution of the ionizing photon production rate $\log_{10}(\xi_{\rm ion,0}$[Hz erg^{-1}]), derived using Equation 12.

surements for RXCJ0600-z6-3, as well as additional literature values. By calculating the median value of the $\xi_{\rm ion,0}$ 2D map (Figure 56), we can also infer a "resolved" $\xi_{\rm ion,0}$ estimate, shown in Figure 57 as the turquoise star, which yields $\log_{10}(\xi_{\rm ion,0})$=25.34 ± 0.12. Similarly to the discrepancy that we find on the stellar mass estimates, resolving the galaxy yields a non-negligible offset in $\xi_{\rm ion,0}$ of $\sim$ 0.4 dex. Thus, we also see the effects of outshining in the inferred ionizing photon production efficiency, given that the youngest region dominates the inferred spatially-integrated $\xi_{\rm ion,0}$. Our result suggests that spatially-integrated estimates could overestimate the $\xi_{\rm ion,0}$ measurement, at least for targets such as the one presented here with multiple star forming clumps. Additional works with larger statistical samples are necessary to study this further.

The galaxy RXCJ0600-z6-3, when considering the spatially-integrated estimate, has one of the largest $\xi_{\rm ion,0}$ values amongst all samples displayed in Figure 57. It is only surpassed by the very faint population from Atek et al. (2023) ($M_{\rm UV} > -16.5$), which reach a striking value of $\log_{10}(\xi_{\rm ion,0})$=25.8 ± 0.05, and potentially by the galaxies from Fujimoto et al. (2023c), within the uncertainties. On the other hand, the considerably lower resolved estimate is consistent with the canonical value $\log_{10}(\xi_{\rm ion,0})$=25.2 ± 0.1 (Robertson et al. 2013). This target is above (below) the fits derived by Stefanon et al. (2022); Matthee et al. (2017) and

Simmonds et al. (2023) in the integrated (resolved) measurement. Stefanon et al. (2022) obtained the fit from a compilation of measurements up to $z \sim 8$, including the ones displayed here from the works of Bouwens et al. (2016); Matthee et al. (2017); Shivaei et al. (2018); Lam et al. (2019), and Atek et al. (2022). The trend derived by Simmonds et al. (2023) is performed on a sample of 677 at $z \sim 4-9$ from the JADES survey (Eisenstein et al. 2023) observed with NIRCam imaging. The values from Fujimoto et al. (2023c) are from CEERS NIRCam-selected $z \gtrsim 8$ galaxy candidates, spectroscopically confirmed with NIRSpec. Both our $\xi_{\rm ion,0}$ estimates are consistent within the uncertainties with the sample from Prieto-Lyon et al. (2023), particularly with their Lyman-α-emitting galaxies, with a median value of $\log_{10}(\xi_{\rm ion,0})$=25.39 ± 0.64, given that the large scatter that we find across a single galaxy, is also observed within the galaxy population they study at $z \sim 3-7$.

The turquoise shaded rectangle in Figure 57 shows the range of values that are found in the 2D map shown in Figure 56. We see that some pixels within the galaxy surpass all other literature values, and others go as low as the canonical value, hinting once more at the complex internal structure of this galaxy, displaying a very broad range of $\xi_{\rm ion,0}$ values. The large differences in $\xi_{\rm ion,0}$ may indicate that some of the regions are undergoing recent bursts of star formation (traced by stronger Hα emission over the last few Myr), whereas others are forming stars over larger timescales (>100 Myr, with stronger UV emission instead), which is also found on our spatially-resolved SED fitting analysis. Differences of $\sim$0.4 dex in the $\xi_{\rm ion,0}$ have also been found between two clumps of MACS1149-JD1 at $z = 9.1$ (Álvarez-Márquez et al. 2023a). The spatially-integrated estimate (orange star symbol) falls at an intermediate value, given that, albeit being dominated by the youngest stars, we also find a bright central UV clump (Figure 55, right map), which then yields a more moderate $\xi_{\rm ion,0}$ value. As we would expect, $\xi_{\rm ion,0}$ strongly correlates with the age of the stellar population, as seen in the age map from Figure 51. The pixel-by-pixel analysis yields a broad range of stellar ages and $\xi_{\rm ion,0}$ values. The youngest stars are responsible for most of the ionizing photon production, dominating then the integrated value. The oldest stars do not contribute as significantly to $\xi_{\rm ion,0}$, and are outshined in the spatially-integrated analysis. Therefore, a spatially-resolved analysis yields a lower value of $\xi_{\rm ion,0}$. This large interval of values could imply very different scenarios in terms of the contribution by this galaxy to the end of reionisation – from being one of the largest contributors found so far, to being lower than the derived trends from e.g. Stefanon et al. (2022) and consistent with the canonical values (Robertson et al. 2013).

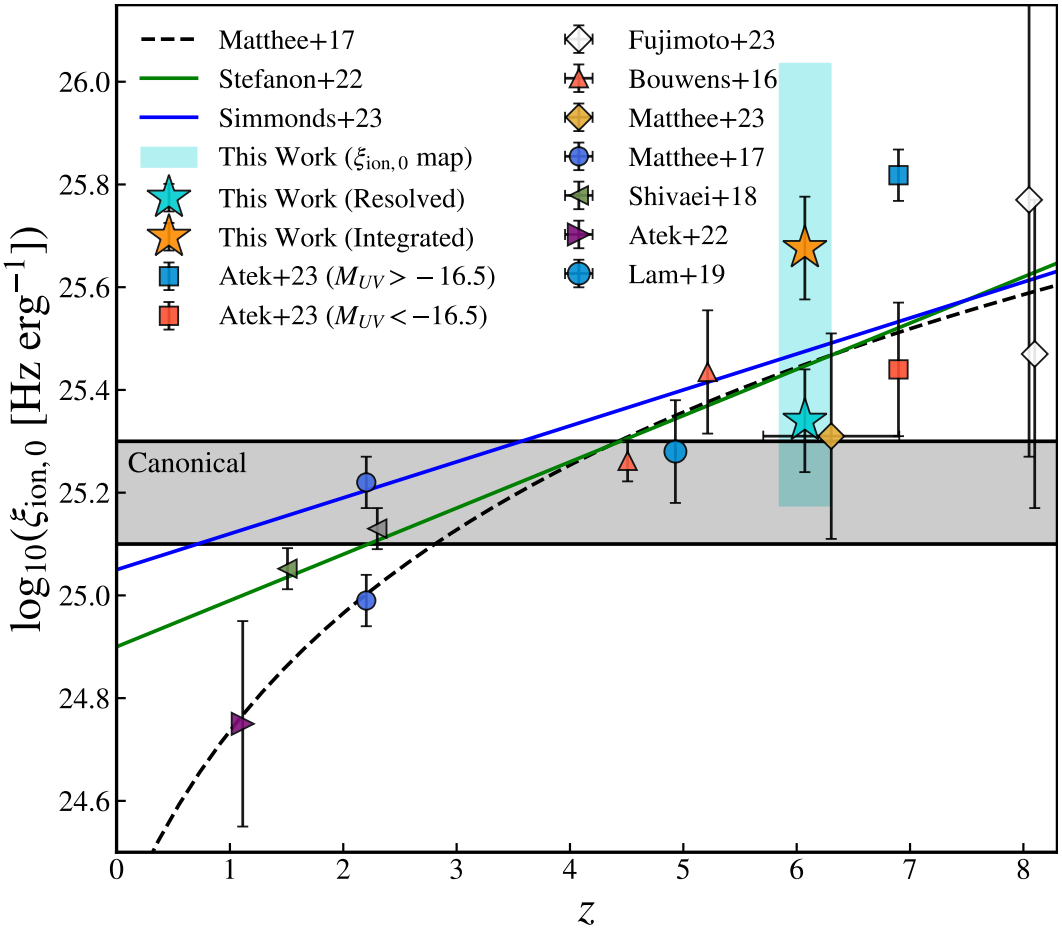

Figure 57: Evolution of the ionizing photon production with redshift. The stars correspond to this work, with the orange and turquoise representing the integrated and resolved $\xi_{ion,0}$ estimates, respectively. The turquoise shaded region shows the range of values of the 2D $\xi_{ion,0}$ map displayed in Figure 56. The grey shaded region indicates the canonical values (Robertson et al. 2013). The rest of literature values are from Bouwens et al. (2016); Matthee et al. (2017); Shivaei et al. (2018); Lam et al. (2019); Atek et al. (2022, 2023); Matthee et al. (2023); Fujimoto et al. (2023c), as well as the trends from Matthee et al. (2017); Stefanon et al. (2022), and Simmonds et al. (2023).

4.4.5 *Caveats*

Despite seemingly providing the best agreement in the SFH shape with respect to the resolved CSFH, and besides not being able to reproduce the observed IFU line strengths, the double-power law SFH parameterisation has more caveats to be considered. With the priors that we impose and specify in Table 8, the BAGPIPES modeling has seven free parameters in total. As explained throughout, we only have five bands available with NIRCam, which may not be enough to constrain all free parameters without yielding extra degeneracies between them. Similarly,

this caveat applies to the log-normal SFH, which has six free parameters in the fits.

Therefore, despite being one of the most basic forms, the constant SFH has five free parameters, which equals the amount of data points we have to constrain them. Albeit its simplicity, it should still be a reasonable parameterisation on a pixel-by-pixel basis, as discussed before.

It is worth noting that with the CSFH, most mass shows as residing in the outer shell of older stars. Given the strong lines in the center, only young, less massive stars are *seen*. In reality, this region can also be a mixture of young and older stellar populations, which would increase the total mass of the galaxy. Therefore, the "true" stellar mass of the galaxy is most likely *larger* than what a spatially-resolved analysis can recover, making the discrepancy with respect to single-aperture photometric estimates even larger.

4.5 SUMMARY AND CONCLUSIONS

We have performed pixel-by-pixel SED modelling on the NIRCam images for RXCJ0600-z6-3, one of the multiple images of a highly-lensed galaxy at $z = 6.072$ behind the galaxy cluster RXCJ0600-2007. We have built maps of the physical properties such as the stellar mass, the star formation rate, and the age of the stellar population. We have tested various parameterisations of the star formation history, and studied the effects on the retrieved stellar masses. We have tested our photometric-only estimates with measurements from NIRSpec IFU data, aiding us in verifying the conclusions from our methodology. We have studied the potential contribution to the end of reionization of this interesting galaxy. The main results of our work are as follows:

- Analogous to the findings of Giménez-Arteaga et al. (2023), the galaxy displays a young clump of stellar populations embedded within a shell of older stars.

- The line fluxes inferred from NIRCam photometry with a CSFH can reproduce the spatial distribution and strength of the NIRSpec IFU emission line maps.

- From a spatially-integrated perspective, with photometry-only modelling we retrieve consistent values of the EW and line fluxes of [O III]+Hβ and Hα+[N II] when compared to the IFU spectra estimates.

- Consistent to recent findings in observations and simulations (e.g., Sorba & Sawicki 2018; Giménez-Arteaga et al. 2023; Narayanan et al. 2023a), outshining affects our stellar mass values when comparing resolved versus unresolved estimates.

- A double-power law SFH displays star formation over extended timescales, matching the resolved CSFH curve, but cannot reproduce the strength of the IFU emission lines. Other parametric SFH shapes yield ~ 0.5 dex lower stellar masses than the CSFH resolved estimate.

- The ionizing photon production efficiency estimate is additionally affected by outshining. Resolving the galaxy yields ~ 0.4 dex lower $\xi_{\rm ion,0}$, which could hint at spatially-integrated studies overestimating the contribution to reionisation of targets similar to the one studied here.

The problem of outshining is being studied in observations and simulations. Broadly covered and larger statistical samples are needed to investigate this problem across cosmic time, and constrain better the systematics that it introduces in our physical estimates. The work presented here gives confidence to photometric-only analyses, but stresses the importance of combining these with NIRSpec IFU or spectroscopic data, in order to break photometric degeneracies and constrain the physical properties with more accuracy.

This study puts emphasis on the importance of studying galaxies as the complex systems that they are. Given the unprecedented resolution of the instruments on board *JWST*, resolving the stellar populations of galaxies, when possible, can give us different views on their internal structure and properties, when compared to the well established aperture photometry approach. By addressing the challenge of inferring robust stellar masses of high redshift galaxies, resolved studies can aid our understanding of the first stages of mass assembly and galaxy evolution.

ACKNOWLEDGEMENTS

The Cosmic Dawn Center (DAWN) is funded by the Danish National Research Foundation under grant DNRF140. This work is based on observations made with the NASA/ESA/CSA *James Webb Space Telescope*. The data were obtained from the Mikulski Archive for Space Telescopes at the Space Telescope Science Institute, which is operated by the Association of Universities for Research in Astronomy, Inc., under NASA contract NAS 5-03127 for *JWST*. These observations are associated with program ID. 1567, as part of a Cycle 1 GO Proposal (PI: S. Fujimoto, Fujimoto et al. 2021a). S.F. acknowledges the support from NASA through the NASA Hubble Fellowship grant HST-HF2-51505.001-A awarded by the Space Telescope Science Institute, which is operated by the Association of Universities for Research in Astronomy, Incorporated, under NASA contract NAS5-26555. Cloud-based data processing and file storage for this work is provided by the AWS Cloud Credits for Research program.
Facilities: *JWST* (NIRCam), *JWST* (NIRSpec)
Software: Astropy (Astropy Collaboration et al. 2013, 2022), Matplotlib (Hunter

2007), NumPy (Harris et al. 2020), SciPy (Virtanen et al. 2020), `grizli` (Brammer 2019; Brammer & Matharu 2021; Brammer et al. 2022)

APPENDIX

4.6 STAR FORMATION HISTORIES

In §4.3.1, we described the setup used within BAGPIPES to model the SEDs. We use different SFH parameterisations. Here we specify the SFH forms and priors imposed, which can be found on Table 8.

SFH model	Priors
Constant	Maximum age $\in$ [1 Myr, 1 Gyr]
Log-normal	Age of the Universe at peak SF $\in$ [1 Myr, 1 Gyr]
	Full width at half maximum SF $\in$ [0, 1 Gyr]
Exponentially Declining	Time since SFH began $\in$ [1 Myr, 1 Gyr]
	Timescale of decrease $\tau \in$ [0, 10]
Double-Power Law	Falling slope index $\in$ [0, 10]
	Rising slope index $\in$ [0, 10]
	Age of the Universe at turnover $\tau \in$ [1 Myr, 1 Gyr]

Table 8: Different parametric forms of the star formation history that we use with BAGPIPES. Each model has its own parameters and we specify the uniform priors used in this work.

5

CONCLUSIONS

In this thesis, I have presented a series of studies on galaxies spanning from the early Universe to the present day, with a primary focus on utilising photometric observations obtained with the *Hubble Space Telescope* and *JWST*.

In Chapter 2, our study on a sample of local star-forming galaxies introduces novel methods for inferring robust emission line fluxes from both narrow and broad-band imaging data. We find that the Paschen-β emission line transition consistently yields higher star formation rates than the usual Hα star formation diagnostic. This underscores the limitations of the classical Balmer decrement in capturing star formation in heavily obscured regions within galaxies, emphasizing the value of redder lines like the Paschen series for exploring these dust-enshrouded sites of star formation.

Extending our approach from the local Universe, where we resolve stellar populations and galaxy components, Chapters 3 and 4 apply spatially-resolved analyses to the high-redshift Universe. Our findings reveal intricate structures featuring multiple star-forming clumps, with galaxies exhibiting young central clumps embedded within a shell of older stellar populations. The dominance of strong line emission regions in the integrated light of these galaxies introduces a bias towards very young ages (<10 Myr), resulting in underestimated stellar masses. This phenomenon of *outshining*, previously encountered at lower redshifts and in simulations, is now observed at high-z as well. These results could significantly impact our understanding of the build up of stellar mass in the early Universe and the process of galaxy formation, as indicated by the presence of evolved older stars being outshone by the youngest stellar populations. Additionally, a detailed view into a strongly-magnified galaxy at $z \sim 6$ in Chapter 4 sheds light into its complex internal structure, emphasizing the importance of spatially-resolved analyses in reionisation studies, given the broad range of ionizing photon production efficiency values encountered across the galaxy that would indicate significantly different contributions to reionisation.

This thesis highlights the importance of spatially-resolved analyses to understand galaxies across cosmic time as the complex systems that they are.

5.1 OUTLOOK

In this rapidly advancing field, especially with the deployment of *JWST*, new studies are emerging daily, with some delving into the themes presented in this dissertation. Here we discuss some of these studies in connection to our work and explore future perspectives based on the topics covered.

Building on the research presented in Chapter 2, a prospective avenue involves extending the study to higher redshifts. A systematic census of Paschen emission in galaxies can give us a more complete picture of the obscured star formation activity across cosmic time. With the capabilities of *JWST*, Paschen lines are no longer only accessible at $z < 0.3$, with initial analyses at higher redshifts already reported. For instance, the Mid-Infrared Instrument (MIRI) onboard *JWST* has unveiled a highly obscured starburst at $z = 6.9$ (Álvarez-Márquez et al. 2023b), exhibiting nebular extinction values consistent to those found in our low-z sample. Using *JWST*/NIRSpec, Reddy et al. (2023) have constrained star formation and dust attenuation in 63 galaxies at $z \sim 1-3$ through Paschen lines. In agreement with our findings, their derived SFRs from Paschen lines exceed by $\sim 25\%$ the SFRs from Balmer lines.

Upcoming surveys will extend our existing Paschen studies, enhancing the current sample in terms of both statistical significance and redshift coverage. For instance, the Cycle 1 Program ID 1963 (PIs: C. Williams, S. Tacchella, M. Maseda, Williams et al. 2021), known as the *JWST* Extragalactic Medium-band Survey (JEMS, Williams et al. 2023), is a NIRCam and NIRISS medium-band imaging survey that targets the Hubble Ultra Deep Field. The Paschen-α and Paschen-β lines are probed at $z \sim 1.2-2.8$ through imaging at 4 μm. Despite their faintness compared to the Balmer lines, the sensitivity of *JWST* instruments allows the detection of these lines through medium-band photometry. Figure 58 illustrates the emission lines to be explored in the upcoming *JWST*/NIRCam Cycle 2 Program ID 4111 (PI: K. Suess, Suess et al. 2023), where 50,000 sources will be spatially-resolved at $z = 0.3-12$, with Paschen lines traced up to $z \sim 3$.

With the enhanced resolution capabilities of the *JWST* instruments and the anticipation of upcoming surveys, the potential arises to resolve the structures of the earliest galaxies and their components. Beyond merely tracing spectral features at higher redshifts, medium-band programs offer a valuable tool to unravel the complexities addressed in Chapters 3 and 4. We need to understand the prevalence of outshining in galaxies across cosmic time, to be able to incorporate into our modelling to prevent inferring wrong physical estimates, such as the ages of stellar populations and stellar masses. To achieve this, surveys with expansive statistical samples and broad redshift coverage will be crucial, providing essential insights (e.g., the Deep UNCOVER-ALMA Legacy High-Z Survey, DUALZ, Fujimoto et al. 2023b). Simulations offer a direct means of testing these phenomena, and efforts should be made to establish connections with observa-

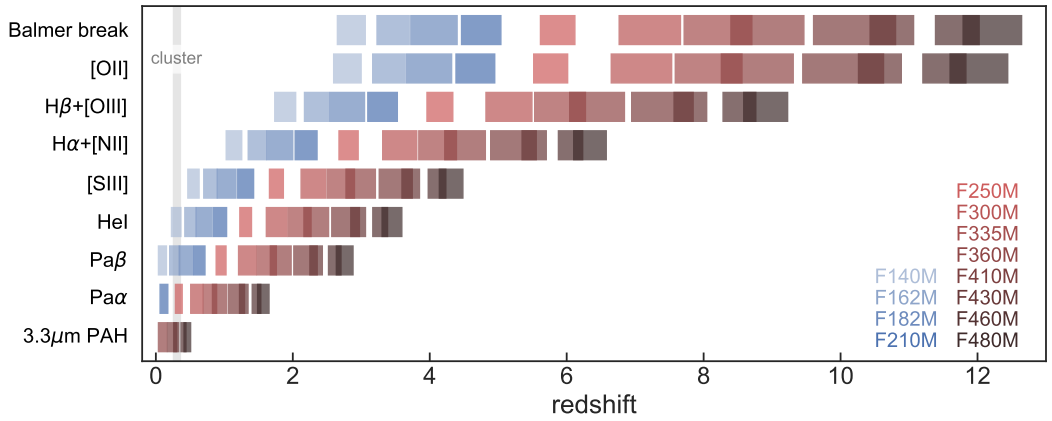

Figure 58: Spectral features that will be probed in the upcoming *JWST*/NIRCam medium-band program by Suess et al. (2023), as a function of redshift. Figure from the accepted Cycle 2 proposal "Medium bands, Mega Science: spatially-resolved R 15 spectrophotometry of 50,000 sources at $z = 0.3-12$". Credit: Wren Suess (Suess et al. 2023).

tions of high-redshift galaxies, where constraints on star formation history, age, and dust obscuration through SED modelling are more challenging.

As introduced in §1.5.4, the determination of stellar masses for galaxies observed by *JWST* at high redshifts has been a significant point of debate since the initial observations were released. The issue of outshining has been a relevant aspect of this discussion. Some studies are incorporating our findings, along with potential systematic differences arising from varying SFHs, by introducing additional uncertainties into their stellar mass estimates (e.g., Heintz et al. 2023c, for the galaxy at $z \sim 8.5$ examined in Chapter 3), or to motivate the use of non-parametric SFHs that can incorporate older stellar populations (e.g., Heintz et al. 2023a). Notably, outshining and spatial resolution are gradually gaining presence as potential additional sources of uncertainty when reporting stellar mass estimates (e.g., Fujimoto et al. 2023a; Valentino et al. 2023; Abdurro'uf et al. 2023; Laursen 2023). Furthermore, the challenge of outshining has been a subject of recent investigation in simulations. Narayanan et al. (2023a) observe that the integrated spectra of galaxies are predominantly influenced by the most recent bursts of star formation, obscuring previous star-forming episodes and complicating the accurate estimation of stellar masses. Consistent with our findings, they identify order-of-magnitude uncertainties in resulting stellar masses due to outshining. Additionally, new simulations such as the Sphinx20 (Katz et al. 2023), will provide a crucial benchmark for interpreting *JWST* observations, offering mock images and spectra to enhance our understanding of high-redshift galaxy physics.

More and more studies are performing spatially-resolved analyses, in addition to the common integrated results in the high-z regime (e.g., Nelson et al. 2023). These contribute to the growing body of 2D and radial studies of high-

redshift galaxies (e.g., Pérez-González et al. 2023), providing insights into disk and bulge growth (e.g., Shen et al. 2023a). Young clumps of stars surrounded by older stellar populations are being found even at $z \sim 9.3$ (Boyett et al. 2023). This is also the case for MACS1149-JD1, a gravitationally lensed galaxy at $z = 9.1$ from the CAnadian NIRISS Unbiased Cluster Survey (CANUCS, Cycle 1 GTO Program ID 1208 Willott et al. 2023), where the bulk of stellar mass resides in the evolved stellar population, underlying three star-forming components (Bradač et al. 2023). Furthermore, two clumps with distinct mass-weighted ages are found in the obscured submillimeter galaxy HDF850.1 at $z = 5.18$ (Sun et al. 2023). Ono et al. (2023) find that for star-forming galaxies at $z = 4-10$ without clear signs of merger activity, star-formation occurs mainly near the mass centers, aligning with the initial phases of inside-out galaxy formation, which can be further studied with the insights that spatially resolved SED analyses offer.

In the study by Papovich et al. (2023), leveraging data from CEERS and *JWST*/MIRI, the authors analyse stellar population parameters for galaxies within the redshift range of $4 < z < 9$, and emphasize the crucial role of *JWST*/MIRI observations in accurately constraining stellar mass buildup in galaxies at very high redshifts. Tanaka et al. (2023) highlight the outshining problem in reconstructing SFHs for galaxies undergoing strong rejuvenation. Based partially on our results, they suggest that spatially resolved SED fitting could serve as a potential solution. When studying dynamical masses of JADES galaxies at $z \geq 6$ with *JWST*/NIRSpec, de Graaff et al. (2023) also suggest imaging at longer wavelengths with *JWST*/MIRI and spatially resolved SED fitting as potential improvements to refine stellar mass estimates, especially in cases where the outshining effect may lead to a significant underestimate. Furthermore, Song et al. (2023) utilise spatially resolved photometry in the CEERS field to study the conflict between resolved and unresolved stellar mass estimations, highlighting that the lack of rest-frame NIR data can lead to an overestimation of stellar mass due to wrongful estimates of the stellar age and dust attenuation. With the inclusion of *JWST* NIR photometry, the study finds a plausible solution to the conflict, demonstrating no significant disparity between resolved and unresolved stellar mass estimates up to redshift $z \sim 3$. Additional analyses extending to higher redshifts and larger statistical samples are necessary to test this further. Addressing biases in stellar population recovery, Rusakov et al. (2023) emphasise the need to consider biases in modelling temperature-dependent IMFs and spatially-integrated galaxy properties.

In the pursuit of understanding early galaxies, Jain et al. (2023) address challenges by advocating for spatially resolved analyses and exploring flexible star-formation histories. The study involves detailed measurements of SFHs for ~ 970 galaxies at redshifts $z = 0.5-2.0$. By adopting simple and flexible SFH models on both spatially resolved and unresolved scales, the research showcases the effectiveness of spatially resolved analyses in capturing the complex SFHs with

bursty star formation occurring on kiloparsec scales. This study aligns with our work presented in Chapter 3, emphasizing the importance of spatially resolved analyses in revealing older underlying stellar populations and impacting our understanding of the nature of these galaxies. This is also emphasized from a cosmological perspective in Forconi et al. (2023), where they discuss the potential disagreement of the early *JWST* galaxies with Planck's Cosmic Microwave Background (CMB) polarization measurements. They underscore that our findings potentially intensify tensions with ΛCDM predictions.

Collectively these works, as well as this dissertation, underscore the complexities and considerations of physical properties determinations for high-redshift galaxies, emphasizing the need for advancements in observational techniques and simulations to enhance our understanding of these distant objects. Together, these studies highlight the transformative impact of *JWST* in unraveling the intricacies of galaxy properties and challenging existing cosmological paradigms, and most importantly, they emphasize and agree on the importance of spatially resolved SED modelling analyses.

Looking into the future, larger and deeper surveys combined with the latest set of simulations will be necessary to study all these effects further. Constraining outshining across cosmic time would allow us to improve our SED modelling techniques. Resolved SED fitting on a pixel-by-pixel basis with more flexible SFHs such as non-parametric models, more flexible IMFs, and NIR and medium-band/IFU coverage to break the multiple degeneracies discussed throughout, could significantly change our current picture of early galaxies and their evolution. Additionally, these codes should improve in computational speed, to make these analyses feasible for large statistical samples. The power of resolving galaxies has only just begun to be discovered and exploited, with works such as Sorba & Sawicki (2018) using spatially-resolved analyses to solve the mass missing problem, i.e. the long-standing discrepancy between the SFRD and the SMD of the Universe. The next decade of observations will be an exciting time to study the various known scaling relations and physical properties in a new resolved approach, potentially (re)solving some of the current biases and problems in the field of galaxy formation and evolution.

LIST OF PUBLICATIONS

1. **Giménez-Arteaga**, Brammer, Marchesini et al. 2022, *"High-resolution Hubble Space Telescope Imaging Survey of Local Star-forming Galaxies. I. Spatially Resolved Obscured Star Formation with Hα and Paschen-β Recombination Lines"*, The Astrophysical Journal Supplement Series, Volume 263, Issue 1, doi: 10.3847/1538-4365/ac958c

2. Fujimoto, Ouchi, Nakajima et al. 2022, *"JWST and ALMA Multiple-Line Study in and around a Galaxy at z=8.496: Optical to FIR Line Ratios and the Onset of an Outflow Promoting Ionizing Photon Escape"*, Submitted to the Astrophysical Journal, doi: 10.48550/arXiv.2212.06863

3. Jin, Sillassen, Magdis et al. 2023, *"Massive galaxy formation caught in action at $z \sim 5$ with JWST"*, Astronomy & Astrophysics, Volume 670, doi: 10.1051/0004-6361/202245724

4. Brinch, Greve, Weaver et al. 2023, *"COSMOS2020: Identification of High-z Protocluster Candidates in COSMOS"*, The Astrophysical Journal, Volume 943, Issue 2, doi: 10.3847/1538-4357/ac9d96

5. Heintz, **Giménez-Arteaga**, Fujimoto et al. 2023, *"The Gas and Stellar Content of a Metal-poor Galaxy at z = 8.496 as Revealed by JWST and ALMA"*, The Astrophysical Journal Letters, Volume 944, Issue 2, doi: 10.3847/2041-8213/acb2cf

6. Valentino, Brammer, Gould et al. 2023, *"An Atlas of Color-selected Quiescent Galaxies at $z > 3$ in Public JWST Fields"*, The Astrophysical Journal, Volume 947, Number 1, doi: 10.3847/1538-4357/acbefa

7. **Giménez-Arteaga**, Oesch, Brammer et al. 2023a, *"Spatially Resolved Properties of Galaxies at $5 < z < 9$ in the SMACS0723 JWST ERO Field"*, The Astrophysical Journal, Volume 948, Issue 2, id.126, 13 pp., doi: 10.3847/1538-4357/acc5ea

8. Heintz, Brammer, **Giménez-Arteaga** et al. 2023, *"Dilution of chemical enrichment in galaxies 600 Myr after the Big Bang"*, Nature Astronomy (2023), doi: 10.1038/s41550-023-02078-7

9. Valentino, Fujimoto, **Giménez-Arteaga** et al. 2023, *"The cold interstellar medium of a normal sub-L* galaxy at the end of Reionization"*, Submitted to

Astronomy & Astrophysics

10. Nelson, Brammer, **Giménez-Arteaga** et al. 2023, *"FRESCO: An extended, massive, rapidly rotating galaxy at z = 5.3"*, Submitted to ApJL, doi: arXiv:2310.06887

11. **Giménez-Arteaga**, Fujimoto, Valentino et al. 2023b, *"Outshining in the Spatially Resolved Analysis of a Strongly Lensed Galaxy at $z = 6.072$ with JWST NIRCam"*, To be submitted to Astronomy & Astrophysics

12. Fujimoto et al. 2023, *"Early Galaxy Assembly Probed by IFU Trio of JWST , ALMA, and MUSE: From Young Star Clusters to Dynamical Interplay of Inflow and Outflow at $z = 6$"*, To be submitted to the Astrophysical Journal

APPENDIX

Here we present additional Appendix sections from Chapter 2.

INDIVIDUAL GALAXIES

Figures 59-81 display the three-colour composites, Hα and Paβ emission line maps, extinction maps inferred from the gas and the stellar population, as well as SFR and stellar mass maps for each galaxy presented in this paper.

ADDITIONAL GALAXIES

Due to the availability of L_{IR} and 24μm flux measurements, we exclude from our analysis 29 additional galaxies. These targets also often have spatial extent larger than the Field of View (FoV) of the instrument. Nonetheless, we have processed the HST data of these additional targets following the same reduction process explained in §2.2, and the reduced mosaics are also publicly available[1]. Table 9 summarises the filter coverage of the additional targets.

[1] http://cosmos.phy.tufts.edu/dustycosmos/

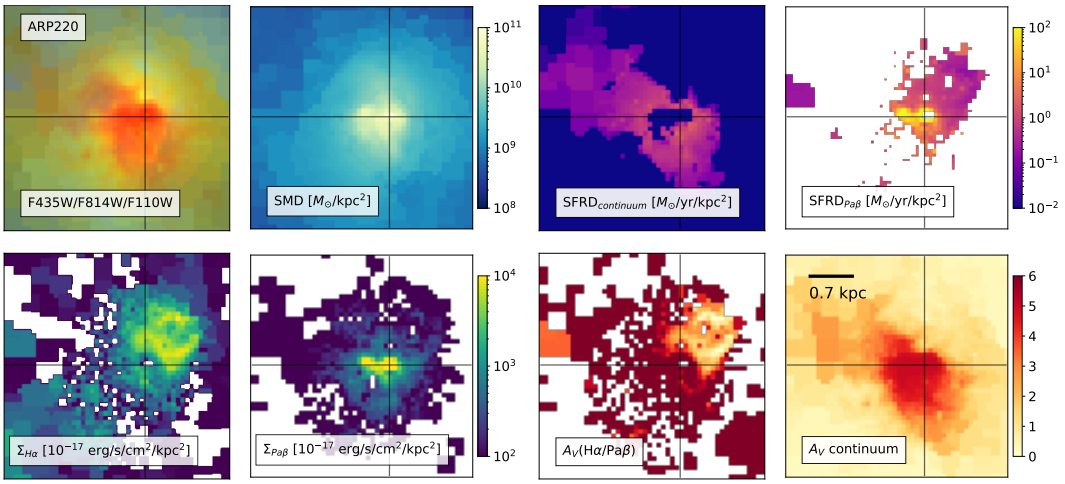

Figure 59: Output of the spatially-resolved SED-fit on Arp 220. The top row, from left to right, shows the RGB image (built combining three broadband filters), the stellar mass density map, and the SFRD maps inferred with the stellar continuum and with the Paβ emission line flux. The bottom row shows the resulting Hα and Paβ surface density flux maps, as well as the A_V inferred from the empirical Balmer-to-Paschen decrement, and the stellar continuum. The cross is centered on the brightest F110W pixel. The physical scale is indicated on the A_V continuum panel (bottom right).

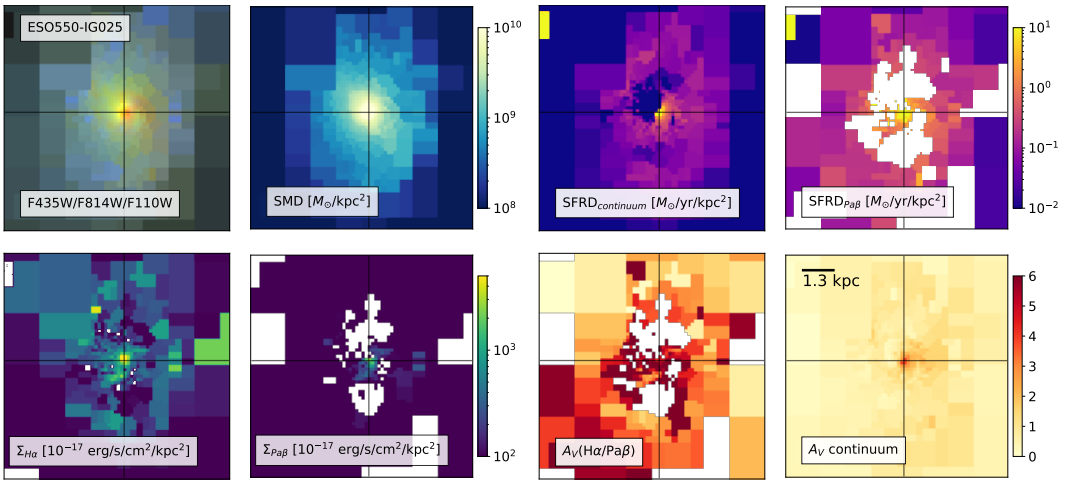

Figure 60: Maps of the physical properties inferred with our SED-fitting code for ESO550-IG025. See Figure 59 for more details.

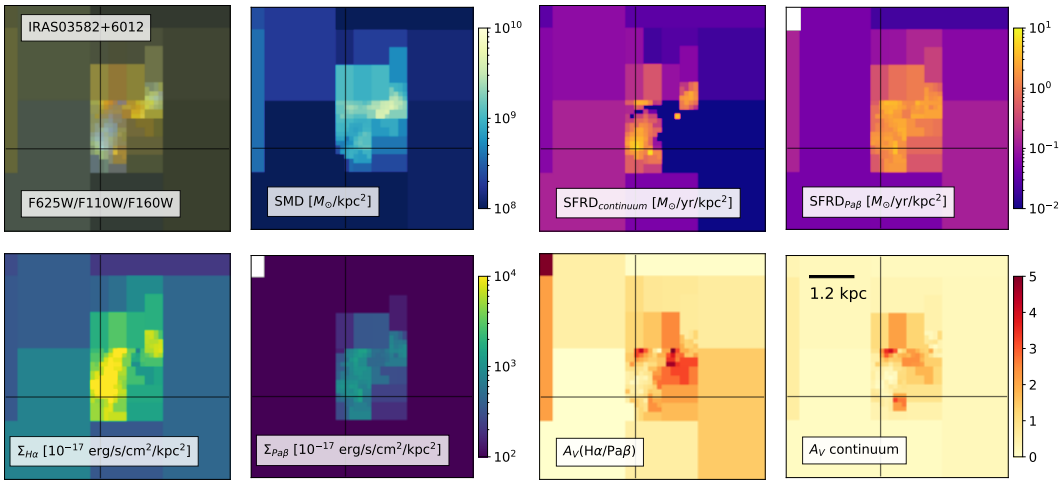

Figure 61: Maps of the physical properties inferred with our SED-fitting code for IRAS03582+6012. See Figure 59 for more details.

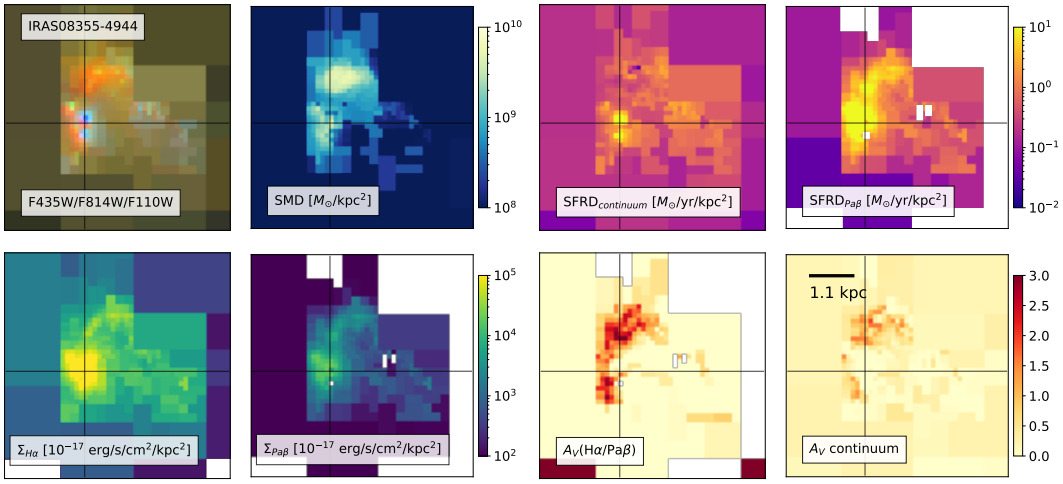

Figure 62: Maps of the physical properties inferred with our SED-fitting code for IRAS08355-4944. See Figure 59 for more details.

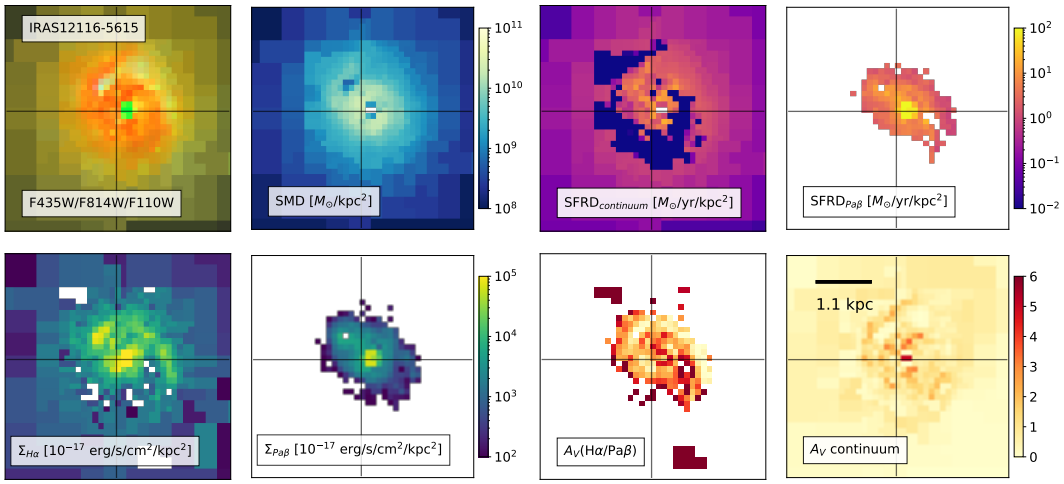

Figure 63: Maps of the physical properties inferred with our SED-fitting code for IRAS12116-5615. See Figure 59 for more details.

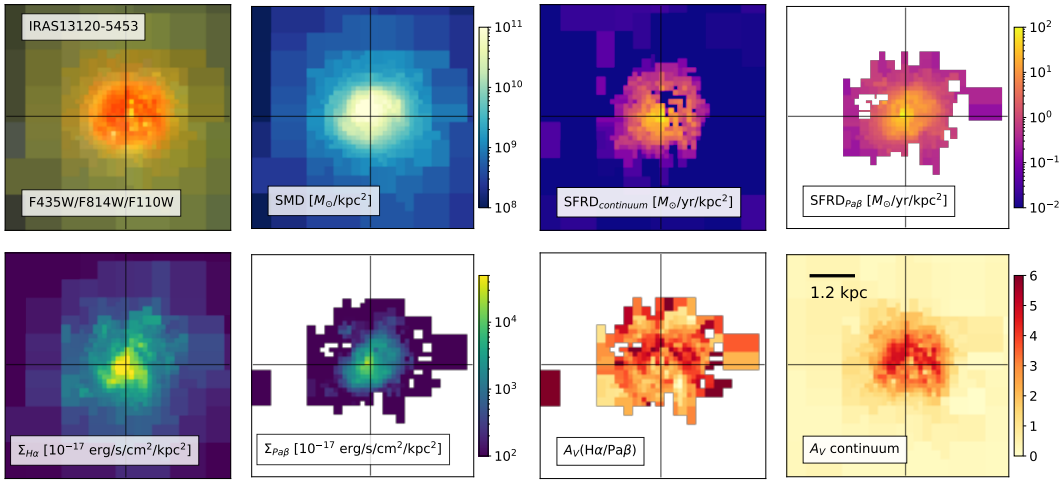

Figure 64: Maps of the physical properties inferred with our SED-fitting code for IRAS13120-5453. See Figure 59 for more details.

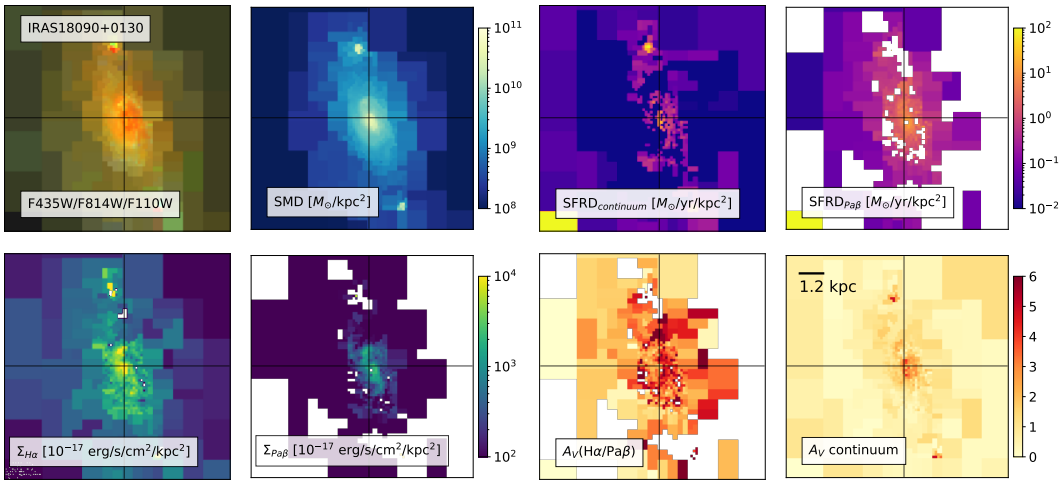

Figure 65: Maps of the physical properties inferred with our SED-fitting code for IRAS18090+0130. See Figure 59 for more details.

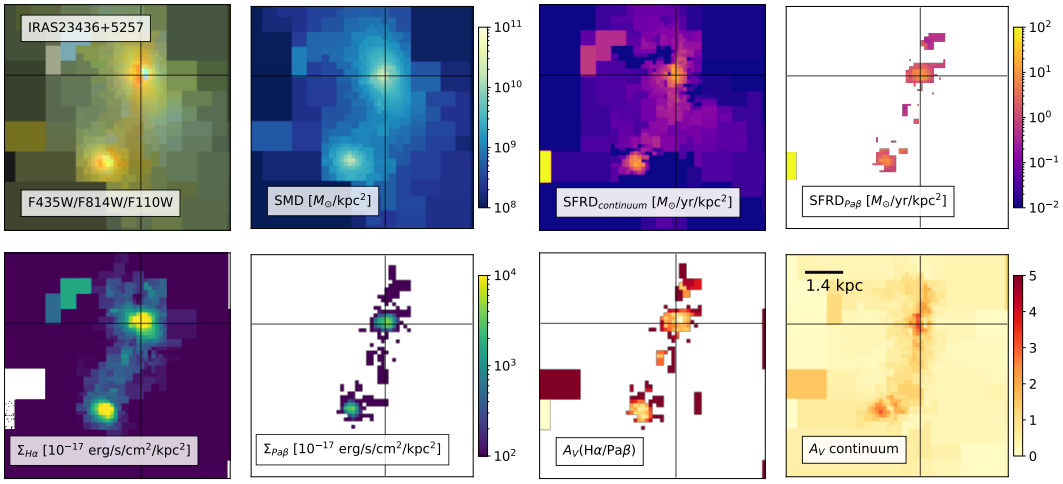

Figure 66: Maps of the physical properties inferred with our SED-fitting code for IRAS23436+5257. See Figure 59 for more details.

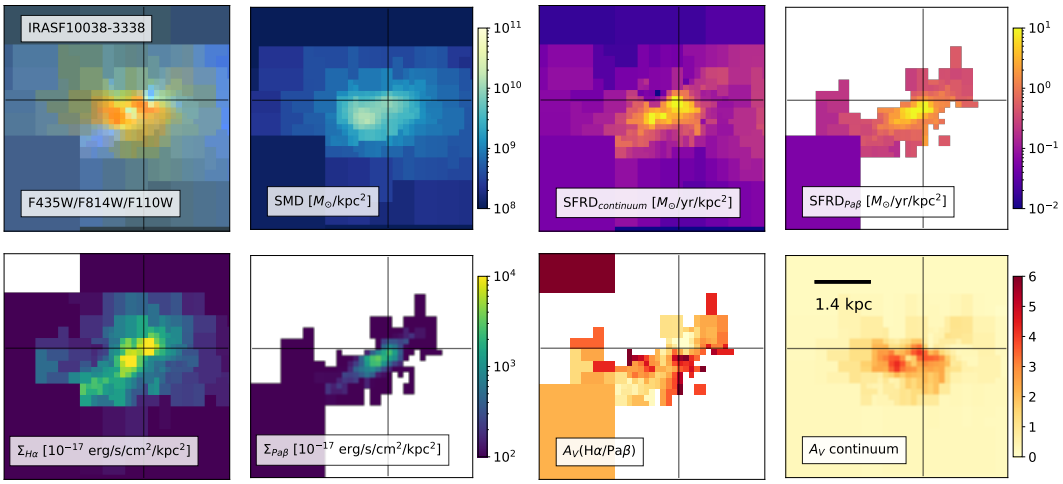

Figure 67: Maps of the physical properties inferred with our SED-fitting code for IRASF10038-3338. See Figure 59 for more details.

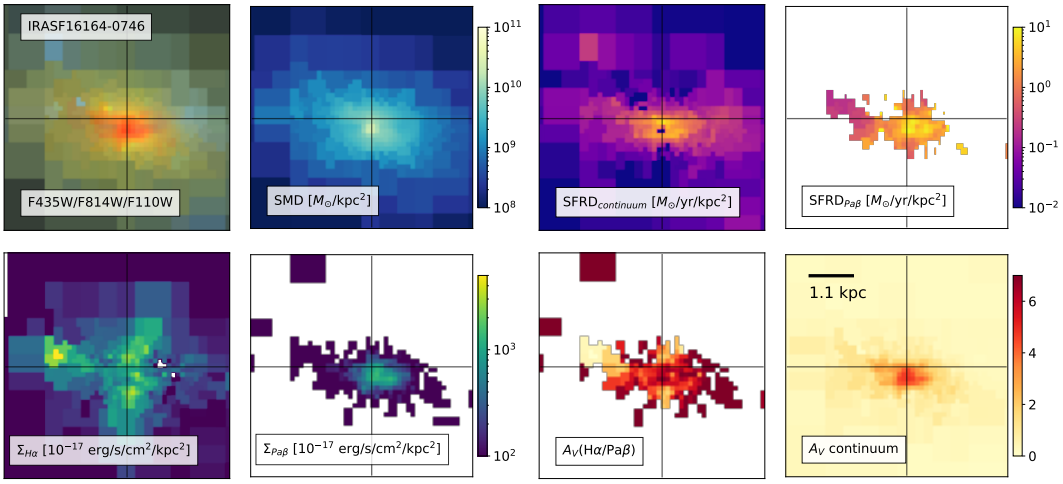

Figure 68: Maps of the physical properties inferred with our SED-fitting code for IRASF16164-0746. See Figure 59 for more details.

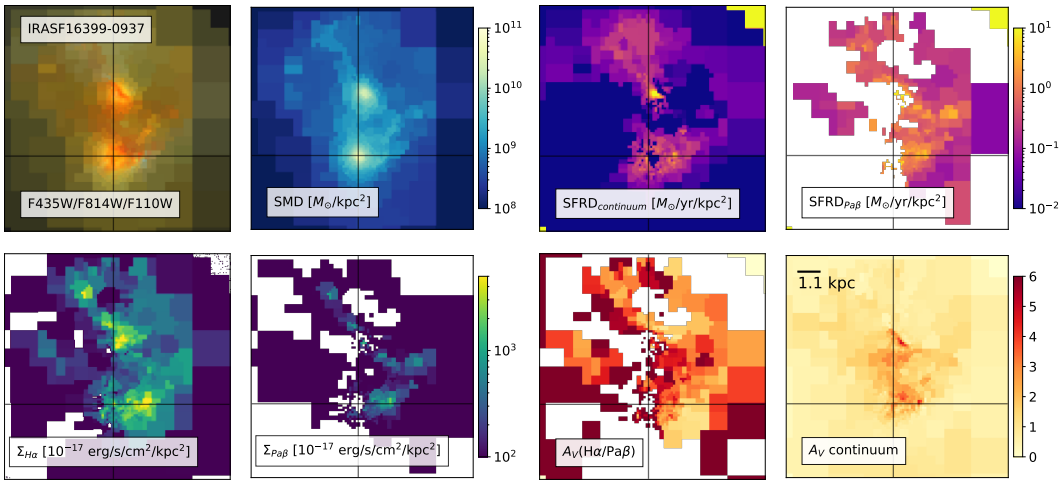

Figure 69: Maps of the physical properties inferred with our SED-fitting code for IRASF16399-0937. See Figure 59 for more details.

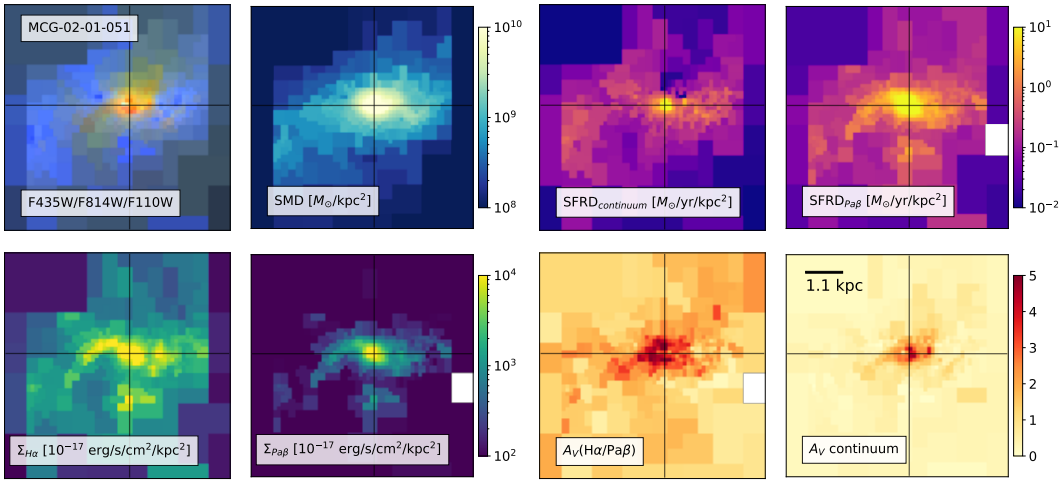

Figure 70: Maps of the physical properties inferred with our SED-fitting code for MCG-02-01-051. See Figure 59 for more details.

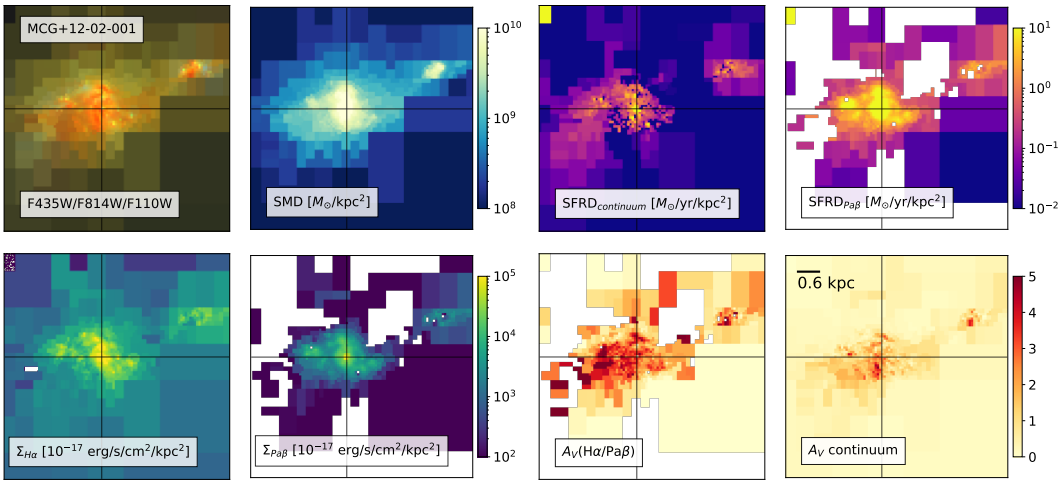

Figure 71: Maps of the physical properties inferred with our SED-fitting code for MCG+12-02-001. See Figure 59 for more details.

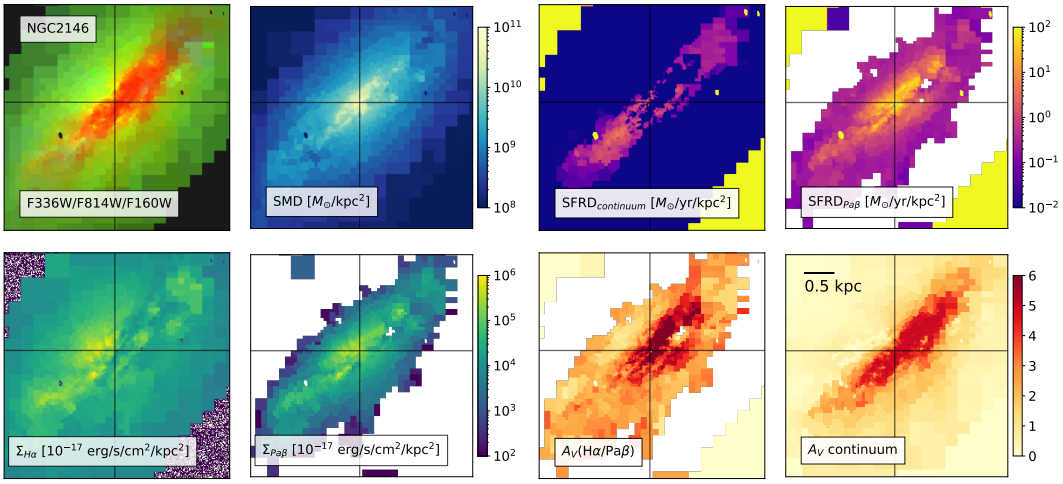

Figure 72: Maps of the physical properties inferred with our SED-fitting code for NGC2146. See Figure 59 for more details.

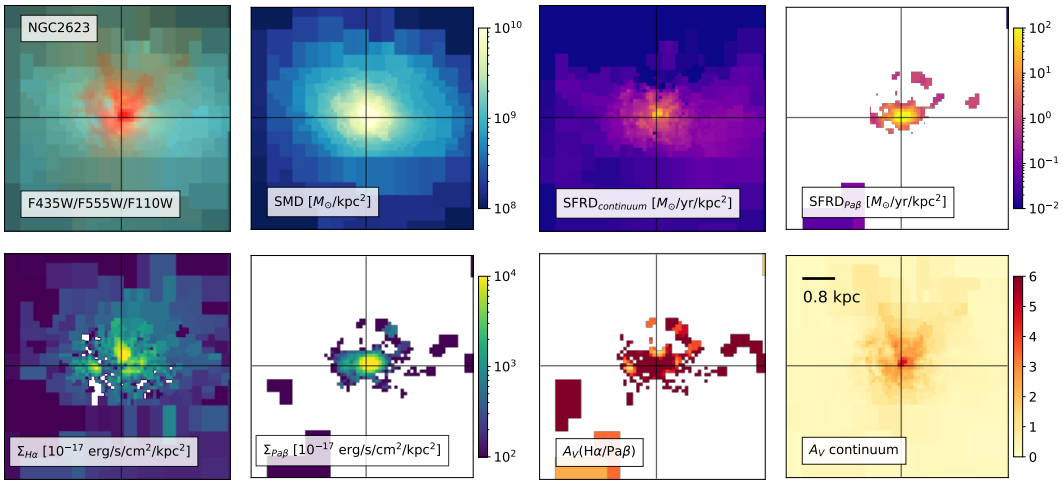

Figure 73: Maps of the physical properties inferred with our SED-fitting code for NGC2623. See Figure 59 for more details.

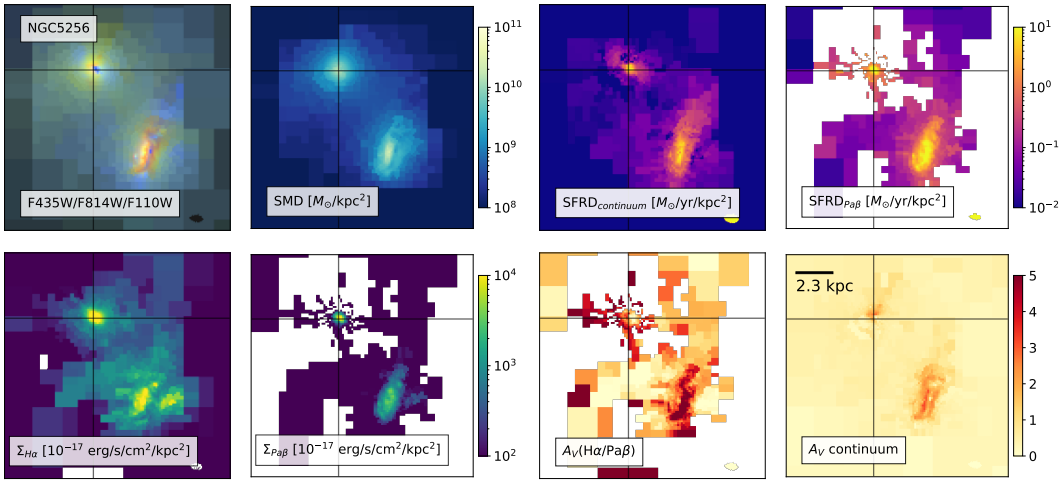

Figure 74: Maps of the physical properties inferred with our SED-fitting code for NGC5256. See Figure 59 for more details.

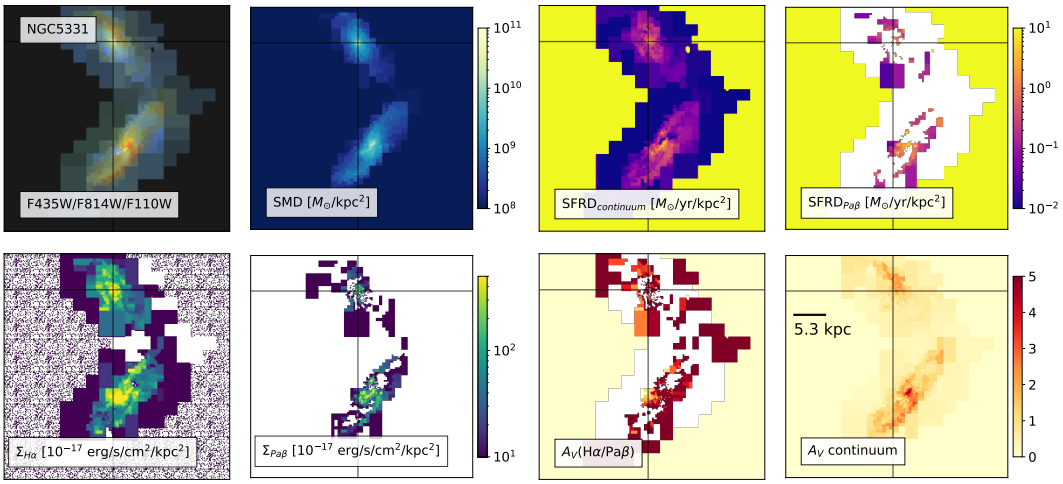

Figure 75: Maps of the physical properties inferred with our SED-fitting code for NGC5331. See Figure 59 for more details.

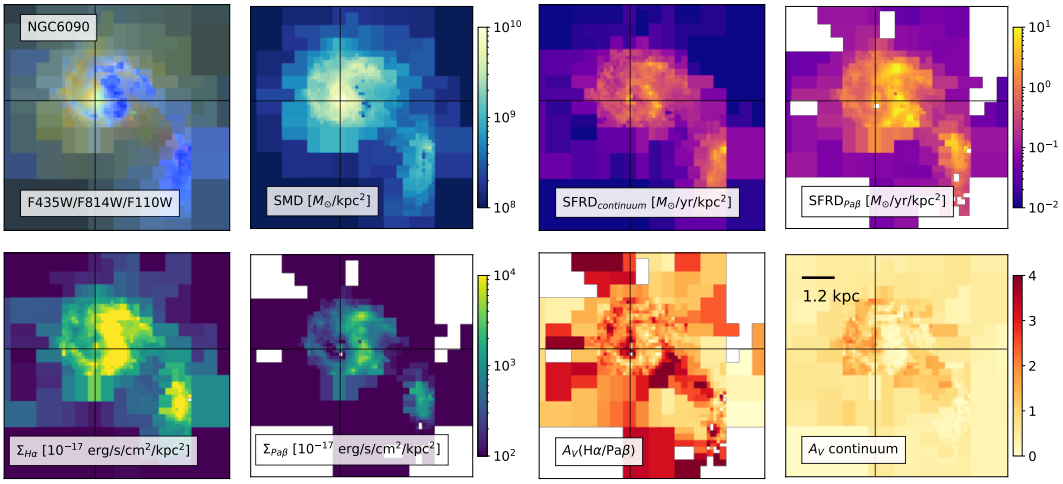

Figure 76: Maps of the physical properties inferred with our SED-fitting code for NGC6090. See Figure 59 for more details.

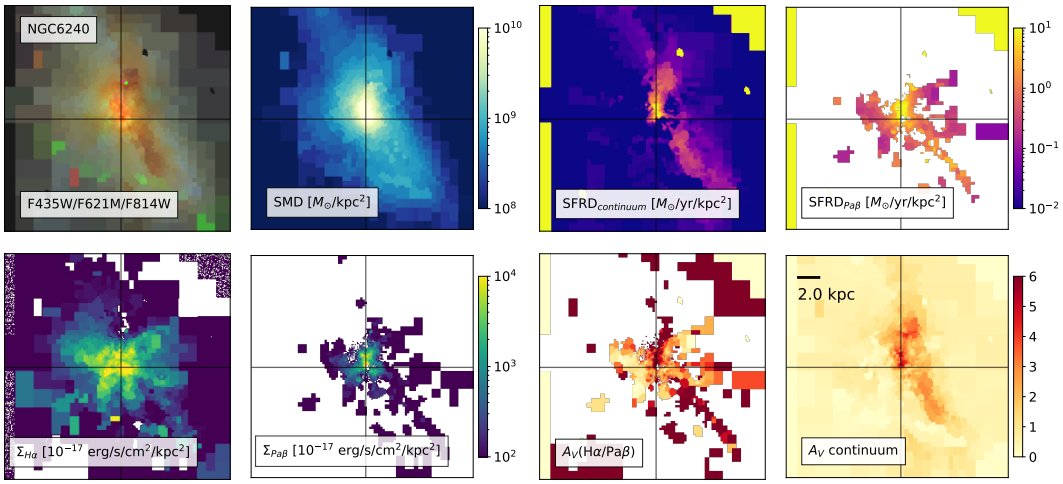

Figure 77: Maps of the physical properties inferred with our SED-fitting code for NGC6240. See Figure 59 for more details.

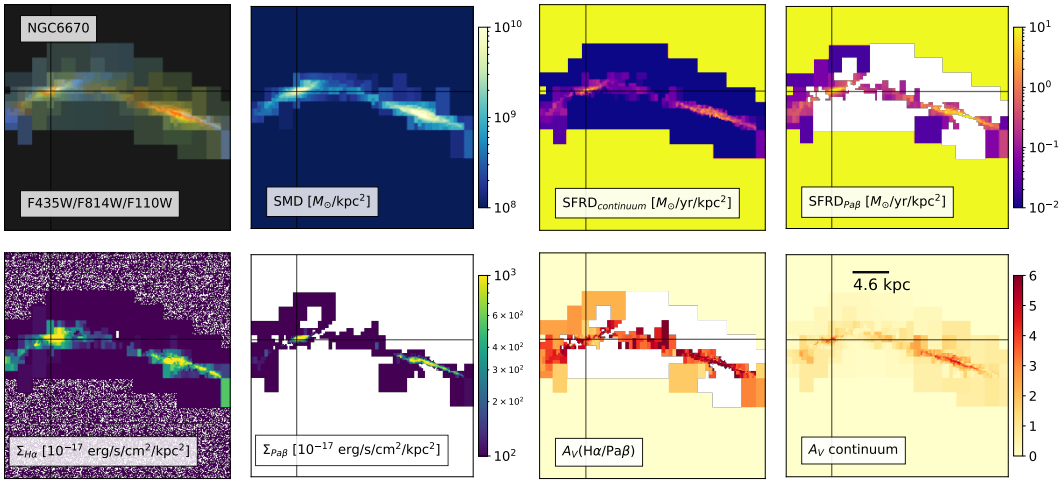

Figure 78: Maps of the physical properties inferred with our SED-fitting code for NGC6670. See Figure 59 for more details.

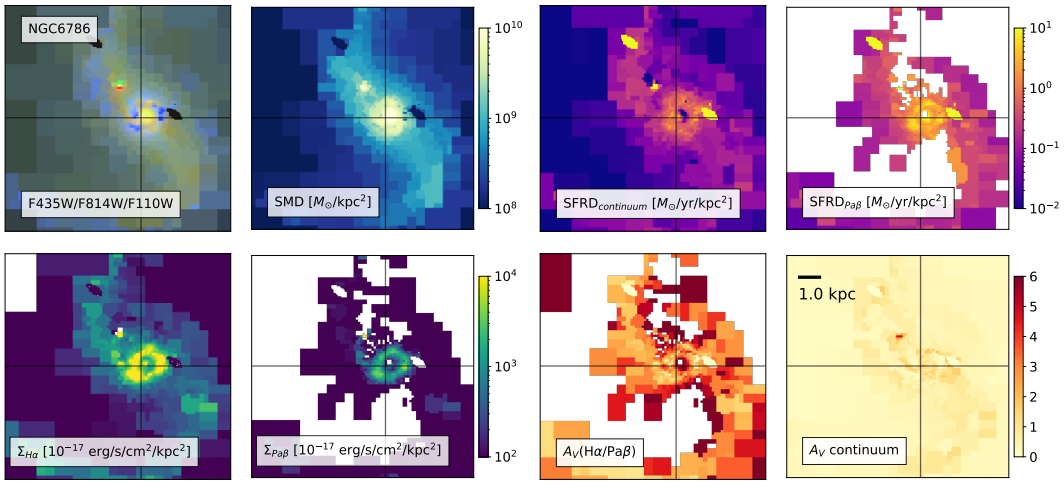

Figure 79: Maps of the physical properties inferred with our SED-fitting code for NGC6786. See Figure 59 for more details.

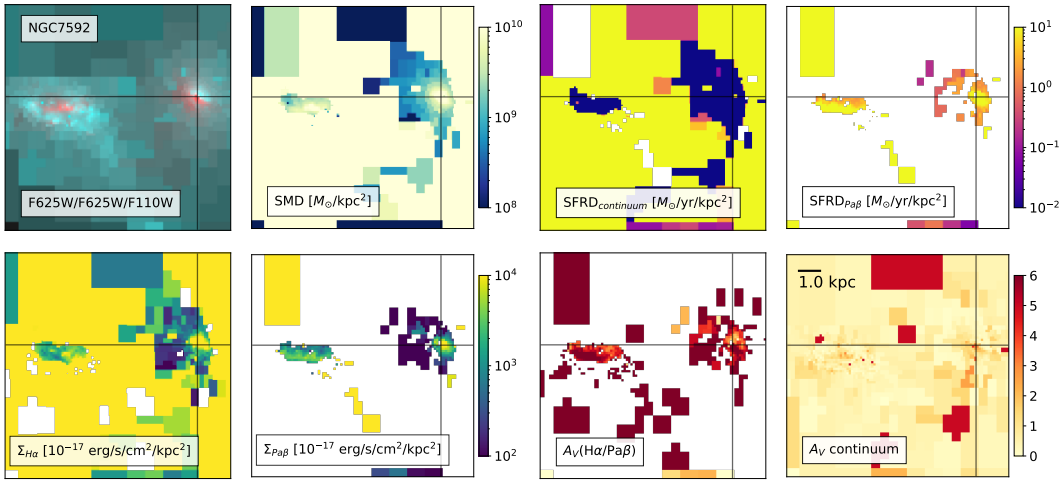

Figure 80: Maps of the physical properties inferred with our SED-fitting code for NGC7592. See Figure 59 for more details.

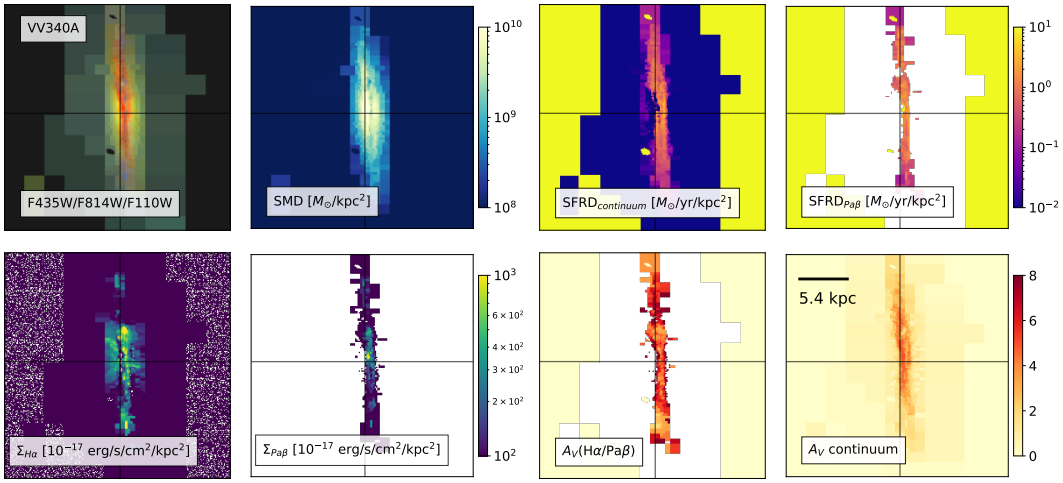

Figure 81: Maps of the physical properties inferred with our SED-fitting code for VV340A. See Figure 59 for more details.

Target	R.A. [deg]	Dec. [deg]	$z^{\dagger}$	$\log(\frac{L_{IR}}{L_{\odot}})$	UV WFC3/UVIS	Optical WFC3/UVIS, ACS/WFC	IR WFC3/IR
ESO338-IG004	291.99308	-41.57523	0.0095	-		F550M, FR656N	f110w, f130n
MCG+00-29-023	170.30109	-2.984167	0.0247	11.4*		f625w, f673n	f110w, f132n
M51	202.46958	47.19526	0.0016	10.4*	F225W, F275W, F336W	F435W, F555W, F606W, F658N, F673N, F689M, F814W	F110W, F128N
M82	148.96846	69.67970	0.0007	10.8*	F225W, F280N, F336W, F373N	F435W, F487N, F502N, F547M, F555W, F658N, F660N, F673N, F814W	f110w, f128n, F160W, F164N
M83	204.25383	-29.86576	0.0017	10.1*	F225W, F336W, F373N	F435W, F438W, F487N, F502N, F547M, F555W, F657N, F658N, F660N, F673N, F814W	F110W, F125W, F128N, F140W, F160W, F164N
NGC0253	11.88806	-25.2888	0.0009	10.4*		F475W, F606W, F814W	F110W, F128N, F130N, F160W, F164N
NGC1140	43.63976	-10.0285	0.0050	-		F625W, F658N	F110W, F128N, F160W, F164N
NGC1396	54.52743	-35.43992	0.0029	-		F475W, F606W, F625W, F658N, F850LP	f110w, f128n
NGC1482	58.6622	-20.50245	0.0063	10.8*		F621M, F657N	F110W, F128N, F160W, F164N
NGC2551	126.20956	73.41200	0.0077	-		F625W, F658N	f110w, f128n
NGC2681	133.38641	51.31371	0.0023	9.5*		F658N, F814W	f128n, f139m
NGC2841	140.51106	50.97648	0.0019	10.1**	F225W, F336W	F435W, F438W, F547M, F657N, F658N, F814W	F110W, f128n, f139m, F160W
NGC2985	147.59264	72.27865	0.0043	10.2*		F658N, F814W	f110w, f128n
NGC3358	160.88763	-36.41071	0.0101	-		f625w, f665n	f110w, f128n, f130n
NGC3738	173.95085	54.52373	0.0007	-		F438W, F606W, F658N, F814W	F110W, F128N, F160W
NGC4038	180.47084	-18.86759	0.0056	10.8*	F336W	F435W, F487N, F502N, F550M, F555W, F606W, F625W, FR656N, F658N, F673N, F814W	F110W, F128N, F160W, F164N

Table 3. (Continues below)

Target	R.A. [deg]	Dec. [deg]	$z^{\dagger}$	$\log(\frac{L_{IR}}{L_{\odot}})$	UV WFC3/UVIS	Optical WFC3/UVIS, ACS/WFC	IR WFC3/IR
NGC4214	183.91323	36.32689	0.0010	8.9*	F225W, F336W, F373N	F438W, F487N, F502N, F547M, F657N, F673N, F814W	F110W, F128N, F160W, F164N
NGC5128	201.36506	-43.01911	0.0018	10.1*	F225W, F336W	F438W, F487N, F502N, F547M, F657N, F673N, F814W	F128N, F160W, F164N
NGC6217	248.16340	78.19821	0.0046	10.3*		F435W, F625W, F658N, F814W	f110w, f128n
NGC6690	278.70935	70.52389	0.0016	-		F625W, F658N	f110w, f128n
NGC6946	308.718	60.1539	0.0001	10.9**		F435W, F547M, F555W, F606W, F657N, F673N, F814W	F110W, F128N, F160W, F164N
NGC6951	309.30865	66.10564	0.0048	10.6*		F555W, F658N, F814W	f110w, f128n
NGC7090	324.12027	-54.55732	0.0028	9.2*		F606W, F625W, F658N, F814W	f110w, f128n
PGC4798	20.01106	14.36153	0.0312	11.6*		F435W, f673n, F814W	f110w, f132n
SDSS-J110501.98 +594103.5	166.25825	59.68431	0.0338	-	F336W	F438W, F502N, F673N, F775W	f110w, f132n
SDSS-J172823.84 +573243.4	262.09933	57.54539	0.0290	-	F336W	F438W, F502N, F673N, F775W	f110w, f132n
SDSS220141.64 +115124.3	330.4235	11.85675	0.0296	-		FQ508N, F621M, F673N, F763M	f110w, f132n
UGC5626	156.11644	57.39251	0.0085	-		F625W, F658N	f110w, f130n

†The redshifts were extracted from the NASA/IPAC Extragalactic Database (NED), though we note that some of the closest targets are not necessarily in the Hubble flow.

*Infrared luminosity from the IRAS Revised Bright Galaxy Sample (Sanders et al. 2003).

**Infrared luminosity from the KINGFISH Survey (Kennicutt et al. 2011).

Table 9: (Continued) Sources in the sample of nearby star-forming galaxies presented in this work that are not part of the GOALS Survey (Armus et al. 2009). All targets have available reduced multi-band data, but are excluded in the analysis presented in this work. The filters added by the Cycle 23 SNAP program (HST-14095, Brammer 2015) are indicated with small caps, whereas the rest are archival data.

BIBLIOGRAPHY

Abdurro'uf, Coe, D., Jung, I., et al. 2023, ApJ, 945, 117

Abdurro'uf, Lin, Y.-T., Hirashita, H., et al. 2022, ApJ, 926, 81

Abramson, L. E., Gladders, M. D., Dressler, A., et al. 2015, ApJ, 801, L12

Abramson, L. E., Gladders, M. D., Dressler, A., et al. 2016, ApJ, 832, 7

Alonso-Herrero, A., Rieke, G. H., Rieke, M. J., et al. 2006, ApJ, 650, 835

Álvarez-Márquez, J., Colina, L., Crespo Gómez, A., et al. 2023a, arXiv e-prints, arXiv:2309.06319

Álvarez-Márquez, J., Crespo Gómez, A., Colina, L., et al. 2023b, A&A, 671, A105

Arellano-Córdova, K. Z., Berg, D. A., Chisholm, J., et al. 2022, ApJ, 940, L23

Armus, L., Mazzarella, J. M., Evans, A. S., et al. 2009, PASP, 121, 559

Arrabal Haro, P., Dickinson, M., Finkelstein, S. L., et al. 2023, Nature, 622, 707

Arribas, S., Colina, L., Alonso-Herrero, A., et al. 2012, A&A, 541, A20

Astropy Collaboration, Price-Whelan, A. M., Lim, P. L., et al. 2022, ApJ, 935, 167

Astropy Collaboration, Robitaille, T. P., Tollerud, E. J., et al. 2013, A&A, 558, A33

Atek, H., Furtak, L. J., Oesch, P., et al. 2022, MNRAS, 511, 4464

Atek, H., Shuntov, M., Furtak, L. J., et al. 2023, MNRAS, 519, 1201

Bacon, R., Accardo, M., Adjali, L., et al. 2010, in Society of Photo-Optical Instrumentation Engineers (SPIE) Conference Series, Vol. 7735, Ground-based and Airborne Instrumentation for Astronomy III, ed. I. S. McLean, S. K. Ramsay, & H. Takami, 773508

Baldwin, J. A., Phillips, M. M., & Terlevich, R. 1981, PASP, 93, 5

Beers, T. C., Flynn, K., & Gebhardt, K. 1990, AJ, 100, 32

Belfiore, F., Maiolino, R., Bundy, K., et al. 2015, MNRAS, 449, 867

Belfiore, F., Maiolino, R., Maraston, C., et al. 2016, MNRAS, 461, 3111

Belfiore, F., Maiolino, R., Tremonti, C., et al. 2017, MNRAS, 469, 151

Bell, E. F., Phleps, S., Somerville, R. S., et al. 2006, ApJ, 652, 270

Bellocchi, E., Pereira-Santaella, M., Colina, L., et al. 2022, A&A, 664, A60

Bertin, E. & Arnouts, S. 1996, A&AS, 117, 393

Béthermin, M., Fudamoto, Y., Ginolfi, M., et al. 2020, A&A, 643, A2

Bigiel, F., Leroy, A., Walter, F., et al. 2010, AJ, 140, 1194

Bischetti, M., Feruglio, C., Piconcelli, E., et al. 2021, A&A, 645, A33

Bisigello, L., Caputi, K. I., Colina, L., et al. 2019, ApJS, 243, 27

Böker, T., Arribas, S., Lützgendorf, N., et al. 2022, A&A, 661, A82

Bolatto, A. D., Wolfire, M., & Leroy, A. K. 2013, ARA&A, 51, 207

Boroson, T. 1981, ApJS, 46, 177

Boucaud, A., Bocchio, M., Abergel, A., et al. 2016, A&A, 596, A63

Bouwens, R., González-López, J., Aravena, M., et al. 2020, ApJ, 902, 112

Bouwens, R., Illingworth, G., Oesch, P., et al. 2023a, MNRAS, 523, 1009

Bouwens, R. J., Illingworth, G. D., Oesch, P. A., et al. 2015a, ApJ, 811, 140

Bouwens, R. J., Illingworth, G. D., Oesch, P. A., et al. 2015b, ApJ, 803, 34

Bouwens, R. J., Smit, R., Labbé, I., et al. 2016, ApJ, 831, 176

Bouwens, R. J., Smit, R., Schouws, S., et al. 2022, ApJ, 931, 160

Bouwens, R. J., Stefanon, M., Brammer, G., et al. 2023b, MNRAS, 523, 1036

Bowler, R. A. A., Bourne, N., Dunlop, J. S., McLure, R. J., & McLeod, D. J. 2018, MNRAS, 481, 1631

Bowler, R. A. A., Cullen, F., McLure, R. J., Dunlop, J. S., & Avison, A. 2022, MNRAS, 510, 5088

Boyett, K., Trenti, M., Leethochawalit, N., et al. 2023, arXiv e-prints, arXiv:2303.00306

Bradač, M., Strait, V., Mowla, L., et al. 2023, arXiv e-prints, arXiv:2308.13288

Brammer, G. 2015, Calibrating the Dusty Cosmos: Extinction Maps of Nearby Galaxies, HST Proposal id.14095. Cycle 23

Brammer, G. 2019, Grizli: Grism redshift and line analysis software, Astrophysics Source Code Library, record ascl:1905.001

Brammer, G. & Matharu, J. 2021, gbrammer/grizli: Release 2021, Zenodo

Brammer, G., Strait, V., Matharu, J., & Momcheva, I. 2022, grizli, Zenodo

Brammer, G. B., van Dokkum, P. G., & Coppi, P. 2008, ApJ, 686, 1503

Brammer, G. B., van Dokkum, P. G., Franx, M., et al. 2012, ApJS, 200, 13

Brammer, G. B., Whitaker, K. E., van Dokkum, P. G., et al. 2009, ApJ, 706, L173

Brinchmann, J. 2023, MNRAS, 525, 2087

Brinchmann, J., Charlot, S., White, S. D. M., et al. 2004, MNRAS, 351, 1151

Brinchmann, J. & Ellis, R. S. 2000, ApJ, 536, L77

Bromm, V. 2013, Reports on Progress in Physics, 76, 112901

Bromm, V. & Yoshida, N. 2011, ARA&A, 49, 373

Bruzual, G. & Charlot, S. 2003, MNRAS, 344, 1000

Buat, V., Noll, S., Burgarella, D., et al. 2012, A&A, 545, A141

Bundy, K., Bershady, M. A., Law, D. R., et al. 2015, ApJ, 798, 7

Calabrò, A., Daddi, E., Cassata, P., et al. 2018, ApJ, 862, L22

Calzetti, D. 2001, New A Rev., 45, 601

Calzetti, D., Armus, L., Bohlin, R. C., et al. 2000, ApJ, 533, 682

Calzetti, D., Battisti, A. J., Shivaei, I., et al. 2021, ApJ, 913, 37

Calzetti, D., Kennicutt, R. C., J., Bianchi, L., et al. 2005, ApJ, 633, 871

Calzetti, D., Kennicutt, R. C., Engelbracht, C. W., et al. 2007, ApJ, 666, 870

Calzetti, D., Kinney, A. L., & Storchi-Bergmann, T. 1994, ApJ, 429, 582

Calzetti, D., Kinney, A. L., & Storchi-Bergmann, T. 1996, ApJ, 458, 132

Capak, P. L., Carilli, C., Jones, G., et al. 2015, Nature, 522, 455

Cappellari, M. & Copin, Y. 2003, MNRAS, 342, 345

Cardelli, J. A., Clayton, G. C., & Mathis, J. S. 1989, ApJ, 345, 245

Carnall, A. C., Begley, R., McLeod, D. J., et al. 2023, MNRAS, 518, L45

Carnall, A. C., McLure, R. J., Dunlop, J. S., et al. 2019, MNRAS, 490, 417

Carnall, A. C., McLure, R. J., Dunlop, J. S., & Davé, R. 2018, MNRAS, 480, 4379

Casey, C. M., Akins, H. B., Shuntov, M., et al. 2023, arXiv e-prints, arXiv:2308.10932

Casey, C. M., Berta, S., Béthermin, M., et al. 2012, ApJ, 761, 140

Chabrier, G. 2003, PASP, 115, 763

Chatzikos, M., Bianchi, S., Camilloni, F., et al. 2023, Rev. Mexicana Astron. Astrofis., 59, 327

Chen, Z., Stark, D. P., Endsley, R., et al. 2023, MNRAS, 518, 5607

Chu, J. K., Sanders, D. B., Larson, K. L., et al. 2017, ApJS, 229, 25

Ciesla, L., Elbaz, D., & Fensch, J. 2017, A&A, 608, A41

Ciotti, L., Lanzoni, B., & Volonteri, M. 2007, ApJ, 658, 65

Claeyssens, A., Adamo, A., Richard, J., et al. 2023, MNRAS, 520, 2180

Clarke, L., Scarlata, C., Mehta, V., et al. 2021, ApJ, 912, L22

Clayton, G. C., Gordon, K. D., & Wolff, M. J. 2000, ApJS, 129, 147

Cleri, N. J., Trump, J. R., Backhaus, B. E., et al. 2022, ApJ, 929, 3

Closs, M. F., Ferruit, P., Lobb, D. R., et al. 2008, in Society of Photo-Optical Instrumentation Engineers (SPIE) Conference Series, Vol. 7010, Space Telescopes and Instrumentation 2008: Optical, Infrared, and Millimeter, ed. J. Oschmann, Jacobus M., M. W. M. de Graauw, & H. A. MacEwen, 701011

Coe, D., Salmon, B., Bradač, M., et al. 2019, ApJ, 884, 85

Coe, D., Zitrin, A., Carrasco, M., et al. 2013, ApJ, 762, 32

Conroy, C. 2013, ARA&A, 51, 393

Conroy, C. & Gunn, J. E. 2010a, FSPS: Flexible Stellar Population Synthesis, Astrophysics Source Code Library, record ascl:1010.043

Conroy, C. & Gunn, J. E. 2010b, ApJ, 712, 833

Conroy, C., Gunn, J. E., & White, M. 2009, ApJ, 699, 486

Conroy, C. & van Dokkum, P. G. 2012, ApJ, 760, 71

Conroy, C., White, M., & Gunn, J. E. 2010, ApJ, 708, 58

Conselice, C. J. 2014, ARA&A, 52, 291

Cortzen, I., Garrett, J., Magdis, G., et al. 2019, MNRAS, 482, 1618

Crain, R. A. & van de Voort, F. 2023, ARA&A, 61, 473

Curti, M., D'Eugenio, F., Carniani, S., et al. 2023a, MNRAS, 518, 425

Curti, M., Maiolino, R., Curtis-Lake, E., et al. 2023b, arXiv e-prints, arXiv:2304.08516

Curti, M., Mannucci, F., Cresci, G., & Maiolino, R. 2020, MNRAS, 491, 944

Curtis-Lake, E., Carniani, S., Cameron, A., et al. 2023, Nature Astronomy, 7, 622

Daddi, E., Cimatti, A., Renzini, A., et al. 2004, ApJ, 617, 746

Dayal, P. & Ferrara, A. 2018, Physics Reports, 780, 1

De Barros, S., Oesch, P. A., Labbé, I., et al. 2019, MNRAS, 489, 2355

de Graaff, A., Rix, H.-W., Carniani, S., et al. 2023, arXiv e-prints, arXiv:2308.09742

De Lucia, G. & Blaizot, J. 2007, MNRAS, 375, 2

De Marchi, G. & Panagia, N. 2014, MNRAS, 445, 93

Decarli, R., Walter, F., Venemans, B. P., et al. 2017, Nature, 545, 457

Djorgovski, S. & Davis, M. 1987, ApJ, 313, 59

Donnan, C. T., McLeod, D. J., Dunlop, J. S., et al. 2023a, MNRAS, 518, 6011

Donnan, C. T., McLeod, D. J., McLure, R. J., et al. 2023b, MNRAS, 520, 4554

Draine, B. T. 2003, ApJ, 598, 1017

Draine, B. T. 2009, in Astronomical Society of the Pacific Conference Series, Vol. 414, Cosmic Dust - Near and Far, ed. T. Henning, E. Grün, & J. Steinacker, 453

Draine, B. T. & Li, A. 2007, ApJ, 657, 810

Drory, N., Bender, R., & Hopp, U. 2004, ApJ, 616, L103

Duc, P.-A., Cuillandre, J.-C., Karabal, E., et al. 2015, MNRAS, 446, 120

Dumas, G., Schinnerer, E., Tabatabaei, F. S., et al. 2011, AJ, 141, 41

Dwek, E. 1998, ApJ, 501, 643

Eisenstein, D. J., Willott, C., Alberts, S., et al. 2023, arXiv e-prints, arXiv:2306.02465

Elbaz, D., Dickinson, M., Hwang, H. S., et al. 2011, A&A, 533, A119

Ellis, R. S., McLure, R. J., Dunlop, J. S., et al. 2013, ApJ, 763, L7

Endsley, R., Stark, D. P., Whitler, L., et al. 2023, MNRAS, 524, 2312

Faber, S. M. 1977, in Evolution of Galaxies and Stellar Populations, ed. B. M. Tinsley & D. C. Larson, Richard B. Gehret, 157

Fan, X., Strauss, M. A., Becker, R. H., et al. 2006, AJ, 132, 117

Ferland, G. J., Chatzikos, M., Guzmán, F., et al. 2017, Rev. Mexicana Astron. Astrofis., 53, 385

Feroz, F. & Hobson, M. P. 2008, MNRAS, 384, 449

Feroz, F., Hobson, M. P., & Bridges, M. 2009, MNRAS, 398, 1601

Ferrara, A., Bianchi, S., Cimatti, A., & Giovanardi, C. 1999, ApJS, 123, 437

Ferrarese, L. & Merritt, D. 2000, ApJ, 539, L9

Fetherolf, T., Reddy, N. A., Shapley, A. E., et al. 2020, MNRAS, 498, 5009

Finkelstein, S. L., Bagley, M. B., Ferguson, H. C., et al. 2023, ApJ, 946, L13

Fitzpatrick, E. L. 1999, PASP, 111, 63

Fitzpatrick, E. L. & Massa, D. 1990, ApJS, 72, 163

Fitzpatrick, E. L. & Massa, D. 2007, ApJ, 663, 320

Fitzpatrick, E. L. & Massa, D. 2009, ApJ, 699, 1209

Forconi, M., Ruchika, Melchiorri, A., Mena, O., & Menci, N. 2023, , 2023, 012

Foreman-Mackey, D. 2016, The Journal of Open Source Software, 1, 24

Förster Schreiber, N. M. & Wuyts, S. 2020, ARA&A, 58, 661

Fraser-McKelvie, A., Aragón-Salamanca, A., Merrifield, M., et al. 2018, MNRAS, 481, 5580

French, K. D. 2021, PASP, 133, 072001

Frogel, J. A. 1988, ARA&A, 26, 51

Fudamoto, Y., Smit, R., Bowler, R. A. A., et al. 2022, ApJ, 934, 144

Fujimoto, S., Ao, Y., Bartosch Caminha, G., et al. 2021a, Early Galaxy Assembly Uncovered with ALMA and JWST: A Remarkably UV and [CII] Bright, Strongly Lensed Sub-L* Galaxy at z=6.072, JWST Proposal. Cycle 1, ID. #1567

Fujimoto, S., Arrabal Haro, P., Dickinson, M., et al. 2023a, ApJ, 949, L25

Fujimoto, S., Bezanson, R., Labbe, I., et al. 2023b, arXiv e-prints, arXiv:2309.07834

Fujimoto, S., Kohno, K., Ouchi, M., et al. 2023c, arXiv e-prints, arXiv:2303.01658

Fujimoto, S., Oguri, M., Brammer, G., et al. 2021b, ApJ, 911, 99

Fujimoto, S., Ouchi, M., Ferrara, A., et al. 2019, ApJ, 887, 107

Fujimoto, S., Ouchi, M., Nakajima, K., et al. 2022, arXiv e-prints, arXiv:2212.06863

Fumagalli, M., Labbé, I., Patel, S. G., et al. 2014, ApJ, 796, 35

Fumagalli, M., O'Meara, J. M., & Prochaska, J. X. 2011, Science, 334, 1245

Furtak, L. J., Shuntov, M., Atek, H., et al. 2023, MNRAS, 519, 3064

Galilei, G. 1710, Dialogo sopra i due Massimi Sistemi del Mondo Tolemaico E Copernicano

Gallerani, S., Maiolino, R., Juarez, Y., et al. 2010, A&A, 523, A85

Giallongo, E., D'Odorico, S., Fontana, A., et al. 1998, AJ, 115, 2169

Giménez-Arteaga, C., Brammer, G. B., Marchesini, D., et al. 2022, ApJS, 263, 17

Giménez-Arteaga, C., Oesch, P. A., Brammer, G. B., et al. 2023, ApJ, 948, 126

Ginolfi, M., Jones, G. C., Béthermin, M., et al. 2020, A&A, 633, A90

Gonzaga, S., Hack, W., Fruchter, A., & Mack, J. 2012, The DrizzlePac Handbook

Gordon, K. D. & Clayton, G. C. 1998, ApJ, 500, 816

Gordon, K. D., Clayton, G. C., Misselt, K. A., Landolt, A. U., & Wolff, M. J. 2003, ApJ, 594, 279

Goto, T. 2005, MNRAS, 357, 937

Graham, A. W. & Driver, S. P. 2007, ApJ, 655, 77

Graves, G. J. & Faber, S. M. 2010, ApJ, 717, 803

Greener, M. J., Aragón-Salamanca, A., Merrifield, M. R., et al. 2020, MNRAS, 495, 2305

Grogin, N. A., Kocevski, D. D., Faber, S. M., et al. 2011, ApJS, 197, 35

Hainline, K. N., Johnson, B. D., Robertson, B., et al. 2023, arXiv e-prints, arXiv:2306.02468

Harikane, Y., Nakajima, K., Ouchi, M., et al. 2023a, arXiv e-prints, arXiv:2304.06658

Harikane, Y., Ouchi, M., Inoue, A. K., et al. 2020, ApJ, 896, 93

Harikane, Y., Ouchi, M., Oguri, M., et al. 2023b, ApJS, 265, 5

Harikane, Y., Zhang, Y., Nakajima, K., et al. 2023c, arXiv e-prints, arXiv:2303.11946

Häring, N. & Rix, H.-W. 2004, ApJ, 604, L89

Harris, C. R., Millman, K. J., van der Walt, S. J., et al. 2020, Nature, 585, 357

Haskell, P., Das, S., Smith, D. J. B., et al. 2023, arXiv e-prints, arXiv:2310.16097

Heger, A. & Woosley, S. E. 2002, ApJ, 567, 532

Heintz, K. E., Brammer, G. B., Giménez-Arteaga, C., et al. 2023a, Nature Astronomy [[arXiv]2212.02890]

Heintz, K. E., De Cia, A., Thöne, C. C., et al. 2023b, arXiv e-prints, arXiv:2308.14812

Heintz, K. E., Giménez-Arteaga, C., Fujimoto, S., et al. 2023c, ApJ, 944, L30

Heintz, K. E., Watson, D., Oesch, P. A., Narayanan, D., & Madden, S. C. 2021, ApJ, 922, 147

Herschel, W. 1802, Philosophical Transactions of the Royal Society of London Series I, 92, 477

Hill, A. R., Muzzin, A., Franx, M., et al. 2017, ApJ, 837, 147

Hopkins, P. F., Hernquist, L., Cox, T. J., et al. 2006, ApJS, 163, 1

Hopkins, P. F., Hernquist, L., Cox, T. J., & Kereš, D. 2008, ApJS, 175, 356

Hoyle, F. & Wickramasinghe, N. C. 1970, Nature, 226, 62

Hsiao, T. Y.-Y., Coe, D., Abdurro'uf, et al. 2023, ApJ, 949, L34

Hubble, E. 1929, Proceedings of the National Academy of Science, 15, 168

Hubble, E. P. 1926, ApJ, 64, 321

Hunter, J. D. 2007, Computing in Science & Engineering, 9, 90

Hutter, A., Dayal, P., Yepes, G., et al. 2021, MNRAS, 503, 3698

Illingworth, G. D., Magee, D., Oesch, P. A., et al. 2013, ApJS, 209, 6

Iwasawa, K., Sanders, D. B., Teng, S. H., et al. 2011, A&A, 529, A106

Iyer, K. G., Tacchella, S., Genel, S., et al. 2020, MNRAS, 498, 430

Jain, S., Tacchella, S., & Mosleh, M. 2023, MNRAS[[arXiv]2310.18462]

Jakobsen, P., Ferruit, P., Alves de Oliveira, C., et al. 2022, A&A, 661, A80

Jermyn, A. S., Steinhardt, C. L., & Tout, C. A. 2018, MNRAS, 480, 4265

Jin, J.-J., Zhu, Y.-N., Wu, H., et al. 2019, ApJS, 244, 33

Johnson, B., Foreman-Mackey, D., Sick, J., et al. 2021, dfm/python-fsps: python-fsps v0.4.1rc1, Zenodo

Johnson, B. & Leja, J. 2017, Bd-J/Prospector: Initial Release

Jones, A. P. & Nuth, J. A. 2011, A&A, 530, A44

Jones, G. C., Béthermin, M., Fudamoto, Y., et al. 2020, MNRAS, 491, L18

Katz, H., Rosdahl, J., Kimm, T., et al. 2023, arXiv e-prints, arXiv:2309.03269

Kennicutt, Robert C., J. 1998, ARA&A, 36, 189

Kennicutt, Robert C., J., Armus, L., Bendo, G., et al. 2003, PASP, 115, 928

Kennicutt, Robert C., J., Calzetti, D., Walter, F., et al. 2007, ApJ, 671, 333

Kennicutt, Robert C., J., Hao, C.-N., Calzetti, D., et al. 2009, ApJ, 703, 1672

Kennicutt, R. C., Calzetti, D., Aniano, G., et al. 2011, PASP, 123, 1347

Kennicutt, R. C. & Evans, N. J. 2012, ARA&A, 50, 531

Kewley, L. J., Dopita, M. A., Leitherer, C., et al. 2013a, ApJ, 774, 100

Kewley, L. J., Geller, M. J., & Jansen, R. A. 2004, AJ, 127, 2002

Kewley, L. J., Geller, M. J., Jansen, R. A., & Dopita, M. A. 2002, AJ, 124, 3135

Kewley, L. J., Maier, C., Yabe, K., et al. 2013b, ApJ, 774, L10

Kewley, L. J., Nicholls, D. C., & Sutherland, R. S. 2019, ARA&A, 57, 511

Kilgard, R. E., Dorn-Wallenstein, T., Kuntz, K. D., & Desjardins, T. D. 2014, in American Astronomical Society Meeting Abstracts, Vol. 224, American Astronomical Society Meeting Abstracts #224, 314.02

Killi, M., Watson, D., Fujimoto, S., et al. 2023, MNRAS, 521, 2526

King, A. & Pounds, K. 2015, ARA&A, 53, 115

Koekemoer, A. M., Faber, S. M., Ferguson, H. C., et al. 2011, ApJS, 197, 36

Kormendy, J. & Gebhardt, K. 2001, in American Institute of Physics Conference Series, Vol. 586, 20th Texas Symposium on relativistic astrophysics, ed. J. C. Wheeler & H. Martel, 363–381

Kormendy, J. & Ho, L. C. 2013, ARA&A, 51, 511

Kreckel, K., Groves, B., Schinnerer, E., et al. 2013, ApJ, 771, 62

Kriek, M. & Conroy, C. 2013, ApJ, 775, L16

Kroupa, P. 2001, MNRAS, 322, 231

Labbé, I., Oesch, P. A., Bouwens, R. J., et al. 2013, ApJ, 777, L19

Labbé, I., van Dokkum, P., Nelson, E., et al. 2023, Nature, 616, 266

Lacey, C. & Cole, S. 1993, MNRAS, 262, 627

Laigle, C., McCracken, H. J., Ilbert, O., et al. 2016, ApJS, 224, 24

Lam, D., Bouwens, R. J., Labbé, I., et al. 2019, A&A, 627, A164

Lambas, D. G., Alonso, S., Mesa, V., & O'Mill, A. L. 2012, A&A, 539, A45

Lang, D., Hogg, D. W., & Mykytyn, D. 2016, The Tractor: Probabilistic astronomical source detection and measurement, Astrophysics Source Code Library, record ascl:1604.008

Laporte, N., Ellis, R. S., Witten, C. E. C., & Roberts-Borsani, G. 2023, MNRAS, 523, 3018

Laporte, N., Zitrin, A., Ellis, R. S., et al. 2021, MNRAS, 505, 4838

Laursen, P. 2023, in Multiplicity of Time Scales in Complex Systems, 71

Lawrence, A., Warren, S. J., Almaini, O., et al. 2007, MNRAS, 379, 1599

Le Fèvre, O., Abraham, R., Lilly, S. J., et al. 2000, MNRAS, 311, 565

Le Fèvre, O., Saisse, M., Mancini, D., et al. 2003, in Society of Photo-Optical Instrumentation Engineers (SPIE) Conference Series, Vol. 4841, Instrument Design and Performance for Optical/Infrared Ground-based Telescopes, ed. M. Iye & A. F. M. Moorwood, 1670–1681

Le Fèvre, O., Vettolani, G., Garilli, B., et al. 2005, A&A, 439, 845

Leavitt, H. S. & Pickering, E. C. 1912, Harvard College Observatory Circular, 173, 1

Leethochawalit, N., Trenti, M., Santini, P., et al. 2023, ApJ, 942, L26

Leja, J., Johnson, B. D., Conroy, C., et al. 2019, ApJ, 877, 140

Leja, J., Johnson, B. D., Conroy, C., van Dokkum, P. G., & Byler, N. 2017, ApJ, 837, 170

Leja, J., Speagle, J. S., Johnson, B. D., et al. 2020, ApJ, 893, 111

Leja, J., van Dokkum, P. G., Franx, M., & Whitaker, K. E. 2015, ApJ, 798, 115

Leroy, A. K., Bolatto, A., Gordon, K., et al. 2011, ApJ, 737, 12

Leslie, S. K., Schinnerer, E., Liu, D., et al. 2020, ApJ, 899, 58

Linden, S. T., Evans, A. S., Larson, K., et al. 2021, ApJ, 923, 278

Linden, S. T., Song, Y., Evans, A. S., et al. 2019, ApJ, 881, 70

Liu, G., Calzetti, D., Hong, S., et al. 2013, ApJ, 778, L41

Lower, S., Narayanan, D., Leja, J., et al. 2020, ApJ, 904, 33

Lucy, L. B. 1974, AJ, 79, 745

Lupton, R., Blanton, M. R., Fekete, G., et al. 2004, PASP, 116, 133

Lynden-Bell, D. 1969, Nature, 223, 690

Lyu, C., Peng, Y., Jing, Y., et al. 2023, arXiv e-prints, arXiv:2310.10733

Madau, P. & Dickinson, M. 2014, ARA&A, 52, 415

Magnelli, B., Popesso, P., Berta, S., et al. 2013, A&A, 553, A132

Magorrian, J., Tremaine, S., Richstone, D., et al. 1998, AJ, 115, 2285

Maiolino, R. & Mannucci, F. 2019, A&A Rev., 27, 3

Maiolino, R., Scholtz, J., Curtis-Lake, E., et al. 2023, arXiv e-prints, arXiv:2308.01230

Man, A. & Belli, S. 2018, Nature Astronomy, 2, 695

Mannucci, F., Cresci, G., Maiolino, R., Marconi, A., & Gnerucci, A. 2010, MNRAS, 408, 2115

Maraston, C. 2005, MNRAS, 362, 799

Maraston, C., Pforr, J., Henriques, B. M., et al. 2013, MNRAS, 435, 2764

Maraston, C., Pforr, J., Renzini, A., et al. 2010, MNRAS, 407, 830

Marchesini, D., Muzzin, A., Stefanon, M., et al. 2014, ApJ, 794, 65

Marsan, Z. C., Marchesini, D., Muzzin, A., et al. 2019, ApJ, 871, 201

Marsan, Z. C., Muzzin, A., Marchesini, D., et al. 2022, ApJ, 924, 25

Martín-Navarro, I., La Barbera, F., Vazdekis, A., Falcón-Barroso, J., & Ferreras, I. 2015, MNRAS, 447, 1033

Martis, N. S., Marchesini, D. M., Muzzin, A., et al. 2019, ApJ, 882, 65

Mason, C. A., Trenti, M., & Treu, T. 2023, MNRAS, 521, 497

Mason, C. A., Treu, T., de Barros, S., et al. 2018, ApJ, 857, L11

Matthee, J., Mackenzie, R., Simcoe, R. A., et al. 2023, ApJ, 950, 67

Matthee, J., Pezzulli, G., Mackenzie, R., et al. 2020, MNRAS, 498, 3043

Matthee, J., Sobral, D., Best, P., et al. 2017, MNRAS, 465, 3637

Matthee, J., Sobral, D., Boogaard, L. A., et al. 2019, ApJ, 881, 124

McCracken, H. J., Milvang-Jensen, B., Dunlop, J., et al. 2012, A&A, 544, A156

McLure, R. J., Dunlop, J. S., Bowler, R. A. A., et al. 2013, MNRAS, 432, 2696

Michałowski, M. J., Murphy, E. J., Hjorth, J., et al. 2010, A&A, 522, A15

Miller, G. E. & Scalo, J. M. 1979, ApJS, 41, 513

Mingozzi, M., Cresci, G., Venturi, G., et al. 2019, A&A, 622, A146

Mitchell, P. D., Lacey, C. G., Baugh, C. M., & Cole, S. 2013, MNRAS, 435, 87

Mitchell, P. D., Lacey, C. G., Cole, S., & Baugh, C. M. 2014, MNRAS, 444, 2637

Moffat, A. F. J. 1969, A&A, 3, 455

Morselli, L., Popesso, P., Cibinel, A., et al. 2019, A&A, 626, A61

Mortlock, A., McLure, R. J., Bowler, R. A. A., et al. 2017, MNRAS, 465, 672

Moustakas, J., Kennicutt, Robert C., J., Tremonti, C. A., et al. 2010, ApJS, 190, 233

Murphy, E. J., Dong, D., Momjian, E., et al. 2018, ApJS, 234, 24

Muzzin, A., Marchesini, D., Stefanon, M., et al. 2013, ApJ, 777, 18

Muzzin, A., Marchesini, D., van Dokkum, P. G., et al. 2009, ApJ, 701, 1839

Muzzin, A., van Dokkum, P., Kriek, M., et al. 2010, ApJ, 725, 742

Naidu, R. P., Oesch, P. A., Setton, D. J., et al. 2022a, arXiv e-prints, arXiv:2208.02794

Naidu, R. P., Oesch, P. A., van Dokkum, P., et al. 2022b, ApJ, 940, L14

Nakajima, K. & Maiolino, R. 2022, MNRAS, 513, 5134

Nakajima, K., Ouchi, M., Isobe, Y., et al. 2023, arXiv e-prints, arXiv:2301.12825

Narayanan, D., Conroy, C., Davé, R., Johnson, B. D., & Popping, G. 2018, ApJ, 869, 70

Narayanan, D., Krumholz, M. R., Ostriker, E. C., & Hernquist, L. 2012, MNRAS, 421, 3127

Narayanan, D., Lower, S., Torrey, P., et al. 2023a, arXiv e-prints, arXiv:2306.10118

Narayanan, D., Smith, J. D. T., Hensley, B. S., et al. 2023b, ApJ, 951, 100

Nelson, E. J., Brammer, G., Gimenez-Arteaga, C., et al. 2023, arXiv e-prints, arXiv:2310.06887

Nelson, E. J., Tadaki, K.-i., Tacconi, L. J., et al. 2019, ApJ, 870, 130

Noeske, K. G., Weiner, B. J., Faber, S. M., et al. 2007, ApJ, 660, L43

Noguchi, M. 2023, MNRAS, 522, 4691

Oesch, P. A., Bouwens, R. J., Illingworth, G. D., et al. 2015, ApJ, 808, 104

Oesch, P. A., Bouwens, R. J., Illingworth, G. D., et al. 2013, ApJ, 773, 75

Oesch, P. A., Bouwens, R. J., Illingworth, G. D., et al. 2014, ApJ, 786, 108

Oesch, P. A., Brammer, G., Naidu, R. P., et al. 2023, MNRAS, 525, 2864

Oesch, P. A., Brammer, G., van Dokkum, P. G., et al. 2016, ApJ, 819, 129

Oguri, M. 2010, glafic: Software Package for Analyzing Gravitational Lensing, Astrophysics Source Code Library, record ascl:1010.012

O'Leary, J. A., Moster, B. P., Naab, T., & Somerville, R. S. 2021, MNRAS, 501, 3215

Ono, Y., Harikane, Y., Ouchi, M., et al. 2023, arXiv e-prints, arXiv:2309.02790

Osterbrock, D. E. 1989, Astrophysics of gaseous nebulae and active galactic nuclei

Pacifici, C., Iyer, K. G., Mobasher, B., et al. 2023, ApJ, 944, 141

Pallottini, A., Ferrara, A., Gallerani, S., et al. 2022, MNRAS, 513, 5621

Pang, X., Pasquali, A., & Grebel, E. K. 2011, AJ, 142, 132

Papovich, C., Cole, J. W., Yang, G., et al. 2023, ApJ, 949, L18

Papovich, C., Dickinson, M., & Ferguson, H. C. 2001, ApJ, 559, 620

Papovich, C., Finkelstein, S. L., Ferguson, H. C., Lotz, J. M., & Giavalisco, M. 2011, MNRAS, 412, 1123

Parkin, T. J., Wilson, C. D., Schirm, M. R. P., et al. 2013, ApJ, 776, 65

Paulino-Afonso, A., González-Gaitán, S., Galbany, L., et al. 2022, A&A, 662, A86

Pawlik, M. M., McAlpine, S., Trayford, J. W., et al. 2019, Nature Astronomy, 3, 440

Penzias, A. A. & Wilson, R. W. 1965, ApJ, 142, 419

Pereira-Santaella, M., Colina, L., Alonso-Herrero, A., et al. 2015, MNRAS, 454, 3679

Pereira-Santaella, M., Colina, L., García-Burillo, S., et al. 2021, A&A, 651, A42

Pérez-González, P. G., Barro, G., Annunziatella, M., et al. 2023, ApJ, 946, L16

Pérez-González, P. G., Rieke, G. H., Egami, E., et al. 2005, ApJ, 630, 82

Perna, M., Arribas, S., Catalán-Torrecilla, C., et al. 2020, A&A, 643, A139

Perna, M., Arribas, S., Pereira Santaella, M., et al. 2021, A&A, 646, A101

Perna, M., Cresci, G., Brusa, M., et al. 2019, A&A, 623, A171

Perrin, M. D., Sivaramakrishnan, A., Lajoie, C.-P., et al. 2014, in Society of Photo-Optical Instrumentation Engineers (SPIE) Conference Series, Vol. 9143, Space Telescopes and Instrumentation 2014: Optical, Infrared, and Millimeter Wave, ed. J. Oschmann, Jacobus M., M. Clampin, G. G. Fazio, & H. A. MacEwen, 91433X

Perrin, M. D., Soummer, R., Elliott, E. M., Lallo, M. D., & Sivaramakrishnan, A. 2012, in Society of Photo-Optical Instrumentation Engineers (SPIE) Conference Series, Vol. 8442, Space Telescopes and Instrumentation 2012: Optical, Infrared, and Millimeter Wave, ed. M. C. Clampin, G. G. Fazio, H. A. MacEwen, & J. Oschmann, Jacobus M., 84423D

Pforr, J., Maraston, C., & Tonini, C. 2012, MNRAS, 422, 3285

Pforr, J., Maraston, C., & Tonini, C. 2013, MNRAS, 435, 1389

Piqueras López, J., Colina, L., Arribas, S., Pereira-Santaella, M., & Alonso-Herrero, A. 2016, A&A, 590, A67

Pontoppidan, K. M., Barrientes, J., Blome, C., et al. 2022, ApJ, 936, L14

Pope, A., Armus, L., Murphy, E., et al. 2019, BAAS, 51, 330

Pope, A., Chary, R.-R., Alexander, D. M., et al. 2008, ApJ, 675, 1171

Popescu, C. C., Tuffs, R. J., Dopita, M. A., et al. 2011, A&A, 527, A109

Prevot, M. L., Lequeux, J., Maurice, E., Prevot, L., & Rocca-Volmerange, B. 1984, A&A, 132, 389

Prieto-Lyon, G., Strait, V., Mason, C. A., et al. 2023, A&A, 672, A186

Puglisi, A., Daddi, E., Renzini, A., et al. 2017, ApJ, 838, L18

Rafelski, M., Neeleman, M., Fumagalli, M., Wolfe, A. M., & Prochaska, J. X. 2014, ApJ, 782, L29

Ramburuth-Hurt, T., De Cia, A., Krogager, J. K., et al. 2023, A&A, 672, A68

Reddy, N., Dickinson, M., Elbaz, D., et al. 2012, ApJ, 744, 154

Reddy, N. A., Kriek, M., Shapley, A. E., et al. 2015, ApJ, 806, 259

Reddy, N. A., Topping, M. W., Sanders, R. L., Shapley, A. E., & Brammer, G. 2023, ApJ, 948, 83

Renaud, F., Bournaud, F., Agertz, O., et al. 2019, A&A, 625, A65

Rhoads, J. E., Wold, I. G. B., Harish, S., et al. 2023, ApJ, 942, L14

Ricci, C., Privon, G. C., Pfeifle, R. W., et al. 2021, MNRAS, 506, 5935

Richardson, W. H. 1972, Journal of the Optical Society of America (1917-1983), 62, 55

Richstone, D., Ajhar, E. A., Bender, R., et al. 1998, Nature, 385, A14

Rieke, G. H., Alonso-Herrero, A., Weiner, B. J., et al. 2009, ApJ, 692, 556

Rieke, G. H. & Lebofsky, M. J. 1985, ApJ, 288, 618

Rieke, M. J., Kelly, D., & Horner, S. 2005, in Society of Photo-Optical Instrumentation Engineers (SPIE) Conference Series, Vol. 5904, Cryogenic Optical Systems and Instruments XI, ed. J. B. Heaney & L. G. Burriesci, 1–8

Rieke, M. J., Kelly, D. M., Misselt, K., et al. 2023, PASP, 135, 028001

Rizzo, F., Roman-Oliveira, F., Fraternali, F., et al. 2023, arXiv e-prints, arXiv:2303.16227

Roberts-Borsani, G. W., Ellis, R. S., & Laporte, N. 2020, MNRAS, 497, 3440

Robertson, B. E. 2022, ARA&A, 60, 121

Robertson, B. E., Furlanetto, S. R., Schneider, E., et al. 2013, ApJ, 768, 71

Robertson, B. E., Tacchella, S., Johnson, B. D., et al. 2023, Nature Astronomy, 7, 611

Rochberg, F. 2004, The Heavenly Writing: Divination, Horoscopy, and Astronomy in Mesopotamian Culture (Cambridge University Press)

Rodighiero, G., Bisigello, L., Iani, E., et al. 2023, MNRAS, 518, L19

Rodrigo, C. & Solano, E. 2020, in XIV.0 Scientific Meeting (virtual) of the Spanish Astronomical Society, 182

Roebuck, E., Sajina, A., Hayward, C. C., et al. 2019, ApJ, 881, 18

Romano, M., Cassata, P., Morselli, L., et al. 2021, A&A, 653, A111

Rosdahl, J., Katz, H., Blaizot, J., et al. 2018, MNRAS, 479, 994

Rudnick, G., Franx, M., Rix, H.-W., et al. 2001, AJ, 122, 2205

Rudnick, G., Rix, H.-W., Franx, M., et al. 2003, ApJ, 599, 847

Rusakov, V., Steinhardt, C. L., & Sneppen, A. 2023, ApJS, 268, 10

Russell, H. N. 1914, Popular Astronomy, 22, 275

Sahu, K. 2021, in WFC3 Data Handbook v. 5, Vol. 5, 5

Salim, S., Boquien, M., & Lee, J. C. 2018, ApJ, 859, 11

Salim, S. & Narayanan, D. 2020, ARA&A, 58, 529

Salmon, B., Papovich, C., Long, J., et al. 2016, ApJ, 827, 20

Salpeter, E. E. 1955, ApJ, 121, 161

Sánchez, S. F., Kennicutt, R. C., Gil de Paz, A., et al. 2012, A&A, 538, A8

Sanders, D. B., Mazzarella, J. M., Kim, D. C., Surace, J. A., & Soifer, B. T. 2003, AJ, 126, 1607

Sanders, D. B. & Mirabel, I. F. 1996, ARA&A, 34, 749

Sarangi, A., Matsuura, M., & Micelotta, E. R. 2019, in Supernovae. Series: Space Sciences Series of ISSI, ed. A. Bykov, C. Roger, J. Raymond, F.-K. Thielemann, M. Falanga, & R. von Steiger, Vol. 68, 313–360

Savage, B. D. & Mathis, J. S. 1979, ARA&A, 17, 73

Sawicki, M. & Yee, H. K. C. 1998, AJ, 115, 1329

Schaerer, D. & de Barros, S. 2009, A&A, 502, 423

Schaerer, D., Marques-Chaves, R., Barrufet, L., et al. 2022, A&A, 665, L4

Schinnerer, E., Meidt, S. E., Pety, J., et al. 2013, ApJ, 779, 42

Schlafly, E. F. & Finkbeiner, D. P. 2011, ApJ, 737, 103

Schneider, R., Valiante, R., Ventura, P., et al. 2014, MNRAS, 442, 1440

Schreiber, C., Pannella, M., Elbaz, D., et al. 2015, A&A, 575, A74

Scoville, N., Aussel, H., Brusa, M., et al. 2007, ApJS, 172, 1

Shapley, A. E., Steidel, C. C., Adelberger, K. L., et al. 2001, ApJ, 562, 95

Shapley, A. E., Steidel, C. C., Erb, D. K., et al. 2005, ApJ, 626, 698

Shen, L., Papovich, C., Matharu, J., et al. 2023a, arXiv e-prints, arXiv:2310.13745

Shen, X., Vogelsberger, M., Boylan-Kolchin, M., Tacchella, S., & Kannan, R. 2023b, MNRAS, 525, 3254

Shipley, H. V., Lange-Vagle, D., Marchesini, D., et al. 2018, ApJS, 235, 14

Shivaei, I., Reddy, N. A., Siana, B., et al. 2018, ApJ, 855, 42

Silva, A., Marchesini, D., Silverman, J. D., et al. 2018, ApJ, 868, 46

Simmonds, C., Tacchella, S., Hainline, K., et al. 2023, arXiv e-prints, arXiv:2310.01112

Skelton, R. E., Whitaker, K. E., Momcheva, I. G., et al. 2014, ApJS, 214, 24

Smit, R., Bouwens, R. J., Carniani, S., et al. 2018, Nature, 553, 178

Smit, R., Bouwens, R. J., Franx, M., et al. 2015, ApJ, 801, 122

Smit, R., Bouwens, R. J., Labbé, I., et al. 2016, ApJ, 833, 254

Smit, R., Bouwens, R. J., Labbé, I., et al. 2014, ApJ, 784, 58

Sneppen, A., Steinhardt, C. L., Hensley, H., et al. 2022, ApJ, 931, 57

Somerville, R. S. & Davé, R. 2015, ARA&A, 53, 51

Sommovigo, L., Ferrara, A., Carniani, S., et al. 2022, MNRAS, 517, 5930

Sommovigo, L., Ferrara, A., Pallottini, A., et al. 2020, MNRAS, 497, 956

Song, J., Fang, G., Lin, Z., Gu, Y., & Kong, X. 2023, ApJ, 958, 82

Song, M., Finkelstein, S. L., Ashby, M. L. N., et al. 2016, ApJ, 825, 5

Song, Y., Linden, S. T., Evans, A. S., et al. 2021, ApJ, 916, 73

Sorba, R. & Sawicki, M. 2015, MNRAS, 452, 235

Sorba, R. & Sawicki, M. 2018, MNRAS, 476, 1532

Sparre, M., Hayward, C. C., Springel, V., et al. 2015, MNRAS, 447, 3548

Springel, V., White, S. D. M., Jenkins, A., et al. 2005, Nature, 435, 629

Stark, D. P., Schenker, M. A., Ellis, R., et al. 2013, ApJ, 763, 129

Stefanon, M., Bouwens, R. J., Illingworth, G. D., et al. 2022, ApJ, 935, 94

Stefanon, M., Bouwens, R. J., Labbé, I., et al. 2021, ApJ, 922, 29

Stefanon, M., Marchesini, D., Muzzin, A., et al. 2015, ApJ, 803, 11

Steidel, C. C., Adelberger, K. L., Shapley, A. E., et al. 2003, ApJ, 592, 728

Steinhardt, C. L., Sneppen, A., Mostafa, B., et al. 2022, ApJ, 931, 58

Strait, V., Bradač, M., Coe, D., et al. 2021, ApJ, 910, 135

Strait, V., Brammer, G., Muzzin, A., et al. 2023, ApJ, 949, L23

Suess, K., Atek, H., Bezanson, R., et al. 2023, Medium bands, Mega Science: spatially-resolved R 15 spectrophotometry of 50,000 sources at z=0.3-12, JWST Proposal. Cycle 2, ID. #4111

Suess, K. A., Kriek, M., Price, S. H., & Barro, G. 2019, ApJ, 885, L22

Suess, K. A., Leja, J., Johnson, B. D., et al. 2022, ApJ, 935, 146

Sugahara, Y., Inoue, A. K., Fudamoto, Y., et al. 2022, ApJ, 935, 119

Sun, F., Helton, J. M., Egami, E., et al. 2023, arXiv e-prints, arXiv:2309.04529

Tacchella, S., Johnson, B. D., Robertson, B. E., et al. 2023, MNRAS, 522, 6236

Tacconi, L. J., Genzel, R., & Sternberg, A. 2020, ARA&A, 58, 157

Tanaka, T. S., Shimasaku, K., Tacchella, S., et al. 2023, arXiv e-prints, arXiv:2307.14235

Tang, M., Stark, D. P., & Ellis, R. S. 2022, MNRAS, 513, 5211

Tateuchi, K., Konishi, M., Motohara, K., et al. 2015, ApJS, 217, 1

Tinsley, B. M. 1980, Fund. Cosmic Phys., 5, 287

Toft, S., Smolčić, V., Magnelli, B., et al. 2014, ApJ, 782, 68

Topping, M. W., Stark, D. P., Endsley, R., et al. 2022, MNRAS, 516, 975

Torres-Albà, N., Iwasawa, K., Díaz-Santos, T., et al. 2018, A&A, 620, A140

Trager, S. C., Faber, S. M., & Dressler, A. 2008, MNRAS, 386, 715

Trebitsch, M., Volonteri, M., & Dubois, Y. 2020, MNRAS, 494, 3453

Tremaine, S., Gebhardt, K., Bender, R., et al. 2002, ApJ, 574, 740

Treu, T., Calabrò, A., Castellano, M., et al. 2023, ApJ, 942, L28

Treu, T., Schmidt, K. B., Trenti, M., Bradley, L. D., & Stiavelli, M. 2013, ApJ, 775, L29

Trump, J. R., Arrabal Haro, P., Simons, R. C., et al. 2023, ApJ, 945, 35

Trussler, J. A. A., Conselice, C. J., Adams, N. J., et al. 2023, MNRAS, 525, 5328

Tumlinson, J., Peeples, M. S., & Werk, J. K. 2017, ARA&A, 55, 389

U, V., Medling, A. M., Inami, H., et al. 2019, ApJ, 871, 166

U, V., Sanders, D. B., Mazzarella, J. M., et al. 2012, ApJS, 203, 9

Vale Asari, N., Wild, V., de Amorim, A. L., et al. 2020, MNRAS, 498, 4205

Valentino, F., Brammer, G., Gould, K. M. L., et al. 2023, ApJ, 947, 20

Valentino, F., Magdis, G. E., Daddi, E., et al. 2020a, ApJ, 890, 24

Valentino, F., Tanaka, M., Davidzon, I., et al. 2020b, ApJ, 889, 93

van der Wel, A., Straughn, A. N., Rix, H. W., et al. 2011, ApJ, 742, 111

van Dishoeck, E. F. & Black, J. H. 1988, ApJ, 334, 771

van Dishoeck, E. F. & Blake, G. A. 1998, ARA&A, 36, 317

Vanzella, E., Calura, F., Meneghetti, M., et al. 2017, MNRAS, 467, 4304

Vanzella, E., Claeyssens, A., Welch, B., et al. 2023, ApJ, 945, 53

Veilleux, S., Maiolino, R., Bolatto, A. D., & Aalto, S. 2020, A&A Rev., 28, 2

Virtanen, P., Gommers, R., Oliphant, T. E., et al. 2020, Nature Methods, 17, 261

Vizgan, D., Greve, T. R., Olsen, K. P., et al. 2022a, ApJ, 929, 92

Vizgan, D., Heintz, K. E., Greve, T. R., et al. 2022b, ApJ, 939, L1

Vulcani, B., Trenti, M., Calvi, V., et al. 2017, ApJ, 836, 239

Wakelam, V., Bron, E., Cazaux, S., et al. 2017, Molecular Astrophysics, 9, 1

Walcher, J., Groves, B., Budavári, T., & Dale, D. 2011, Ap&SS, 331, 1

Wang, B., Leja, J., Atek, H., et al. 2023, arXiv e-prints, arXiv:2310.06781

Wang, R., Wagg, J., Carilli, C. L., et al. 2013, ApJ, 773, 44

Watson, D., Christensen, L., Knudsen, K. K., et al. 2015, Nature, 519, 327

Weaver, J. R., Kauffmann, O. B., Ilbert, O., et al. 2022, ApJS, 258, 11

Weigel, A. K., Schawinski, K., Caplar, N., et al. 2017, ApJ, 845, 145

Welch, B., Coe, D., Diego, J. M., et al. 2022a, Nature, 603, 815

Welch, B., Coe, D., Zackrisson, E., et al. 2022b, ApJ, 940, L1

Whitaker, K. E., van Dokkum, P. G., Brammer, G., & Franx, M. 2012, ApJ, 754, L29

White, S. D. M. & Frenk, C. S. 1991, ApJ, 379, 52

White, S. D. M. & Rees, M. J. 1978, MNRAS, 183, 341

Whitler, L., Stark, D. P., Endsley, R., et al. 2023, MNRAS, 519, 5859

Williams, C. C., Maseda, M., Tacchella, S., et al. 2021, UDF medium band survey: Using H-alpha emission to reconstruct Ly-alpha escape during the Epoch of Reionization, JWST Proposal. Cycle 1, ID. #1963

Williams, C. C., Tacchella, S., Maseda, M. V., et al. 2023, ApJS, 268, 64

Williams, R. E., Blacker, B., Dickinson, M., et al. 1996, AJ, 112, 1335

Willott, C. J., Abraham, R. G., Asada, Y., et al. 2023, CANUCS: The CAnadian NIRISS Unbiased Cluster Survey, JWST Proposal. Cycle 3, ID. #4527

Witstok, J., Jones, G. C., Maiolino, R., Smit, R., & Schneider, R. 2023, MNRAS, 523, 3119

Wright, E. L. 2006, PASP, 118, 1711

Wuyts, S., Förster Schreiber, N. M., Genzel, R., et al. 2012, ApJ, 753, 114

Wuyts, S., Förster Schreiber, N. M., Nelson, E. J., et al. 2013, ApJ, 779, 135

Xiao, M., Oesch, P., Elbaz, D., et al. 2023, arXiv e-prints, arXiv:2309.02492

Yang, J., Wang, F., Fan, X., et al. 2020, ApJ, 904, 26

Yin, J., Shen, S., & Hao, L. 2023, arXiv e-prints, arXiv:2310.06785

Yung, L. Y. A., Somerville, R. S., Finkelstein, S. L., Wilkins, S. M., & Gardner, J. P. 2023, arXiv e-prints, arXiv:2304.04348

Zavala, J. A., Buat, V., Casey, C. M., et al. 2023, ApJ, 943, L9

Zavala, J. A., Casey, C. M., Manning, S. M., et al. 2021, ApJ, 909, 165

Zibetti, S., Charlot, S., & Rix, H.-W. 2009, MNRAS, 400, 1181

Zitrin, A., Broadhurst, T., Coe, D., et al. 2011, MNRAS, 413, 1753